Advanced High-Fidelity Reactor Simulators Based on Neutron Transport and Subchannel Methodologies

Zur Erlangung des akademischen Grades
Doktor der Ingenieurwissenschaften (Dr.-Ing.)
der Fakultät für Maschinenbau
Karlsruhe Institut für Technologie

angenommene

Dissertation

von

Miriam Knebel geb. Däubler

geboren in Bremen

Hauptreferent:	Prof. Dr.-Ing. Robert Stieglitz Karlsruhe Institut für Technologie
Korreferent:	Univ.-Prof. Rafael Macián-Juan, Ph.D. Technische Universität München (TUM)
Tag der mündlichen Prüfung:	01.06.2017

2017

Acknowledgements

Firstly, I would like to express my deepest gratitude to my advisor Professor Dr.-Ing. Robert Stieglitz and Dr. Victor Sanchez for giving me the opportunity to do this doctoral research study and for their patient guidance, encouragement and useful feedback during my research work. Furthermore, I am grateful to Professor Rafael Macián-Juan from the Technical University of Munich who agreed to be my second advisor.

Moreover, I wish to thank my colleagues, Dr. Javier Jimenez and Dr. Uwe Imke, for their valuable technical support. I very much appreciate the time they spent advising me. I wish to acknowledge the help concerning DYN3D provided by Dr. Sören Kliem and his colleagues from the Research Center Dresden-Rossendorf.

I would like to show my gratitude to the members of the Institute of Nuclear Fission of the Polytechnic University of Madrid (UPM), first and foremost Dr. Carolina Ahnert, who gave me the opportunity to intern at their institute and to learn how to generate cross section tables.

My special thanks go to Serpent developer team of VTT Technical Research Centre of Finland, especially Jaakko Leppänen, who contributed substantially to my understanding of the inner workings of the Monte Carlo code. Without their forthcoming support, the extent of the work done with Serpent in this thesis would not have been possible.

Last but not least, I would like to thank my friends and, in particular, my family for their continuous encouragement, deep trust and love.

I dedicate this doctoral thesis to my parents, Wolfgang and Elisabeth, as they have supported me unconditionally all my life.

Kerpen, February 2017 Miriam Knebel

Abstract

State-of-the-art nuclear reactor simulators suffer from a number of limitations, which are first and foremost due to their low spatial and energy resolution as well as employing low order neutron transport approximations. The next generation of reactor simulators currently being developed consists of two classes: pin-homogenized and pin-resolved reactor simulators. In this doctoral research study, one tool of each class is developed and assessed for pressurized water reactor (PWR) applications.

An internal coupling between the continuous energy Monte Carlo code Serpent 2 and the sub-channel code SUBCHANFLOW has been implemented to arrive at a pin-resolved reactor simulator. As a pin-homogenized reactor simulator, the development of DYNSUB was continued and concentrated on extending the first version of the tool into a fully functional simulator. Since DYNSUB unlike Serpent 2/SUBCHANFLOW requires pre-computed tables containing effective macroscopic cross sections, a calculation route to determine such multi-dimensional cross section tables for DYNSUB with or without homogenization corrections has been set up. This calculation route supports U.S. NRC production tool SCALE/TRITON and the currently developed Serpent 2 as lattice codes.

The verification and validation analysis following the multi-level methodology provides proof of the reliability of both simulation computer codes. First, Serpent 2's neutron transport model has been tested by modeling VENUS-1 and VENUS-2 critical experiments, which represent modern PWRs. Thereafter, the coupled code Monte Carlo thermal-hydraulics code has been verified by a code-to-code benchmark with TRIPOLI4/SUBCHANFLOW as well as MCNP5/SUBCHANFLOW. Moreover, its simulations captured the hot zero power physics measurements included in the BEAVRS benchmark well. DYNSUB has been successfully applied to analyze a main coolant pump trip, a rod ejection accident, a boron dilution and a main steam line break design basis accident scenario from international benchmarks. Since the computational accuracy achieved by DYNSUB is comparable to other benchmark participants, it has been shown that DYNSUB is fully capable to depict transient reactor problems of PWRs. By studying the Special Power Excursion Reactor Test III rod ejection accident experiments with the Serpent 2-DYNSUB code sequence, on the one hand, DYNSUB has been validated for modeling rod ejection and other reactivity-insertion accidents in PWRs. On the other hand, it has been shown for the first time that the Serpent 2 methodology to determine homogenized few-group constants performs well for hot full power conditions and reactivity insertion accidents since previous reported V&V work for cross sections tables created with Serpent 2 was limited to steady-states at hot zero power conditions. Finally, it has been demonstrated that

both DYNSUB and Serpent 2/SUBCHANFLOW may be used to analyze realistic, industry-like cases with a pin-by-pin/sub-channel resolution by calculating the exercise 2 of the OECD/NEA and U.S. NRC PWR MOX/UO_2 core transient benchmark with high accuracy, i.e. a full PWR core at hot full power conditions. Moreover, DYNSUB has been used to study the hot zero power rod ejection scenario of the same benchmark. This is the first time that a safety relevant transient scenario for a full PWR core is simulated by means of a pin-by-pin simplified transport solution coupled to a sub-channel thermal-hydraulics model. However, an analysis of the numerical performance of both tools for these full PWR core cases reveals that by now neither runs efficiently enough, even on medium-sized computing clusters, for a routine application.

Kurzfassung

Die Genauigkeit heutiger Standardrechenprogramme zur Simulation von Kernreaktoren ist aufgrund ihrer geringen räumlichen und energetischen Auflösung sowie der Verwendung von Näherungen niedriger Ordnung der Neutronentransportgleichung begrenzt. Die nächste Generation derartiger Rechenprogramme, die sich im Moment in der Entwicklung befindet, lässt sich in zwei Typen unterteilen: Programme, die Kernbrennstäbe räumlich homogenisieren, und solche, die Geometrie und Materialien der Brennstäbe im Detail darstellen. Im Rahmen dieser Arbeit ist je ein Programm pro Typ entwickelt worden, das auslegungsrelevante Transienten von Druckwasserreaktoren (DWR) mit hoher räumlicher, energetischer und zeitlicher Auflösung berechnet.

Um einzelne Brennstäbe räumlich vollständig zu erfassen, ist das Unterkanal Thermohydraulik Programm SUBCHANFLOW in das Monte Carlo Neutronentransport Programm Serpent 2 integriert worden. Zur homogenisierten Darstellung der Brennstäbe wurde das Programm DYNSUB in eine voll funktionsfähige Version weiterentwickelt. Da DYNSUB anders als Serpent 2/SUBCHANFLOW im Voraus berechnete Tabellen effektiver makroskopischer Wirkungsquerschnitte benötigt, wurde eine Prozedur zur Erstellung mehrdimensionaler Wirkungsquerschnittstabellen für DYNSUB erarbeitet. Diese Tabellen können Homogenisierungskorrekturen enthalten. Die Prozedur erlaubt die Verwendung des Standardprogramms der U.S. NRC SCALE/TRITON oder des sich in Entwicklung befindenden Serpent 2 als Spektralrechenprogramm.

Für beide Rechenprogramme sind sowohl die ursprünglichen, eigenständigen Programmbestandteile als auch ihre Kopplung verifiziert und validiert worden. Durch die Arbeiten konnte der Nachweis der Zuverlässigkeit für beide Programme erbracht werden. Zunächst ist hierfür das Neutronentransportmodel von Serpent 2 mit Hilfe der kritischen Experimente VENUS-1 und VENUS-2 validiert worden, die moderne DWRs darstellen. Danach ist die Kopplung von Serpent 2 und SUBCHANFLOW durch einen Vergleich mit den verwandten Rechenprogrammen TRIPOLI4/SUBCHANFLOW und MCNP5/SUBCHANFLOW verifiziert worden. Außerdem ist gezeigt worden, dass Serpent 2/SUBCHANFLOW in der Lage ist, die Nullleistungsexperimente des BEAVRS Benchmarks mit hoher Genauigkeit nachzurechnen. DYNSUB wurde seinerseits verwendet, um Szenarien aus internationalen Benchmarks zum Ausfall einer Hauptkühlmittelpumpe, zum Auswurf eines Steuerelements, zur Verdünnung der Borkonzentration und zum Bruch einer Frischdampfleitung zu untersuchen. Da DYNSUB diese Auslegungsstörfälle mit einer mit anderen Benchmark Teilnehmern vergleichbaren Genauigkeit berechnete, ist DYNSUBs volle

Funktionsfähigkeit nachgewiesen worden. Durch das Analysieren der Special Power Excursion Reactor Test III Experimente zum Steuerelementauswurf mit DYNSUB und Serpent 2 als seinem Spektralrechenprogramm konnte einerseits DYNSUB für die Berechnung von Steuerelementauswurf sowie anderen Störfällen mit Reaktivitätszufuhr validiert werden. Andererseits konnte erstmalig gezeigt werden, dass Serpent 2s Methoden zur Berechnung von homogenisierten Wirkungsquerschnitten in wenigen Energiegruppen auch für die Simulation von stationären Vollleistungszuständen und Störfällen mit Reaktivitätszufuhr geeignet sind. Bisherige Verifizierungs- und Validierungsarbeiten für mit Serpent 2 erzeugte Wirkungsquerschnittstabellen waren auf stationäre Nullleistungszustände beschränkt. Zum Abschluss ist gezeigt worden, dass sowohl DYNSUB als auch Serpent 2/SUBCHANFLOW verwendet werden können, um realistische, industrienahe Probleme mit einer Brennstab/Unterkanal-Auflösung zu simulieren. Hierzu wurde die zweite Aufgabe des OECD/NEA und U.S. NRC „PWR MOX/UO_2 core transient benchmark“, die Berechnung eines Reaktorkerns eines kommerziellen DWR unter Volllast, mit hoher Genauigkeit durchgeführt. Zusätzlich wurde mit DYNSUB ein Steuerelementauswurf ausgehend von einem Nullleistungszustand mit derselben Auflösung simuliert. Damit ist erstmalig ein sicherheitsrelevanter Auslegungsstörfall eines DWR mit einer Brennstab/Unterkanal-Auflösung unter Verwendung der „simplified transport“ Näherung gelöst worden. Allerdings zeigt die Analyse der numerischen Leistungsfähigkeit beider Rechenprogramme, dass gegenwärtig selbst auf mittelgroßen Parallelrechnern keine hinreichende Effizienz zur routinemäßigen Anwendung gegeben ist.

Publications related to this thesis

1. M. Daeubler, N. Trost, J. Jimenz and V. Sanchez, 2013. Recent Developments in DYNSUB: new models, code optimization and parallelization. In *Proceedings of the M&C 2013 conference*. Sun Valley, Idaho, USA

2. M. Däubler, J. Jimenez, V. Sanchez, 2013. DYNSUB: A high-fidelity coupled code system for reactor core safety assessment. In *Proceedings of the Jahrestagung Kerntechnik 2013*. Berlin, Germany

3. M. Däubler, J. Jimenez, V. Sanchez, 2014. Assessment of homogenization methodologies for pin-by-pin neutron transport calculations using DYN3D. In *Proceedings of the Jahrestagung Kerntechnik 2014*. Frankfurt, Germany

4. M. Daeubler, J. Jimenez, V. Sanchez, 2014. Generation and Application of Interface Discontinuity Factors in the Reactor Simulator DYN3D. In *Proceedings of the ICAPP 2014 conference*. Charlotte, North Carolina, USA

5. M. Daeubler, J. Jimenez, V. Sanchez, 2014. Development of a high-fidelity Monte Carlo thermal-hydraulics coupled code system Serpent/SUBCHANFLOW – First results. In *Proceedings of the PHYSOR 2014 conference*. Kyoto, Japan

6. M. Daeubler, N. Trost, J. Jimenez, V. Sanchez, R. Stieglitz, R. Macian-Juan, 2014. Static and transient pin-by-pin simulations of a full PWR core with the extended coupled code system DYNSUB. *Annals of Nuclear Energy*, http://dx.doi.org/10.1016/j.anucene.2014.09.057

7. L. Mercatali, A. Venturini, M. Daeubler, V.H. Sanchez, 2015. SCALE and SERPENT solutions of the OECD VVER-1000 LEU and MOX burnup computational benchmark, *Annals of Nuclear Energy*, http://dx.doi.org/10.1016/j.anucene.2015.03.036

8. M. Daeubler, A. Ivanov, B. L. Sjenitzer, V. Sanchez, R. Stieglitz, R. Macian-Juan, 2015. High-fidelity coupled Monte Carlo neutron transport and thermal-hydraulic simulations using Serpent 2/SUBCHANFLOW, *Annals of Nuclear Energy*, http://dx.doi.org/10.1016/j.anucene.2015.03.040

9. M. Knebel, L. Mercatali, V. Sanchez, R. Stieglitz, R. Macian-Juan, 2016. Validation of the Serpent 2-DYNSUB code sequence using the Special Power Excursion Reactor Test III (SPERT III), *Annals of Nuclear Energy,* http://dx.doi.org/10.1016/j.anucene.2016.01.005

Contents

Nomenclature

Symbol	Description	Physical Unit
α	weighting coefficient	
β_{eff}	effective delayed neutron fraction	
c_b	boron concentration	ppm
$\boldsymbol{D}$	streaming operator	
D	diffusion coefficient	cm
E	energy	J
E	parallel efficiency	
ε_X	convergence criterion for physical quantity X	
f	pseudo material mixing fraction, CR insertion fraction	
f^s	interface discontinuity factor	
$\boldsymbol{F}$	fission operator	
$\mathrm{F_{xy}}$	assembly peaking factor	
$\mathrm{F_z}$	axial peaking factor	
$\mathrm{F_q}$	point peaking factor	
g	energy group index	
$\vec{\mathrm{g}}$	gravity	$\mathrm{m/s^2}$
i	iteration index, node index	
J_+	outgoing partial neutron current	$1/(\mathrm{cm^2\,eV\,s})$
J_-	incoming partial neutron current	$1/(\mathrm{cm^2\,eV\,s})$
k	spatial index	
k_{eff}	effective multiplication factor	
l	neutron path length	cm
L	transverse neutron leakage	$1/(\mathrm{cm^3\,eV\,s})$
λ	inverse of neutron transport equation k-eigenvalues	
$\boldsymbol{M}$	transport operator	
N	number of elements	
n	iteration index	
p	sampling probability	
φ	unrelaxed normalized angular neutron flux	$1/(\mathrm{cm^2\,sr\,eV\,s})$
$\tilde{\varphi}$	relaxed normalized angular neutron flux	$1/(\mathrm{cm^2\,sr\,eV\,s})$
Φ	scalar neutron flux	$1/(\mathrm{cm^2\,eV\,s})$
ϕ	node average scalar neutron flux	$1/(\mathrm{cm^2\,eV\,s})$
ϕ^s	scalar neutron surface flux	$1/(\mathrm{cm^2\,eV\,s})$
φ	azimuthal angle, spatial coordinate	°
$\vec{r}$	spatial vector	cm

r	radius, spatial coordinate	cm
ρ	mass density	kg/m^3
$\rho(\omega)$	frequency spectrum of scattering nucleus	
ξ	uniformly distributed random number in [0,1]	
σ	Monte Carlo relative uncertainty	
Σ	macroscopic incident neutron cross section	1/cm
Σ_{maj}	macroscopic majorant cross section	1/cm
Σ_{tot}	macroscopic total cross section	1/cm
Σ_R	macroscopic removal cross section	1/cm
$\boldsymbol{S}$	scattering operator	
S	neutron source	1/(cm^3 sr eV s)
S	parallel speed up	
$S(\alpha,\beta)$	scattering function for incoherent, inelastic neutron scattering	
t	time	s
T	temperature	K
$\boldsymbol{T}$	absorption operator	
θ	relaxation coefficient	
$\vec{X}$	solution field of physical quantity X	
x	spatial coordinate	cm
y	spatial coordinate	cm
z	spatial coordinate	cm

In this thesis, 1.00000(0.00001) is to be read as 1.00000 ± 0.00001. The quantity in brackets is always one standard deviation.

List of Acronyms

1D	one-dimensional
2D	two-dimensional
3D	three-dimensional
ACMFD	Analytic Coarse Mesh Finite Difference
ADF	assembly discontinuity factor
AIC	silver-indium-cadmium
ANSI	American National Standards Institute
API	application programming interface
ARI	all rods in
ARO	all rods out
BBH	black-box homogenization
BC	boundary condition
BDBA	beyond design basis accident
BE	best-estimate
BEAVRS	Benchmark for Evaluation and Validation of Reactor Simulations
BiCGStab	biconjugate gradient stabilized
BWR	boiling water reactor
CBC	critical boron concentration
CBY	COBAYA3
CBY/SCF	COBAYA3/SUBCHANFLOW
CE	continuous energy
CFD	computational fluid dynamics
CH	channel
CR	control rod
CRW	control rod bank worth
CSG	combinatorial solid geometry
DBA	design basis accident
DBRC	Doppler broadening rejection correction
DCS	self-powered neutron detector based reactor power
DES	detached eddy simulation
DIN	Deutsches Institut für Normung
DNS	direct numerical simulation
DT	delta-tracking
ENDF	evaluated nuclear data file

EOC	end of cycle
ESC	extended step characteristic
EWE	error-weighted error
FOM	Figure of Merit
GET	generalized equivalence theory
GUI	graphical user interface
HFP	hot full power
HPMC	High Performance Monte Carlo
HZP	hot zero power
I&C	instrumentation and control
IAPWS	International Association for the Properties of Water and Steam
IBE	improved best-estimate
ICMS	in-core monitoring system
IDF	interface discontinuity factor
IFBA	integral fuel burnable absorber
JEFF	Joint Evaluated Fission and Fusion File
KIT	Karlsruhe Institute of Technology
LES	large eddy simulation
LF	laboratory frame
LPRC	load-off and reactor power controller
LWR	light water reactor
MC	Monte Carlo
MG	multi-group
MOC	method of characteristics
MPI	message passing interface
MSIV	main steam isolation valve
MSLB	main steam line break
NEM	nodal expansion method
NFC	neutron flux control
NPP	nuclear power plant
PM	pesudo material
PPR	pin power reconstruction
PWE	power-weighted error
PWR	pressurized water reactor
RANS	Reynolds-averaged Navier-Stokes
REA	rod ejection accident
RIA	reactivity-initiated accident
RPV	reactor pressure vessel

SA	severe accident
SBCH	sub-channel
SCALE	Standardized Computer Analyses for Licensing Evaluation
SCF	SUBCHANFLOW
SIG	scale input generator
SOR	successive over-relaxation
SP_3	simplified transport
SPERT	Special Power Excursion Reactor Test
SPH	super-homogenization factor
SPND	self-powered neutron detector
SRW	shutdown bank worth
SSS2	Serpent 2
ST	surface tracking
TF	target frame
TH	thermal-hydraulics
TMI	Three Mile Island
TMS	target motion sampling
TR	transient rod
U.S. NRC	United States Nuclear Regulatory Commission
UFS	Uniform-Fission-Site
V&V	verification and validation
VVER	Vodo-Vodyanoi Energetichesky Reaktor (engl. water water power reactor)
VVUQ	verification, validation and uncertainty quantification
WABA	wet annular burnable absorber
XS	cross section

1 Introduction

1.1 Motivation

In order to assess the safety of nuclear power plants (NPP), on the one hand, extensive experimental programs are carried out. On the other hand, plants are modeled numerically and their behavior under given external and internal conditions is studied applying simulation computer codes. The events to be studied in a safety assessment are classified as nominal operation, operational transients, design basis accidents (DBA), beyond design basis accidents (BDBA) and severe accidents (SA). Since many different areas of physics play a role in NPPs, the corresponding simulation codes are often modular, each module handling one specific or a set of similar physical aspects of the entire system. Hence, such simulation tools are often referred to as multi-physics tools. Currently no multi-physics simulation code is able to handle all possible scenarios for a NPP ranging from nominal operation to severe accidents. Here, the focus is on multi-physics tools commonly applied to study nominal operation, operational transients and design basis accidents, i.e. all situations a NPP has been designed to cope with. These tools are commonly referred to as reactor simulators.

The majority of nuclear power plants producing electricity belong to the class of light water reactors (LWR). By now, the two major LWR designs built are pressurized water reactors (PWR) and boiling water reactors (BWR). Since the PWR is the most common electricity-generating nuclear reactor worldwide, this work focuses on PWRs.

Before defining and discussing the state-of-the-art of reactor simulators in section 1.3, the PWR will be briefly introduced in section 1.2.

1.2 Overview of current pressurized water reactors

In a PWR, the heat is generated by the fission of uranium or plutonium and transferred to the primary coolant. The high pressure in the primary system prevents the coolant from boiling at nominal conditions. The heated coolant then flows through steam generators in which it transfers its thermal energy to the secondary system. In that secondary system, the generated steam drives a turbine spinning an electrical generator. Passing the turbine, the steam is cooled down and later condensed in a condenser. Then the condensate is pressurized again and re-injected into the steam generators to close the cycle. A drawing of a four loop PWR primary system is shown in Figure 1.

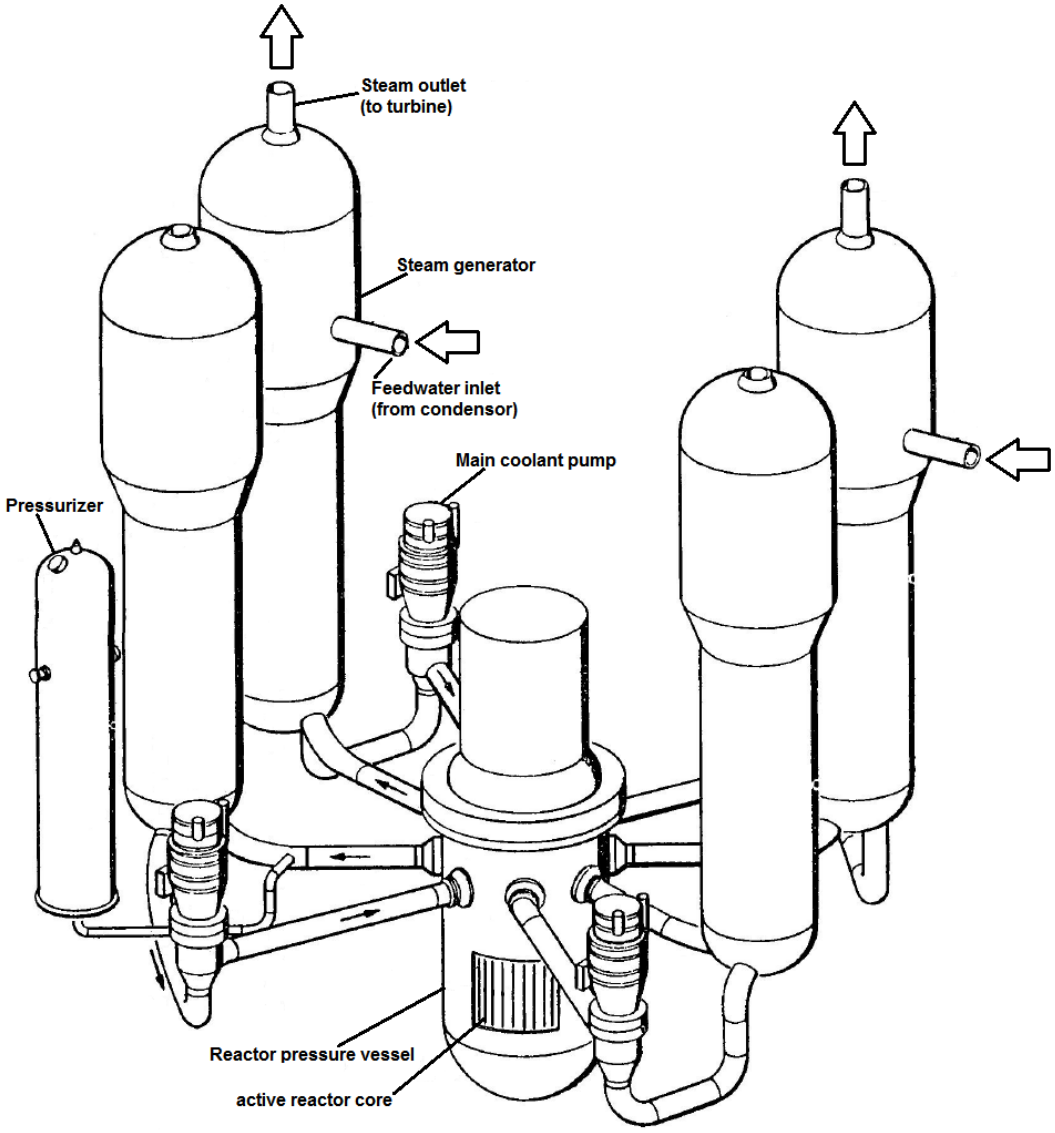

Figure 1: Drawing of a 4-loop PWR primary system, adapted from (United States Nuclear Regulatory Commission, 1975)

As can be seen in Figure 1, the primary system of PWRs usually consists of multiple coolant loops called trains. Depending on the design, there are 2-6 primary loops containing one steam generator and one main coolant pump each. The single pressurizer of the primary system is located in the hot leg of one of the loops. The active reactor core generates heat by nuclear fission and is enclosed in the reactor pressure vessel. A more detailed view of a typical reactor pressure vessel is depicted in Figure 2. The term active reactor core generally refers to the region inside the baffle and between lower and upper core plate. All simulation tools developed in this context handle only the active reactor core of PWRs. The rest of the primary system as well as the secondary system are taken into account using boundary conditions.

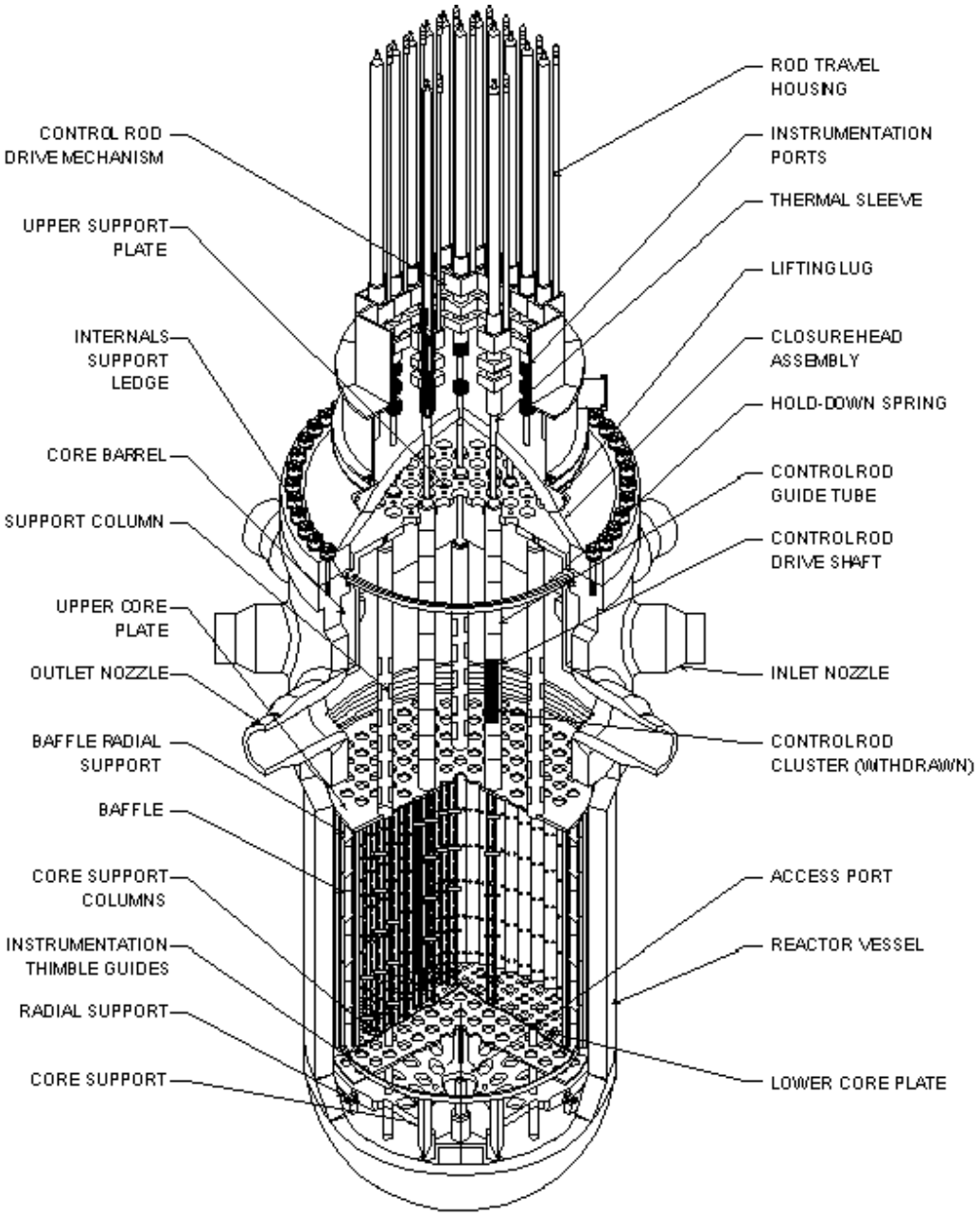

Figure 2: Detailed display of typical PWR pressure vessel and its internal structures (Colson, n.d.)

Fuel assemblies occupy the largest fraction of the active reactor core volume within the baffle. In current PWR designs, fuel assemblies have square or hexagonal cross sections. An exemplary Westinghouse 17x17 square lattice fuel assembly is illustrated in Figure 3. It consists of a 17x17 array of cylindrical fuel rods. Laterally, fuel rods are kept in place by a number of spacer grids. Some fuel rods are replaced with thimble tubes also called guide tubes. The fingers of the rod cluster control or control assembly move in these tubes. Together with the bottom and top nozzle as well as the spacer grids the guide tubes form the skeleton of the fuel assembly.

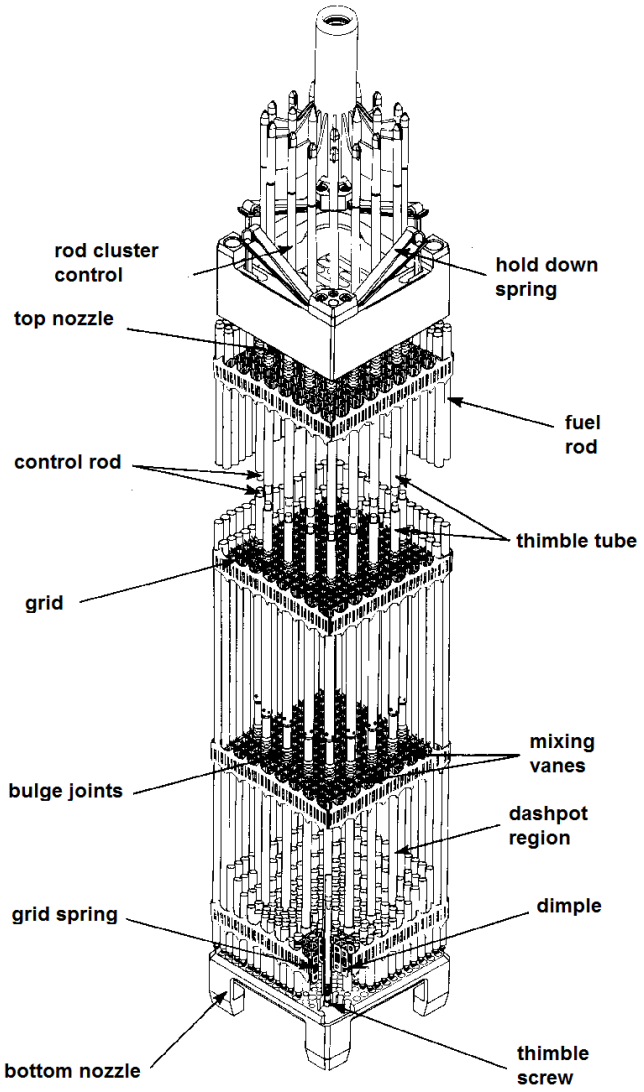

Figure 3: Exemplary Westinghouse 17x17 PWR fuel assembly adapted from (Anon., 2013)

In order to describe the spatial and temporal power generation within a PWR core, coupled neutron and photon radiation transport is required. Both types of radiation contribute to the energy deposited in the system. As the transport of both is determined by the densities and temperatures of the materials they interact with, it is necessary to additionally treat the heat conduction problem in solid structures, the transfer of heat from solids to coolant as well as the fluid mechanics of the coolant flow. Moreover, in certain situations the thermo-mechanical response of the fuel rods and the fluid-structure mechanical interactions need to be evaluated. Especially under accident conditions, possible chemical reactions between reactor structural materials and water cannot be excluded and, hence, require additional modeling.

Unlike fossil thermal power plants, PWRs are not refueled continuously. They usually operate for 12, 18 or 24 months with one core loading. This period of time is referred to as one cycle or

reactor year. At the end of one cycle, the reactor is shut down and maintained. Most of the currently operating PWRs utilize a multi-batch scheme, in which fuel assemblies stay in the active core for multiple reactor years. Only part of the core loading is exchanged during an outage. As a consequence of operation cycles, one needs to consider how the material composition and properties of the nuclear fuel change under irradiation, which is termed as fuel burn-up.

1.3 State-of-the-art reactor simulations

State-of-the-art tools to describe PWR behavior do not compute coupled neutron and photon transport. Instead these computer codes transport neutrons in a reactor core and estimate the total heating power, i.e. direct fission power and gamma heating, using experimentally determined heating values.

The distribution of a neutron population in a reactor, i.e. the neutron flux, is captured by the Boltzmann neutron transport equation. The latter phase space balance equation describes the mean neutron flux obtained from averaging over an infinite number of single neutron histories. There are generally two approaches to obtain an estimate for this mean neutron flux. On the one hand, one can apply numerical methods to solve the linear differo-integral Boltzmann transport equation in an approximate manner. All such approaches are usually referred to as deterministic methods. On the other hand, one could simulate a large number of single neutron histories in order to obtain an estimate of the mean neutron flux using statistical methods. The latter approaches are called Monte Carlo methods.

All state-of-the-art reactor simulators employ deterministic methods to solve the neutron transport problem. The process of any deterministic neutronics analysis is summarized in Figure 4. After measuring microscopic incident neutron cross sections (XS) at several energies, these are combined with theoretical models to obtain continuously varying functions over the energy domain of interest. These results are summarized in Evaluated Nuclear Data Files such as ENDF/B or JEFF.

Since any numerical method to solve the neutron transport equation results in a discretization of both the spatial and energy dependence of mean neutron flux, effective microscopic incident neutron cross sections have to be used, which take this discretization into account. In literature, this effect is often referred to as resonance self-shielding processing. While modern high accuracy deterministic codes may do self-shielding calculations on-the-fly, state-of-the-art tools do not. These computations are done externally using specialized tools commonly called lattice codes. The self-shielded microscopic cross sections are then combined into macroscopic material-wise cross sections as these are required to solve the Boltzmann equation.

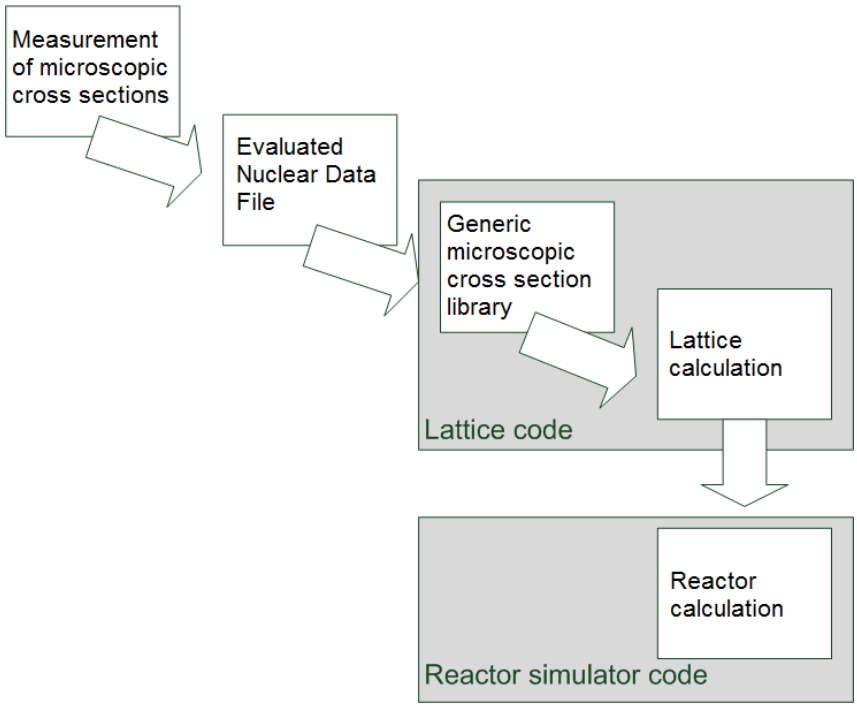

Figure 4: Waterfall model of a deterministic reactor physics analysis

Moreover, reactor simulators may employ such coarse calculation meshes that several different physical materials occupy the corresponding volume in the reactor core. Consequently, the macroscopic effective cross sections of these materials have to be combined into a single set of macroscopic cross sections using a process called homogenization. Homogenized cross sections are also computed using lattice codes. The latter utilize high order approximations of the neutron transport equation on simplified but representative parts of the reactor system in question. These parts are usually referred to as spectral geometries.

Homogenized effective macroscopic cross sections vary with temperature and density of the materials they represent. To account for variations that occur, for instance, over the axial height of the active reactor core, they are tabulated in so called branched cross section libraries. These libraries contain homogenized effective macroscopic cross sections for different thermal-hydraulic state points. Often these state points are defined in terms of coolant density, coolant and fuel temperatures as well as amount of soluble neutron poisons. To consider the change of fuel material compositions during an operation cycle, such cross section libraries also include fuel burn-up as state point variable.

To be able to look up cross sections from the branched cross section libraries, reactor simulator codes need to evaluate the heat conduction problem in solid structures, the heat transfer from solids to the coolant as well as the fluid mechanics of the coolant flow. The coolant water of a PWR is assumed to be a Newtonian fluid. Thus, its single-phase behavior can be described by the Navier-Stokes equation (momentum balance) together with a conservation equation for

mass, a conservation equation for internal energy as well as energetic and thermo-dynamic constitutive equations. For most technical applications, the Navier-Stokes equations have no analytical solution, since they are non-linear partial differential equations. Methods to numerically solve the TH problem differ in terms of the discretization schemes used such as finite volume, finite elements, spectral elements or boundary elements. Moreover, they apply different approximations to model turbulence, e.g. Reynolds-averaged Navier-Stokes Simulation (RANS), Large Eddy Simulation (LES), Detached Eddy Simulation (DES) and Direct Numerical Simulation (DNS). For any of these computational fluid dynamics (CFD) methods, the support of two-phase flows is at different development levels. Two-phase flows, however, may appear in a PWR primary system under accident conditions.

Furthermore, even the computationally least demanding CFD solutions exhibit unacceptably high solution times for routine applications in reactor simulator tools. As a result, most codes revert to computational models based on one-dimensional stream-line theory. In stream-line theory, a set of one-dimensional equations is derived by averaging the local mass, momentum and energy conservation equations over the flow cross section of a pipe, tube or coolant channel. Multi-dimensional effects are handled by coupling terms between the non-linear equations or experimentally derived correlations.

Unlike computational fluid dynamics, one-dimensional two-phase flow models have been successfully derived. All models treat steam and water as inter-penetrating continua. The local balance equations predict only macroscopic flow properties. Their source terms represent the interfacial transfer of mass, momentum and energy. One-dimensional two-phase flow models vary in whether or not they allow for mechanical and thermal non-equilibria between the different phases. Both the one-dimensional single- and two-phase models require several constitutive equations to be closed.

State-of-the-art reactor simulators solve the lowest order approximation of the Boltzmann neutron transport equation, i.e. neutron diffusion theory, or the next higher approximation, i.e. simplified transport (SP_3), with a very coarse energy discretization of usually two energy groups to obtain a fuel assembly-wise power distribution in a reactor core. These powers are passed to simplified fuel rod models to evaluate the heat transfer from the fuel to the coolant, one effective fuel rod per fuel assembly. The coolant fluid flow is generally described using one-dimensional two-phase flow models. In both, neutronics and thermal-hydraulics, the spatial resolution is on the level of fuel assemblies. That means, one fuel assembly is radially represented by a single neutronics mesh cell and a single one-dimensional coolant channel. Here further on, this type of reactor simulator is also referred to as assembly-homogenized. Powers of individual fuel rods cannot be computed directly. In detail, they are re-estimated using pin

power reconstruction techniques (PPR) (Rempe, et al., 1989; Grimm, et al., 1996; Collins, et al., 2012).

Currently, assembly-homogenized, nodal reactor simulators are industrial standard. Commonly known examples are Studsvik Scandpower's Simulate3K (Borkowsky, 1997) and the U.S. NRC code system TRACE/PARCS (Xu, 2006). These tools are often referred to as best-estimate (BE) solutions (Bousbia-Salah & D'Auria, 2007). Even though extensive research on verification, validation and qualification has been carried out for these BE codes (Ivanov, et al., 2007a), several areas of active research remain for their further improvement:

- Branched cross section library generation and parameterization of such libraries (Ivanov, et al., 2007a; Ivanov & Avramova, 2007)
- Enhancement of numerical meshing, mesh qualification and improved inter-mesh mapping schemes (Ivanov & Avramova, 2007)
- Improved accuracy and efficiency of coupled code numerics (Ragusa & Mahadevan, 2009; Ragusa & Mahadevan, 2008; Ellis, et al., 2013)
- Evaluated nuclear data is subject to measurement and theoretical model uncertainties, parts of nuclear power systems are manufactured with production tolerances and the physical models in the multi-physics codes themselves often describe phenomena that have not been fully understood. As a result, uncertainty and sensitivity quantification needs to be performed for any best-estimate tool (Bousbia-Salah & D'Auria, 2007; Avramova & Ivanov, 2010). To this end, several methodologies are being developed (Glaeser, 2008; Williams & Rearden, 2008; Anchel, et al., 2012; Unal, et al., 2011).

Furthermore, it is commonly understood that state-of-the-art reactor simulators are challenged by, for example, reactor cores loaded with both uranium and mixed uranium-plutonium oxide fuel assemblies, increasing discharge burn-up of the fuel and new advanced reactor types being investigated. Deficiencies of these coarse mesh, low order methods can be classified into four basic categories: spatial discretization effect, spatial homogenization effect, group collapsing effect and transport effect (Downar, et al., 2000). Results obtained with state-of-the-art reactor simulators may be improved by considering more energy groups, applying higher order approximations of the neutron transport equation and increasing spatial resolution of the simulation. As a consequence of the latter potential for improvement and steadily increasing, cheaply available computing power, efforts to develop the reactor simulators of the future have begun. All new code developments in academia belong either to the class of pin-homogenized or pin-resolved multi-physics tools. A graphic summary of the three reactor simulators categories discussed is shown in Figure 5.

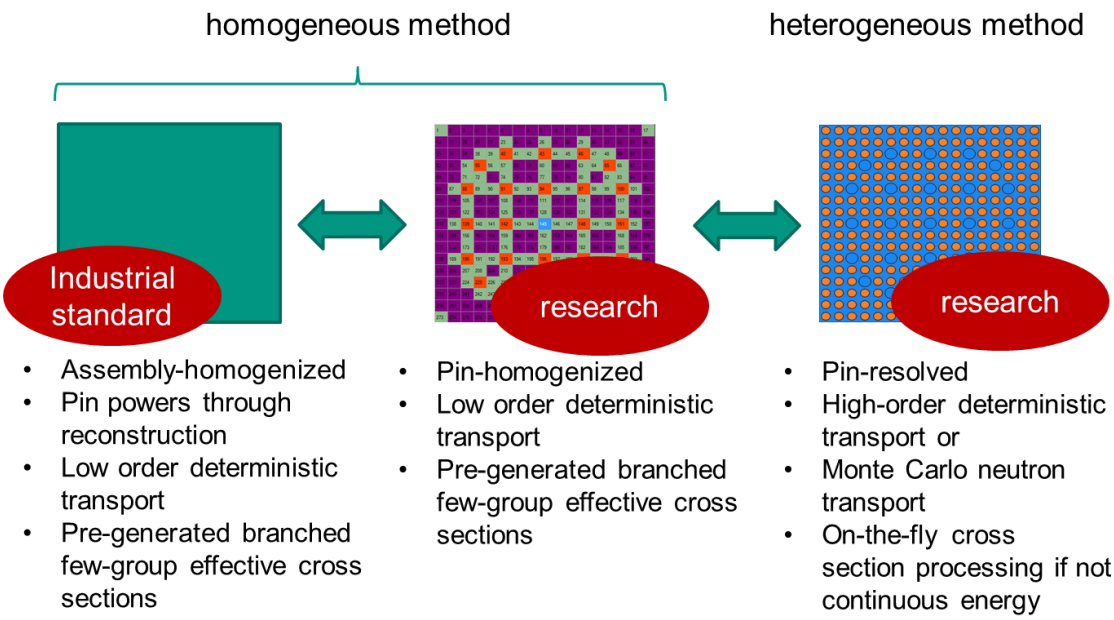

Figure 5: Comparison of the neutronic calculation route of three types of reactor simulator codes

Pin-homogenized reactor simulators are the evolutionary successors of the industrial coupled codes. They are essentially BE tools, that allow for refined spatial and energy resolution, i.e. computational mesh cells covering single fuel pin cells in neutronics and sub-channels in the thermal-hydraulics models as well as a multi-group solution of low order neutron transport. While the spatial discretization and group collapsing effects are certainly reduced, issues arising from spatial homogenization and low order transport approximations remain. Consequently, most of the limitations and approximations common to state-of-the-art codes also apply to pin-homogenized multi-physics tools. While methodologies to obtain reasonably accurate few-group effective assembly-homogenized cross sections are relatively well developed, efforts to extend these to the level of homogenized fuel pins are on-going. The main challenge is to properly treat discontinuities of the homogenized fluxes at pin cell boundaries (Yamamoto, et al., 2004a; Yamamoto, et al., 2004b; Takeda, et al., 2008; Kozlowski, 2011; Grundmann & Mittag, 2011; Herrero, et al., 2012).

To achieve multi-physics solutions of higher fidelity than those of pin-homogenized reactor simulators, one needs to refrain from using homogenization as one major source of modeling errors. This implies using a high enough spatial resolution to resolve the actual geometry and the different materials the structures of fuel and pins consist of. Reactor simulators under development to apply such high spatial resolutions are referred to as pin-resolved or heterogeneous to emphasize that no homogenization is required. Pin-resolved reactor simulators come in two flavors: simulators employing deterministic high order neutron transport and simulators based on Monte Carlo continuous energy neutron transport.

Several deterministic pin-resolved reactor simulators are currently being developed: DeCART/STAR-CD has been used to study an academic PWR minicore under hot full power conditions (Weber, et al., 2007). DeCART/STAR-CCM+ was later employed to analyze a full PWR reactor core operating at nominal power (Kochunas, et al., 2012). Steady-state and transient scenarios for BWR Atrium fuel assemblies were evaluated using TORT-TD/CTF (Magedanz, et al., 2012). Finally, nTRACER/MATRA successfully performed core follow calculations for the first three cycles of a commercial OPR1000 PWR (Jung, et al., 2013) and the two cycles of a PWR described in the BEAVRS benchmark (Ryu, et al., 2014). Of the above tools, TORT-TD/CTF is the only one capable of transient simulations. However, unlike DeCART and nTRACER, it requires cross section tables pre-generated by lattice codes. Both DeCART and nTRACER prepare their cross sections on-the-fly using the sub-group method to treat spatial and energy self-shielding. Moreover, two of the tools employ sub-channel thermal-hydraulics models (COBRA-TF, MATRA) and two computational fluid dynamics tools (STAR-CD, STAR-CCM+). Besides DeCART and nTRACER, several other pin-resolved deterministic reactor simulators are currently being developed and designed to run in parallel, e.g. MPACT (Kochunas, et al., 2013), Denovo (Jarrell, et al., 2012), PROTEUS-S_n (Shemon, et al., 2014) and UNIC (Kaushik, et al., 2009). These code developments aim at petascale super-computers, since only these machines offer sufficient computational power to finish routinely studied, engineering sized problems in an acceptable time. For example, Denovo coupled to XSProc and COBRA-TF was used to simulate a full PWR core at hot full power conditions. The problem is based on the Watts Bar Unit 1 initial core. Depending on the concentration of soluble boron in the coolant the simulations took between 10 and 15 hours on 18,769 cores of the super-computer Titan (Palmtag, et al., 2014). Furthermore, the parallel computational framework MOOSE for coupled systems of non-linear equations is developed at Idaho National Laboratory (Gaston, et al., 2009). Among other multi-physics applications, a comprehensive nuclear reactor multi-physics tool is being built based on MOOSE (Gaston, et al., 2012; Williamson, et al., 2012; Gleicher, et al., 2014).

Compared to high order deterministic neutron transport tools, Monte Carlo continuous energy neutron transport codes have the advantage of neither using spatial nor energy discretization. As a result, the cross sections they employ do not need any self-shielding treatment. In other words, continuous energy Monte Carlo neutron transport solutions are completely free of spatial discretization and group collapsing effects. However, numerical algorithms employed in Monte Carlo tools have been reported to introduce artificial and sometimes even unphysical effects. Nonetheless Monte Carlo tools certainly suffer from the least number of limitations in physics modeling, hence, numerous groups work on reactor simulators using Monte Carlo neutron transport (Li & Wang, 2012; Vazquez, et al., 2012; Espel, et al., 2013; Ivanov, et al., 2013; Gill, et al., 2014; Kotlyar, et al., 2011; Bernnat, et al., 2012; Kelly, et al., 2014; Sjenitzer, et al.,

2015). Most of these coupled codes still employ sub-channel or even channel thermal-hydraulics models, only one utilizes CFD to handle the TH problem (Li & Wang, 2012). Of the above coupled codes, only TRIPOLI4/SUBCHANFLOW is capable of simulating reactor transients (Sjenitzer, et al., 2015). In numerical methods for solving the Boltzmann neutron transport equation, it is generally well understood, how to extend a steady-state solution into a transient one needed for reactor dynamics simulations. For continuous energy Monte Carlo, however, Sjenitzer was the first to succeed in developing a corresponding method. Like the deterministic pin-resolved reactor simulators, Monte Carlo based ones require large scale parallel computers to be run on and finish in a reasonable amount of time.

In a recent publication, Smith and Forget tried to derive a generally accepted definition of high-fidelity, ab-initio or in-silico multi-physics tool (Smith & Forget, 2013). Any pin-homogenized reactor simulator cannot reach the described high-fidelity simulation goals. Only pin-resolved simulation codes have the chance to develop into a high-fidelity description of nuclear reactors. Moreover, the computational resources consumed by such high-fidelity tools are expected to be enormous. Early estimates of Smith and Forget forecast a memory consumption of at least 1TB only to store the nuclide composition of a standard U.S. PWR. The actual memory consumption to solve coupled neutron-gamma transport, thermal-hydraulics, fuel performance and depletion will be significantly higher than that. Moreover, numerical solvers to tackle the coupled non-linear equations of all areas of physics involved simultaneously and corresponding pre-conditioners are subject of on-going research. In the coming decades, only large computing clusters and super-computers will provide the necessary computing power and level of parallelism.

Pin-homogenized reactor simulators, however, have the potential to provide a cost-effective improved best-estimate (IBE) description of LWR behavior for both static and transient relevant scenarios. Cost-effectiveness refers to well-optimized codes for small computing clusters users or customers commonly have at their disposal. Pin-homogenized reactor simulators could bridge the gap until truly high-fidelity multi-physics tools are mature enough and become readily available and applicable. Fittingly, nuclear industry is interested in pin-homogenized solutions as next industrial standard and has started working on new codes systems, for example, the ARCADIA code system of AREVA (Porsch, et al., 2012) and AEGIS-SCOPE2 of Nuclear Fuels Industries (Tatsumi & Yamamoto, 2003; Yamamoto & Ikeno, 2005; Yamamoto, et al., 2010).

1.4 Main thesis objectives

In this thesis, both a pin-homogenized and a pin-resolved reactor simulator are developed and applied to study PWRs. Both tools are to be assessed concerning quality and solution time. The areas of physics to be included in both simulation codes are neutron radiation transport, coolant fluid flow, heat conduction in the fuel rods and heat transfer to the coolant. The ultimate goal of this work is to demonstrate that both tools can be used to analyze realistic, engineering-sized and industry-like full PWR reactor cores at hot full power conditions with a reasonable accuracy in an adequate amount of time.

The method to develop both pieces of software is illustrated in Figure 6. Based on a conceptual PWR active reactor core model, corresponding mathematical models are derived and implemented. For each part of the mathematical model the code is verified. Afterwards, a simulation using the entirety or a large fraction of the developed software is performed. The retrieved simulation results are consistency proved with the mathematical model as a whole. The solution verification is executed either via code-to-code benchmarks or with the help of manufactured solutions.

In a next step, the uncertainties of the simulation results are quantified. The simulation results combined with their uncertainties, here called simulation outcomes, are compared quantitatively to available experimental data. This process is termed as validation. If an acceptable agreement is not achieved, the conceptual and mathematical models are improved so that they more accurately reflect physical reality. What constitutes an acceptable agreement and, consequently, acceptable level of uncertainty in the simulation outcomes depends on the engineering problem at hand. For example, if a simulation is to be used to prove that the isothermal Doppler temperature reactivity coefficient is negative, both the nominal value of the coefficient needs to be negative and its uncertainty has to be sufficiently small. The latter ensures that the upper confidence bound falls on the negative semi-axis.

This iterative process is often abbreviated to VVUQ, i.e. verification, validation and uncertainty quantification. Due to time constraints, simulation uncertainties will not be quantified here. The validation step will be performed using the simulation results, not the simulation outcomes.

If experimental data has too low resolution or is incomplete, it is often complemented with simulations that are considered to have a higher fidelity than the one to be assessed, for example, a pin-resolved reactor simulator can produce a reference solution to test a pin-homogenized code.

At the Karlsruhe Institute of Technology (KIT), the development of a pin-homogenized reactor simulator named DYNSUB has already commenced in a previous doctoral thesis. A first version of the tool has been implemented and limited efforts to perform code and solution

verification have been undertaken (Gomez-Torres, et al., 2012a; Gomez-Torres, et al., 2012b). Consequently, in this work the first version of code will be extended into a fully functional pin-homogenized reactor simulator. Moreover, DYNSUB's solution is to be verified by code-to-code and validated by code-to-data benchmarks. Last but not least, no tool chain to prepare few-group effective cross sections for DYNSUB exists so far at KIT making the tool dependent on support of third parties. To remedy this, a tool chain using both a deterministic and a Monte Carlo neutron transport based lattice code is to be established and submitted to verification and validation (V&V).

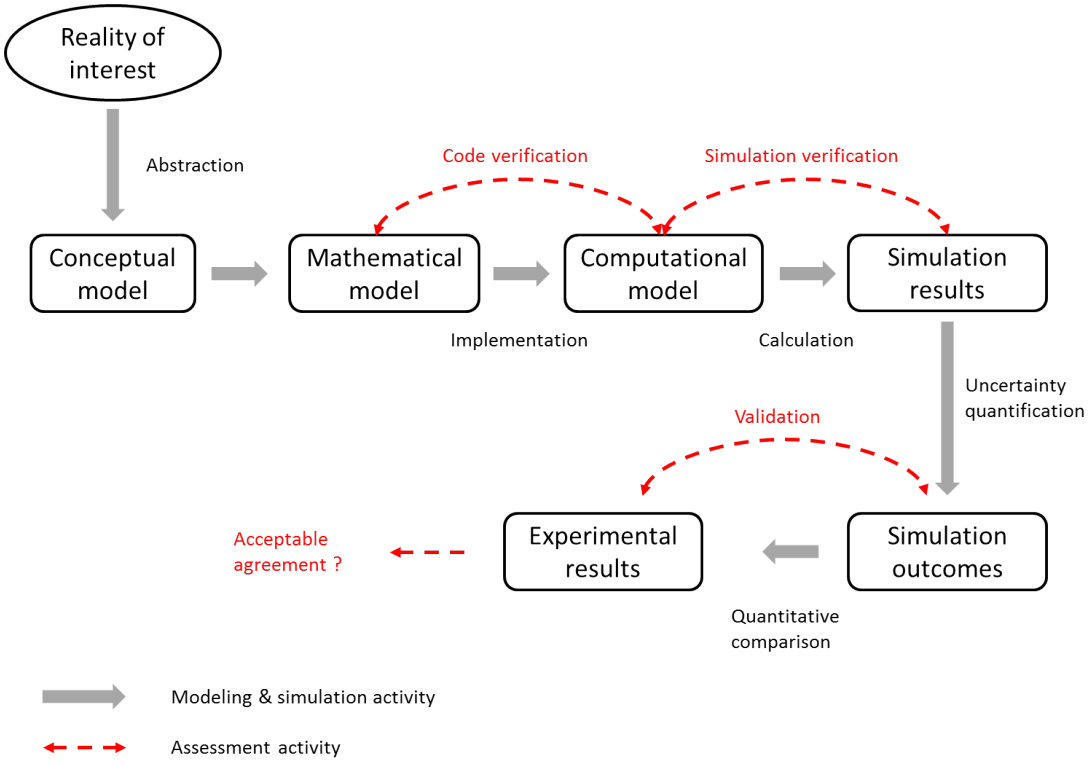

Figure 6: Flowchart for verification, validation and uncertainty quantification (VVUQ) methodology for simulation software development applied in this work.

Unlike for the pin-homogenized case, no previous work has been done on a pin-resolved reactor simulator. A new development employing continuous energy Monte Carlo neutron transport is to be done. Monte Carlo neutron transport was chosen over a high order deterministic solution, since it uses the least approximations concerning the underlying physics. This new code development aims at producing a leading edge Monte Carlo neutron transport simulation tool including thermal-hydraulic feedback based on the existing Serpent 2 code. Additionally, this tool can be utilized to produce reference solutions to foster improving DYNSUB.

1.5 Structure of this thesis

In the following chapter, implementation of the pin-resolved reactor simulator Serpent 2/SUBCHANFLOW and most important code verification efforts are summarized. The solution verification and validation of the pin-resolved tool are discussed in detail in chapter 3. Extending pin-homogenized DYNSUB and establishing a cross section preparation tool chain are presented in chapter 4 followed by DYNSUB V&V utilizing international benchmarks in chapter 5. Afterwards, in chapter 6 both Serpent 2/SUBCHANFLOW and the Serpent 2-DYNSUB tool chain are employed to model the Special Power Excursion Reactor Test III (SPERT III). Finally, both pin-homogenized DYNSUB and pin-resolved Serpent 2/SUBCHANFLOW pin-by-pin simulations of industry-like problems are analyzed in chapter 7. At last, the overall achievements and open issues are summarized.

2 Pin-resolved Reactor Simulator Serpent 2/SUBCHANFLOW

2.1 State-of-the-art of Monte Carlo neutron transport based reactor simulators

Monte Carlo neutron transport with thermal-hydraulic feedback is also an actively developed and quickly progressing field. Up to now, most existing Monte Carlo neutron transport tools, which can consider thermal-hydraulic feedback, were either applied to small academic problems using a high spatial resolution in the thermal-hydraulics model (Li & Wang, 2012; Vazquez, et al., 2012; Espel, et al., 2013; Ivanov, et al., 2013; Gill, et al., 2014) or to full LWR core models only utilizing a spatially coarse TH description (Kotlyar, et al., 2011; Bernnat, et al., 2012). Ivanov recently published the only pin and sub-channel level resolved simulation of a quarter PWR core (Ivanov, et al., 2014; Ivanov, et al., 2015). Besides large-scale neutron transport simulations with spatially refined thermal-hydraulics models, core follow calculations for realistic LWR models employing Monte Carlo neutron transport coupled to a thermal-hydraulics and a depletion solver are becoming feasible. The code MC21 was successfully applied to study cycle 1 of the BEAVRS benchmark (Horelik, et al., 2016) core with a simplified power history (Kelly, et al., 2014). A quarter core model with 379,000 depletion zones was used. In each zone, 200 isotopes were tracked. The thermal-hydraulic feedback in each fuel assembly was described using four sub-channels per FA.

Most of the above simulation tools are coupled externally, i.e. the Monte Carlo neutron transport tool and the thermal-hydraulics code communicate via in- and output files read/write operations. External couplings generally employ driver scripts or wrapper codes. Such an approach is simple, as it does not require any adaption of the source of any involved tool. However, to be able to handle thermal-hydraulic state point fields, the Monte Carlo geometry in external couplings needs to be subdivided into a multitude of cells each corresponding to one set of TH information. This process is not only error prone but also limits the application of the coupled code to small, academic problems.

Alternatively, an internal coupling approach can be utilized as done for MCNP5 and SUBCHANFLOW (Ivanov, et al., 2013; Ivanov, et al., 2014). In an internal coupling, the thermal-hydraulics tool is integrated into the Monte Carlo neutron transport tool as a module. More importantly, the thermal-hydraulic state point information is separated from the geometry description allowing for treating arbitrary problem sizes.

In order to handle the temperature dependence of nuclear data in Monte Carlo neutron transport, two distinct practical methodologies exist. On-the-fly schemes, as the name suggests, compute the effects of temperature on free atom cross sections during the transport simulation and introduce negligible approximations. Such schemes are available or being developed in MCNP6 (Martin, et al., 2013), Serpent 2 (Viitanen & Leppänen, 2012a; Viitanen & Leppänen, 2012b) and OpenMC (Forget, et al., 2014).

However, most coupled Monte Carlo thermal-hydraulics solutions adapt stochastic mixing or a pseudo-materials ansatz as an approach to treat the temperature dependence of nuclear data (Bernnat, et al., 2012; Vazquez, et al., 2012; Ivanov, et al., 2014). Stochastic mixing is beneficial compared to a brute force temperature treatment in Monte Carlo neutron transport. In a brute force treatment, one would pre-generate nuclear data at very small temperature intervals (say 1 K) and load the entire library into memory for usage during the transport cycle. This consumes an enormous amount of memory. The pseudo material approach is able to reduce this consumption by allowing for larger temperature spacing of the nuclear data, e.g. 50 K. But unlike on-the-fly schemes, the pseudo-material approach is effectively an interpolation technique which is approximate by nature.

2.2 Goals for Serpent 2/SUBCHANFLOW development

Here, the efforts undertaken to develop a pin-resolved Monte Carlo neutron transport based reactor simulator capable of handling realistic reactor cores are presented.

In section 2.1, it was discussed that only tools utilizing an internal coupling approach can readily, reliably be used to model large scale problems. Out of the methods to treat the temperature dependence of nuclear data, the on-the-fly schemes are the most accurate. Consequently, the Monte Carlo thermal-hydraulics tool should be internally coupled and utilize an on-the-fly scheme. Such a tool would then employ even less approximations than the currently most sophisticated pin-resolved Monte Carlo neutron transport based reactor simulator MCNP5/SUBCHANFLOW (Ivanov, et al., 2014; Ivanov, et al., 2015).

Out of the stochastic neutron transport codes offering on-the-fly temperature treatment schemes, Serpent 2 (Leppänen, 2013) was chosen. Since the pin-resolved tool being developed is to be used for comparative assessment with pin-homogenized DYNSUB (see chapters 6 and 7), the fact that Serpent was originally designed and optimized to be used as lattice code to generate effective few-group cross section libraries for deterministic tools led to this decision. Serpent 2 offers the unique possibility to provide a reference solution and few-group cross section sets for a given problem to a deterministic reactor simulator easily eliminating the need to use a third

tool such as a classical deterministic lattice code. The latter would only introduce further error sources and complicate the performance analysis of the deterministic reactor simulator.

Though conceptually a high-fidelity, in-silico or ab-initio multi-physics tool should employ CFD as the thermal-hydraulics model with the least approximations, CFD tools are not yet mature enough and their computational cost is too high. To allow for simulating pressurized and boiling water reactors as well as Generation IV designs, the Karlsruhe Institute of Technology in-house sub-channel thermal-hydraulics code SUBCHANFLOW (SCF) (Sanchez, et al., 2010) is used in this context.

2.3 Simulation codes employed

2.3.1 Monte Carlo code Serpent 2

Serpent 2 (Leppänen, 2013) is a three-dimensional continuous-energy (CE) Monte Carlo neutron transport code. It uses a universe-based combinatorial solid geometry (CSG) model as most other Monte Carlo tools. Neutrons are tracked in the geometry using a combination of surface tracking (ST) and Woodcock delta-tracking (DT). ST is used as a fallback in case the efficiency of DT is too low (Leppänen, 2010).

Serpent's CE cross sections are given in ACE format. The physics of all interactions are based on classical collision kinematics, ENDF reaction laws and probability table sampling in the unresolved resonance region. All CE cross sections are reconstructed on an unionized energy grid (Leppänen, 2009). Furthermore, a built-in Doppler-broadening pre-processor routine allows for converting any ACE format cross sections to a higher temperature. This function is useful if the required temperature is not in the data library. It has been validated and its numerical efficiency has been proven (Viitanen, 2009). However, the Doppler broadening pre-processor is not capable of adjusting temperatures of unresolved resonance probability tables or inelastic neutron scattering data $S(\alpha, \beta)$.

A new feature recently introduced into Serpent 2 is a multi-physics interface (Leppänen, 2012). The interface may be utilized to exchange data with thermal-hydraulics and fuel performance codes. Currently, it comprises four types of sub-interfaces, which differ in terms of the used format for passing data between the external solver in question and Serpent. One may employ piecewise constant distributions on regular meshes (type 1), weighted averages of point-wise values (type 2), a user-defined functional dependence (type 3) or unstructured three-dimensional meshes (type 4) (Leppänen, 2012; Leppänen, et al., 2014d).

Utilizing the multi-physics interface implies that Serpent uses the target motion sampling (TMS) method to treat the temperature dependence of the continuous-energy cross sections

(Leppänen, 2012). TMS has been implemented in Serpent recently (Viitanen & Leppänen, 2012a; Viitanen & Leppänen, 2012b). By now, unresolved resonances and bound-atom scattering cannot yet be treated with TMS (Viitanen & Leppänen, 2012b; Viitanen & Leppänen, 2013) severely limiting the applicability of the method for nuclear engineering applications. A methodology to circumvent this limitation for thermal bound-atom scattering is discussed in section 2.4.

In its original form the TMS method relies on 0 K continuous energy cross sections and does not require a Doppler Broadening Rejection Correction (DBRC) (Viitanen & Leppänen, 2012a; Becker, et al., 2009). One measure to improve the numerical performance of TMS in Serpent is to use a basis library of continuous-energy cross sections for temperatures higher than absolute zero (Viitanen & Leppänen, 2013). However, in the latter case, one has to apply DBRC again. Unfortunately, up to now, the TMS implementation in Serpent 2 is incompatible with DBRC. In this work, basis libraries of continuous-energy cross sections for temperatures higher than absolute zero are employed for reasons of computational efficiency but no resonance upscattering is considered.

2.3.2 Sub-channel code SUBCHANFLOW

The sub-channel code SUBCHANFLOW solves three mixture balance equations for mass, momentum and energy in axial direction as well as an additional lateral momentum equation at sub-channel or fuel assembly level (Sanchez, et al., 2010). A fully implicit method is used to solve steady-state and transient problems. Three kinds of solvers are available: a direct Gauss elimination solver for small problems, a SOR and a BiCGStab iterative solver. Because of the numerical algorithm employed, SUBCHANFLOW is restricted only to vertical upward flow.

For water the thermophysical properties and state functions, the IAPWS-IF97 formulations (Cooper & Dooley, 2007) have been adopted. The heat conduction in a fuel pin is solved with a standard finite volume method. The heat transfer coefficient between fuel pin and reactor coolant is determined by using empirical correlations depending on the heat transfer mode and flow regimes. Void fraction, pressure drop, wall friction and turbulent mixing are also calculated by means of constitutive relations. SUBCHANFLOW is being validated using experimental data relevant for PWR (Imke & Sanchez, 2012), BWR (Jaeger, et al., 2013) and liquid metal cooled systems.

2.4 Stochastic mixing fall back for the Target Motion Sampling (TMS) method

2.4.1 Implementation

The TMS method is a stochastic method to account for the effect of thermal motion in a Monte Carlo neutron transport calculation. It is based on sampling the target velocities from a Maxwell-Boltzmann distribution at the collision sites. Followed by a transformation into the target-frame to solve the reaction physics for a given temperature. Using this method, the total macroscopic cross section becomes a distributed quantity. This can be handled by applying rejection sampling techniques. A detailed description of TMS can be found in (Viitanen & Leppänen, 2012a; Viitanen & Leppänen, 2012b; Viitanen & Leppänen, 2013).

TMS cannot be used for thermal bound-atom scattering since the chemically bound target atoms do not have velocities that are distributed according to Maxwell-Boltzmann in a thermal energy range. If the temperature dependent velocity distributions of the chemically bound targets were known for all the thermal energy range, the TMS could be extended to cover the thermal bound-atom scattering in a straightforward manner.

Conceptually, only an on-the-fly method for sampling thermal scattering data is in line with both TMS and an internal coupling. However, currently just one such method is being developed at Rensselaer Polytechnic Institute (Pavlou & Ji, 2014). As this method has not yet reached maturity to be implemented in Serpent 2, the pseudo-material approach is to be applied for the nuclides affected by thermal bound-atom scattering.

In the pseudo-material approach, each material nuclide is represented by two sets of nuclear data. The data sets are evaluated at temperatures T_{low} and T_{high} enclosing the actual temperature T of the material of interest. In the case of linear mixing, the fraction of nuclide with the lower temperature is obtained from equation (1).

$$f = \frac{T_{\mathrm{high}} - T}{T_{\mathrm{high}} - T_{\mathrm{low}}} \,. \tag{1}$$

Accordingly, the fraction of the cross sections evaluated at the higher temperature T_{high} is $(1 - f)$. The stochastic mixing approach is not an interpolation in the classical sense. No nuclear data is ever generated at temperature T. The method relies on the stochastic nature of the neutron transport process. For a sufficiently large number of neutron histories, the above approach is equivalent to using the below expression for the cross sections, which is effectively a linear interpolation.

$$\Sigma(T) = f\,\Sigma_{\text{low}}(T_{\text{low}}) + (1-f)\,\Sigma_{\text{high}}(T_{\text{high}})\,. \tag{2}$$

Van der Marck was one of the first to propose the stochastic mixing approach (van der Marck, et al., 2005). He used a square root mixing coefficient instead of the linear one presented in equation (1). Slightly later, Trumbull assessed different interpolation techniques for free atom cross sections at different temperatures (Trumbull, 2006). He showed that for the linear interpolation of free atom cross sections (see equation (2)) the linear interpolation coefficient is more accurate than the square root one in all his test cases. Hence, in Serpent 2/SUBCHANFLOW a linear mixing coefficient is utilized.

The neutron tracking algorithm of Serpent 2 consists of six high level steps in case of Woodcock delta-tracking, which are listed below. In that listing, LF refers to the laboratory frame and TF to a target frame. In the first version of the TMS method, the latter was the target-at-rest frame. In the updated version of TMS, the target may still have a non-negligible motion relative to the "target frame". Thus, free atom cross sections evaluated at any temperature below the temperature of the target in the LF may be used as basis for the TMS method (for more details see (Viitanen & Leppänen, 2013)). Furthermore, $\xi \in [0,1]$ is a uniformly distributed random number. Σ_{maj} refers to the majorant cross section and $\Sigma_{\text{maj,n}}$ to the nuclide-wise majorant. Moreover, E_{LF} is the energy of the tracked neutron in the laboratory frame, E_{TF} the energy of the very same neutron in the target frame.

1. Sample the neutron path length l from:

$$l = \frac{-\log(\xi)}{\Sigma_{\text{maj}}(E_{\text{LF}})}\,. \tag{3}$$

2. Accept collision point candidate based on relative local material density

$$\xi < \frac{\rho(\vec{r})}{\rho_{\text{max}}}\,. \tag{4}$$

3. Sample collision nuclide n with a probability of p_n based on nuclide-wise majorant:

$$p_n = \frac{\Sigma_{\text{maj,n}}(E_{\text{LF}})}{\Sigma_{\text{maj}}(E_{\text{LF}})}\,. \tag{5}$$

4. Sample velocity and direction of target from Maxwell-Boltzmann distribution, switch into TF
5. Accept collision point candidate based on:

$$\xi < \frac{\Sigma_{\text{tot,n}}(\vec{r},E_{\text{TF}})}{\Sigma_{\text{maj}}(E_{\text{LF}})}\,. \tag{6}$$

6. Sample reaction type based on nuclide microscopic cross sections.

For the above tracking algorithm the majorant cross sections is defined by equation (7).

$$\Sigma_{\mathrm{maj}}(E_{\mathrm{LF}}) \geq \Sigma_{\mathrm{tot}}(\vec{r}, E_{\mathrm{TF}}, T, \rho) \quad \forall\ \vec{r}, E_{\mathrm{TF}}, T, \rho\ . \tag{7}$$

In case of Woodcock delta-tracking, the majorant cross section is evaluated using multiple materials and valid for the entire problem geometry or large parts thereof. In some parts of geometry surface tracking maybe employed because of DT efficiency issues. For ST, the majorant cross section is determined for each cell in the geometry, i.e. effectively all materials separately.

The tracking algorithm presented above is almost identical for ST. However, after sampling the neutron path length l, the distance to the nearest cell surface is computed. If the neutron path length should exceed that distance, the neutron is moved to the surface and the tracking is restarted at step 1. Otherwise, steps 2 through 6 are executed.

The use of majorant cross sections in the DT and ST neutron transport allows for the Serpent geometry to be completely unaffected by thermal-hydraulic state point information. In addition, continuously varying density and temperature distributions can be handled. Consequently, any stochastic mixing fall back implemented in Serpent should preserve both features of the Serpent 2 methodology.

Revisiting how to compute the majorant cross section (cp. equation (7)), one finds that Serpent 2 requires to have a pre-determined temperature and density range. In case of the density, however, the maximum of a macroscopic cross section is always found at the maximum density of a material. Hence, specifying the maximum expectable density is sufficient.

For the stochastic mixing fall back, Serpent identifies any material in the problem definition that is affected by the internal interface and has $\mathrm{S}(\alpha, \beta)$ scattering laws associated with at least one of its constituent nuclides. For each of those nuclides the nuclear data evaluation of the $\mathrm{S}(\alpha, \beta)$ is determined. Afterwards, all $\mathrm{S}(\alpha, \beta)$ tables of that nuclear data evaluation necessary to cover the specified coolant temperature range are loaded into memory. Serpent's internal Doppler pre-processor is then used to prepare free atom cross sections at the temperatures the scattering law tables were evaluated. At the end of this process, Serpent holds $N \geq 2$ additional fully defined scattering nuclides in memory, that may be used for the stochastic mixing fall back.

With the introduction of the stochastic mixing fall back, solely the fourth step of the delta- and surface-tracking algorithm is changed as illustrated below.

4. *If nuclide n has no thermal scattering data associated with it:*

   sample velocity and direction of target from Maxwell-Boltzmann distribution, switch into TF

   else

   identify two scattering nuclides with temperatures enclosing the local temperature, compute the mixing fraction f (see equation (1)) and use it to sample which scattering nuclide to use, do NOT transform into TF

As the stochastic mixing or pseudo-material approach includes no transformation into a target frame, one has to adapt equation (7), when computing the nuclide-wise majorant for the nuclides with associated thermal bound-atom scattering data. In those cases, the total macroscopic cross section on the right hand side has to be evaluated for neutron energies in the laboratory frame E_{LF}.

2.4.2 Verification of stochastic mixing fall back implementation

After the implementation of the stochastic mixing fall back for TMS, the coding done has been verified. One selected code verification case is presented here, in which the fall back algorithm has to recover a known, exact reference solution.

An infinite lattice of 3.65755 m long fresh 4.2 wt% enriched uranium oxide (UOX) fuel pins is studied employing ENDF/B VII.0 evaluated nuclear data. The pin is surrounded by light water as coolant forming a square pin cell with 1.26 cm side length. The remaining geometry and material details of the model are summarized in Table 46 in Appendix A.

The water surrounding the UOX fuel pin has been divided into two axial zones of equal height. In the first zone, the temperature of the water is set to 500 K and in the second one to 600 K. The temperature of the fuel pellet is assumed to be 900 K, clad and gas gap are kept at 600 K throughout the model. The two water zones have been modeled using two separate approaches. In the reference model, the cell containing the water has been subdivided axially. For each of the two new cells a water material at 500 K and 600 K respectively has been defined. In the stochastic mixing fall back model, Serpent 2's multi-physics interface has been utilized to change the temperature of the water in both axial zones. By employing the interface, TMS is enabled and pseudo material mixing fall back is applied for hydrogen bound in water. As the ENDF/B VII.0 evaluated nuclear data includes $\mathrm{S}(\alpha,\beta)$ scattering laws for hydrogen bound in water at 500 K and 600 K, the fall back algorithm should recover the reference solution. To prove this, the neutron spectra in all materials of the model are tallied in the SCALE 238 energy

group structure, which was especially optimized for thermal light water reactors. The spectra are normalized scalar neutron flux.

In order to ensure sufficient statistics for the fine energy group structure tallies, $2 \cdot 10^6$ neutrons are simulated per cycle. 600 active cycles followed 20 inactive cycles. Based on the Shannon entropy, the latter is enough to converge the fission source.

The 238-group neutron spectrum in the first water zone obtained with stochastic mixing fall back is compared to the reference solution in Figure 7. For visibility, the statistical uncertainty of the tallied spectra is not plotted. In the inset graph of Figure 7, however, which displays the relative difference between both results, the error bars show the propagated statistical uncertainty. The abbreviation PM refers to pseudo material.

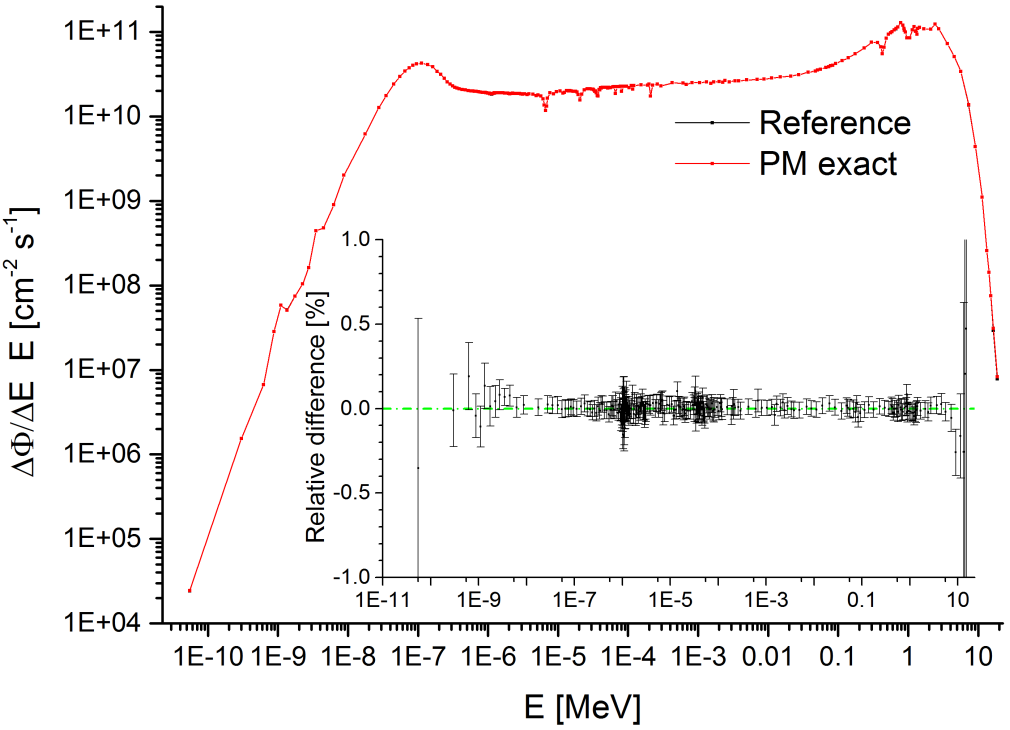

Figure 7: Comparison of neutron spectra normalized to scalar neutron flux in first water zone of the fall back verification model predicted with and without stochastic mixing fall back

In this particular light water reactor problem, there is no significant number of neutrons with energies below 10^{-9} MeV and above 15 MeV. As a consequence of the insufficient statistics, deviations in the neutron spectra occur. For the remaining energy range, the relative difference is almost zero. Nevertheless, there are some regions especially around 1 eV and in the epithermal energy range, in which non-negligible differences are observed. Trying to understand whether these differences indicate a flaw in the fall back algorithm, replica runs of the reference Serpent 2 model have been performed and the differences between the spectra of these runs are analyzed. The relative difference proves to exhibit an identical behavior. So

Figure 7 in fact depicts the difference between two "replica" runs as the PM model used a different seed for the random number generator. What exactly causes Serpent replica runs to have non-negligible differences mostly around 1 eV is a subject of on-going investigations. The epithermal scattering treatment in Serpent 2 might be at the root of the problem (Sutton, et al., 2009).

No new additional deviations have been observed for the other materials in the verification model. Hence, without a loss of generality, they are not presented here. From the results obtained one can conclude that the stochastic mixing fall back algorithm is correctly implemented.

2.4.3 Pre-interpolated $S(\alpha, \beta)$ tables

For stochastic mixing as interpolation technique, the maximum acceptable temperature spacing of nuclear data sets needs to be assessed. Trumbull assessed this question for free atom continuous-energy cross sections (Trumbull, 2006). He defined relative differences of less than 0.1 % between interpolated and reference cross section in every point to be acceptable. He found that for nuclides with a complex resonance structure even the smallest applied data set spacing of 28 K could not satisfy his criterion. For other nuclides, however, temperature spacing of up to 111 K produced acceptable results.

Most moderator materials in thermal reactors do not exhibit complex resonance structures in their free atom cross sections. Thus, based on Trumbull's findings one expects that large temperature spacing of the scattering nuclides for the stochastic mixing fall back algorithm is acceptable. To verify this hypothesis, the verification model introduced in subsection 2.4.2 is employed. The $S(\alpha, \beta)$ scattering tables for 500 K and 600 K are removed from Serpent 2's ENDF/B VII.0 library forcing the code to apply true pseudo material mixing. As the ENDF/B VII.0 $S(\alpha, \beta)$ evaluations are provided in 50 K intervals in that temperature range, the interpolation for both water zones is done over a 100 K interval.

Without loss of generality, only the results for the first water zone are discussed in the following. Analyzing the neutron spectrum relative differences as high as 2.25 % are observed in the thermal energy range (see Figure 59 in Appendix A). While the stochastic mixing of free atom cross sections for hydrogen over the 100 K temperature interval leads to no detectable change in simulation results, the introduction of $S(\alpha, \beta)$ in the process does.

Besides cross sections the $S(\alpha, \beta)$ scattering data tables include distributions for the out-going energies and angles of the interacting neutrons. The linear interpolation like stochastic mixing leads to good results for cross sections and out-going neutron energy distributions. However, the angular distribution needs to be handled with an inverse interpolation scheme. For large

temperature spacing of the scattering nuclides employed by Serpent 2 the effect of using a linear instead of an inverse interpolation on the angles becomes large. As a result, one would like to increase the number of thermal scattering data files evaluated at unique temperatures.

Serpent 2 employs $S(\alpha,\beta)$ tables prepared by the LEAPR-THERMR-ACER sequence of the nuclear data processing tool NJOY. The module LEAPR requires frequency spectra $\rho(\omega)$ of the scattering nucleus at each temperature a $S(\alpha,\beta)$ scattering law is to be generated. Thus, unfortunately, thermal scattering data tables for Serpent can be generated at temperatures that are defined by the availability of $\rho(\omega)$. For both ENDF/B VII.0 and JEFF 3.1.1, 9 and 11 temperature points are available spanning roughly 300 K to 800 K for ENDF/B and 300 K to 1000 K for JEFF. Mattes and Keinert provide an interpolation scheme for $\rho(\omega)$ in their report (Mattes & Keinert, 2005). It has been assessed whether interpolating the frequency spectrum and then running LEAPR-THERMR-ACER is more accurate than interpolating $S(\alpha,\beta)$ tables for given frequency spectra. In all test cases, no clear advantage of interpolating the frequency spectra with the method of Mattes and Keinert has been observed.

Consequently, at the moment the option of choice to improve the accuracy of the stochastic mixing with $S(\alpha,\beta)$ scattering laws is to interpolate cross sections and out-going energies linearly and angles inversely as this proved to produce the most accurate results. For Serpent 2/SUBCHANFLOW this interpolation is not done on-the-fly but interpolated thermal scattering data are prepared.

Nevertheless, the question of how large a spacing of interpolated scattering data tables could be remains to be answered. To this end, the infinite lattice of finite height UOX fuel pins is studied once more. Like for the first test presented in this section, Serpent 2 is forced to interpolate as the thermal scattering data sets belonging to the exact solution have been removed from its library. By adding newly generated and externally interpolated $S(\alpha,\beta)$ tables to the library, Serpent uses a 20 K, 10 K and 5 K temperature interval in the stochastic mixing method. It is the aim of the following test to determine the remaining errors relative to the reference solution.

Going from a 100 K to a 20 K temperature increment of the thermal scattering data already significantly reduces the observed errors in the neutron flux from maximum of 2.25 % to 0.65 % for thermal energies above 10^{-9} MeV (cp. Figure 59 and Figure 60 in Appendix A). The maximal difference between the stochastic mixing and the reference solution are basically the same for 10 K and 5 K spaced data sets. However, the mean square error 0.105 % of the 5 K case is significantly lower than 0.163 % for the 10 K case (cp. Figure 61 and Figure 62 in Appendix A).

If memory consumption does not prohibit the usage of 5 K spaced thermal scattering data, it is the best choice in terms of accuracy. The temperature spacing test has been repeated with

JEFF 3.1.1 evaluated nuclear data instead of ENDF/B VII.0 and the same behavior has been observed.

2.5 Internal coupling of Serpent 2 and SUBCHANFLOW

In order to integrate SUBCHANFLOW into Serpent 2, it has been modularized and compiled into a static library. At the moment, coupled calculations are only supported by Serpent 2/SUBCHANFLOW for k-eigenvalue criticality source calculations, not for external source or burn-up mode.

SUBCHANFLOW employs regular meshes to describe its thermal-hydraulic domain. As a consequence, the internal interface between Serpent and its module SUBCHANFLOW is based on the data structures and processing routines of the type 1 multi-physics interface already present in the Monte Carlo code.

In order to improve user friendliness and reduce modeling errors, the geometry description required by SUBCHANFLOW is prepared automatically by Serpent 2 based on its CSG geometry and passed to the thermal-hydraulics module. Currently, this internal geometry pre-processor for SUBCHANFLOW is limited to reactors with square fuel lattices.

2.5.1 Coupled iteration algorithm

The coupled iteration algorithm of Serpent 2 and its thermal-hydraulics module SUBCHANFLOW is visualized in Figure 8. Functions framed with black boxes refer to original Serpent 2 code. Green boxes indicate extended Serpent 2 subroutines. Red boxes enclose features programmed solely for the integration of SUBCHANFLOW.

The Monte Carlo tool Serpent 2 offers three different parallel modes: shared memory parallelization using the OpenMP API, distributed memory parallelization employing pure MPI (Message Passing Interface) and, finally, a hybrid parallel mode for distributed memory. The latter approach has a clear advantage in terms of memory consumption compared to a pure MPI implementation as Serpent duplicates its entire memory for each MPI process. However, SUBCHANFLOW can only run in parallel on shared memory systems. Hence, if Serpent 2 is executed employing MPI, the thermal-hydraulics module is only run by the MPI process with rank 0. Furthermore, it is the task of the rank 0 process to collect the power tallies of all other MPI processes before executing SUBCHANFLOW and broadcasting the new thermal-hydraulic state point information to the other processes. In case of hybrid parallel execution of coupled code system, SUBCHANFLOW will run in parallel utilizing all the threads available to that master MPI process.

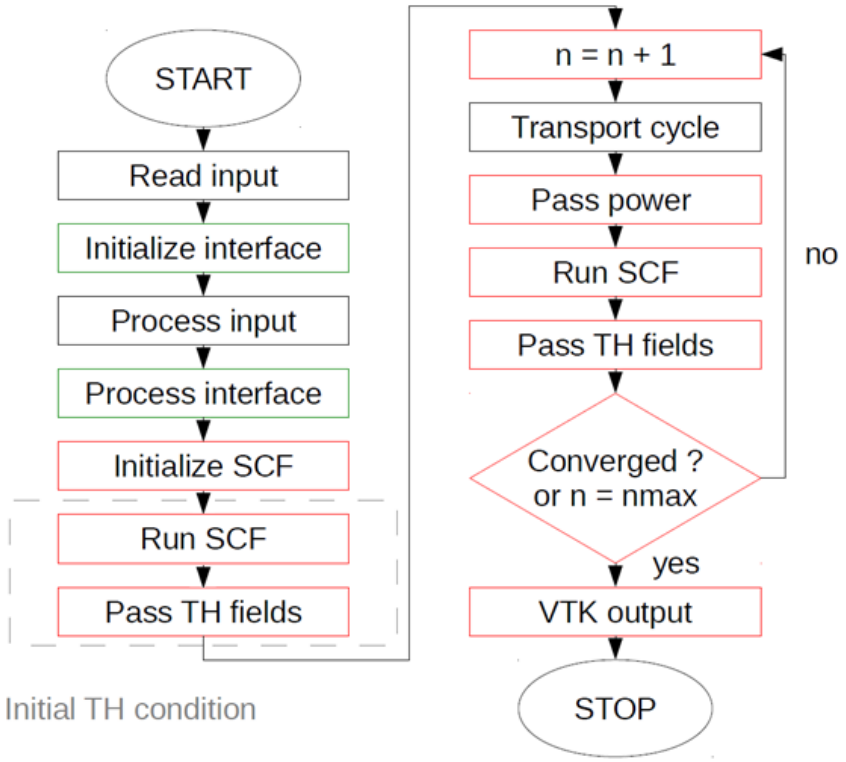

Figure 8: Flowchart of internal coupling of Serpent and SUBCHANFLOW, black boxes indicate original, green boxes extended existing and red boxes completely new coding.

2.5.2 Spatial mapping between neutronics and thermal-hydraulics

The internal coupling of Serpent 2 and SUBCHANFLOW supports channel and sub-channel thermal-hydraulics models. Depending on the model option selected, the radial feedback meshing is determined based on the core lattice and, in case of sub-channel models, also the fuel assembly lattices in the CSG model.

The multi-physics interface of Serpent 2 is a material based interface, i.e. each feedback mesh is linked with a material in the model. In this case, type 1 feedback meshes are employed which hold the piecewise constant density and temperature distributions of the material of interest. The feedback meshes are completely independent of the Monte Carlo geometry and are superimposed on it.

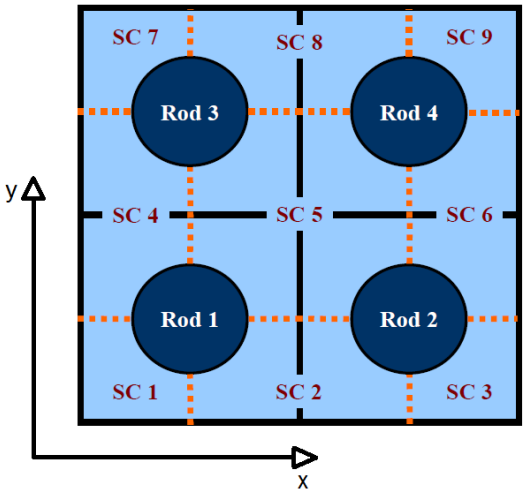

Figure 9: Exemplary comparison of Serpent 2's multiphysics interface and SUBCHANFLOW regular meshes for a 2x2 fuel pin cluster in the x-y plane at a height z: multi-physics interface mesh cell boundaries (black) and sub-channel boundaries in the TH model (orange), adapted from (Gomez-Torres, et al., 2012a)

As part of the multi-physics interface, Serpent 2 has the capability to detect fuel pin structures that completely consist of or contain materials affected by the interface automatically. Moreover, it sets up axially segmented power tallies in these pins. In case of a channel thermal-hydraulics model fuel pins are grouped according to the fuel assemblies they belong to and powers per axial assembly segment are computed based on tallied pin powers. If sub-channel thermal-hydraulics model is used instead, the pin powers are passed directly to the pin structures of SUBCHANFLOW. In the latter case, Serpent employs fuel pin centered feedback meshes while SUBCHANFLOW always utilizes a coolant-centered sub-channel model due to the fact that its closure relations are only validated for this case (see Figure 9). Consequently, for square fuel lattices, four SUBCHANFLOW sub-channels in the x-y plane correspond to one fuel pin in Serpent 2. The necessary spatial interpolation of the coolant properties is done automatically.

In order to use the determined powers in a thermal-hydraulics calculation, the fuel pins in the neutron transport model must be linked to their counterpart in the SUBCHANFLOW model. The linking is made complex by the fact that several Serpent fuel or cladding materials may correspond to one or more sets of thermo-physical properties for SUBCHANFLOW. For example, LWR core to be analyzed may be loaded with fuel assemblies of identical type but with different burn-up and each containing fuel rods of different initial enrichment. For Serpent 2, a multitude of materials may be needed to describe this core loading. However, if the empirical correlation to describe thermal conductivity and specific heat capacity of the fuel were to depend only on temperature but not burn-up and initial enrichment, SUBCHANFLOW would only use one set of thermo-physical properties for all rods. In order to automatize the mapping

of Serpent 2 materials to sets of thermo-physical properties, a material naming convention has been introduced.

As mentioned above, volume averaged heating powers per axial fuel pin or assembly segment are passed from Serpent 2 to SUBCHANFLOW. Even though technically possible, the radial dependence of the power production in each fuel pin is currently not modeled due to the excessively large number of neutron histories necessary to obtain statistically significant results. Nevertheless, the fuel in each fuel rod is discretized into ten radial zones in each axial segment. This discretization scheme allows for studying the axial and radial heat conduction inside the fuel rods and heat transfer from the fuel to the coolant with SUBCHANFLOW. Since Serpent's gamma and coupled neutron-gamma transport model is still under development, only pure neutron transport simulations are considered. Furthermore, even though the capability to tally recoil energies from the neutron slowing down process has recently been added to Serpent 2, to keep the first version of the coupling simple it is not used. Hence, the coolant and structures like fuel rod clads are not heated directly. Accordingly, only effective Doppler, gap and clad temperatures for each rod are provided to Serpent 2 by the sub-channel code. Effective fuel Doppler temperatures T_{Doppler} are determined from fuel center line $T_{f,c}$ and fuel pellet surface temperatures $T_{f,s}$ using equation (8).

$$T_{\mathrm{Doppler}} = (1-\alpha)\, T_{f,c} + \alpha\, T_{f,s}\ , \tag{8}$$

where α denotes an input parameter to be specified by the user. In the Serpent 2 model, the temperature of the clad is set to the algebraic average of the inner cladding surface temperature $T_{\mathrm{clad,i}}$ and outer cladding surface temperature $T_{\mathrm{clad,o}}$. Correspondingly, the mean gas temperature in the gap is assumed to be the algebraic average of inner cladding surface temperature $T_{\mathrm{clad,i}}$ and fuel pellet surface temperature $T_{f,s}$.

All thermo-mechanical effects like thermal expansion and irradiation induced effects such as irradiation creep are neglected. Moreover, as the current version of the coupling focuses on LWR, the temperature dependence of the densities of all materials except the coolant is assumed to marginally influence the overall result and is, resultantly, not accounted for.

2.5.3 Convergence Checking

To check the convergence of the coupled fields carrying the feedback between iterations, the relative l^2-norm or Euclidean norm of Doppler temperature and moderator density distribution are computed according to equation (9). The vector $\vec{X}$ describes the solution field of Doppler

temperature or moderator density, n denotes the current iteration step and $n-1$ the previous step.

$$\frac{\Delta\vec{X}}{\vec{X}} = \frac{\|\vec{X}^n - \vec{X}^{n-1}\|_{l^2}}{\|\vec{X}^n\|_{l^2}} \leq \varepsilon_X \,. \tag{9}$$

The convergence criterion ε_X is defined by the user, e.g. $\varepsilon_X = 10^{-4}$. The l^2-norm or Euclidean norm is preferred over the commonly applied maximum or ∞-norm as it includes information on all off the solution space and not just a single point in space.

Besides checking the convergence of fuel temperature and moderator density, the relative change in eigenvalue is monitored according to equation (10), again employing a user-specified convergence criterion.

$$\Delta k_{\text{eff}} \leq \varepsilon_{\text{keff}} \,. \tag{10}$$

It is generally understood, that the convergence of coupled Monte Carlo thermal-hydraulic code systems is limited by the maximum statistical uncertainty of the Monte Carlo power tallies. Then, it is beneficial to reduce this maximum uncertainty by applying global variance reduction techniques. While for small models a decent convergence of the coupled solution may still be achieved without global variance reduction techniques, these prove to be essential for more realistic, larger models like an entire LWR reactor core.

In 2010, the Uniform-Fission-Site (UFS) method has been implemented in Serpent by VTT, similar to the one used in the Monte Carlo code MC21 (Kelly, et al., 2012). With this method one tries to increase the number of fission source points in regions, where the fission powers is low in order to decrease statistical uncertainties. In Serpent 2, a regular Cartesian mesh is superimposed on the geometry. In the mesh cells, either collision points, neutron flux or fissions are tallied during the inactive cycles of a calculation. The collected results are used to adjust the number of fission neutrons being emitted in the active cycles. Here, the regular mesh of the UFS method is chosen to be identical to the feedback meshes used by the internal interface. Furthermore, collision points are scored during the inactive cycles of a criticality source simulation. However, the number of inactive neutron histories has to be sufficiently large to provide good statistics for the UFS method.

With a setup of the Picard iteration (as realized in Serpent 2/SUBCHANFLOW), it is crucial that the power distribution tallied is based on a converged fission source. Brown proposed to use the Shannon entropy to measure the convergence of the fission source distribution (Brown, 2006). Serpent 2 has the capability to compute the x-, y- and z-components of the Shannon entropy. If necessary, the Shannon entropy can also be evaluated on a mesh superimposed on

the geometry. The latter option is especially useful for large models to detect possible unphysical asymmetries in the neutron flux solution. Therefore, it is employed to assess the convergence of the fission source for the developed coupled code.

Furthermore, a method to improve the convergence of the fission source as well as the symmetry of the neutron flux solution is discussed in section 2.6, the Wielandt shift.

2.5.4 Implementation of an under-relaxation scheme

Past research on deterministic reactor simulators as well as coupled Monte Carlo thermal-hydraulic code systems has emphasized the usefulness of under-relaxation schemes to achieve both a faster and a smoother coupled convergence. Recently, Dufek and Hoogenboom have derived a stable relaxation scheme for coupled Monte Carlo neutron transport and thermal-hydraulics simulations (Dufek & Hoogenboom, 2014). In their scheme, the relaxed normalized neutron flux $\tilde{\varphi}^n$ obtained in iteration step n is given in terms of the unrelaxed normalized neutron flux φ solutions of all steps (see equation (11)).

$$\tilde{\varphi}^n = \frac{1}{n}\sum_{i=1}^{n} \varphi^i \,. \tag{11}$$

Fortunately, equation (11) can be rewritten in a recursion form, see equation (12). The second form is preferable, since the old relaxed flux distribution needs to be stored, while the memory demand of the former version increases linearly with each iteration.

$$\tilde{\varphi}^n = \left(1 - \frac{1}{n}\right) \tilde{\varphi}^{n-1} + \frac{1}{n} \varphi^n \,. \tag{12}$$

From equation (11) the benefit of this relaxation scheme for a coupled Monte Carlo thermal-hydraulics calculation becomes obvious. Combining the flux solutions of all previous iteration steps leads to a reduction of the statistical errors in the relaxed fluxes.

In the final version of the coupling scheme of Dufek and Hoogenboom, the number of neutron histories per iteration step is allowed to vary. As a consequence, the prefactor $1/n$ changes too. The authors argue that the initial flux shape is probably a pretty poor approximation of the real solution and, hence, so are the thermal-hydraulic fields. In order to save computational resources, the number of neutron histories should be increased per iteration step. They provide algebraic equations to compute the neutron histories per iteration based on the number of neutron histories for the first iteration. The latter has to be based on engineering judgment.

To achieve a high computational efficiency, Serpent 2/SUBCHANFLOW should only be run starting from a realistic initial power shape. Therefore, the use of variable step and sample sizes has not been implemented. The relaxation scheme utilized is that given in equation (12). However, it is actually applied to power distributions instead of the neutron flux distributions. Since Serpent has no fully functioning gamma-transport mode yet, the power is computed based on fission reaction rates and empirical heating values directly proportional to fission energy. The fission reaction rates themselves are proportional to the neutron flux levels.

2.6 Wielandt shift implementation

The Wielandt shift is a method to improve the convergence of the power method used to execute k-eigenvalue criticality source calculations. The convergence of the power method is poor for a full PWR core, because it is a loosely coupled system. The mean free path of neutrons of all energies is significantly smaller than the spatial extend of the core. A method to improve convergence would have to improve the coupling of the spatial regions without changing the underlying physics – a fair game. One such method is the Wielandt shift.

The static neutron transport equation can be written in the following operator form

$$\mathbf{M}\,\varphi = \frac{1}{k_{\text{eff}}}\,\mathbf{F}\,\varphi = \lambda\,\mathbf{F}\,\varphi\,, \tag{13}$$

with $\mathbf{M} = \mathbf{D} + \mathbf{T} + \mathbf{S}$, where $\mathbf{D}$ is the streaming operator, $\mathbf{T}$ the absorption operator and $\mathbf{S}$ the scattering operator. Furthermore, $\mathbf{F}$ is the fission operator. The Wielandt method relies on modifying the transport operator $\mathbf{M}$. A fixed fission source is subtracted from both sides of equation (13) yielding equation (14). As can directly be seen from equation (14), the eigenfunctions of the modified neutron transport equation are identical to those of the original equation. The eigenvalues, however, are not.

$$(\mathbf{M} - \lambda_{\text{shift}}\mathbf{F})\,\varphi = (\lambda - \lambda_{\text{shift}})\,\mathbf{F}\,\varphi\,. \tag{14}$$

The change in eigenvalue spectrum leads to an improved convergence behavior of the power iteration if $\lambda > \lambda_{\text{shift}} = 1/k_{\text{shift}}$, see e.g. (Brown, 2007).

During a criticality source simulation Serpent 2 stores the fission neutrons of cycle i as fission source for cycle $i + 1$. The information for the tracking of these neutrons is held in the fission bank. Neutrons that have not been absorbed in an interaction but only scattered are appended to

the queue. Any neutron stored in the queue will be reused in the current cycle i of the criticality source calculation.

Another way of looking at the Wielandt shift method is to say that part of the fission source is treated as scattering. Consequently, it may be easily implemented in Serpent 2 by sampling which of the fission neutrons of a cycle to move to the fission bank based on the probability p_{bank} and which to the queue with the probability $1 - p_{\text{bank}}$. This probability is given in equation (15).

$$p_{\text{bank}} = 1 - \frac{\lambda_{\text{shift}}}{\lambda}. \tag{15}$$

The implementation of the Wielandt shift in Serpent 2 has been verified using the exercise 1 of the OECD/NEA and U.S. NRC PWR MOX/UO_2 core transient benchmark (Kozlowski & Downar, 2003), a two-dimensional hot zero power state (HZP). The loading pattern for a quarter of the Westinghouse 4-loop PWR core investigated is shown in Figure 10.

A 2D HZP Serpent 2 simulation with fixed thermal-hydraulic conditions has been carried out, which are listed in Table 1. For the neutron transport calculation all control and shutdown banks are considered to be fully withdrawn. ENDF/B VII.0 evaluated nuclear data are employed. Serpent 2's internal Doppler pre-processor is used to broaden cross sections from a 300 K base library to 560 K for this case. Serpent 2 simulated $4 \cdot 10^6$ neutrons per cycle. Based on the Shannon entropy distribution evaluated on a 5x5 mesh superimposed on the geometry, 100 inactive cycles were employed. To tally power, 600 active cycles followed. During the implementation test, the fission source convergence has been assessed for different choices of k_{shift}. Using the average fission chain length as defined by Brown (Brown, 2007), the number of active cycles has been adjusted to yield approximately the same number of collisions simulated in total.

Table 1: Fixed thermal-hydraulic conditions for the exercise 1 of the OECD/NEA and U.S. NRC PWR MOX/UO_2 core transient benchmark depicted in Figure 10

Parameter	Value
Core power	1 W
Core temperature (coolant, fuel)	560 K
Boron concentration	1000 ppm

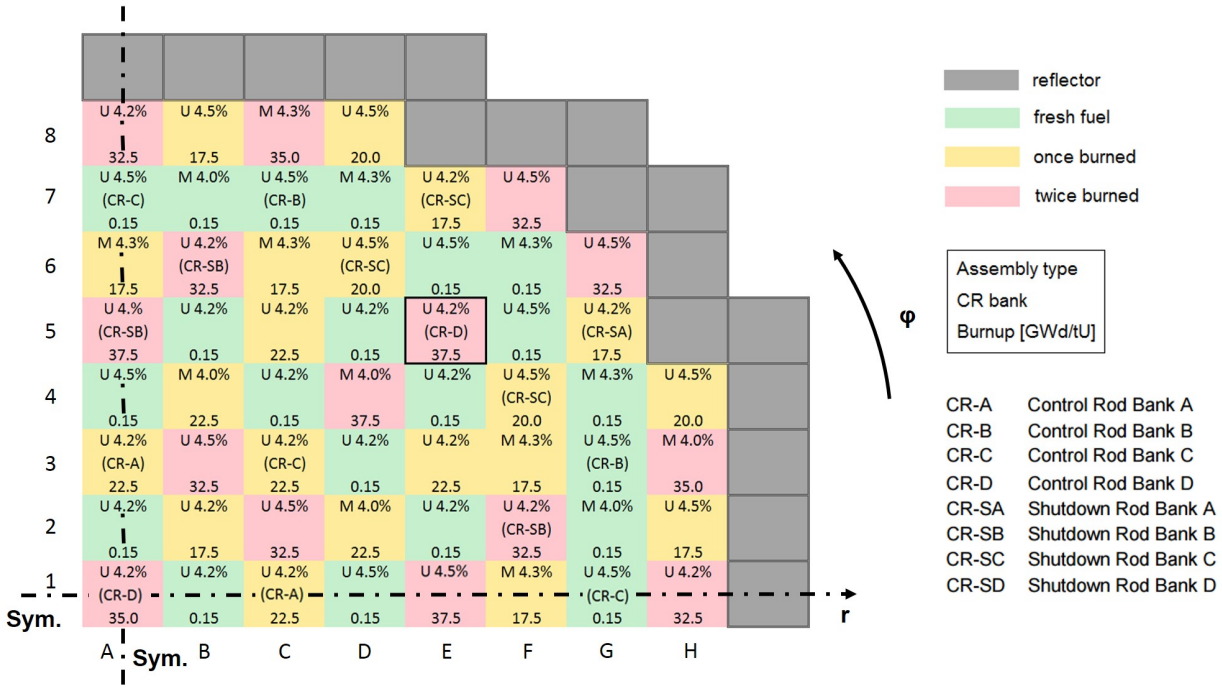

Figure 10: Layout of a quarter of the PWR core of the OECD/NEA and U.S. NRC PWR MOX/UO_2 core transient benchmark (Kozlowski & Downar, 2003); shown assembly types consist of an indicator of the fuel type (U – UOX, M – MOX) followed by the initial enrichment

To examine the influence of Wielandt's method on local reaction rates, assembly powers have been tallied in all Serpent 2 runs. The figure of merit (FOM) given in equation (16) is employed to evaluate that influence. Here, N is the number of tally bins, t the average wall clock time and σ_i relative uncertainty of each tally bin estimated based on 10 replica runs.

$$FOM = \frac{N}{t \sum_i \sigma_i}. \tag{16}$$

The results of the implementation tests are listed in Table 2. Utilizing the modified transport operator, Serpent 2 reproduces the reference eigenvalue obtained with an unchanged transport operator within the statistical uncertainty. The number of cycles to converge the fission source and the number of active cycles steadily decreases with decreasing difference between shift eigenvalue and true eigenvalue of the system. This is due to the increasing length of the fission chains simulated in one cycle. Correspondingly, the unwanted inter-cycle correlation in stochastic neutron transport process is reduced. At the same time, an improvement of the FOM for the assembly power tally is observed.

Ivanov reported that Wielandt's method leads to more symmetric tallies since it diminishes the inter-cycle correlations in a criticality source calculation (Ivanov, et al., 2014). The PWR core studied in the OECD/NEA and U.S. NRC PWR MOX/UO_2 core transient benchmark has an eightfold symmetry. Therefore, it is an excellent test case for tally symmetry. Employing the unchanged transport operator, Serpent 2's assembly power tally exhibited a maximal asymmetry of 2.41 % on average. Running the neutron transport with a shift eigenvalue of 1.10 lead to a reduction of this asymmetry to 0.77 % on average.

Table 2: Comparison of eigenvalues, number of cycles until convergence and FOM obtained by Serpent 2 using Wielandt's method with different eigenvalue shifts for the exercise 1 of the OECD/NEA and U.S. NRC PWR MOX/UO_2 core transient benchmark

k_{shift}	SSS2 k_{eff}	# inactive cycle	# active cycles	FOM
∞	1.05862(0.00005)	100	600	1.47
1.30	1.05864(0.00004)	30	200	2.49
1.16	1.05863(0.00004)	14	140	3.07
1.10	1.05862(0.00003)	7	60	6.81

The neutron transport equation solved by deterministic methods describes the behavior of the mean neutron flux averaged over an infinite number of single particle histories. This mean neutron flux always exhibits the symmetry of the underlying reactor core geometry. Monte Carlo methods, however, can only simulate a limited number of neutron histories. In the latter, the physical effect of particle clustering becomes visible. The neutron flux solution no longer necessarily exhibits the symmetry of the reactor core loading. Dumonteil et al. discuss particle clustering in detail (Dumonteil, et al., 2014). Since Monte Carlo neutron transport is intended to be used to estimate the mean neutron flux obtainable with deterministic solutions, the handling the tally asymmetry is crucial for large problems such as full PWR core even though it reflects a physical reality. In order to estimate this mean neutron flux within a reasonable amount of time, the Wielandt shift is an essential feature of the coupled code system Serpent 2/SUBCHANFLOW. However, the increasing length of the fission chains in one cycle leads to a steep increase in computation time. The Serpent 2 solution not using Wielandt shift (ref. Table 2) consumed 272 CPUh. The one employing a shift of 1.10 needed 715 CPUh on an Intel Xeon E5-2670 processor. One might argue that running the conventional Serpent 2 for 715 CPUh should also significantly improve the symmetry of the tallies. In fact, the symmetry improves by roughly 40 % compared to the run taking 272 CPUh. Using Wielandt's method, the tally symmetry is, however, improved by almost 70 % compared to the reference run.

Unfortunately, this limits the application of Wielandt's method to 2D cases and for producing converged fission source files for 3D coupled simulations. Running a full 3D HFP coupled simulation with Wielandt shift enabled requires larger computational resources than available to finish in a reasonable amount of time. Hence, all 3D coupled Monte Carlo and thermal-hydraulics simulations presented here employ the Uniform Fission Site method to reduce global variance.

2.7 Conclusion and next steps

An internal coupling between the Monte Carlo code Serpent 2 and the sub-channel code SUBCHANFLOW has been developed. This coupling is based on Serpent 2's universal multi-physics interface. With the multi-physics interface, the TMS method as on-the-fly treatment of the temperature dependence is employed. TMS in its current form can treat neither thermal bound-atom scattering nor unresolved resonances. To lift the former of both limitations, a fall back to stochastic mixing has been implemented in Serpent 2 to enable the simulation of thermal reactors with improved physics compared to the original Serpent 2 version. This implementation has been successfully verified by benchmarking it with a known reference solution. Thereafter, a study to find the optimum temperature spacing of $S(\alpha, \beta)$ scattering tables for this fall back algorithm has been conducted. If available computer memory does not prove to be prohibitive, $S(\alpha, \beta)$ scattering laws should be prepared in 5 K intervals.

Moreover, the Wielandt shift as method to improve convergence behavior of the power method used to solve the steady-state neutron transport problem has been introduced into Serpent 2. Its capability to speed up convergence and reduce asymmetries in the neutron flux distribution has been proven by analyzing a 2D slice of a full Westinghouse 4-loop PWR core. Unfortunately, employing Wielandt's method yields a significant increase in the computing time limiting its routine application.

The next step in the software development process for the pin-resolved reactor simulator Serpent 2/SUBCHANFLOW is the verification and validation of the solutions produced by the constituent codes and the coupled code system.

3 Verification and Validation of Serpent 2/SUBCHANFLOW

This paragraph discusses the solution verification and validation of the pin-resolved reactor simulator Serpent 2/SUBCHANFLOW. The multilevel validation methodology developed for BE tools is also applied to SSS2/SCF (Ivanov, et al., 2007a). Like most BE codes, this pin-resolved reactor simulator is implemented by coupling two existing stand-alone simulation tools. In the multilevel validation methodology, both the proper validation of the constituent stand-alone codes and the coupled code system must be guaranteed.

SUBCHANFLOW is validated using experimental data relevant for PWRs, for example, the NUPEC PWR tests (Imke & Sanchez, 2012). As a beta version Serpent 2, however, is usually benchmarked against other continuous energy Monte Carlo codes for solution verification. To the knowledge of the author, it has not yet been validated for PWR systems using available critical experiments. As a result, Serpent 2 is first used to study VENUS-1 and VENUS-2 critical experiments representing modern square fuel lattice PWRs loaded with both UOX and MOX fuels (Moon, et al., 2006; Na, et al., 2000; Messaoudi, et al., 2004). Afterwards, the SSS2/SCF solution is verified by a code-to-code comparison with an external coupling of TRIPOLI4 and SUBCHANFLOW (Sjenitzer, et al., 2015) as well as the internally coupled code MCNP5/SUBCHANFLOW (Ivanov, et al., 2013; Ivanov, et al., 2014). Finally, first efforts to validate Serpent 2/SUBCHANFLOW using one state of the cycle 1 of the BEAVRS benchmark (Horelik, et al., 2016) are undertaken. The hot zero power physics tests are studied to assess the coupling, the TMS temperature treatment and the stochastic mixing fall back method.

Once this basic level of V&V has been reached for the pin-resolved reactor simulator, it may be employed to produce reference solutions for the pin-homogenized DYNSUB.

3.1 Validation of Serpent 2 for square lattice PWRs

3.1.1 VENUS-1 critical experiment

The VENUS facility (Vulcain Experimental NUclear Study) is a pool-type zero-power critical facility located at SCK•CEN in Mol, Belgium. The VENUS-1 core configuration as modeled with Serpent 2 is illustrated in Figure 11. As seen in the illustration, the mock-up PWR core is positioned eccentrically in the jacket inner wall.

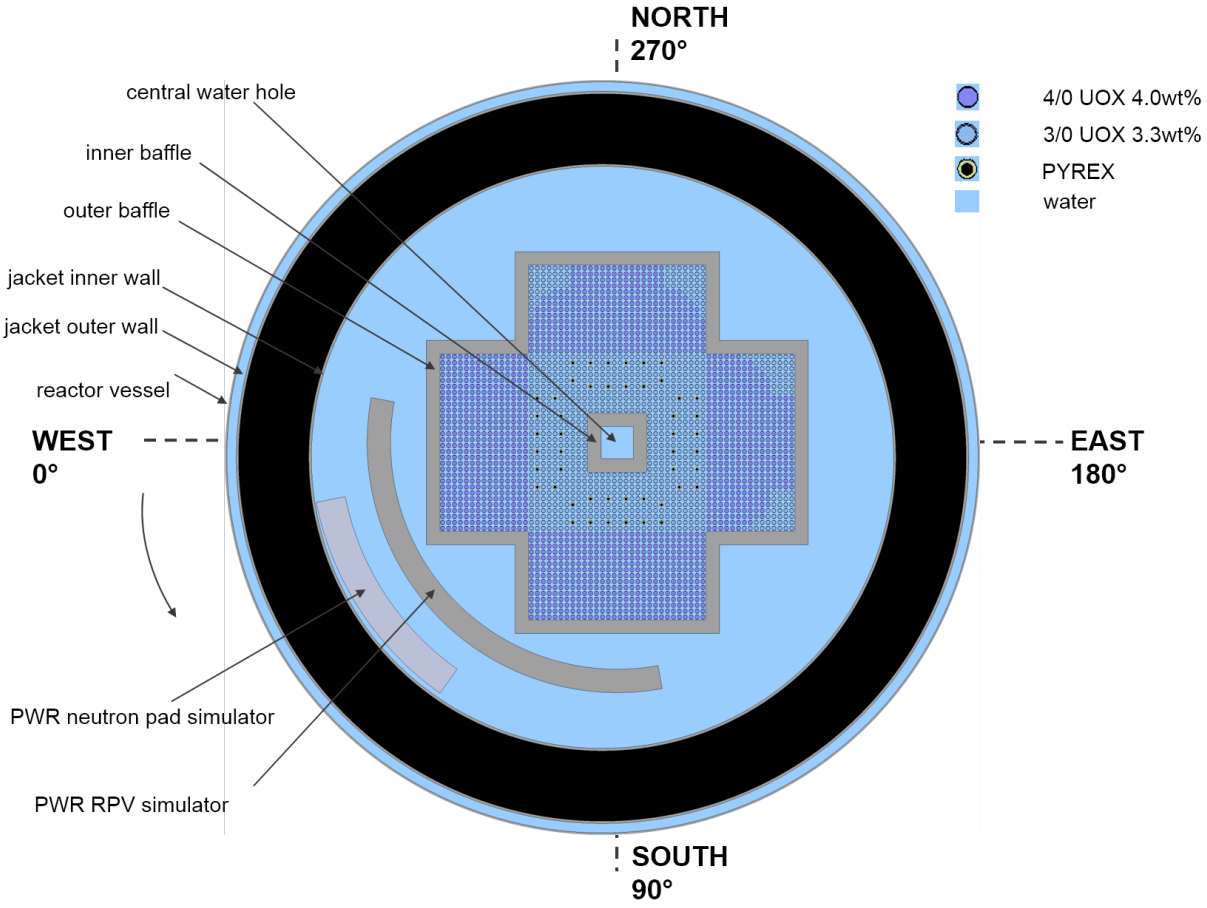

Figure 11: VENUS-1 core configuration, horizontal cut at core mid plane

The central water hole is enclosed by the inner baffle made from stainless steel. Outside the inner baffle, the 3/0 fuel region is located. It is loaded with 3.3 wt% enriched UOX fuel rods with a zircaloy cladding. They are spaced with a pitch of 1.26 cm to represent the fuel of a second generation Westinghouse PWR. Moreover, this fuel zone includes 12 PYREX poison rods per quadrant to simulate PWR poison clusters. A PYREX poison rod consists of an elemental boron core enclosed in a cylindrical Corning PYREX borosilicate glas rod, hence, its name. The rod itself is placed in a stainless steel clad. Except for corner areas in the east and north quadrants made up of 3/0 fuel rods, the remainder of the fuel belongs to the 4/0 fuel region. The fuel rods in that region contain 4.0 wt% enriched UOX pellets. Their cladding is made from stainless steel. This type of fuel rods is typical for a first generation Westinghouse PWR, however, it is loaded with 1.26 cm pitch of the second generation fuel assemblies.

The fuel zone as a whole is surrounded by the stainless steel outer baffle. The 0°-90° sector (see Figure 11) also includes a mockup of the reactor pressure vessel and a neutron pad. The rest of the volume up to the jacket inner wall is filled with water. Between jacket inner and outer wall there is air displayed as black in Figure 11. Finally, the gap amid jacket outer wall and reactor vessel is flooded with water.

The entire system is kept at room temperature, i.e. 296.15(1.5) K. All geometry and material composition data required for creating a detailed Serpent 2 Monte Carlo model is given in the OECD/NEA report (Moon, et al., 2006).

During the VENUS-1 experiments gamma scans were performed to determine the core power distribution. Moreover, in-core and ex-core activation foils as well as the vertical bucklings in the core and the core exterior were measured. The results of the different measurement techniques for determining fission rates were cross checked and showed a good agreement (Moon, et al., 2006). For the validation of Serpent 2 as reactor simulator, only the power distribution measurements are considered here.

The power measurements were done for 56 fuel rods in 0°-45° sector of the core, 23 in the 3/0 and 33 in the 4/0 fuel region. The gamma activity of ^{140}La was measured after an irradiation period of 8 h at 90 % of the maximum power of the critical facility. The obtained data was corrected for decay and self-shielding effects. The pin power distribution in the sector of interest was completed by interpolating data directly obtained in the experiment. For the reader's reference, the complete experimental pin power distribution is presented in Figure 63 in Appendix B. In that graphics, directly measured pin powers are underlined. All other values are interpolated. The measurement uncertainty was 1.1 %, which corresponds to 1.7 standard deviations. The error of the interpolated data is estimated to be 2 % (one standard deviation).

A two-dimensional Serpent 2 model has been constructed as suggested in the OECD/NEA report (Moon, et al., 2006). The Monte Carlo code used ENDF/B VII.0 nuclear data broadened to 300 K. 1000 active cycles of 10^6 neutrons each followed 200 inactive cycles. Wielandt's method has been utilized to improve statistics at the boundaries of the VENUS-1 core. The simulation met the set target of a statistical uncertainty of less than 0.01 % on all tallied pin powers.

The errors relative to the experimentally obtained values of the pin power distribution computed with Serpent 2 are depicted in Figure 12. The x-y- coordinate system in the figure has its origin the center of the central water hole. Most of the relative errors are below 1 %, only a few exceed 2 %. The largest relative errors between calculation and measurement accumulate in the areas, where the 0°-45° fuel section borders the inner and outer baffle. As the majority of the directly gamma scanned pins lie in these regions, Serpent 2 is not able to reproduce the local powers even within three standard deviations. For the inner fuel rods, SSS2 results do fall within three standard deviations for all measurements. In that region, the bulk of interpolated pin powers are also correctly predicted within a quoted 2 % uncertainty.

Serpent 2s misevaluation of the pin powers closer to the inner and outer baffle is due to wrongly determined neutron flux gradients. These are most likely caused by inaccurate material composition and/or cross section data for the baffles. Moreover, the accuracy of the description

of the geometric set-up and the homogeneity of the actual baffle materials is not known. However, in literature, a more accurate description of VENUS-1 structural materials and the set-up is not available.

The OECD/NEA report includes a Monte Carlo solution for the VENUS-1 pin powers evaluated with MCNP (Moon, et al., 2006). The relative errors between this solution and the measurements (see Figure 64 in Appendix B) exhibit the same behavior and are of the same magnitude as the ones between Serpent 2 and the experimental data. Therefore, Serpent 2's performance can be considered satisfactory as it is equivalent to the quality of the MCNP reference.

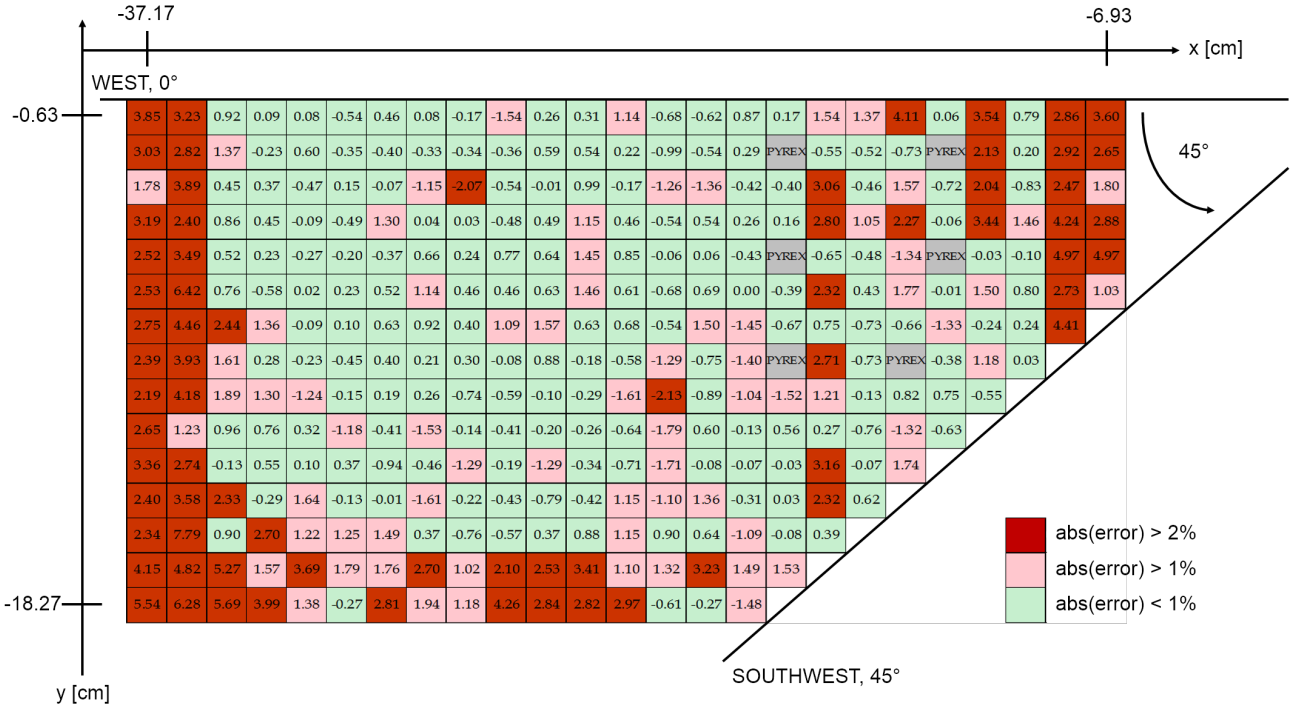

Figure 12: Relative error (C/E-1) in percent for VENUS-1 pin power distribution as computed with SSS2, origin of the x-y-coordinate system is the center of the central water hole

3.1.2 VENUS-2 critical experiment

Modern day PWRs may employ a mixture of UOX and MOX fuels. To ensure that Serpent 2 can be also be utilized to study such systems, a critical experiment including MOX fuels is analyzed. The VENUS-2 core loading is such an experiment. The radial configuration of the VENUS-2 core inside the jacket inner wall is shown in Figure 13. Like in the illustration, the actual core was placed eccentrically into the jacket inner wall to make room for RPV and neutron pad mock-ups. The inner most fuel region consists of 3/0 fuel pins identical to those of VENUS-1. In this region, one finds 10 PYREX rods per quadrant to simulate burnable poison

rods used in PWRs. The fuel region further away from the central water hole is loaded with 4/0 fuel rods already used in the earlier experiments (see Figure 13). Finally, the third fuel region

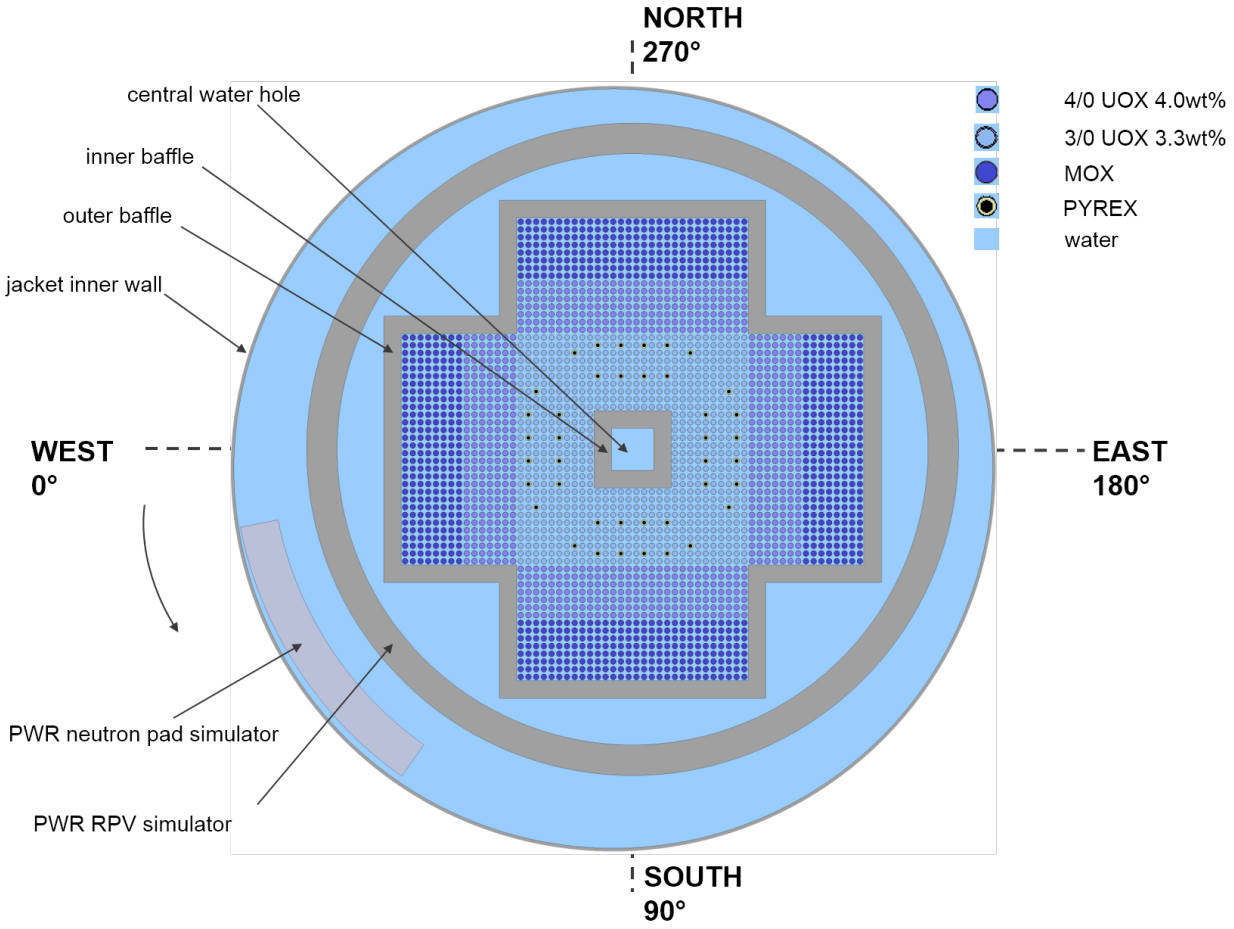

Figure 13: VENUS-2 core configuration, horizontal cut at core mid plane

includes MOX fuel rods enriched 2.0 wt% in ^{235}U and 2.7 wt% in high grade Plutonium.

Like for VENUS-1 experiments entire reactor is at 296.15(1.5) K. All geometry and material composition data required for creating a detailed Serpent 2 Monte Carlo model is given in the OECD/NEA reports (Na, et al., 2000; Messaoudi, et al., 2004). As VENUS-2 experiments were processed into an OECD/NEA benchmark, SSS2's performance is assessed by comparing with existing benchmark solutions.

During the VENUS-2 experiments gamma scans were conducted to measure the pin-wise power and detailed axial pin power distributions in six selected fuel rods. The pin-wise power measurements were done for 121 fuel rods in 0°-45° sector of the core, 41 in the 3/0, 35 in the 4/0 fuel and 45 MOX region. The gamma activity of ^{140}La was measured after an irradiation period of 13.5 h at 90 % of the maximum power of the VENUS-2. The obtained data was again adjusted for decay and self-shielding effects. The pin power distribution in the sector in question was completed by interpolating data directly attained in the experiment. For the reader's reference, the complete experimental pin power distribution is presented in Figure 65 in

Appendix B. In that figure, directly measured pin powers are in bold face. All other values are interpolated. The measurement uncertainty was 1.7 % for the UOX fuel and 2.5 % for the MOX fuel both of which correspond to 1.65 standard deviations. The MOX measurement uncertainty is higher due to the lower thermal fission yield of Ba-140, the mother nucleus of La-140, for the fission of plutonium isotopes. One standard deviation of the interpolated data is estimated to be 2 %.

Moreover, the axial power distribution in six selected pins was determined after an irradiation of 8 h at 90 % maximum power again looking at the ^{140}La activity. The positions of pins 30 and 74 (3/0 fuel), pins 115 and 131 (4/0 fuel) as well as pins 249 and 315 (MOX fuel) are documented in Figure 66 in Appendix B. In addition, the complete set of experimentally obtained axial pin power distributions was normalized to one and is shown in Figure 67 in Appendix B. The reported uncertainty of the measurements, i.e. one standard deviation, is 2.2 % for UOX and 3.4 % for MOX fuel pins.

A three-dimensional Monte Carlo model was developed. The model does not use any symmetry conditions as the VENUS-2 core exhibits neither a radial nor an axial symmetry. Serpent 2 employs ENDF/B VII.0 nuclear data broadened to 300 K. 1000 active cycles of $4 \cdot 10^6$ neutrons each followed 200 inactive cycles. The Wielandt shift option is enabled in SSS2 in order to obtain good statistics especially for the axial pin power distributions. The simulation met the set target of a statistical uncertainty of less than 0.01 % on all tallied pin powers including axial distributions.

The eigenvalue predicted by Serpent 2 for the critical experiment is compared to measured and benchmark average calculated values in Table 3. An acceptable agreement is observed. It is interesting to note that SSS2 like the benchmark Monte Carlo neutron transport solutions tends to overestimate VENUS-2 criticality. To estimate the influence of the nuclear data library used on the VENUS-2 eigenvalue, the Serpent 2 calculations have been repeated using the ENDF/B VI.8 nuclear data. An eigenvalue of 0.99745(0.00001) is obtained. Both eigenvalues predicted by Serpent 2 differ by 599 pcm emphasizing the benchmark's sensitivity to nuclear data. The benchmark solutions quoted here used ENDF/V, ENDF/VI, JEFF 2.2 and JENDL 3.2.

Generally, the differences between the measured and calculated eigenvalues are in the expected range for evaluating thermal spectrum criticality benchmarks with LEU fuels using Monte Carlo techniques (Marck, 2012; Marck, 2006). The former studies used MCNP. Moreover, Marck discovered that ENDF/B VI.8 exhibits a trend to underestimate criticality for LEU fueled thermal spectrum benchmarks (Marck, 2006).

Table 3: Comparison of SSS2 eigenvalue for VENUS-2 with experimental and benchmark simulated data (Messaoudi, et al., 2004)

	VENUS-2 eigenvalue
Measurement	1.00000(0.00032)
Serpent 2	1.00344(0.00001)
Benchmark average	1.00122(0.00394)
Benchmark average deterministic methods	0.99828(0.00402)
Benchmark average Monte Carlo methods	1.00232(0.00341)

The relative errors between the pin power distribution computed with Serpent 2 and the measured one are presented in Figure 14. The origin of the x-y-coordinate system lies at the center of the central water hole. The direction of coordinate axis is identical to those used in (Na, et al., 2000). For less than half of the fuel pins the relative errors are below 2 %.

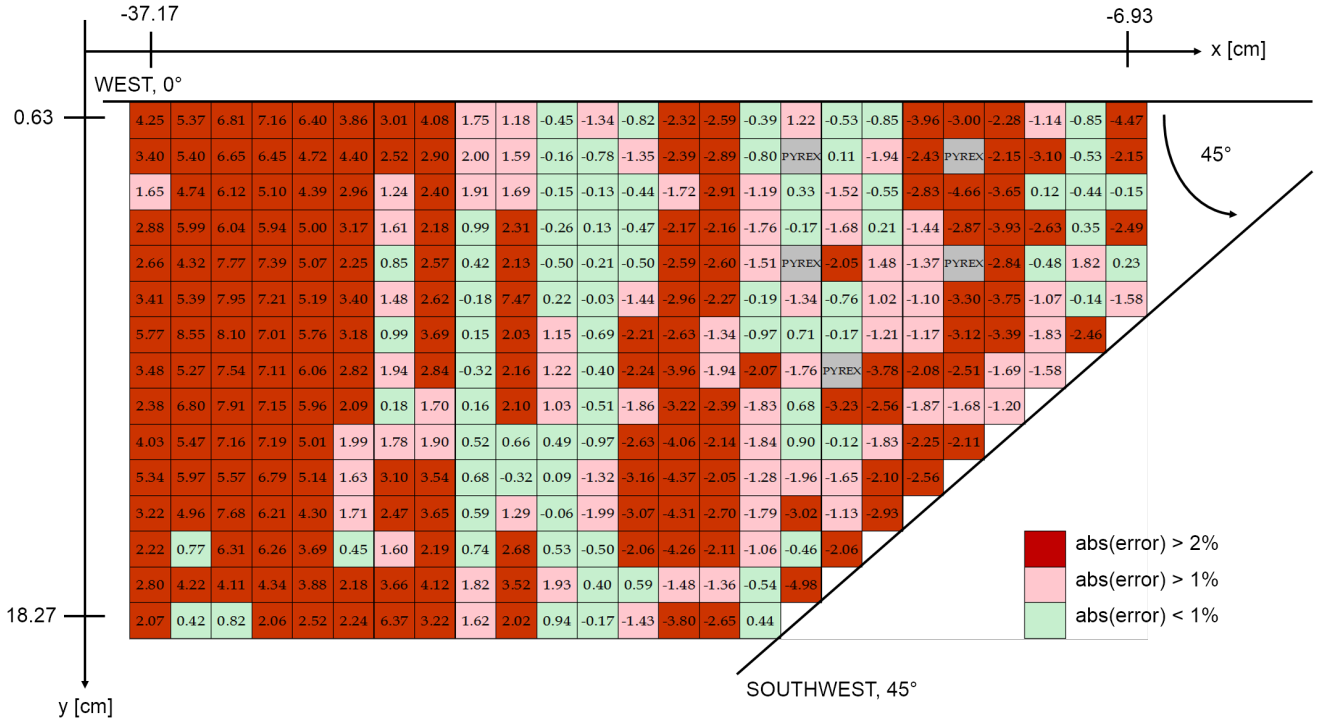

Figure 14: Relative error (C/E-1) in percent for VENUS-2 pin power distribution as evaluated with SSS2, origin of the x-y-coordinate system is the center of the central water hole

The largest C/E errors are observed in the MOX fuel region but they are also higher at the interface between the 3/0 and 4/0 fuel regions. Furthermore, except for a few positions is seen in

the UOX fuel regions pin powers are underestimated. In the MOX fuel region, however, pin powers are generally overestimated.

The above analysis is summarized and contrasted with benchmark results in Table 4. In the benchmark, it was found that calculated pin powers are systematically high in MOX fuels and low in UOX fuels since this was reflected in all combinations of codes, numerical methods and nuclear data sets. In the benchmark report, the authors state the corresponding observations have been made in operating power reactors (Na, et al., 2000). However, they do not offer an explanation for either. As shown in Table 4, Serpent 2 predictions are comparable to the benchmark results concerning the magnitude of the relative errors.

Table 4: Comparison of relative (C/E-1) errors per geometrical area in percent for pin power distribution of VENUS-2 predicted by SSS2 and benchmark participants (Na, et al., 2000)

Fuel zone	Benchmark average	SSS2
UOX 3.3 wt%	-1.57(1.56)	-1.52(1.39)
UOX 4 wt%	-0.74(1.77)	-0.58(1.97)
MOX	4.30(2.22)	4.17(2.08)
All pins	0.85(3.39)	0.89(3.15)

The axial power measurements in the six selected pins were normalized to one per rod. Hence, the following comparison with Serpent 2 predictions only assesses the axial power shapes but not the absolute power level in each investigated fuel pin.

The relative errors between the axial power shapes determined with Serpent 2 and the gamma scan measurements are shown in Figure 15. At most of the axial positions for all six fuel rods the relative errors are below 2 %. The two MOX fuel pins exhibit the largest number of zones with higher differences compared to the measurements. Considering the measurement uncertainties, Serpent 2 reproduces all axial measurements in both MOX and UOX fuel pins within two standard deviations. Though Serpent 2 is unable to capture the overall power level in the fuel pins correctly, the axial power shapes are predicted satisfactorily.

The quality of the prediction of the axial power shapes, the fact that all combinations of codes, numerical methods and nuclear data sets behave similarly, indicates that the effect of the overestimation of MOX and underestimation of the UOX pin powers might have been introduced during the evaluation of VENUS-2 pin power measurements themselves. This is underlined by all participants employing almost identical 3D core models and the observation

that switching nuclear data libraries for Serpent 2 had no influence on the systematically high prediction of MOX pin powers.

Axial position [cm]	MOX		UOX 4%		UOX 3.3%	
	325	240	131	115	74	30
110	-1.201	0.000	0.935	0.619	0.932	0.926
112	2.247	-0.273	0.551	1.955	0.273	0.824
114	2.506	3.291	0.495	0.746	1.754	0.247
116	1.370	4.481	0.454	0.000	0.907	0.682
118	2.146	-0.209	-0.210	0.847	-1.040	-0.210
120	1.200	-0.592	0.198	0.199	0.800	-0.594
122	-0.759	2.132	-0.942	0.380	-0.189	0.763
124	-0.912	0.183	1.107	0.735	-0.545	0.000
126	-0.179	0.179	-0.709	0.359	-0.710	0.722
128	1.616	2.330	-1.049	0.355	0.710	0.176
130	-0.523	0.882	0.352	1.064	-0.525	1.246
132	-0.353	-1.903	0.177	-1.049	0.000	-0.176
134	0.179	-0.887	-0.712	-0.178	-0.179	0.000
136	-0.547	-2.500	-0.547	-2.162	-0.183	0.183
138	-0.945	-1.313	-0.566	0.573	0.000	0.573
140	-0.593	-0.787	-0.198	-0.593	-0.199	-0.397
142	-1.247	0.000	-0.210	-0.210	-0.210	0.211
144	0.000	-1.124	1.139	-0.897	0.226	-1.345
146	-1.703	-1.942	0.496	-1.937	-0.733	-0.737
148	-1.333	-1.093	-0.274	-0.820	-0.273	-1.626
150	-0.906	0.000	0.312	1.246	-0.615	-3.561

abs(error) > 2%
abs(error) > 1%
abs(error) < 1%

Figure 15: Relative error (C/E-1) in percent for VENUS-2 axial pin power shape measurements as predicted with SSS2, for positions of numbered fuel pins see Figure 66 in Appendix B

Each fuel pin investigated was measured separately on a gamma scanner after cooling down. To determine pin power distributions from gamma-spectrometry measurements focused on the 1.596 MeV line of La-140, one needs to determine activity of the mother Ba-140 at the time of the shutdown of the VENUS-2 experiment. Ba-140 is a direct fission product with a thermal yield of 6.2145 % for U-235 and 5.3545 % for Pu-239 according to ENDF/B VII.0. For UOX fuel rods, the overall number of fissions or average fission rate during 13.5 h of the experiment can be determined from the measured, self-shielding- and decay-corrected Ba-140 activity using the U-235 thermal fission yield corrected for a small amount of fast U-238 fissions. For MOX fuel rods, however, the convert the Ba-140 activity into the overall number of fissions that occurred the relative number of thermal fissions in Pu-239, Pu-240, Pu-241, Pu242 and U-235 is needed. Moreover, this relation needs to be corrected for the small amount of fast fissions in U-238 and the plutonium isotopes. While this relation depends on the a priori known MOX composition, the local neutron flux spectrum and the fission cross section evaluation used play an important role. How this relation was determined in the experiment is not included in the

corresponding report (Messaoudi, et al., 2004). It only reports the used fission yields for U-235 und Pu-239 to be 6.3 % and 5.5 % respectively. Given the fact, that the small amount of fast fissions leads to a reduction of the effective Ba-140 fission yields for both nuclides, the values used to evaluate VENUS-2 measurements seem high comparing to ENDF/B VII.0 data. The effect is more pronounced for Pu-239 which could account for part of the MOX fuel pin power overestimation by benchmark participants. However, the report is unclear, whether the Pu-239 value has been adjusted to account for fissions in Pu-240, Pu-241 and Pu-242 which would increase it slightly.

Unfortunately, the measured La-140 or derived Ba-140 activities are not part of the VENUS-2 related reports. These would offer the possibility to check the Serpent 2 model and to identify the cause of the systematically high MOX pin powers directly without inferring pin powers and interpolating them to obtain a full power map. Serpent 2 could be run in burn-up mode to determine the build-up of both nuclides in all fuel pins for 13.5 h of operation at 90 % power. Such an approach is preferred for validating modern reactor simulators such as AREVA's MICROBURN-B2 (Misu, et al., 2000).

To sum up, Serpent 2 is as suitable as other available tools to describe the MOX and UOX fueled VENUS-2 critical experiment. It exhibits the same systematic overestimation of MOX and underestimation of UOX pin powers as all the codes and numerical methods in the VENUS-2 benchmark. Due to a lack of data on the VENUS-2 experiment, a detailed analysis on the cause of this effect could not be performed. Further work on how to improve the modeling of reactor cores loaded with both types of oxide fuels should be done in the future.

Based on Serpent 2's performance describing both the VENUS-1 and VENUS-2 critical experiments, the Monte Carlo code is considered to be sufficiently accurate to simulate square fuel lattice PWRs. Nevertheless, the validation base of SSS2 needs to be extended by analyzing more critical experiments to determine in more detail where deviations arise from.

3.2 Solution verification of Serpent 2/SUBCHANFLOW

3.2.1 Channel thermal-hydraulics

The first case studied to verify the Serpent 2/SUBCHANFLOW solution employing a channel level thermal-hydraulics model is 3x3 PWR fuel assembly cluster surrounded by one row of water reflectors as illustrated in Figure 16. Furthermore, the minicore is embedded between top and bottom water reflectors in axial direction. This case was defined as part of the NURISP boron dilution benchmark (Kliem, et al., 2011). Both the 17x17-25 MOX and 17x17-25 UOX fuel assemblies have no burn-up. Their initial enrichment can be read from Figure 16. The

geometry and material definition of the fuel assemblies in the NURISP boron dilution benchmark were taken from the OECD/NEA and U.S. NRC PWR MOX/UO_2 core transient benchmark (Kozlowski & Downar, 2003). A summary of the HFP operating conditions for this minicore are given in Table 5.

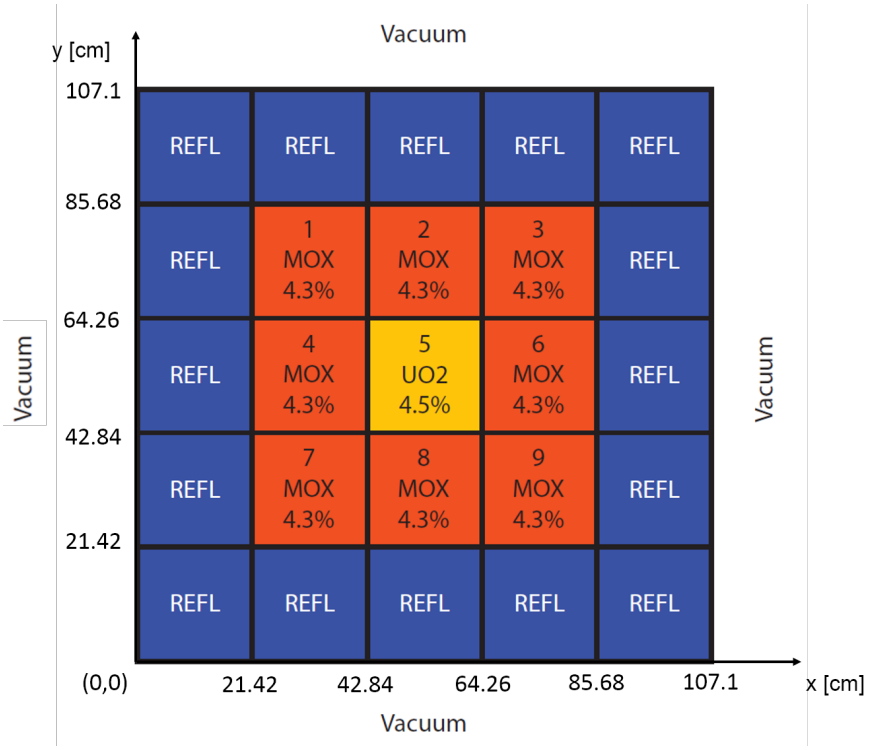

Figure 16: Layout of the 3x3 PWR fuel assembly reflected minicore of the NURISP boron dilution benchmark. MOX and UO2 assemblies numbering and initial fuel enrichment are indicated, adapted from (Sjenitzer, et al., 2015)

For this reflected 3x3 fuel assembly cluster the parameter α in the expression to evaluate the effective Doppler temperature (see equation (8)) has been set to $5/9$ to be consistent with the given TRIPOLI4/SUBCHANFLOW solution.

Table 5: HFP operating conditions of reflected 3x3 minicore of NURISP boron dilution benchmark (Kliem, et al., 2011)

Quantity	Value
Power	100 MW
Core mass flow rate	739.08 kg/s
Outlet pressure	15.4 MPa
Core inlet temperature	560 K
Boron concentration	200 ppm

Both Serpent 2 and TRIPOLI4 utilize JEFF 3.1.1 evaluated nuclear data. For Serpent 2's stochastic mixing fall back for TMS, a 5 K spacing of $S(\alpha,\beta)$ scattering data sets is chosen. TRIPOLI4 employed a 50 K spaced cross section library for its pseudo-materials. Like Serpent 2, it employs linear mixing coefficients. In the Serpent 2/SUBCHANFLOW model, there are 20 axial layers in the thermal-hydraulic feedback mesh. In TRIPOLI4, the geometry was divided into 17 axial layers for the external coupling.

Serpent 2/SUBCHANFLOW used 400 inactive and 1200 active cycles of $5 \cdot 10^6$ neutrons each per coupled iteration. Setting Doppler temperature and moderator density coupled convergence targets to 1 %, Serpent 2/SUBCHANFLOW converged after only 4 iterations. The overall calculation consumed 11 CPU-month on the 128 cores of 16 Intel Xeon E5-2670 processors of KIT SCC's IC2 cluster. The fraction of wall clock time spent for solving the channel level thermal-hydraulics problems is negligible.

A comparison of the minicore eigenvalues predicted by Serpent 2/SUBCHANFLOW and TRIPOLI4/SUBCHANFLOW is given in Table 6. TRIPOLI4/SUBCHANFLOW solution used a significantly lower number of neutron histories. The difference in eigenvalue of 36(43) pcm is statistically not significant.

Table 6: Comparison of NURISP minicore HFP k-eigenvalue predicted by SSS2/SCF and TRIPOLI4/SCF (Sjenitzer, et al., 2015)

Coupled Code	k_{eff}
TRIPOLI4/SCF	1.01861(0.00043)
SSS2/SCF	1.01825(0.00002)

Looking at the spatially integrated power maps as predicted by both coupled codes in Figure 17, a good agreement is observed. However, due to the relatively small number of neutron histories the TRIPOLI4 flux solution is not perfectly symmetric even though the underlying geometry is. The maximum relative difference between Serpent 2/SUBCHANFLOW and TRIPOLI4/SUBCHANFLOW results is 1.6 %. It is statistically significant as the corresponding uncertainties in the power tally are below 0.5 % in the last iteration of both coupled solutions. In case of Serpent 2/SUBCHANFLOW the statistical uncertainties of the power tallies in the last iteration can only be an estimate of the true uncertainty in the power distributions. The use of the relaxation scheme introduced in equation (12) in subsection 2.5.4 couples the different iterations and their combined uncertainty would have to be evaluated. Until now, no mathematical expression is available to this end.

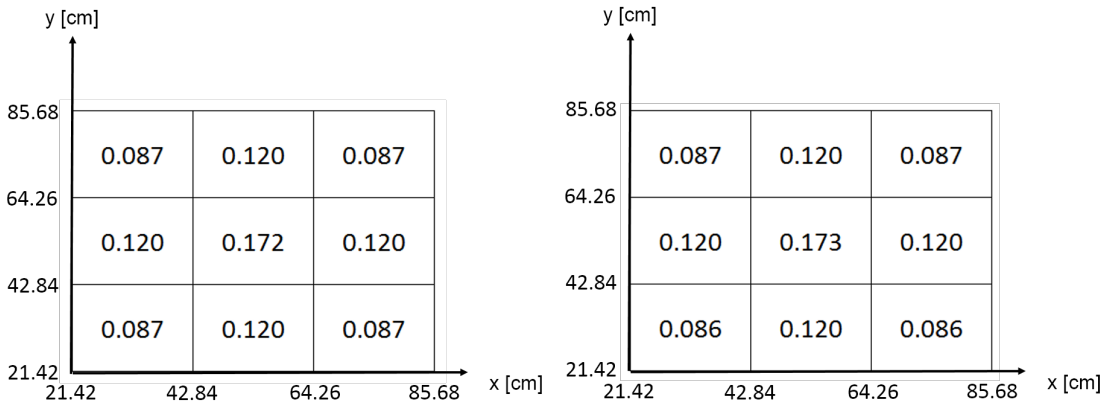

Figure 17: Normalized radial power map of 3x3 reflected minicore as predicted by Serpent 2/SUBCHANFLOW [left] and TRIPOLI4/SUBCHANFLOW [right] (Sjenitzer, et al., 2015)

Moving from the power maps to the axial power distribution of each individual assembly, the deviations between both coupled solutions are more pronounced. Without a loss of generality, the following discussion is limited to the central fuel assembly of the minicore, assembly number 5 (see Figure 16).

The normalized axial radially integrated power profile of this fuel assembly as predicted by Serpent 2/SUBCHANFLOW and TRIPOLI4/SUBCHANFLOW is illustrated in Figure 18. Both profiles exhibit a similar shape. The profile predicted by Serpent 2/SUBCHANFLOW is slightly more shifted to the lower half of assembly number 5.

In order to quantitatively compare both simulation results, Serpent 2/SUBCHANFLOW powers have been histopolated to the lower number of axial layers employed by the other solution. At the bottom of this particular fuel assembly local differences in power as high as 30 % of the Serpent 2/SUBCHANFLOW solution are observed. In most of the axial bins, however, the relative differences between both solutions are well below 10 %. These differences are significant as the statistical uncertainty in power has been below 1.1 % everywhere for TRIPOLI4 and below 0.2 % for Serpent 2.

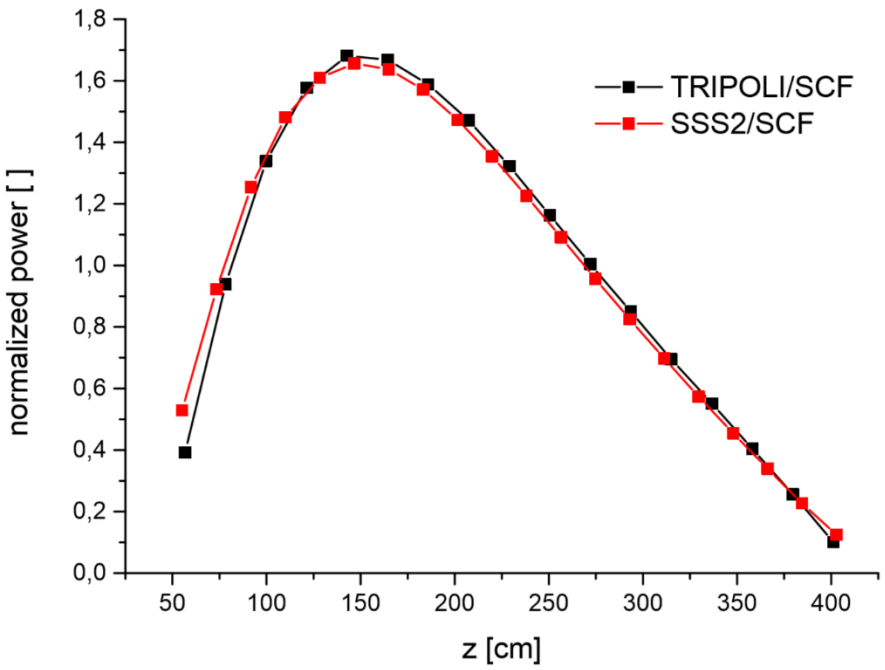

Figure 18: Comparison of normalized axial radially integrated power profile in fuel assembly 5 of the minicore of SSS2/SCF and TRIPOLI4/SCF (Sjenitzer, et al., 2015), the origin of the z-axis is located at the bottom of the bottom water reflector

The axial distribution of the coolant temperature in the channel belonging to assembly 5 is depicted in Figure 19. As the largest deviations in power between both coupled solutions appear in low power regions, the coolant temperature profiles match very well.

The question remains, how to estimate the statistical uncertainty of the thermal-hydraulic data fields. Up to now no method to determine the true statistical uncertainty of the thermal-hydraulic state point information or the neutron flux during a single coupled calculation exists. The only option is to perform a sufficiently large number of replica runs, i.e. repeating the coupled simulation with different starting values of the seed of the random number generator. Thereafter, the spread of the results of the replica runs are analyzed with statistical methods in order to approximate mean and standard deviation.

Since no statistical uncertainty information is available for the TRIPOLI4/SUBCHANFLOW solution and performing a sufficiently large number of replica runs corresponds to using a large amount of computational resources, the comparison of thermal-hydraulic fields is only done qualitatively in the remainder of this subsection.

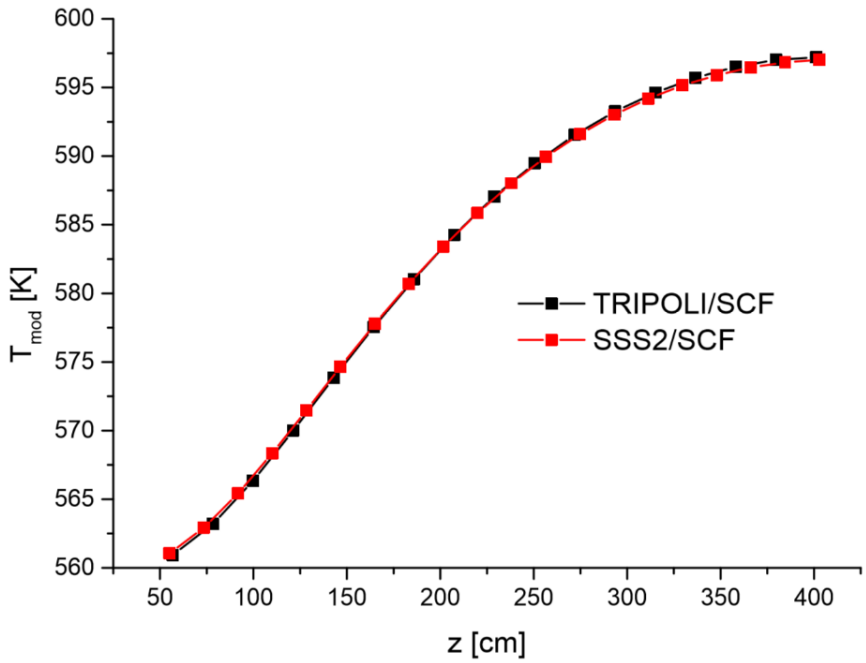

Figure 19: Comparison of the axial moderator temperature distribution in Kelvin in central fuel assembly of the minicore of SSS2/SCF and TRIPOLI4/SCF (Sjenitzer, et al., 2015), the origin of the z-axis is located at the bottom of the bottom water reflector

The versions of SUBCHANFLOW used together with TRIPOLI4 and Serpent 2 utilize the same water/steam tables. As a result, no new insight is to be gained from comparing moderator density profiles for the central assembly. Instead, the axial profile of the effective Doppler temperatures determined by both coupled codes is analyzed. The local differences between both solutions exhibit the same behavior as the differences in power, as was to be expected.

Since Serpent 2 and TRIPOLI4 receive their feedback information from two versions of the same thermal-hydraulics tool and it has been verified that both thermal-hydraulic models are comparable in terms of constituent relations and options employed, the observed deviations can be attributed only to differences in the neutronics solution. Unfortunately, as neither the publications nor TRIPOLI4/SCF simulation data provided by B. Sjenitzer include a full TRIPOLI neutronics input description and a neutron flux distribution, the origin of the observed discrepancies between both coupled tools cannot be determined definitely. However, the following differences in terms of neutronics could be identified: Both Monte Carlo codes used ACE libraries prepared from the JEFF 3.1.1 nuclear data evaluation. However, they did not utilize the same library. Serpent 2 employed an ACE library built from JEFF 3.1.1 nuclear data while TRIPOLI used the ENDF formatted JEFF 3.1.1 information directly. More importantly, the methodology for treating the temperature dependence of nuclear data is different between both solutions. While the TMS method employed by Serpent 2 is in principle as accurate as the employed ACE cross section files, the pseudo material mixing approach used by TRIPOLI4 is not. Only a slight approximation is introduced in TMS through the cut-off condition of the

infinite tail of the Maxwell-Boltzmann distribution. Last but not least, TRIPOLI4 applied a resonance upscattering correction while Serpent 2 does not as it is incompatible with TMS at this point in time.

3.2.2 Subchannel thermal-hydraulics

The second solution verification case analyzed is also a 3x3 PWR fuel assembly cluster shown in Figure 20. This case has been developed in the framework of the High Performance Monte Carlo Project (HPMC), which was performed under 7th EURATOM Framework Programme (HPMC-295971). Like for the previous channel level thermal-hydraulics case, the 17x17-25 MOX and 17x17-25 UOX assemblies, the minicore consists of, are fresh. Moreover, their geometry and material specification has been taken from the OECD/NEA and U.S. NRC PWR MOX/UO_2 core transient benchmark (Kozlowski & Downar, 2003). In the UOX assembly, however, the integral burnable absorber rods (IFBA) are replaced with unpoisoned fuel pins.

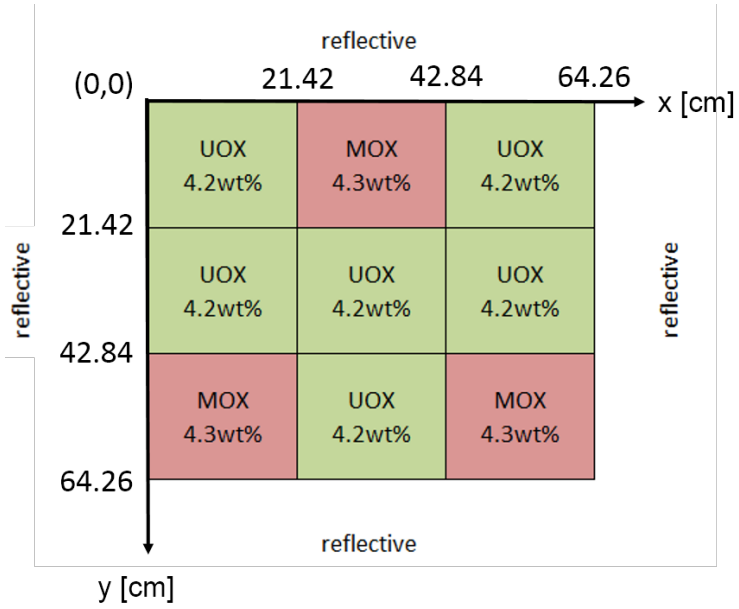

Figure 20: Layout of the 3x3 PWR fuel assembly cluster as defined in HPMC project, for MOX and UOX assemblies their fuel initial enrichment is indicated

The hot full power operating conditions for this case are given in Table 7.

For this verification case employing a sub-channel thermal-hydraulics model, Serpent 2/SUBCHANFLOW is benchmarked against an internal coupling of MCNP5 and SUBCHANFLOW (Ivanov, et al., 2013; Ivanov, et al., 2014; Ivanov, et al., 2015). Both Serpent 2 and MCNP5 employed JEFF 3.1.1 evaluated nuclear data. Like for the channel thermal-hydraulics case, 5 K spaced of $S(\alpha,\beta)$ scattering data sets are included in Serpent 2's library. MCNP5 utilized a 50 K spaced cross section library for its pseudo material approach to

treat temperature dependence of nuclear cross sections. Like in Serpent 2, linear mixing coefficients are used. The $S(\alpha, \beta)$ tables, however, are interpolated on-the-fly (Ivanov, et al., 2015).

Table 7: HFP operating conditions of HPMC project 3x3 fuel assembly cluster benchmark

Quantity	Value
Power	166.24 MW
Core mass flow rate	739.09 kg/s
Outlet pressure	15.45 MPa
Core inlet temperature	560 K
Boron concentration	1200 ppm

Both coupled codes model the axial dependence of the thermal-hydraulic state point information in 20 axial layers. The coefficient α for calculating the effective Doppler temperatures is set to 0.7.

Serpent 2/SUBCHANFLOW tracked a total of $6 \cdot 10^9$ neutrons per coupled iteration. Setting Doppler temperature and moderator density coupled convergence targets to 0.05 %, Serpent 2/SUBCHANFLOW converged after only 8 iterations. 32 h have been spent on the 256 cores of 32 Intel Xeon E5-2670 processors of the IC2 compute cluster to obtain the final results, i.e. a total of 11.2 CPU-months. Unlike the channel level thermal-hydraulics case, SUBCHANFLOW takes 3 % of the overall run time to solve for the flow and temperature fields in its sub-channel geometry. MCNP5/SUBCHANFLOW simulated 10^9 neutron histories per coupled iteration step. It required 23 iterations for the maximum change in fuel Doppler temperature to fall below 0.03 %.

The effective multiplication factor (k_{eff}) predicted by both coupled codes is listed in Table 8. A significant difference of 40(2) pcm is observed. In the following, pin power distributions and thermal-hydraulic parameter fields are analyzed to identify factors contributing to this deviation.

Table 8: Comparison of HPMC 3x3 minicore HFP k-eigenvalue predicted by MCNP5/SCF and SSS2/SCF

Coupled Code	k_{eff}
MCNP5/SCF	1.22247(0.00002)
SSS2/SCF	1.22287(0.00001)

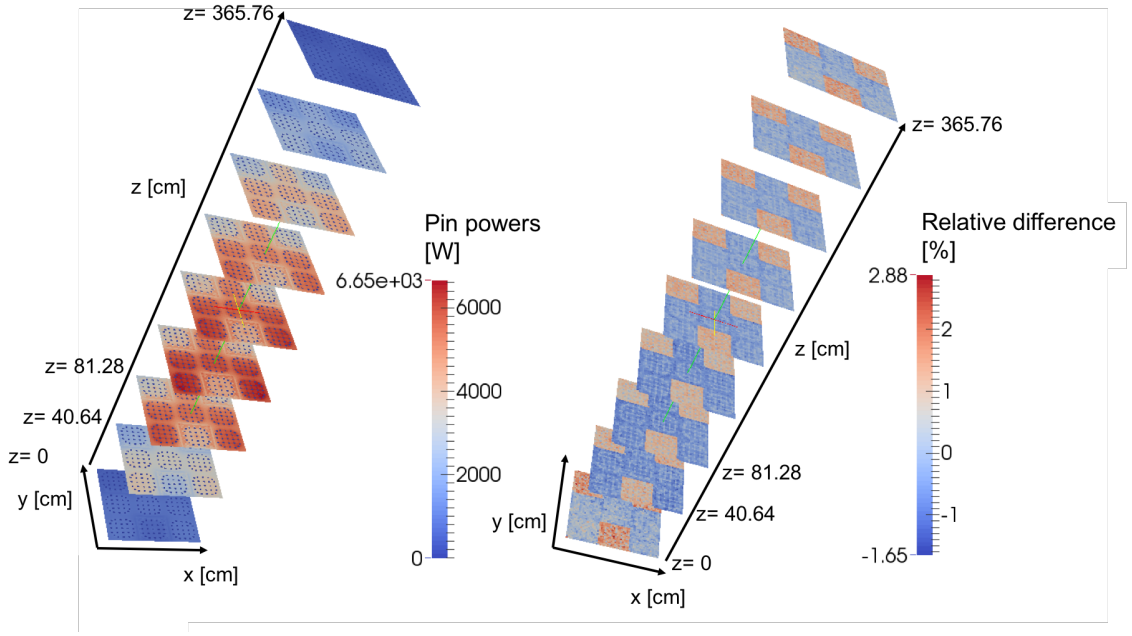

Figure 21: Axial pin power distribution in Watts as evaluated by SSS2/SCF [left], relative differences between MCNP5/SCF and SSS2/SCF pin power fields in percent [right] at nine equidistantly spaced horizontal cuts

The pin powers computed with Serpent 2/SUBCHANFLOW are depicted in Figure 21. To improve readability only 9 horizontal cuts through the minicore are displayed. The power is shifted slightly into the lower half of the minicore. Furthermore, the unpoisoned UOX fuel assemblies produce significantly more power than the MOX ones including wet annular burnable absorber (WABA) rods.

The fact that the minicore has one symmetry axis in radial direction can be used to test the quality and the convergence of the Monte Carlo solutions of SSS2/SCF and MCNP5/SCF. Evaluated based on the pin power distribution, the maximal relative difference between two symmetry calculation nodes is $3.2 \cdot 10^{-3}$ for Serpent 2/SUBCHANFLOW and $4.6 \cdot 10^{-3}$ for MCNP5/SUBCHANFLOW. In both cases, the found asymmetry in the solution is larger than the alleged convergence of the coupled solution.

The relative differences between the pin power fields predicted by both coupled codes are also included in Figure 21. The maximum relative difference of 2.88 % occurs on axial layer 20 at the top of the minicore which is a low power region. The corresponding absolute difference in power is 9.99 W. The maximum absolute difference in pin power of 93.54 W, however, is found in the high power region near the center of the minicore at z=192.02 cm. Generally, one observes that MCNP5/SCF predicts higher pin powers in the MOX fuel assemblies and correspondingly lower ones in the UOX assemblies than Serpent 2/SUBCHANFLOW.

The relative differences in fuel Doppler temperature fields computed by both Monte Carlo neutron transport tools follow the observation of the deviations in pin powers (cp. Figure 68 in

Appendix C). A maximum relative difference of 0.950 % is observed for the very pin segment with an absolute difference in power of 93.54 W at z=192.02 cm. The fuel Doppler temperature evaluated by MCNP5/SCF is 9.46 K higher than the one obtained with Serpent 2/SUBCHANFLOW.

The local moderator temperature distribution behaves like both fuel Doppler temperatures and pin power fields (cp. Figure 69 in Appendix C). While observed differences in fuel Doppler temperatures are smaller than those in pin powers, the moderator temperature fields are even less sensitive to power changes. The maximal difference in moderator temperature between MCNP5/SCF and SSS2/SCF solutions is as low as 0.07 %.

As both coupled codes utilize the same sub-channel thermal-hydraulics tool and it has been proven that the thermal-hydraulics models especially the closure relations used are compatible, the encountered differences in the coupled fields can be attributed only to deviations in the neutron transport model.

Serpent 2 and MCNP5 employed the same JEFF 3.1.1 ACE nuclear data library. While the internal coupling of MCNP5/SUBCHANFLOW applied the pseudo material approach and interpolated its $S(\alpha,\beta)$ tables on-the-fly, SSS2/SCF utilized TMS for all nuclides but hydrogen in water. For the latter, the stochastic mixing fall back algorithm has been used. Additionally, it has to be pointed out that MCNP5 has the probability table treatment for the unresolved resonance range on by default. As the use of the probability tables is not yet compatible with Serpent 2's TMS method, the unresolved resonance range of all included nuclides is neglected. Finally, unlike SSS2/SCF the temperature of the cladding and the gas gap in the fuel rods are not updated by MCNP5/SUBCHANFLOW (Ivanov, et al., 2014). They are kept at hot zero power conditions.

3.2.3 Summary of solution verification efforts

In light of the differences in the coupling methodology, treatment of the temperature dependence of CE nuclear data and statistics in case of TRIPOLI4, the SSS2/SCF and the benchmark solutions are considered to be in good agreement. Hence, it may be concluded that the internal coupling presented in chapter 2 has been correctly implemented for both channel and sub-channel level thermal-hydraulics. The two remaining limitations of the coupled code system Serpent 2/SUBCHANFLOW concerning the physics of nuclear reactors are its lack of support for the probability tables of the unresolved resonance description and for the resonance upscattering correction. The former is of minor importance for any LWR and, hence, the PWRs studied in this work. Often the impact of the unresolved resonance description on a LWR simulation is too tiny to be quantified. The effect of the resonance upscattering correction on

criticality and neutron flux is small but measurable. Hence, for Serpent 2/SUBCHANFLOW to become a high-fidelity reactor simulator the latter limitation should be lifted.

3.3 Validation of Serpent 2/SUBCHANFLOW

3.3.1 MIT BEAVRS benchmark

The BEAVRS benchmark (Horelik, et al., 2016) is about a commercial 3411 MW_{th} Westinghouse PWR reactor core. It includes the operation history for the first two cycles. The measured power distributions are available at a number of points in both cycles. These powers were determined using ^{235}U based fission chambers placed into the instrumentation tube of the fuel assemblies. Additionally, control rod bank worths were determined experimentally at the beginning of each of the two cycles.

The BEAVRS initial core was loaded with 17x17 fuel assemblies of three different enrichments: 1.6, 2.4 and 3.1 wt% U-235. To compensate the excess reactivity of the initial core, a total of 1266 burnable absorber pins are inserted into the guide tubes of fuel assemblies. Affected fuel assemblies are either loaded with 6, 12, 15, 16 or 20 of such absorber pins. The control assemblies employ silver-indium-cadmium (AIC) as absorber material. They are grouped in 4 control (A, B, C, D) and 5 shutdown banks (SA, SB, SC, SD, SE). The loading pattern of the initial core and the configurations of inserted burnable absorber pins are shown in Figure 22.

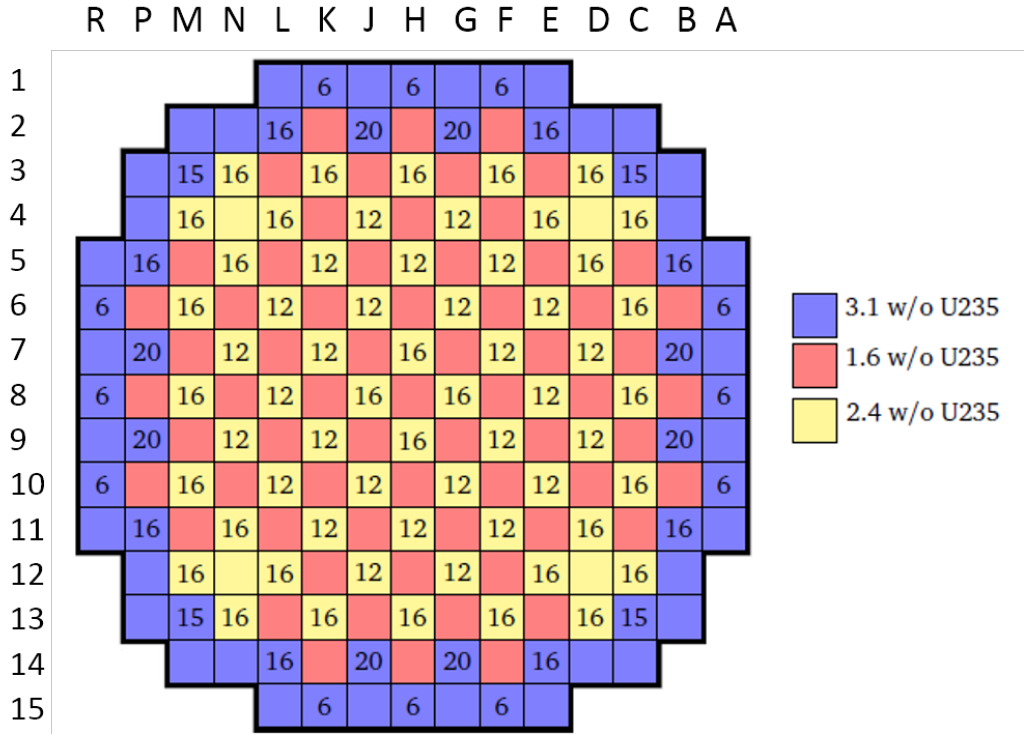

Figure 22: Layout of the BEAVRS initial core, adapted from (Horelik, et al., 2016)

3.3.2 BEAVRS cycle 1 hot zero power physics tests

The hot zero power state of the BEAVRS core cycle 1 represents the starting point of the process of validating the coupled solutions provided by Serpent 2/SUBCHANFLOW with measured data. The power history of cycle 1 is shown in Figure 70 in Appendix D. The HZP operating conditions are summarized in Table 9. Under these conditions, all shutdown banks are fully withdrawn from the core.

Table 9: HZP operating conditions of BEAVRS initial core (Horelik, et al., 2016)

Quantity	Value
Power	25 MW
Core mass flow rate	15229.17 kg/s
Outlet pressure	15.5 MPa
Core inlet temperature	566 K
CR bank A	362.2 cm
CR bank B	362.2 cm
CR bank C	362.2 cm
CR bank D	338.5 cm
Critical boron concentration	975 ppm

Serpent 2/SUBCHANFLOW is used to model the active core of the PWR with a channel level thermal-hydraulics model. It is based on the Serpent 2 model developed at VTT Technical Research Center of Finland. The latter was kindly provided by the former institution. For total thermal power of 25 MW no TH model is necessary. The HZP case is analyzed with SSS2/SCF as a test for the coupling, the TMS temperature treatment and the stochastic mixing fall back. The obtained results are then compared to pure Monte Carlo neutron transport solutions produced with OpenMC and MC21 (Kelly, et al., 2014).

The channel thermal-hydraulics model includes 193 parallel channels consisting of 20 axial segments. Spacer grids are represented using form loss coefficients. The loss coefficient of each spacer grid is assumed to be 1.0. Once more, ENDF/B VII.0 evaluated nuclear data is employed. For Serpent 2's stochastic mixing fall back the 5 K spaced thermal scattering data is used. A fission source file to start the coupled calculation from is produced with a Serpent 2 run utilizing Wielandt's method. The local Doppler temperature and moderator density convergence targets are set to 0.5 %. The convergence criterion for the effective multiplication factor is 5 pcm. For each transport calculation, Serpent 2 employs $5 \cdot 10^6$ neutrons per cycle. An

analysis of the Shannon entropy distribution, evaluated on a 5x5 mesh superimposed on the geometry, led to the conclusion to skip 1000 cycles. 3000 active cycles are executed thereafter.

The hot zero power physics data for the BEAVRS PWR core includes a number of measured critical boron concentrations (CBC) and the corresponding insertions of control and shutdown banks. The core multiplication predicted by SSS2/SCF for these cases is listed in Table 10. The results for the codes OpenMC and nTRACER were taken from literature (Ryu, et al., 2014). OpenMC (Romano & Forget, 2013) is another Monte Carlo neutron transport code and nTRACER (Jung, et al., 2013) a deterministic tool based on the method of characteristics (MOC) as well as on-the-fly cross section processing.

Table 10: Comparison of BEAVRS Cycle 1 criticality calculations and measurements (Horelik, et al., 2016; Ryu, et al., 2014)

Case	Measured CBC [ppm]	OpenMC	nTRACER	SSS2/SCF
ARO	975	0.99920(0.00004)	0.99967	0.99935(0.00001)
D in	902	1.00080(0.00004)	1.00127	1.00127(0.00003)
C,D in	810	1.00023(0.00005)	1.00068	1.00060(0.00003)
A,B,C,D in	686	0.99884(0.00004)	0.99931	0.99923(0.00003)
A,B.C,D, SE,SC,SD in	508	0.99725(0.00004)	0.99816	0.99774(0.00003)

Unfortunately, the BEAVRS benchmark does not provide measurement uncertainties for the CBCs in the above table. Neither does it state, whether these were determined using the off-line or on-line experimental setup of the Westinghouse PWR. Thus, it is not possible to estimate the uncertainty of the CBC data based on measurement technology.

In the case of control and shutdown banks fully withdrawn from the core, SSS2/SCF's eigenvalue is only 65 pcm from critical. For all rodded configurations, this bias is less than 227 pcm.

For the all rods out configuration, assembly powers have been measured in 58 locations throughout the core. First, the axially integrated power measurements are analyzed. They have been normalized such that average axially integrated power is unity. The measurement uncertainty has been estimated to be 3.7 %. The relative differences between the Serpent 2/SUBCHANFLOW simulation and the measurements are displayed in Figure 23. The maximum observed difference is -13.24 % in assembly B13 and there is a noticeable tilt in the field of relative differences. Independently obtained MC21 and OpenMC solutions for this case are reported by Kelly (Kelly, et al., 2014). For both tools, the maximal (C/E-1) occurs also in assembly B13, -12.7 % for MC21 and -13.5 % for OpenMC. Furthermore, these two solutions exhibit the same tilt in relative differences.

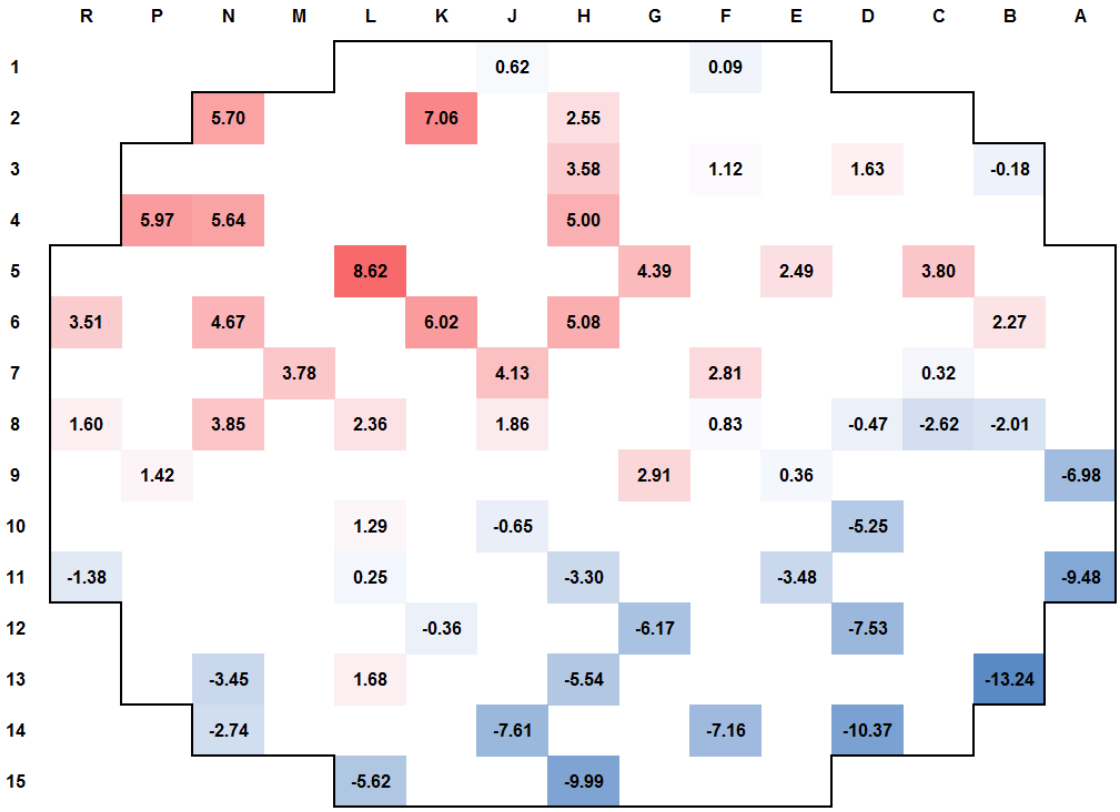

Figure 23: Relative error (C/E-1) in percent for BEAVRS HZP radial power distribution predicted by SSS2/SCF

The measured detector signals are significantly greater than all three solutions in the lower right quadrant in the core and significantly lower in the upper left quadrant. While Serpent 2/SUBCHANFLOW, MC21 and OpenMC produce a symmetric power distribution for the symmetric BEAVRS core loading, the detector signals exhibit a clear NW-SE tilt that cannot be explained based on the core loading. The authors of the BEAVRS benchmark hypothesize that this tilt is caused by a larger water gap in one corner of the core (Horelik, et al., 2016). This gap has its origin in process of the core loading. As fuel assemblies are inserted and

leaning against the baffle, uneven gaps could occur in opposite corners of the core. As the reactor heats up and fuel swells under irradiation, differences in water gaps between fuel assemblies even out. This hypothesis is supported by the fact that the tilt in the measured power maps disappears during cycle one as the reactor reaches full power and its fuel burns.

To illustrate how differences in axially integrated powers translate into axial power profiles, the profile in the assembly with the largest C/E relative error, i.e. B13, and the one in the assembly with smallest C/E relative error, i.e. B03, are shown in Figure 24 and Figure 25.

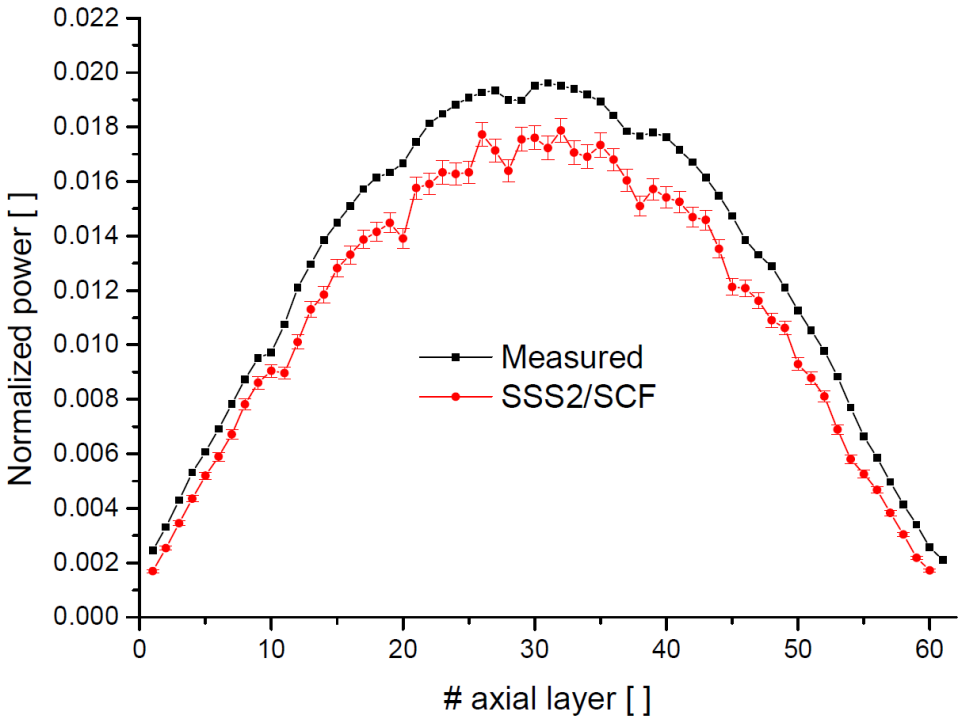

Figure 24: Comparison of SSS2/SCF BEAVRS HZP normalized axial power profiles in assembly with highest C/E relative error, i.e. B13, with experimental data (Horelik, et al., 2016)

While the power shape is well captured in assembly B13, the overall power level is not. In assembly B03, a very good agreement of calculated and experimentally determined power profile is observed. Like for B13, the flux suppression caused by the spacer grids are clearly visible.

Last but not least, measurements of the worth of all control rod and some of the shutdown banks were performed. The associated measurement uncertainties are not specified. The worths computed with Serpent 2/SUBCHANFLOW are compared to the experimental results in Table 11. The MC21 values can be found in (Kelly, et al., 2013). Bank worths evaluated with OpenMC and nTRACER can be found in the paper by Ryu (Ryu, et al., 2014).

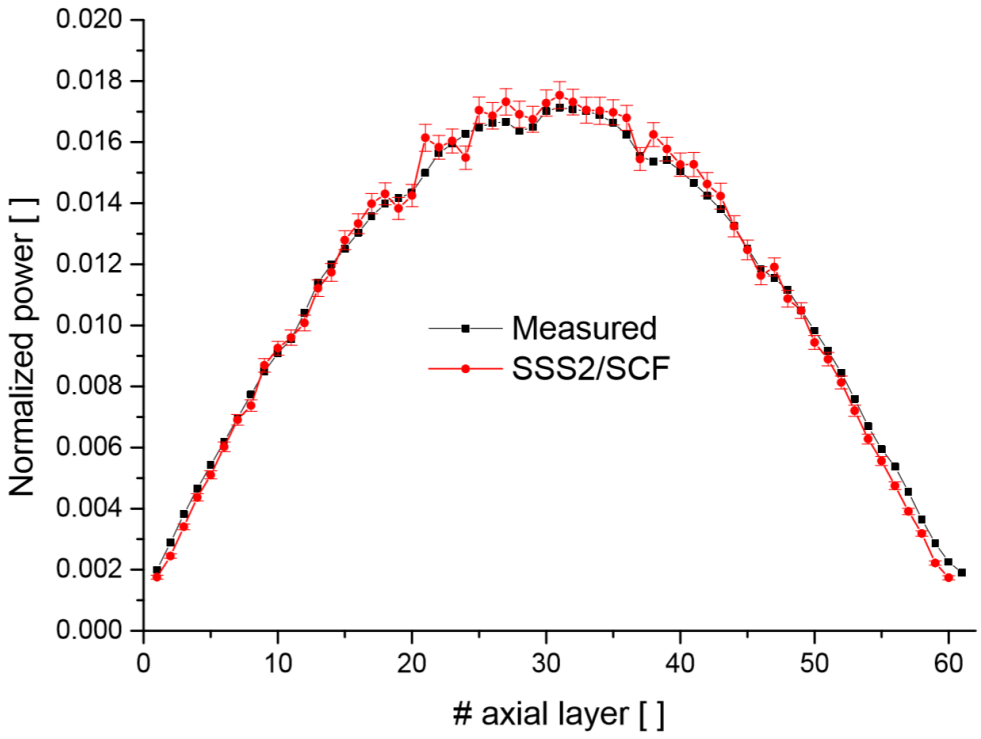

Figure 25: Comparison of SSS2/SCF BEAVRS HZP normalized axial power profiles in assembly with smallest C/E relative error, i.e. B03, with experimental data (Horelik, et al., 2016)

Except the worth of the D control rod banks, all worths are over-predicted by all tools relative to the measured values. The degree of over-prediction varies for banks and tools. For Serpent 2/SUBCHANFLOW, the maximum difference to the measured value occurs for B control rod bank. The deviation is 63 pcm. All in all, the agreement between SSS2/SCF and the experimentally obtained bank worths is acceptable in the view of the other spatial deviations.

Table 11: Comparison of BEAVRS Cycle 1 HZP computed control rod bank worths and measurements (Horelik, et al., 2016; Kelly, et al., 2013; Ryu, et al., 2014)

CR bank	Measured worth [pcm]	MC21 [pcm]	OpenMC [pcm]	nTRACER [pcm]	SSS2/SCF [pcm]
A	788	773	771(6)	782	776(4)
B	1203	1260	1234(7)	1229	1266(5)
C	1171	1172	1197(7)	1181	1198(5)
D	548	574	556(6)	584	594(4)
SE	461	544	501(6)	504	494(4)
SD	772	786	- -	- -	790(4)
SC	1099	1122	- -	- -	1109(5)

It is the opinion of the author that the BEAVRS model discussed above is sufficiently accurate to be the basis of validating the Serpent 2/SUBCHANFLOW using cycle 1 and 2 plant data. The validation efforts are to proceed once the coupled code system has been extended to cover core follow calculations and its numerical performance has been improved enough to allow for finishing such simulations in a reasonable amount of time. Moreover, the observed radial tilt in measured powers slowly disappears with burn-up in cycle 1. Measurements later in the cycle should compare better with simulations.

3.4 Conclusions and next steps

The verification and validation work for Serpent 2/SUBCHANFLOW followed the multilevel validation methodology. As a first step, Serpent 2 is successfully used to model VENUS-1 and VENUS-2 critical experiments scoping UOX and MOX fuel elements. Thereafter, the coupled code SSS2/SCF has been verified by a code-to-code comparison with TRIPOLI4/SUBCHANFLOW as well as MCNP5/SUBCHANFLOW. In both cases, a good agreement between the solutions has been found.

Early efforts to validate Serpent 2/SUBCHANFLOW simulations using the BEAVRS benchmark have been discussed. The physics of the reactor core are found to be captured well by verification simulations of the experiments conducted at HZP. However, the SSS2/SCF validation work using the BEAVRS benchmark can only be completed once the coupled codes has been extended to cover burn-up calculations and is, thus, capable of core follow simulations.

The level of V&V reached for SSS2/SCF is considered to be sufficient for square lattice PWRs to employ the coupled code to produce reference solutions for the detailed assessment of the reactor simulator DYNSUB. Nevertheless, the V&V base for SSS2/SCF on all levels presented in this chapter is neither broad nor comprehensive enough to cover all of pin-resolved reactor simulators functionalities for PWRs. In order to eventually arrive at a production Monte Carlo thermal-hydraulics coupled code, the V&V efforts need to be continued in the near future.

4 Pin-homogenized Reactor Simulator DYNSUB

4.1 State-of-the-art of pin-homogenized reactor simulators

Pin-homogenized tools aim at delivering a cost-effective improved simulation of a nuclear power plant. Cost-effective refers to a better description of the physics involved but executable on commodity computing clusters which usual users/customers actually have at their disposal. These evolutionary tools could bridge the gap until truly high-fidelity reactor simulators are readily available and employable in future.

The parallel production code SCOPE2 delivers such improved cost-effective pin-by-pin simulations concerning in-core fuel management of PWRs. SCOPE2 employs an efficient nodal method for solving the simplified transport equation at pin cell resolution using homogenized effective materials (Tatsumi & Yamamoto, 2003) and has its own simplified internal sub-channel thermal-hydraulics module (Yamamoto & Ikeno, 2005). This code is a new software development and not a coupled code system build from extended state-of-the-art tools. The applicability of SCOPE2 has been proven by performing a large number of core follow calculations for the Japanese PWR fleet (Tatsumi & Yamamoto, 2003; Tatsumi, et al., 2005). To extend the range scenarios that can be treated by SCOPE2, neutron kinetic solvers have been introduced in SCOPE2 (Endo & Tatsumi, 2008). However, no pin-by-pin analysis of a safety relevant transient scenario for a full nuclear reactor core using SCOPE2 has been reported so far.

Another coupled code system COBAYA3/COBRA-TF aims at becoming a cost-effective multi-physics tool. It was used to study a 3D pin-by-pin model of full PWR core under hot zero power and hot full power conditions as defined in the OECD NEA and U.S. NRC PWR MOX/UO_2 core transient benchmark (Kozlowski & Downar, 2003). For the HZP case, comparisons of the homogeneous pin-by-pin diffusion COBAYA3 result with DeCART reference solution were performed (Herrero, et al., 2009). For the HFP case, code-to-code benchmarks with other nodal reactor simulators were carried out (Jimenez, et al., 2010). While both COBAYA3 and COBRA-TF allow for simulating transients, no coupled full core pin-by-pin evaluations of operational occurrences or design basis accident scenarios employing COBAYA3/COBRA-TF have been published yet.

Reading through literature, one can identify four basic methodologies of generating cross sections for pin-homogenized reactor simulators. In this context, the term methodology refers to the type of simplified spectral geometry applied in the heterogeneous lattice transport

simulations and how pin level cross sections are derived from it. In principle, all methodologies use flux-volume weighting to produce pin level few-group homogenized constants.

One could use infinite lattices of a specific pin cell type, as it is done for fuel assemblies with the nodal methods. However, in all tests performed at INR, the accuracy of this methodology was so poor that it is not considered any further. All remaining three methodologies utilize infinite lattices of super-cells of the geometry to generate pin level cross section libraries. The most common choice of a super-cell would be the corresponding fuel assembly. The second methodology then homogenizes all fuel pins of the same type inside the fuel assembly into one effective material. Alternatively, one can create a pin cell cross section set for every unique fuel pin position in the fuel assembly, i.e. exploiting possibly existing symmetries. Moreover, this third methodology can be supplemented by pin level homogenization corrections, the fourth methodology. Two different approaches for the solution of the homogeneous low order system to reproduce the higher order heterogeneous lattice transport quantities of interest have been proposed in literature: super-homogenization factors (SPH) (Hébert, 1993a; Hebért & Mathonniere, 1993b) and interface discontinuity factors (IDF) (Smith, 1986; Sanchez, 2009).

SCOPE2 performs its in-core fuel management simulations based on pin-by-pin cross sections obtained with the fourth methodology. Of the two possible homogenization corrections it utilizes only SPH factors (Yamamoto, et al., 2004a; Yamamoto, et al., 2004b). COBAYA3/COBRA-TF on the other hand focuses on IDF.

The achievable improvement of the solutions obtained with pin-homogenized reactor simulators employing SPH factors or IDF strongly depends on appropriately chosen super-cells as spectral geometries. As a result, the developers of SCOPE2 try to improve the SPH factor generation (Yamamoto, et al., 2004b). Inaccurate pin level IDF were also identified as one major limitation of pin level homogeneous calculations by other researchers (Herrero, et al., 2012; Kozlowski, 2011; Kozlowski, 2005). Both made efforts to improve the IDF generated by making them environment dependent (boundary conditions and neutron spectra). Kozlowski developed a generalized version of IDF, in which a function based on a heterogeneous solution is used to approximately predict environment-dependent IDF based on the homogenous information available during a reactor simulator run. This polynomial function was obtained using a least-squares technique. An implementation of this approach in PARCS was found to have issues with numerical stability and further improvement of the methodology was recommended (Kozlowski, 2005).

Herrero et al. proposed to build a functional fitting of IDF to their environment based on terms of the Analytical Coarse-Mesh Finite Difference Method (ACMFD) formulation of the neutron diffusion approximation (Herrero, et al., 2012). Though the quality of the results obtained by predicting IDF with these functional fittings using the reactor simulator COBAYA3 is

promising, the non-linearity of this method leads to sharp increase in steady-state solution time if numerical stability was to be ensured (Herrero, et al., 2012).

4.2 Status of DYNSUB before this doctoral research study

DYNSUB consists of DYN3D and SUBCHANFLOW. For a brief introduction of SCF please refer to subsection 2.3.2. DYN3D and the status of DYNSUB prior to this work are described shortly in the following.

4.2.1 DYN3D

In DYNSUB, the multi-group version of DYN3D released in December 2009 is embedded. DYN3D's neutronics solver is able to calculate a detailed multi-group fuel assembly and pin level solution of the neutron transport problem using the diffusion approximation or simplified transport (SP_3), based on the developments of Brantley and Larsen (Brantley & Larsen, 2000).

It applies a multi-group nodal expansion method (NEM) using a quadratic transverse leakage approximation. To treat the time dependence, a fully implicit finite difference scheme using exponential transforms is employed (Beckert & Grundmann, 2008). In the DYN3D code, a one-dimensional thermal-hydraulic module FLOCAL is implemented (Grundmann, et al., 2005). It is typically used as a 1D assembly level thermal-hydraulic module.

4.2.2 Description of DYNSUB

In the DYNSUB code (Gomez-Torres, et al., 2012a; Gomez-Torres, et al., 2012b), SUBCHANFLOW replaces the internal thermal-hydraulic module FLOCAL of the reactor simulator DYN3D. It has been serially integrated into DYN3D.

The coupling of the neutronics and thermal-hydraulics modules is internal and limited to pin-by-pin simulations employing simplified transport. At the end of each steady-state iteration or transient time step, neutronics module updates the (time-dependent) pin power distribution used as input for the thermal-hydraulics calculation. The thermal-hydraulics module in turn passes fuel pin temperature distributions (radially and axially for each pin), moderator temperatures and densities back to neutronics. In case of a transient calculation, the latter correspond to the values at the end of a time step.

As DYNSUB's cross section update routine only applies one effective Doppler temperature in the look-up and update process per pin cell, the detailed radial fuel temperature distributions for

each fuel pin computed by SUBCHANFLOW are condensed into one effective Doppler temperature value. The code offers several possibilities for this condensation.

DYNSUB uses a fixed spatial mapping. Axially there is a one to one correspondence between thermal-hydraulic and neutronic axial mesh layers. While the neutronic mesh is fuel pin centered, the thermal-hydraulics mesh is coolant channel centered. Simulation results have to be spatially interpolated before being passed to the other module.

DYNSUB applies the adaptive time step algorithm of DYN3D allowing for having several neutronic time steps inside a thermal-hydraulic one. In terms of coupling numerics for transient simulations, only an explicit marching scheme is available.

A coupled steady-state calculation is considered to be converged, when complementary to the internal convergence criteria of the neutronic and thermal-hydraulic codes convergence criteria on both the local Doppler temperature and local moderator density are met. The same set of convergence criteria is used to control the time step size in case of a transient simulation run.

This first version of DYNSUB misses numerous simple to implement numerical models to cover all possible conditions of a PWR reactor core. For instance, this version cannot handle time-dependent boundary conditions in its thermal-hydraulic model. Moreover, only limited efforts to perform code and solution verification have been undertaken so far (Gomez-Torres, et al., 2012a; Gomez-Torres, et al., 2012b). Last but not least, no tool chain to prepare few-group effective cross sections for DYNSUB existed.

4.3 Goals of DYNSUB development

It is the goal to demonstrate that DYNSUB can be used to analyze realistic, engineering-sized and industry-like cases such as full PWR reactor core at hot full power conditions in a reasonable amount of time (see chapter 7).

In a first step, DYNSUB is to be extended into a fully functional pin-homogenized reactor simulator (cp. section 4.4). Afterwards, DYNSUB's solution is to be verified by code-to-code and validated by code-to-data comparisons. Unfortunately, both pin-homogenized and pin-resolved reactor simulator developments are too recent for any significant database for code-to-code solution verification to build up. This is especially true for transient simulations as no calculation of a safety relevant scenario for a non-academic problem with either a pin-homogenized (see section 4.1) or a pin-resolved reactor simulator has been reported in literature yet (see section 1.3). Hence, the only option to verify and validate DYNSUB's numerical models and algorithms is to study existing international benchmarks for assembly-homogenized or nodal simulation tools (cp. chapter 5). As a consequence, the extension of DYNSUB includes

enabling nodal simulations for square and hexagonal fuel lattices. Further efforts to validate the new DYNSUB version are undertaken in chapter 6, in which DYNSUB is used to model the Special Power Excursion Reactor Test III.

In order to make DYNSUB a readily usable pin-homogenized reactor simulator, a calculation route to produce multi-dimensional cross section tables has to be set up (see section 4.5). Pin-wise cross section generation methodologies 2 through 4 discussed in section 4.1 are to be considered. As improved methodologies for determining IDF and SPH factors have not worked numerically in a satisfactory manner (see section 4.1), these are not implemented in the cross section generation workflow. Hence, the route followed covers determining few-group assembly-homogenized constants for DYNSUB. The U.S. NRC production lattice code SCALE/TRITON is to be used as part of the cross section calculation route. SCALE/TRITON is limited to LWRs but numerous validation studies have been and are carried out, for instance (Bowman & Gill, 2006; Illas, et al., 2012; Hermann, 2000; Hermann, et al., 1995; Sanders & Gauld, 2003). This lattice code is based on high-order deterministic neutron transport as any classical one is. Using CE Monte Carlo neutron transport for obtaining few-group homogenized constants for deterministic reactor simulators like DYNSUB has become a popular research topic as reactor simulators and computational capacities evolve. One of the first Monte Carlo codes conceived as a lattice code was Serpent. A study recently found that generating complete multi-dimensional cross section tables with CE Monte Carlo lattice codes has become feasible (Leppänen & Mattila, 2014). Unlike SCALE/TRITON, the methods to produce few-group homogenized cross sections with Serpent 2 are actively developed by numerous groups. Solution verification is ongoing and first efforts to validate the tool have begun (Leppänen, et al., 2014a; Leppänen, et al., 2014b).

MC lattice codes unlike their deterministic counterparts can handle complicated reactor geometries using the best available knowledge on neutron interactions and introduce no major approximations. As a consequence, they are the method of choice to model novel reactor concepts. Introducing Serpent 2 as lattice code for DYNSUB, hence, allows for quickly extending the range of applicability of DYNSUB from classical LWR to new reactor designs in the future. Since SSS2's transport simulation is inherently three-dimensional, it has the benefit of being able to produce 3D reference solutions. The majority of deterministic lattice codes like SCALE/TRITON, on the other hand, is limited to two dimensions. Thanks to the development of Serpent 2/SUBCHANFLOW here, the unique possibility of producing 3D HFP reference solutions with a lattice code arises.

Both the SCALE/TRITON-DYNSUB and the Serpent 2-DYNSUB code sequence require V&V work to be carried out. Selected solution verification examples for these two tool chains are presented in subsections 4.5.5 and 4.5.6. Subsequently, to limit the extend only validation

efforts focussing on the Serpent 2-DYNSUB code sequence are presented in this work. The latter code sequence has been chosen compared to the package SCALE/TRITON-DYNSUB since a significant contribution to the development of cross section generation methodologies for Serpent 2 can be made. All existing V&V for creating few-group homogenized cross sections with SSS2 so far has been done for HZP operating conditions and only for static calculations (Leppänen, et al., 2014a; Leppänen, et al., 2014b). By modeling SPERT III with DYNSUB and producing static reference solutions with thermal-hydraulic feedback using SSS2/SCF, for the first time multi-dimensional time cross section tables generated with Serpent 2 are assessed under non-zero power and transient conditions (see chapter 6).

4.4 Extension of the internal coupling

The new functionality described below has been assessed in the framework of the solution verification and validation cases discussed in chapter 5. Developments are only shortly summarized here.

DYNSUB's internal coupling has been enhanced to enable pin-by-pin diffusion as well as fuel assembly/channel level resolution modeling for square fuel lattices. Moreover, the nodal simulation capabilities have been developed such that they also include hexagonal fuel lattices as present in VVER type reactors. The capability of low spatial resolution models has been introduced to facilitate the fast scoping calculations, V&V work and simplify identifying the sources of differences in simulations. Both the pin-by-pin and fuel assembly resolution DYNSUB models employ identical solvers, transient time steppers, thermal-hydraulic correlations and coupling algorithms. Hence, comparing reactor models at low and high, i.e. fuel pin cell, resolution only two major sources of differences remain: the spatial resolution and the cross section libraries. This fact enables the author to make a better assessment of international code-to-code benchmarks that have been studied using DYNSUB nodal (see chapter 5) and pin-by-pin (see chapter 7).

Additionally, a flexible axial mapping scheme has been introduced. A one-to-one correspondence between neutronic and thermal-hydraulic axial mesh layers is no longer required. As test calculations have shown that the neutronic mesh needs to have at least approximately 70 axial layers in a western LWR, i.e. an axial spatial resolution of approximately 5 cm, for a mesh independent solution, it has been decided to allow each thermal-hydraulic mesh to correspond to any integer number of neutronic mesh layers. Results are mapped between both meshes.

Another part of the new generalized mapping scheme between the constituent codes DYN3D and SUBCHANFLOW is the capability to model reflectors. Reflector cells may either be

included in both the neutronics and the thermal-hydraulics model or only in the former one. If reflectors are only treated by DYN3D, changing thermal-hydraulic conditions can be approximately taken care of by utilizing several pre-built reflector treatment functions, e.g. the thermal-hydraulic conditions in the reflector can be set to core inlet conditions everywhere or the heat up of the bypass by gamma-heating and coolant mixing above the active core can be accounted for in an simplified manner. The main objective of developing the reflector treatment functions is to keep the thermal-hydraulics full core sub-channel model as small as possible, since it was observed that for large models such as pin-by-pin full core calculations SUBCHANFLOW consumes up to 70 % of the overall computing time. Hence, if no detailed solution of the thermal-hydraulic fields in the reflectors is needed for an accurate description of a scenario, the user should use the simplified description using the pre-built functions.

While applying DYNSUB to find the eigenvalues of large pin level models, it has been observed that steady-state solutions for some problems diverged within one of the early iteration steps. In an analysis it has been found that a relaxation of the steady-state Picard iteration could resolve this issue and lead to convergence in all cases.

In the relaxed form of the Picard iteration, pin powers and thermal-hydraulic properties are weighted with the results from the previous iteration step before being passed from DYN3D to SUBCHANFLOW and vice versa. The following expression is used

$$\vec{X}_{n+1} = \theta\, \vec{X}_{n+1} + (1-\theta)\vec{X}_n\,, \tag{17}$$

with n being the iteration step, θ the relaxation coefficient and $\vec{X}$ the data field being exchanged between the neutronics and thermal-hydraulics code. Optimum θ values have been determined to be in the range of 0.5 - 0.7 for pin-by-pin simulations of a full PWR core.

Besides the solution of a simple eigenvalue problem, DYNSUB's steady-state functionalities have been extended to cover critical boron and (critical) power search. The aim of the critical boron search algorithm is to determine the concentration of chemical shim in the coolant necessary to bring the reactor into a critical state. The (critical) power search algorithm allows to find the reactor thermal power corresponding to a certain, pre-defined core multiplication. Both algorithms are based on a single eigenvalue problem.

As DYNSUB is to be used as a safety analysis tool to study operational transients, operational occurrences and design basis accident scenarios, its coupling scheme has been revised to consider time-dependent thermal-hydraulic boundary conditions for the reactor core. DYNSUB may now be employed to study thermal-hydraulically driven transients if the change of the

boundary conditions with time is a priori known since it includes no module to evaluate the balance of plant nor has it been coupled to a thermal-hydraulic system code yet.

To complete DYNSUB's capability to model PWR, a boron transport model has been added to SUBCHANFLOW. This model has been assessed in detail by Calleja et al. (Calleja, et al., 2014a). A good performance of the boron transport solver compared to that of the sub-channel code FLICA as well as the one of 1D assembly level thermal-hydraulic module FLOCAL has been observed.

In addition, some simple control logic has been included in the internal DYNSUB coupling. Several reactor trip conditions can be evaluated simultaneously, such as high neutron flux or reactor coolant system pressure. The reactor trip conditions are specified in the input along with corresponding delays. The delay refers to the time passing between the point, at which the trip condition has been reached to the time the control rods are free to move. For the control banks affected both insertion depth and insertion time are specified by the user. Consequently, partial SCRAMs and stuck rods can also be accounted for.

After a reactor trip decay heat needs to be taken into account. DYNSUB has no operational method to compute decay heat on-the-fly. As an intermediate solution, the tool can now read and use tabulated decay heat data computed based on international standards such as DIN 25463 or ANSI/ANS-5.1-2005 during a transient simulation. DYNSUB interpolates linearly between points in the tabulated data sets.

The DYN3D MG version in DYNSUB has no functional control rod (CR) decusping model. The only available option is provided by a volume weighting method to determine effective macroscopic cross sections for computational nodes with partially inserted control rods. This method is known to exhibit strong rod cusping and is not accurate enough for the intended applications. An approximate flux weighting method (Dall'Osso, 2002) has been implemented to mitigate this deficiency. Thereby, the effective macroscopic cross sections in a partially rodded node are given by the following expression

$$\Sigma_g = \frac{(1-f)\,\Sigma_{NR,g}\,\phi_{NR,g} + f\,\Sigma_{R,g}\,\phi_{R,g}}{(1-f)\,\phi_{NR,g} + f\,\phi_{R,g}}, \tag{18}$$

with $\phi_{NR,g}$ and $\phi_{R,g}$ being the node average unrodded and rodded scalar fluxes, $\Sigma_{NR,g}$ and $\Sigma_{R,g}$ the macroscopic cross section with and without inserted CR and *f* the fraction of node in axial direction covered by the absorber. The rodded and unrodded scalar fluxes are estimated based on the scalar fluxes computed with DYNSUB for the axial nodes above the partially rodded node (layer *k*+1) , below (layer k-1) and the node itself (layer *k*).

$$\phi_{NR,g} = \frac{\Delta z_{k-1}\,\phi_{k-1,g} + (1-f)\,\Delta z_k\,\phi_{k,g}}{\Delta z_{k-1} + (1-f)\,\Delta z_k}\,; \tag{19}$$

$$\phi_{R,g} = \frac{\Delta z_{k+1}\,\phi_{k+1,g} + f\,\Delta z_k\,\phi_{k,g}}{\Delta z_{k+1} + f\,\Delta z_k}\,. \tag{20}$$

Selected verification cases for this decusping model are discussed in section 5.1. Besides introducing improvements to reduce CR cusping, a model to describe control rods with grey tips has been implemented. The latter control rod type has two axial zones consisting of different absorber materials. The one occupying most of the CR is a black absorber with a very high thermal neutron absorption cross section. In the tip of this rod type, a material with a significantly lower neutron absorption cross section in the thermal energy domain is used, thus it is referred to as grey. CRs with grey tips are present in some VVER designs. Moreover, any control or shutdown bank in DYNSUB can now not only be moved at constant speed but can be accelerated.

The Python scripting language based post-processing tool of the first DYNSUB version proved incapable of handling large cases such as pin-by-pin simulation of a full PWR core. It is limited to processing steady-state simulations. Hence, DYNSUB has been adapted and extended to write MED files. The latter files are native to the open-source SALOME platform (www.salome-platform.org) offering a wide range of post-processing options in its module Post-Pro or ParaView (www.paraview.org). The MED files produced by DYNSUB include fields of heating powers, effective Doppler and moderator temperatures, fuel centerline and cladding outside temperatures, moderator densities, chemical shim concentrations as well as few-group normalized scalar neutron fluxes.

Finally, efforts to improve DYNSUB's numerical performance have been undertaken. Implemented measures and achievements in terms of performance are briefly discussed in Appendix E.

4.5 Cross section generation for DYNSUB

4.5.1 Cross section generation workflow

The workflow to generate multi-dimensional cross section tables for DYNSUB with and without homogenization corrections are shown in Figure 26. Without homogenization corrections, the simulation of spectral geometries with lattice codes is followed by processing the lattice code outputs into a NEMTAB cross section format usable in a DYNSUB production

run. To this end, the tool createXSlib has been developed. It is introduced in subsection 4.5.3. Before that, the two lattice codes employed, SCALE/TRITON and Serpent 2, are discussed.

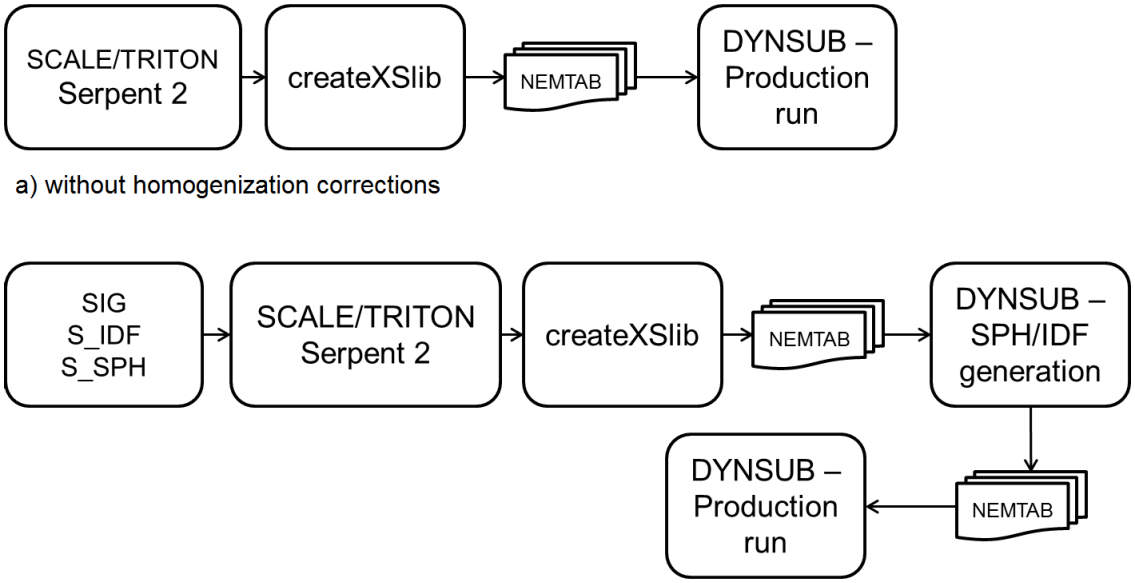

Figure 26: Workflow to generate multi-dimensional cross section tables for DYNSUB without homogenization corrections (a) and with homogenization corrections (b)

If SPH factors or IDF are used as homogenization corrections, a production cross section library cannot be obtained directly from the lattice code outputs with createXSlib. An intermediate library has to be processed with DYNSUB in order to arrive at the final multi-dimensional cross section library. How to actually evaluate SPH factors or IDF for DYNSUB and why it is necessary to work with intermediate XS libraries is explained in subsection 4.5.4.

Finally, selected verification cases for both the SCALE/TRITON-DYNSUB and the Serpent 2-DYNSUB calculation route are presented in subsections 4.5.5 and 4.5.6.

4.5.2 Lattice codes used

To generate multi-dimensional cross section tables for DYNSUB the lattice codes Serpent 2 and SCALE/TRITON are utilized. SCALE/TRITON is shortly presented in the following. Serpent 2 is revisited to take a look at its features as a lattice code.

TRITON (DeHart & Bowman, 2011) is one of the control modules in the SCALE code package. It receives a single input file specifying geometry of and materials in a cross section generation problem. Afterwards, it processes the input file converting it into formats understood by the

sequence modules. TRITON calls each module and is responsible for the exchange of data between different modules.

The first step in any simulation is generating problem-dependent multi-group (MG) cross sections from the generic SCALE libraries. TRITON executes BONAMI to perform a self-shielding of resonances in the unresolved resonance range. The modules CENTRM/PMC or NITAWL may be used to treat resolved resonances. After these calculations have been completed, a problem-dependent MG library has been created that may be used by any subsequent simulation.

In a second step, few-group multi-dimensional cross section libraries are determined by MG transport code NEWT. NEWT performs reactor eigenvalue calculations and uses neutron fluxes obtained to collapse MG cross sections to the desired few-group structure. NEWT has a branch capability for such libraries. It can perturb moderator densities, fuel and moderator temperatures, boron concentration and control rod position. In depletion mode, NEWT also compiles three-group volume weighted cross section libraries for every material in the problem. COUPLE uses these three-group libraries to update ORIGEN-S input data at each burn-up time step. ORIGEN-S then depletes materials using three-group neutron fluxes provided by NEWT. Once the calculations for one burn-up time step have been completed and material compositions have been updated, the entire module sequence is executed again for the next time step until the specified burn-up is reached.

Serpent (Leppänen, 2013) was conceived as a Monte Carlo lattice physics code with the main purpose of generating few-group homogenized constants for deterministic reactor simulators. Serpent 2 is capable of automatically calculating cross section sets for low order deterministic transport simulations in any of its geometry universes, such as few-group reaction cross sections, scattering matrices and cross sections up to Legendre order 7, diffusion coefficients, assembly discontinuity factors and pin power form factors for pin power reconstruction techniques. The computed cross section sets may be corrected for leakages using a deterministic solution of the multi-group B1 equations (Fridman & Leppänen, 2011). Furthermore, Serpent 2 evaluates effective delayed neutron fractions and point kinetics parameters in each transport simulation. The corresponding methodology has been validated by studying numerous critical experiments (Leppänen, et al., 2014c).

Serpent 2 has a built-in depletion solver. Hereby, the evolution of nuclide compositions in fuel being irradiated can be tracked and few-group homogenized cross sections can be generated for the entire life cycles of fuel assemblies. For burn-up calculations during which few-group cross sections for use in deterministic reactor simulators are generated, Serpent 2 has a branch capability (Leppänen, 2014). It can change the density and temperature of any material as well as replace entire materials or parts of the overall geometry, i.e. bodies as well as filling

materials. Consequently, like SCALE/TRITON Serpent 2 is capable of producing complete multi-dimensional cross section tables for deterministic reactor simulators like DYNSUB in a single run.

4.5.3 CreateXSlib and lattice code pre-processors

CreateXSlib is a tool to translate the outputs of the lattice codes SCALE/TRITON and Serpent 2 into multi-dimensional libraries for DYNSUB. It has been developed in its entirety as part of this thesis.

Using CreateXSlib both assembly-homogenized and pin-homogenized few-group cross section tables can be generated. The tool allows for different thermal-hydraulic state parameterizations of these tables. All XS library types may be parameterized using four thermal-hydraulic (TH) state variables, namely fuel temperature, moderator temperature, moderator density and chemical shim concentration (i.e. soluble boron concentration). Furthermore, constant pressure conditions may be assumed, removing moderator temperature from the set of thermal-hydraulic state variables. Reflector XS may be also parameterized using any of the TH variables itself or any combination of two TH variables, e.g. fuel temperature of neighbouring fuel assembly and boron concentration. For verification and debugging purposes, all XS library types may also be created containing exactly one thermal-hydraulic state per burn-up point.

Lattice code inputs for generating pin-by-pin few-group cross sections with homogenization corrections for realistic cases can easily reach several thousand lines in length. The in-house Scale Input Generator (SIG) offers a comprehensive graphical user interface (GUI) as shown in Figure 27. Utilizing the GUI, the user describes the problem to be solved in terms of geometry, material composition and the desired few group structure. SIG then automatically generates the corresponding input for homogenization correction generation.

In case of Serpent 2, a set of scripts (S_IDF, S_SPH) written in the Python scripting language performs a similar job (see Figure 26 b)). This script system takes a Serpent 2 input to generate few-group cross sections for a given fuel assembly level problem, analyzes its structure and outputs the corresponding input for generating pin-wise few-group cross sections with homogenization corrections for Serpent 2.

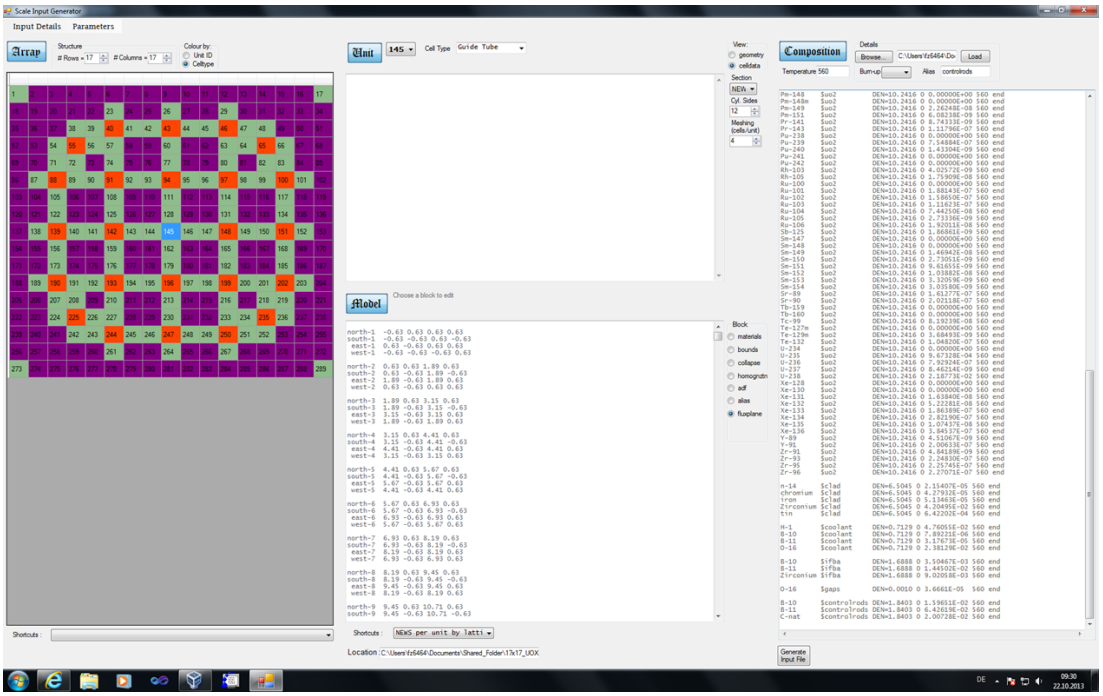

Figure 27: Screenshot of the SIG GUI, model of a 17x17-25 UOX fuel assembly to automatically generate the SCALE/TRITON input needed to obtain homogenization corrections

4.5.4 Homogenization corrections

SPH factors adjust the homogeneous cross sections in order to preserve the cell average reaction rates of the heterogeneous lattice calculation. They are defined as the ratio of the heterogeneous and the homogeneous cell volume averaged fluxes. Since the homogeneous fluxes are a function of the homogeneous cross sections, these factors have to be generated by an iteration of neutron flux calculations described in detail by Hébert (Hébert, 1993a).

For DYNSUB, a SPH factor generation scheme developed for DYN3D (Grundmann & Mittag, 2011) has been extended to allow automatically generating SPH factors for all thermal-hydraulic states in a multi-dimensional cross section library. The original scheme could only treat the nominal thermal-hydraulic condition described in the DYN3D input. Moreover, subroutines have been adapted to linearly interpolate SPH factors to obtain values for thermal-hydraulic states in between the basis points of the multi-dimensional cross section library and to perform material weighting on SPH factors in case of the movement of control rods.

DYNSUB allows the user to apply SPH factors in both pin-by-pin diffusion and simplified transport calculation. At this point it has to be mentioned that no lattice code today is capable of producing the data needed to evaluate the equivalence of the simplified transport equations for the second flux moment, since the current formulation of the simplified transport method does

not provide us with the means to reconstruct an SP_3 solution from a known angular flux (Chao & Yamamoto, 2012). DYNSUB uses the ad hoc assumption that the diffusion SPH factors may also be applied to 'second moment' diffusion coefficient in simplified transport. As the second flux moment is generally several orders of magnitude smaller than the zeroth moment (Beckert & Grundmann, 2008), this approximation is believed to only marginally affect results.

Interface discontinuity factors are another option to enforce the conservation of few-group node volume averaged neutron reaction rates, node surface averaged currents and, as a result, eigenvalues between the higher order heterogeneous lattice transport calculations and the low order homogeneous simulations by reactor simulators like DYNSUB. The former were performed to produce few-group effective incident neutron cross sections. Thus, IDF allow for treating the remainder of homogenization and group condensation errors.

Even though GET and BBH IDF may mathematically be derived for both the diffusion and simplified transport being the lower order operator acting on the homogeneous system (Kozlowski, 2011; Sanchez, 2009), the equivalence of the second flux moment appearing in second order form of the simplified transport equations cannot be evaluated based on an existing heterogeneous angular flux solution for reasons mentioned above. In his work, Kozlowski approximately computed such an SP_3 solution from a heterogeneous angular flux solution in order to be able to generate IDF for the simplified transport method (Kozlowski, 2011). A similar capability for DYNSUB is currently under development. As a result, only the IDF generation for DYNSUB's diffusion approximation solvers is presented and analyzed. For simplicity, in the following discussion of GET and BBH IDF, the few-group indices of all involved physical quantities are omitted.

The GET IDF (Smith, 1986) are defined as the ratio of the heterogeneous few-group scalar interface/boundary flux ϕ_s^{het} obtained from a higher order heterogeneous lattice transport solution and the homogeneous one ϕ_s^{hom} as produced by the low order homogeneous simulation (cp. equation (21)). The GET IDF are interface dependent and, consequently, have the capability to consider the environment of a mesh node, i.e. the leakage to its neighbors.

$$f_{GET}^{S} = \frac{\phi_s^{het}}{\phi_s^{hom}} . \tag{21}$$

In the case of heterogeneous lattice transport calculations for single fuel assemblies with conservative boundary conditions, i.e. vanishing net neutron currents, the general definition of the GET IDF reduces to that of the assembly discontinuity factor (ADF).

While GET IDF are applied to and preserve heterogeneous few-group reference values of interface/boundary neutron fluxes between nodes, BBH IDF (Sanchez, 2009) are applied to and

preserve few-group reference values of interface/boundary partial currents. Hence, one refers to GET IDF as flux discontinuity factors and to BBH IDF as current discontinuity factors. The generic form of BBH IDF for both incoming and outgoing partial currents ($J_{\pm}$) is given by

$$f_{\pm_{BBH}}^{s} = \frac{J_{\pm_s}^{het}}{J_{\pm_s}^{hom}} . \tag{22}$$

Employing current discontinuity factors in DYNSUB would imply extending existing solvers. However, in case of diffusion as the low order operator, it was shown that both current discontinuity factors of an interface/boundary may be represented by a single flux discontinuity factor (Sanchez, 2009) (see equation (23)), which can be formally treated like a GET IDF by 3D reactor simulators.

$$f_{BBH}^{s} = 2\,\frac{J_{-s}^{het} + J_{+s}^{het}}{\phi_s^{hom}} . \tag{23}$$

As can be seen from equations (21) and (23) the homogeneous few-group scalar interface/boundary fluxes ϕ_s^{hom} are mandatory to evaluate both types of IDF. The method of obtaining these fluxes depends on the spatial discretization used by the reactor simulator. DYNSUB's diffusion solvers apply a multi-group nodal expansion method employing a quadratic transverse leakage approximation. The interface/boundary neutron fluxes are not generally part of a NEM solution. Node-to-node coupling is achieved with partial currents. However, it is possible to compute the interface/boundary neutron fluxes based on the expansion of the scalar neutron flux in every mesh node.

In DYNSUB, the 3D diffusion problem is reduced to a one-dimensional (1D) problem by transversely integrating the neutron diffusion equation. In order to find the homogeneous solution, the transverse integrated 1D diffusion equation (cp. equation (24)) has to be solved for each direction *u* and all energy groups *g* in each node *i* of the homogeneous problem.

$$\begin{aligned} -{D_g}^i \frac{d^2}{du^2}\Phi_g^i(u) + {\Sigma_{R,g}}^i \Phi_g^i(u) \\ = S_{g,i}(u) - {L_{g,i}}^{het}(u) \end{aligned} \quad . \tag{24}$$

The transverse leakages ${L_{g,i}}^{het}$ have to be evaluated based on the higher order heterogeneous lattice transport solution consistent with the reactor simulator solver. In DYNSUB, the transverse leakage expansion is determined based on the average transverse leakage in a node,

which are computed from the net surface currents, and the transverse leakages on the surfaces of that node. The latter are evaluated based on the assumption that the second partial derivative of neutron fluxes with respect to space is continuous and, thus, transverse leakages on an interface between nodes become the weighted average of the average transverse leakages of the two adjacent nodes. The boundary conditions (BC) for each 1D problem are given by the heterogeneous net surface currents and node average fluxes.

DYNSUB's existing explicit iterative diffusion flux solvers only accept albedos to be applied to partial currents as BC and partial currents with or without DF as interface conditions. Hence, a new 1D solver to evaluate the equivalence has been implemented in DYNSUB. It solves diffusion problem detailed above. Nodes *i* and each direction *u* are treated one at a time by directly inverting the resulting system of equations employing the Gaussian elimination algorithm.

The IDF generation option can be triggered by a DYNSUB input keyword and is available for both fuel assembly and pin level. To generate discontinuity factors, DYNSUB reads a specific type of multi-level cross section library for each material, which includes heterogeneous few-group quantities necessary for the computation. It executes a neutron flux calculation for each thermal-hydraulic branch of each burn-up point in the library based on which homogeneous surface fluxes and, hence, discontinuity factors are evaluated. At the end, DYNSUB writes a new cross section library now including the discontinuity factors.

4.5.5 Verification of SCALE/TRITON-DYNSUB code sequence

Because of their mathematical derivation, both SPH factors and IDF force a low order neutron transport reactor simulator like DYNSUB to reproduce the high order solution of the lattice code employed if the former is used to model the spectral geometry of the latter. Therefore, modeling spectral geometries with DYNSUB utilizing SPH factors or IDF is the ideal test for the cross section table calculation route. If cross sections and homogenizations are processed in an appropriate manner, a conservation of eigenvalues and reaction rates between DYNSUB and either lattice code will be observed. This verification case is also used to compare the different methodologies for generation pin-by-pin cross sections introduced in section 4.1 for DYNSUB.

In the selected case, the super-cell employed to generate pin level few-group constants is a square lattice pressurized water reactor (PWR) fuel assembly. Reflective boundary conditions are employed. The test case is a fresh 17x17-25 UOX fuel assembly studied at HZP conditions (cp. Figure 28) (Kozlowski & Downar, 2003). This UOX fuel assembly contains fuel pins including zirconium diboride as burnable poison, the integral fuel burnable absorber rods (IFBA) (Kozlowski & Downar, 2003).

Here, the deterministic lattice physics sequence SCALE/TRITON is employed to model the entire UOX fuel assembly. The TRITON control module uses BONAMI/CENTRM/PMC (DeHart & Bowman, 2011) for resonance self-shielding calculations to obtain problem dependent fine group cross section libraries and the 2D multi-group discrete ordinates transport solver NEWT, which uses an Extended Step Characteristic (ESC) approach to treat the integral form of the neutron transport equation (DeHart & Bowman, 2011). The continuous energy and 238-group cross section libraries based on the ENDF/B-VII.0 evaluation distributed with SCALE are taken. Cross section tables in four energy groups are prepared for DYNSUB.

A comparison of the UOX assembly eigenvalue as predicted by SCALE/TRITON and DYNSUB is listed in Table 12. Without IDF or SPH and one set of cross sections per pin type (3M), DYNSUB strongly underestimates the multiplication in the fuel assembly. Including the spectral effects introduced by the neighbors of each fuel pin by employing a cross section library per unique fuel pin position (37M), errors in the eigenvalue reduce by more than two orders of magnitude for the diffusion solution. It has to be kept in mind that diffusion theory has a singularity in the vicinity of strongly absorbing materials. The accuracy of any solution in terms of physics for a fuel assembly containing IFBA rods using neutron diffusion without corrections is questionable. Even with homogenization corrections a diffusion solution is not physically fully correct. However, because of the conservation assumptions the corrections are based on, they provide physically sound BC near a strongly absorbing material. The simplified transport solution clearly performs better for both the 3M and 37M option. Utilizing SPH factors or IDF (289M), DYNSUB fully reproduces the SCALE/TRITON solution within the numerical precision of the computational route.

The maximal pin power errors occurring between DYNSUB and SCALE/TRITON are given in Table 13. DYNSUB's diffusion solution leads to errors as large as 13 %. Employing cross section sets per unique pin positions significantly improves the reaction rate predictions.

Utilizing SPH factors or IDF, the SCALE/TRITON reference solution is recovered. Thus, it may be concluded that the SCALE/TRITON-DYNSUB code sequence with its intermediate processor createXSlib has been setup correctly.

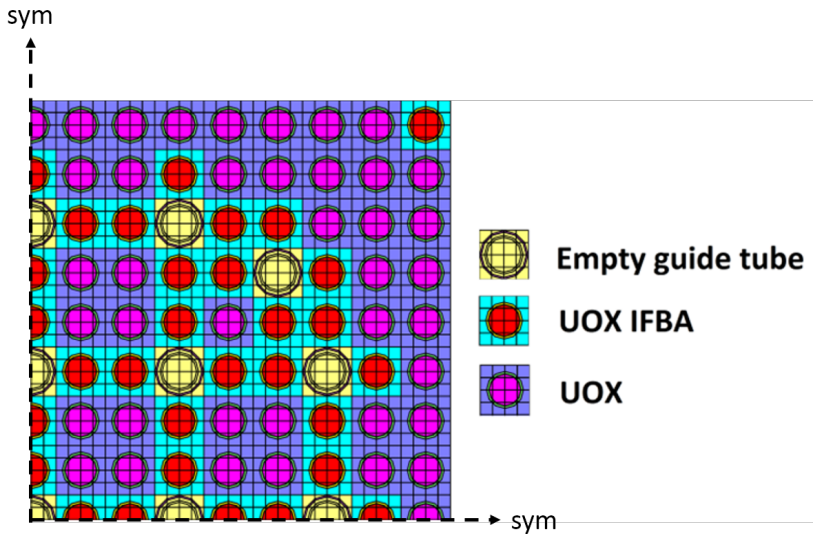

Figure 28: Composition of a quarter of a 17x17-25 UOX fuel assembly and visualization of NEWT ESC transport mesh for the HZP problem formulated by (Kozlowski & Downar, 2003)

Table 12: Comparison of eigenvalues obtained with DYNSUB using different transport approximations and cross section sets with a SCALE reference solution for the UOX fuel assembly of the HZP problem formulated by (Kozlowski & Downar, 2003) and shown in Figure 28

Code	Infinite multiplication factor k_∞[ ]	Relative difference [pcm]
SCALE/TRITON 238g	1.1231457	ref
DYNSUB 4g diff (3M)	1.070184	-5296.17
DYNSUB 4g sp3 (3M)	1.123559	41.33
DYNSUB 4g diff (37M)	1.123647	50.13
DYNSUB 4g sp3 (37M)	1.123479	33.33
DYNSUB 4g (289M) SPH	1.123142	0.37
DYNSUB 4g (289M) GET IDF	1.123144	0.17
DYNSUB 4g (289M) BBH IDF	1.123144	0.17

Table 13: UOX fuel assembly maximum relative pin power errors obtained with DYNSUB using different transport approximations and cross section sets for the HZP problem formulated by (Kozlowski & Downar, 2003) and depicted in Figure 28

Code	Maximum relative pin power error [%]
DYNSUB 4g diff (3M)	12.72
DYNSUB 4g sp3 (3M)	2.16
DYNSUB 4g diff (37M)	0.74
DYNSUB 4g sp3 (37M)	0.54
DYNSUB 4g (289M) SPH	0.01
DYNSUB 4g (289M) GET IDF	0.005
DYNSUB 4g (289M) BBH IDF	0.005

4.5.6 Verification of Serpent 2-DYNSUB code sequence

Here only selected cases of the verification matrix of the Serpent 2-DYNSUB code sequence are described. The first verification case aims attention at a 2D model of MOX fuel assembly under HZP conditions. This case is used to assess three of the pin-by-pin cross section generation methodologies discussed in section 4.1. Thanks to the possibility of obtaining HFP reference solutions using Serpent 2/SUBCHANFLOW, the second verification case is designed to assess a complete multi-dimensional cross section table containing SPH factors created for DYNSUB.

In the first verification case, a fresh 16x16-25 MOX fuel assembly is analyzed under HZP power conditions (see Figure 29 and Table 14). Both types of MOX fuel pins contain 1.45 wt% enriched uranium oxide. The MOX pins in the periphery of the fuel assembly include 1.7 wt% plutonium, the central cones 2.0 wt%. The geometrical configuration corresponds to AREVA designs. The coolant carries 1000 ppm soluble boron. The boundary conditions are chosen to be reflective.

Cross sections in 4-group structure as well as IDF and SPH factors have been determined using results obtained with Serpent 2. Point-wise cross sections based on ENDF/B VII.0 evaluated nuclear data files are employed by the Monte Carlo code. To ensure a sufficiently low statistical uncertainty of the results, $4 \cdot 10^9$ neutron histories are simulated. Unless stated otherwise, all statistical uncertainties hereafter refer to one standard deviation.

Table 14: Geometric properties of 16x16-25 MOX fuel assembly shown in Figure 29

Property	Value / Unit
Assembly pitch	23 cm
Assembly length	4.827 m
Number of fuel pins	231
Number of guide tubes	25
Pin pitch	1.27 cm
Pin outer diameter	1.075 cm
Guide tube outer diameter	1.232 cm

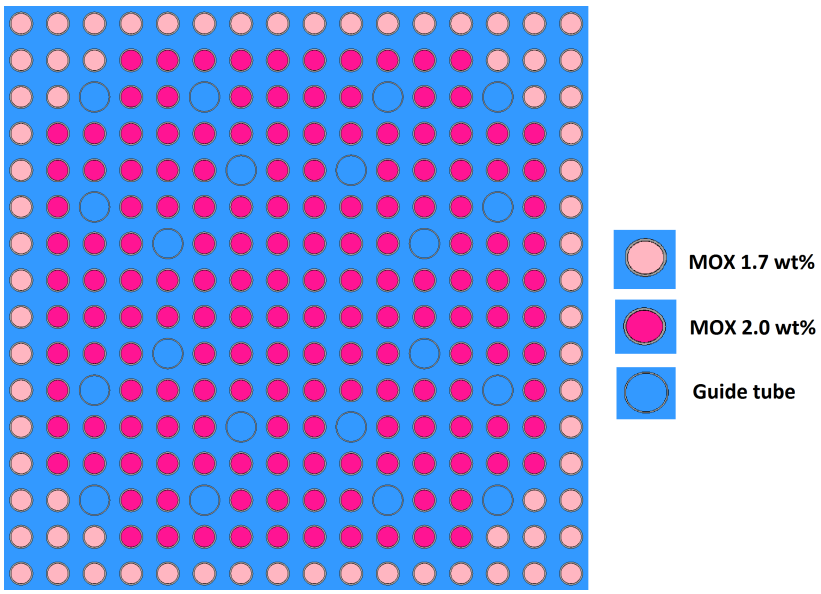

Figure 29: Composition of a 16x16-25 MOX fuel assembly employed to verify the Serpent 2-DYNSUB code sequence

In Table 15, the infinite multiplication factors of the fuel assembly computed by Serpent 2 and DYNSUB for the selected pin level cross section methodologies are listed. DYNSUB's simplified transport solution clearly outperforms the diffusion solution. Furthermore, moving from one cross section set per pin type (3M) to cross section sets per unique pin position (32M) does not significantly improve the eigenvalue prediction. This is due to a high level of error cancellation in the 3M solution. Even though the local reaction rate distributions are significantly worse than for the 32M one (see Table 16), an analysis of the global net neutron balance for the assembly reveals that the negative effects of the worse local neutron flux distribution almost vanish. In the previously studied UOX assembly case (see subsection 4.5.5), the same type of error cancellation is observed for the 3M and 37M simplified transport solutions.

Due to the fact that SPH factors and IDF are mathematically derived to enforce a conservation of both eigenvalue and reaction rates between the heterogeneous Serpent 2 solution and DYNSUB, DYNSUB calculations employing homogenization corrections (256M) reproduce the reference solution exactly.

Table 15: Comparison of computed MOX fuel assembly eigenvalues obtained with DYNSUB using different transport approximations and cross section sets for the problem depicted in Figure 29

Code	Infinite multiplication factor [ ]	Relative difference [pcm]
SSS2 CE	1.08496(0.00003)	ref
DYNSUB 4g diff (3M)	1.087627	266.7
DYNSUB 4g sp3 (3M)	1.086733	177.3
DYNSUB 4g diff (32M)	1.087578	261.8
DYNSUB 4g sp3 (32M)	1.086685	172.5
DYNSUB 4g (256M) SPH	1.084951	0.9
DYNSUB 4g (256M) GET IDF	1.084950	1.0
DYNSUB 4g (256M) BBH IDF	1.084950	1.0

The statistical uncertainty of all pin powers computed with SSS2 is below 0.04 %. The maximum relative errors in percent between the Serpent 2 reference solution and DYNSUB are tabulated in Table 16. If DYNSUB employs homogenization corrections, it recovers the SSS2 pin power results within the statistical uncertainty of the Monte Carlo result. Moving from the 3M to the 32M option does not improve the DYNSUB solution in terms of eigenvalue significantly; but with respect to the pin power the maximum relative error is more than halved.

Since the DYNSUB simulation conserves eigenvalues and reaction rates using either IDF or SPH factors, the Serpent 2-DYNSUB code sequence can be considered physically consistent.

Table 16: MOX fuel assembly maximum relative pin power errors obtained with DYNSUB using different transport approximations and cross section sets for the problem depicted in Figure 29

Code	Maximum relative pin power error [%]
DYNSUB 4g diff (3M)	1.22
DYNSUB 4g sp3 (3M)	1.50
DYNSUB 4g diff (32M)	0.49
DYNSUB 4g sp3 (32M)	0.28
DYNSUB 4g (256M) SPH	0.01
DYNSUB 4g (256M) GET IDF	0.05
DYNSUB 4g (256M) BBH IDF	0.05

In the second verification case, an infinite lattice of 3.65 m high UOX fuel assemblies at HFP conditions is studied. The UOX assembly introduced in subsection 4.5.5 is reused. The thermal power produced by the assembly is set to 18.47 MW and 82.12 kg/s of coolant flow. The pressure at the outlet of the infinite lattice is 15.5 MPa.

One set of cross sections per unique fuel pin position including SPH factors has been prepared based on two-dimensional infinite lattice calculations conducted with Serpent 2. The broad group energy structure of eight groups from the OECD/NEA and U.S. NRC PWR MOX/UO_2 Core Transient Benchmark is applied (Kozlowski & Downar, 2003). In order to model the HFP state of the UOX assembly, 15 branches are considered. Five equidistantly spaced effective Doppler temperature base points between 560 K and 1320 K are used. Moreover, moderator densities of 611.14 kg/m^3, 711.18 kg/m^3 and 752.26 kg/m^3 are taken into account. By not including moderator temperatures in the branch structure, constant pressure conditions are assumed. Since the pressure drop over the entire UOX fuel assembly amounts to 1.25 bar, this is a reasonable simplification. The soluble boron concentration is set to 1000 ppm.

Both the Serpent 2 model to generate few-group cross sections for DYNSUB and the SSS2/SCF model of the infinite lattice of finite height UOX assemblies employ ENDF/B VII.0 CE cross sections. The Serpent 2/SUBCHANFLOW model uses subchannels consisting of 20 axial layers each. The coupled MC/TH code simulates $6 \cdot 10^5$ neutrons per cycle. 200 inactive cycles are followed by 600 active ones. The convergence criterion for the effective multiplication factor is set to 5 pcm. The criteria for both Doppler temperature and moderator density are 0.5 %. The SSS2/SCF calculation converged after seven coupled iterations.

In this test case, DYNSUB solves the simplified transport equation on pin level. The resolution of the DYNSUB calculation mesh is radially identical to that of the feedback mesh of

SSS2/SCF. Mesh sensitivity studies show that DYNSUB requires at least 68 axial layers in the neutronics mesh to provide a mesh independent solution of the neutron flux for the given problem. In this study, DYNSUB and SSS2/SCF share one thermal-hydraulic model with an axial meshing of 20 layers. A neutron calculation mesh with 80 axial layers is used to ensure a properly converged solution.

In a first step, DYNSUB with fixed HZP thermal-hydraulic conditions has been compared to the corresponding SSS2/SCF run. DYNSUB overestimates the multiplication of the infinite lattice of finite height fuel assemblies by 147 pcm, as shown in Table 17. The largest differences in neutron flux levels have been found near the vacuum boundaries, supporting the assumption that DYNSUB misjudges the neutron leakages out of the system. While the employed SPH factors enforces the conservation of reaction rates and eigenvalues for the 2D spectral geometry they were created from, they are not capable to correct for axial leakage effects. Axial discontinuity factors are not considered in this case, since DYNSUB does not support them. Furthermore, they require 3D spectral geometries and new methodologies to be developed to handle the correlations between the cross section data sets for different axial elevations.

Comparing the HFP results for the effective multiplication factor, one finds that DYNSUB predicts a value, which is 34 pcm lower than that of Serpent 2/SUBCHANFLOW. Thus, the power defect reactivity evaluated with the Monte Carlo tool is significantly lower than that of DYNSUB.

Table 17: Comparison of effective multiplication factor of the 3D UOX assembly model for HZP and HFP conditions as well as power defect reactivity as predicted by DYNSUB and SSS2/SCF

Code	HZP k_{eff}	HFP k_{eff}	Power defect in reactivity [pcm]
SSS2/SCF	1.12042(0.00003)	1.11264(0.00003)	624.1(0.043)
DYNSUB	1.12189	1.11230	862.4

In a next step, the axial power profile determined with both tools is compared in Figure 30. The differences in the axial power are below 1.3 % everywhere. However, the power evaluated with

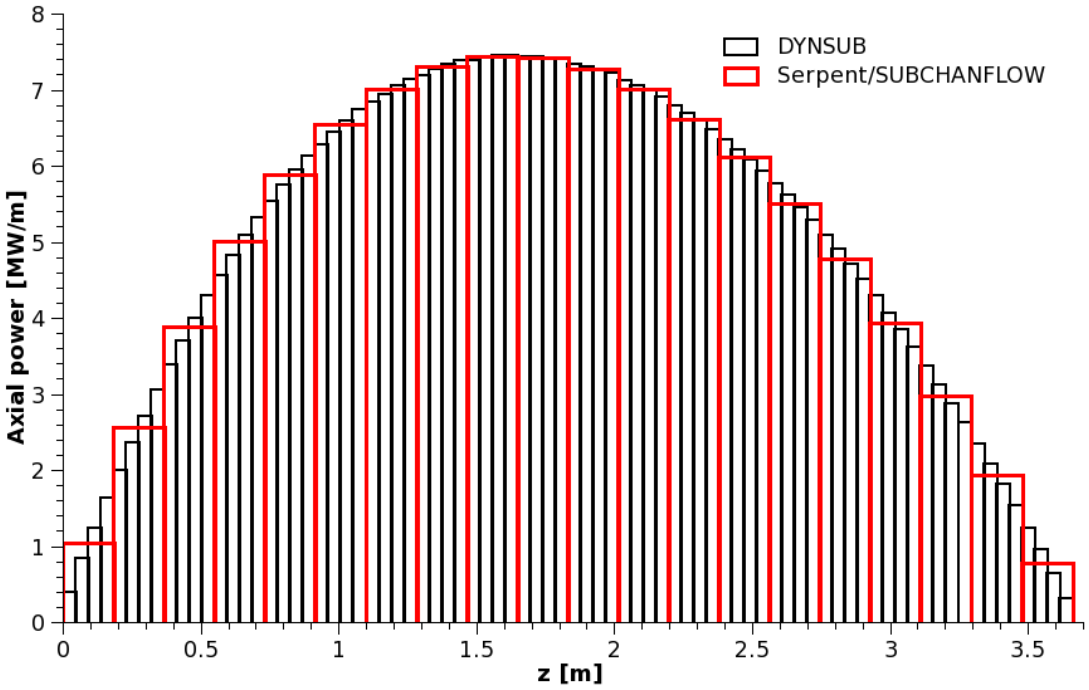

Figure 30: Comparison of UOX assembly axial power as computed with SSS2/SCF and DYNSUB for the 3D HFP UOX assembly problem

SSS2/SCF is higher than DYNSUB's in the lower half of the assemblies and vice versa in the upper half. Extending the scope of the comparison to pin powers, one finds that all local relative pin power differences are less than 3 %. In terms of global thermal-hydraulic properties like the average coolant heat up or the axial coolant profile, results obtained with both tools match very well considering the differences in the power profiles. As an example, the axial dependence of the radially averaged coolant temperature is plotted in Figure 31. Concerning local thermal-hydraulic quantities variations corresponding to the local differences in pin power are observed.

Discrepancies between DYNSUB and the SSS2/SCF reference solution are observed, which can be attributed to comparing a MC with a low order simplified transport solution in case of the neutron transport problem. As a result, Serpent 2-DYNSUB tool chain is deemed to work fine for producing fully branched cross section tables for the pin-homogenized reactor simulator.

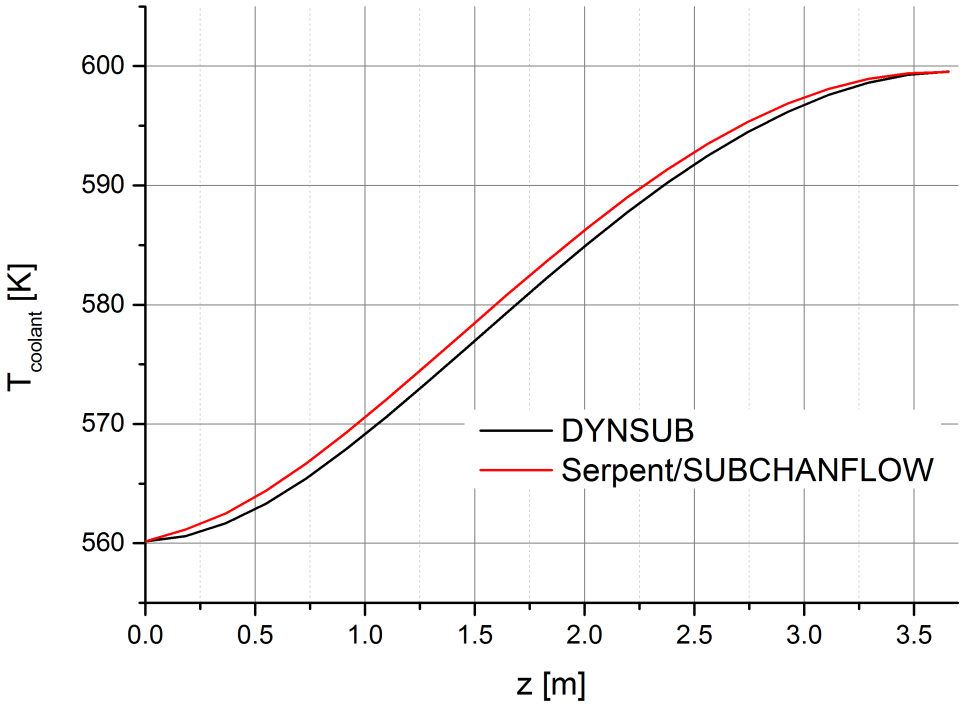

Figure 31: Comparison of radially averaged coolant temperatures evaluated with DYNSUB and SSS2/SCF for the 3D HFP UOX assembly problem

4.5.7 Summary of cross section generation efforts and outlook

A calculation route to determine multi-dimensional cross section tables for DYNSUB with or without homogenization corrections has been developed. This route utilizes either SCALE/TRITON or Serpent 2 as a lattice code. Selected verification cases for both the SCALE/TRITON-DYNSUB and Serpent 2-DYNSUB tool chains have been presented. First efforts to validate the latter sequence are discussed in chapter 6.

Moreover, different homogenization methodologies for evaluating pin level cross section sets for homogeneous pin-by-pin neutron transport calculations using the reactor simulator DYNSUB have been assessed. As expected due to the assumptions of diffusion theory, the pin level diffusion solver struggles in handling fuel assemblies with poisoned fuel pins. Hence, it necessitates homogenization corrections in any realistic case. In all test cases analyzed, DYNSUB's simplified transport solution does relatively well even though no specific homogenization corrections are yet available. In addition, it is observed that one should always apply one cross section set per unique pin position instead of per fuel pin type in a super-cell because of the considerably improved reaction rate prediction.

In the future, more work needs to be done on how to best choose super-cells for pin level cross section generation for engineering-sized application cases. Preliminary investigations done

indicate that such super-cells need to include the surroundings of fuel assemblies of interest to obtain higher fidelity pin-by-pin neutron transport solutions with DYNSUB. The studies can be summarized as follows:

- The reflective boundary conditions applied to the outer boundary of a single fuel assembly super-cell for the generation of pin-level cross sections from an infinite lattice limit the achievable accuracy of the homogeneous pin level solution.
- Efforts to approximately determine SPH factors and IDF for pin-by-pin simplified transport simulations done with DYNSUB should be undertaken.
- The homogenization corrections and the cross section calculation routes developed for DYNSUB as a whole employ only two-dimensional spectral geometries. As a result, neither SPH factors nor IDF can correct DYNSUB's misevaluation of axial leakages. In order to treat this issue, one would have to move to 3D spectral geometries and 3D homogenization corrections that are an active topic of on-going research worldwide.

Especially treating the correlations between cross section sets, i.e. their neighborhood dependence, in the multi-dimensional cross section tables is a problem unsolved so far.

5 Verification and Validation of DYNSUB using international benchmarks

This chapter deals with solution verification and validation of the pin-homogenized reactor simulator. The multilevel validation methodology utilized for SSS2/SCF is also applied to DYNSUB (Ivanov, et al., 2007a). Like most BE codes, the pin-homogenized reactor simulator DYNSUB was created by coupling two existing stand-alone simulation tools. Both, the proper validation of the constituent stand-alone codes and the coupled code system need to be confirmed as part of the validation methodology.

As mentioned in chapter 3, SUBCHANFLOW was validated for PWRs. Also, DYN3D has a broad experimental V&V base, for examples refer to (Mittag, et al., 2005; Rohde, et al., 2009; Hadek & Mittag, 2009). Since both constituent codes can be considered to be sufficiently verified and validated, this chapter looks at verifying and validating coupled neutronics and thermal-hydraulics solutions produced by DYNSUB.

In a first V&V step, DYNSUB is to be assessed with given effective nuclear data, i.e. few-group cross section tables. As discussed in section 4.3, the lack of international benchmarks for pin-homogenized reactor simulators forces the utilization of existing PWR benchmarks for assembly-homogenized solutions. A total of four of these benchmarks have been selected in this verification and validation process in order to cover DYNSUB's overall capabilities. For each benchmark the functionalities of the pin-homogenized reactor simulator to be verified and validated are summarized first. They are followed by a description of the benchmark scenarios and DYNSUB models. Finally, solutions provided by DYNSUB are compared to predictions of other reactor simulators (code-to-code benchmark) or measured plant data (code-to-data benchmark).

5.1 OECD/NEA Kalinin-3 coolant transient benchmark

The OECD/NEA Kalinin-3 coolant transient benchmark is one of the few international benchmarks including measured plant data from Unit 3 of Kalinin NPP. It offers the chance to validate DYNSUB's transient solution for time dependent thermal-hydraulic boundary conditions. The reactor considered is a VVER-1000. Thus, the coupling routines for hexagonal fuel lattices in DYNSUB can be assessed. Since the detailed available measurements are limited to the coolant transient, a code-to-code benchmark is conducted with COBAYA3/SUBCHANFLOW (Calleja, et al., 2014b).

5.1.1 Definition of scenarios and models

The exercise 3a and 3b of this benchmark are considered (Tereshonok, et al., 2008) in which the reactor core is at HZP conditions, the corresponding operating conditions are listed in Table 18. A map of the control bank arrangement can be found in Figure 71 in Appendix F.

Table 18: Operating conditions at HZP of the OECD/NEA Kalinin-3 coolant transient benchmark (Tereshonok, et al., 2008)

Parameter	Value
Core power	2.962 MW
Coolant inlet temperature	552.15 K
Primary system pressure	15.52 MPa
Core mass flow rate	18766.46 kg/s
Boron concentration	660.0 ppm
CR banks #1-9	fully withdrawn
CR bank #10	82.95 % withdrawn

In the DYNSUB model used for all Kalinin-3 simulations, the VVER is modeled using 211 radial nodes corresponding to the fuel assemblies (163) and radial reflectors (48). Axially, 30 equidistant mesh layers are employed for the active core (3.55 m). Axial reflector cells are described by a thicker axial layer (23.6 cm). Radial and axial boundary conditions are zero flux. The two-group diffusion cross section library delivered with the benchmark specification is utilized. This library contains no homogenization corrections such as ADF.

The thermal-hydraulics model contains one laterally coupled channel per fuel assembly. In axial direction, each channel is divided in 30 axial nodes. The top reflector is heated using one of DYNSUB's prebuilt reflector treatment functions and, hence, is not included in the thermal-hydraulics model. The fuel rods of each fuel assembly are represented by an average fuel rod. The latter is radially discretized into 12 nodes to solve the heat conduction problem. 10 nodes describe the fuel pellet, one the gas gap and one the clad. The thermo-physical properties for fuel and clad as well as the gap heat transfer coefficient are taken from the VVER-1000 coolant transient benchmark specification (Ivanov, et al., 2002), because the Kalinin-3 one does not specify any of them.

The following steady-state coupled convergence criteria are used: $\varepsilon_{\text{keff}} < 10^{-5}$ for the eigenvalue, $\varepsilon_{\text{DT}} < 10^{-4}$ for local Doppler temperature and $\varepsilon_{\text{RM}} < 10^{-4}$ for the local moderator density.

Exercise 3b of the OECD/NEA Kalinin-3 coolant transient benchmark consists of two parts. Firstly, a steady-state simulation of the VVER core at hot full power conditions is done. The conditions used are tabulated in Table 19. Secondly, starting from a hot power steady-state, a transient simulation following the switching off one of the four main coolant pumps is to be performed.

Table 19: Operating conditions at HFP of the OECD/NEA Kalinin-3 coolant transient benchmark (Tereshonok, et al., 2008)

Parameter	Value
Core power	2962 MW
Coolant inlet temperature	560.0 K
Primary system pressure	15.52 MPa
Core mass flow rate	18766.46 kg/s
Boron concentration	660.0 ppm
CR banks #1-9	fully withdrawn
CR bank #10	82.95 % withdrawn

The sequence of events in the 300 s transient scenario of exercise 3b is as follows: At zero seconds one of four main cooling pumps is switched off manually. After 1.41 s the load-off and reactor power controller (LRPC) decides to reduce power because of the decreased core mass flow rate. As a result, the CR bank #10 is further inserted into the core starting at 2.7 s into the transient. Once bank #10 has reached 50 % insertion[1], the movement of CR bank #9 is initiated (at about 60.0 s). At 73.0 s, the power load-off threshold is reached and process is stopped by the LPRC. The control over the control and shutdown banks is returned from the LPRC to the control rod controller. The latter is set to keep the reactor power in the range of 66.2-67.3 % nominal. At 73 s, the CR bank #10 is still at 56.6 % insertion. It approximately stays at this position till the end of the transient. Bank #9 reaches a position of 6.9 % insertion at the end of the power reduction process. After 180 s, this bank is completely withdrawn by the control rod controller to maintain reactor power. For an overview of the CR bank movement please refer to Figure 72 in Appendix F.

[1] 0 % insertion for a CR bank corresponds to its tip being at 345.65 cm from the bottom or 9.34 cm below the top of the active core. At 100 % insertion, its tip is aligned with the bottom of the active core.

This transient scenario is based on an actual experiment performed at Kalinin-3. Extensive measured data from the reactor's instrumentation and control system (I&C) is included in the benchmark. However, as DYNSUB cannot evaluate the balance of plant and no coupling to a system code is available, the analysis of the transient scenario is restricted to using a priori determined thermal-hydraulic boundary conditions at core inlet and outlet. Such BC have been computed with the coupled code system ATHLET-BIPR-VVER and were given to benchmark participants. The sole purpose of the DYNSUB simulation is to show that the reactor simulator can reproduce the evolution of measured Kalinin-3 reactor power given time-dependent thermal-hydraulic BC and control rod bank positions. For the transient simulation, a time step of 10 ms is used since a sensitivity showed it to be the maximal time step allowed for achieving a converged solution at the given spatial resolution.

5.1.2 Results for HZP and HFP stationary cases

First, the performance of DYNSUB's implemented support for hexagonal geometries is to be verified using steady-state calculations. Since no detailed reference solutions are included in the Kalinin-3 benchmark documentation, DYNSUB is compared to results obtained with COBAYA3/SUBCHANFLOW (CBY/SCF) (Calleja, et al., 2014b).

An overview of the steady-state simulation results for HZP conditions is listed in Table 20. Both tools agree very well in terms of eigenvalues. A difference of less than 17 pcm is observed. Larger deviations are found for the assembly peaking F_{xy} and axial peaking F_z. Both can be explained by the different number of axial layers used by both coupled codes. DYNSUB employed 30 axial mesh layers in the active core, CBY/SCF only 10.

Table 20: Comparison of Kalinin-3 HZP eigenvalue, assembly and axial peaking factors, shutdown bank worth as well as worths of CR banks #9 and #10 as computed with CBY/SCF and DYNSUB (conditions listed in Table 18)

Quantity	CBY/SCF	DYNSUB
k_{eff} [ ]	1.01157	1.011406
F_{xy} [ ]	1.4373	1.4262
F_z [ ]	1.4612	1.4760
SRW [pcm]	10234.0	10311.0
CRW #9 [pcm]	967.6	968.4
CRW #10 [pcm]	866.7	869.7

The worth of the shutdown banks (SRW) predicted by DYNSUB is 77 pcm higher than that of COBAYA3/SUBCHANFLOW. Evaluations of the worths of the control rod banks #9 and #10 of both code systems, however, lie within a few pcm of each other.

Moving from integral to local parameters, the assembly power distributions computed with both tools have been compared. The relative differences between the CBY/SCF solution and DYNSUB reach up to 2.7 % (see Figure 73 in Appendix F). Additionally, these deviations exhibit a pronounced tilt from left to right. Five out of six symmetry sectors are described using the same cross section data. Only the 60° sector between fuel assembly rows 2-8 and columns 29-42 is modeled by a separate XS table set as it is specified in the benchmark documentation. This affects the power calculation in almost the entire right hand side of the core. A small part of this observation can be attributed to the different axial nodalization. The effect of the nodalization on the global axial power profile can be seen in Figure 74 in Appendix F. While the shapes match generally well, the largest differences in power occur near the reflectors and in the region of the peak in the top half of the active core. More important than the number of axial nodes to explain the observed differences in assembly powers are the numerical solution schemes employed by CBY/SCF and DYNSUB. The former coupled code utilizes triangular prismatic nodes to built hexagonal fuel assemblies, i.e. 6 nodes per fuel assembly (Lozano, et al., 2010). The latter, however, uses special octahedra also called hexagonal prisms. Both types of mesh cells are known to behave significantly different as base of the numerically coarse meshes of assembly-homogenized reactor simulators. The effectively higher mesh resolution achieved in CBY/SCF with six triangular prisms per fuel assembly allows for better capturing neutron flux gradients in the reactor core. The triangular mesh capability recently introduced into DYN3D could not be considered for DYNSUB as it lacks support for the simulation of transients so far (Dürigen, 2013).

The HZP DYNSUB results presented here utilizes the coupled codes extended CR model that includes the capability to simulate grey tip CR and to decusp control assemblies well. To prove that the new CR model performs significantly better than its volume weighting based predecessor extensive verification studies have been carried out for both hexagonal and square fuel lattices.

If CR banks are moved during a transient, their differential worth defines, how the reactor neutron fluxes evolve with time. The differential worth of CR bank #10, which plays an important role in the transient, has been evaluated using three different methods. First a Kalinin-3 DYNSUB model has been constructed that comprises 240 axial layers. This model has been used to compute the reference differential worth of CR bank #10 by aligning the CR tip with mesh cell boundaries, thus, avoiding CR cusping caused by material mixing. The differential worth is computed as quotient of the change in reactor eigenvalue caused by the

withdrawal of the CR bank by one step (1.47917 cm) and the step size. Afterwards, the differential worth of the bank investigated has been once computed using the DYNSUB standard method, i.e. volume weighting, and once employing the new approximate flux weighting. The results of this test are visualized in Figure 32.

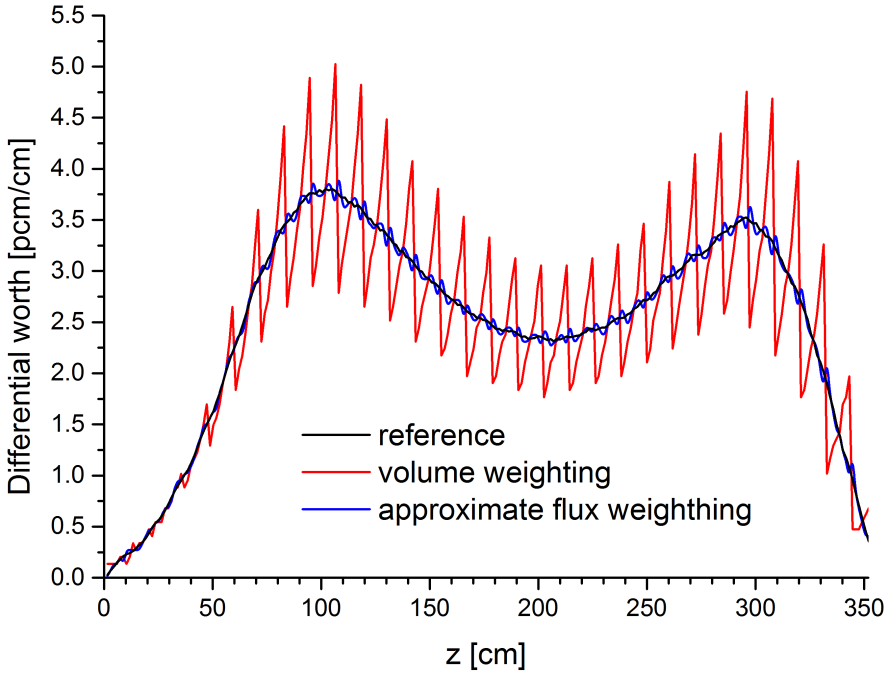

Figure 32: Differential rod worth of CR bank #10 computed by DYNSUB for a given position of the CR tip above the bottom of active core of the OECD/NEA Kalinin-3 coolant transient benchmark VVER under HZP conditions using different CR models.

The differential rod worth of the CR bank #10 exhibits a strong oscillatory behavior around the true values if volume weighting is applied to treat tips of CR lying inside a computational mesh cell. These oscillations distort physics since the evolution of the neutron flux is governed by both the total inserted reactivity and the reactivity insertion rate for any given CR bank position. Utilizing the new implemented approximate flux weighting method, the oscillations in the different worth of CR bank #10 can be substantially reduced leading to a better description of the VVER neutron physics. The remaining verification cases analyzed showed a comparable level of improvement, when using the approximate flux weighting instead of the standard volume weighting to treat CR cusping.

Table 21 summarizes the integral results of the HFP steady-state simulations with CBY/SCF and DYNSUB. Both tools are found to agree very well for both effective multiplication and peaking factors. The predictions of peaking factors match better than in the HZP case as the hot full power CBY/SCF model unlike its HZP counterpart utilized 26 axial mesh layers in the active core. Therefore, the axial power profiles computed by both tools behave almost identical (see Figure 75 in Appendix F). Despite the improved conforming of integral quantities and axial

power profiles, local differences in assembly powers still exhibit a maximum of 2.9 % (see Figure 76 in Appendix F). In contrast to the hot zero power conditions, there is no longer a visible left-right power tilt. Instead, DYNSUB predicts powers to be higher in the row of assemblies next to the radial reflectors and lower in most of the assemblies inside the active core. Like in the HZP case, the differences in assembly power between DYNSUB and CBY/SCF are found to be due to largely different numerical schemes in the neutronics. These schemes lead to significantly different flux gradients especially at the fuel reflector interface. The lack of homogenization corrections in the cross section library, again mostly the lack of reflector ADF, enhances this effect.

Table 21: Comparison of Kalinin-3 HFP eigenvalue, assembly and axial peaking factors as computed with CBY/SCF and DYNSUB (conditions listed in Table 19)

Quantity	CBY/SCF	DYNSUB
k_{eff} [ ]	0.996818	0.996844
F_{xy} [ ]	1.3289	1.3283
F_z [ ]	1.202	1.1920

5.1.3 Main coolant pump trip simulation

As part of the benchmark, data from the three redundant systems to measure reactor power at Unit 3 of NPP Kalinin is available. The systems and their measurement accuracy will be discussed briefly.

The core average power is computed based on thermal-hydraulic measurements such as coolant temperatures and mass flow rates taken in either the primary or secondary circuits. However, these computations cannot consider the signal delay caused by the coolant transport time. Hence, because of the steep power gradients up to the 150th second of the transient studied power values obtained in that way are considered to be unreliable.

Alternatively, the power of the Kalinin-3 core is recorded using self-powered neutron detectors (SPND) placed in the central guide tube of several fuel assemblies. The signals of these detectors are corrected for existing backgrounds. The SPNDs are part of the in-core monitoring system (ICMS) and the power value computed based on their signals is referred to in the benchmark as DCS power.

Finally, the Kalinin-3 reactor power is evaluated based on ex-core ionization chamber neutron flux measurements. The chambers evaluated for the benchmark are located in the area of the

lower part of the core. They are part of the neutron flux control (NFC) system. Consequently, the determined power values are referred to as NFC power.

Unlike core average powers evaluated based on thermal-hydraulic parameter measurements both DCS and NFC powers are accurate even in the presence of steep power gradients. Therefore, both are used as reference for the comparison with DYNSUB. For neither method to obtain Kalinin-3 power levels the benchmark specification quotes measurements uncertainties.

The evolution of reactor power predicted by DYNSUB based on thermal-hydraulic BC produced by ATHLET-BIPR-VVER is compared with the measured data in Figure 33. The DYNSUB power evolution captures the measured behavior satisfactorily.

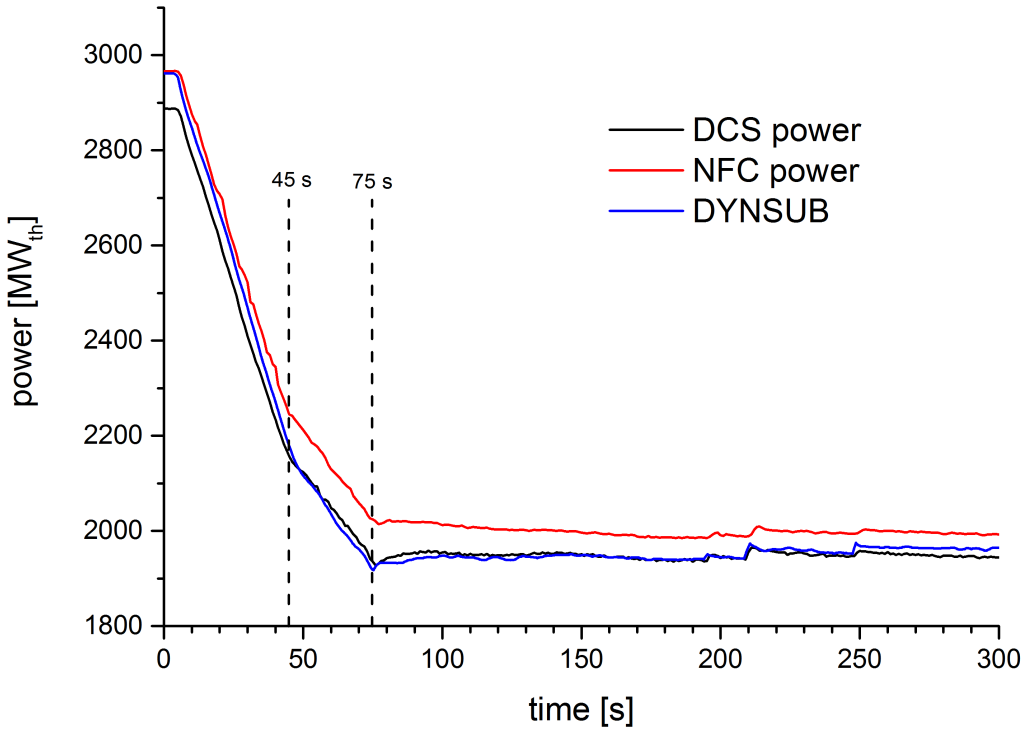

Figure 33: Comparison of the temporal evolution of thermal reactor power predicted by DYNSUB and measurements of the Kalinin-3 benchmark (Tereshonok, et al., 2008)

During the power load-off process two distinct time intervals with largely different power gradients are observed. In the second interval with the lower gradient (45-75 s into the transient), the rate of power decrease evaluated with DYNSUB matches the steepness of both DCS and NFC power curves well. In the first interval (up to 45 s), however, the Kalinin-3 reactor power as seen by DYNSUB is reduced faster than in reality. In the latter interval, reactor power decreases because the CR bank #10 is slowly inserted into the core. Also, the primary coolant heats up until about 44 s into the transient (see Figure 34) due to the reduction of the core mass flow rate. This introduces a negative moderator feedback effect.

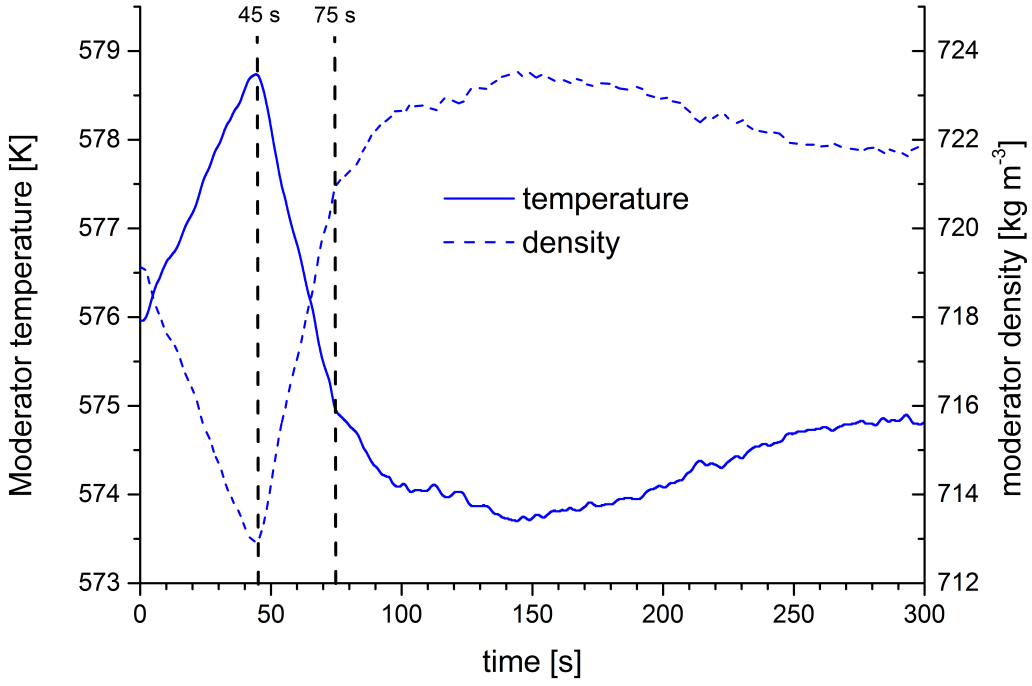

Figure 34: Temporal evolution of the core averaged moderator density and temperature of the Kalinin-3 transient benchmark as computed by DYNSUB.

Most likely, both the differential worth of the CR bank #10 and the moderator feedback are overestimated by DYNSUB. However, the larger part of the observed deviation can be attributed to the different bank worth. Beyond 45 s, the core average coolant temperatures decline now leading to a positive feedback and, thus, a lower power gradient. Oscillations in reactor power after 80 s of transient are mainly due to fluctuations of the core inlet coolant temperature and mass flow rates. Between 190 s and 200 s a slight power increase caused by the removal of CR bank #9 from the core is visible. Followed by two small power control movements of CR bank #10 around 210 s and 250 s. All of the CR bank shifts were initiated by the control rod controller to maintain reactor power.

5.1.4 Summary of Kalinin-3 benchmark

DYNSUB simulation results are found to depict not only qualitatively but also quantitatively the values obtained with COBAYA3/SUBCHANFLOW for steady-state scenarios. Consequently, DYNSUB's coupling routines for hexagonal fuel lattices and reflector models are considered to be verified. Moreover, the new CR decusping model performs significantly better than its predecessor. So, all future simulations rely on it.

DYNSUB is able to correctly represent the temporal evolution of the reactor power for the main pump trip scenario for pre-described thermal-hydraulic boundary conditions.

5.2 OECD/NEA and U.S. NRC PWR MOX/UO_2 core transient benchmark

Unlike the Kalinin-3 coolant transient benchmark, the OECD/NEA and U.S. NRC PWR MOX/UO_2 core transient benchmark does not contain any measured plant data. It is a pure code-to-code benchmark serving only solution verification purposes. The reactor studied in this benchmark is a Westinghouse four-loop PWR. Since this reactor type utilizes square lattice fuels, the coupling routines for square fuel lattices in DYNSUB are verified. As part of the steady-state scenarios critical boron concentrations need to be found allowing for assessing the performance of DYNSUB's newly developed critical boron search algorithm. The transient is a rod ejection accident (REA); a fast transient belonging to the class of reactivity-initiated accidents (RIA).

The OECD/NEA and U.S. NRC PWR MOX/UO_2 core transient benchmark offers cross section libraries with a two-, four- or eight-group energy structure. To ensure the correct implementation of DYNSUB for multi-group neutron transport, the 8G cross sections are used. Moreover, all steady-state and transient simulations are carried out employing both the nodal diffusion and simplified transport solver of DYNSUB in order to ensure that the coupling works satisfyingly for both.

5.2.1 Definition of scenarios and models

The first three parts of the OECD/NEA and U.S. NRC PWR MOX/UO_2 core transient benchmark (Kozlowski & Downar, 2003) contain static, preparatory cases. In the first exercise, 2D simulations with fixed thermal-hydraulic conditions are requested for an all rods out (ARO) as well as an all rods in (ARI) state of the core loading shown in Figure 10 in section 2.6. These fixed conditions are listed in Table 22. Assembly averaged powers, eigenvalues and rod worths are to be determined for these cases.

Table 22: Fixed thermal-hydraulic conditions for the 2D cases of the OECD/NEA and U.S. NRC PWR MOX/UO_2 core transient benchmark (Kozlowski & Downar, 2003)

Parameter	Value
Core power	1 W
Core temperature	560 K
Boron concentration	1000 ppm

In the DYNSUB model, the PWR has been radially discretized into 257 nodes corresponding to fuel assemblies and radial reflectors. One axial layer of a height of 10 cm is modeled. Radial

boundary conditions are zero flux and axial ones are reflection. The eight-group nodal cross section library delivered with the benchmark specification is employed, which includes ADF to reduce homogenization errors. All 2D simulations apply a steady-state convergence criterion of $\varepsilon_{\text{keff}} < 10^{-6}$ for the eigenvalue. DYNSUB simulations are done applying both the diffusion and simplified transport approximation. The diffusion calculations are performed since all other nodal benchmark solutions utilized the diffusion approximation. To verify the DYNSUB implementation for simplified transport, a nodal simplified transport solution is also produced.

In the second exercise of the OECD/NEA and U.S. NRC PWR MOX/UO_2 core transient benchmark, a 3D hot full power scenario is simulated. The conditions are summarized in Table 23. The critical boron concentration is to be determined.

Table 23: Operating conditions at HFP of the OECD/NEA and U.S. NRC PWR MOX/UO_2 core transient benchmark (Kozlowski & Downar, 2003)

Parameter	Value
Core power	3565 MW
Coolant inlet temperature	560 K
Primary system pressure	15.5 MPa
Active core mass flow rate	15849.4 kg/s
Control rod position	ARO

The active core is represented by 22 equidistant axial mesh layers in the neutronics mesh. The thermal-hydraulics model contains one channel per fuel assembly, 193 parallel laterally coupled channels in total. In axial direction, each channel is subdivided in as many nodes as there are neutronic mesh nodes in the active core region. As specified by the benchmark the reflector is kept at core inlet conditions and, hence, is not included in the thermal-hydraulic model. The fuel rods of each fuel assembly are represented by an average fuel rod. This rod is radially divided into 12 nodes to solve the heat conduction problem. 10 nodes describe the fuel pellet, one the gas gap and one the clad. The thermo-physical properties for fuel and clad as well as the gap heat transfer coefficient are taken from the benchmark specification (Kozlowski & Downar, 2003). The same BC and coupled convergence criteria as for the Kalinin-3 models are employed.

In the third exercise of the core transient benchmark, the full 3D core is studied at HZP. The corresponding conditions are listed in Table 24. Like in the HFP case, a critical boron search is conducted. The 3D nodal model is taken from the previous exercise and adapted to capture the change in operating conditions.

Table 24: Operating conditions at HZP of the OECD/NEA and U.S. NRC PWR MOX/UO_2 core transient benchmark (Kozlowski & Downar, 2003)

Parameter	Value
Core power	3.565 kW
Coolant inlet temperature	560 K
Primary system pressure	15.5 MPa
Active core mass flow rate	15849.4 kg/s
Control rod position	All shutdown banks out

The fourth part of the OECD/NEA and U.S. NRC PWR MOX/UO_2 core transient benchmark contains a rod ejection scenario. The control rod bank D of the modeled PWR consists of five control assemblies (see Figure 10). One is situated in the central assembly of the core. The remaining four control assemblies are distributed over the four quadrants. One of the latter D-bank control assemblies is ejected in 0.1 s from the HZP conditions. This fast reactivity insertion will lead to a super prompt-critical power excursion. No reactor trip is considered. The boron concentration as well as the position of all other control and shutdown rod banks remains unchanged during the transient. Participants are asked to study the evolution of the state of the reactor core for 1.0 s in total. DYNSUB employs a fixed time step of 1.0 ms as this leads to a converged solution at the given spatial resolution.

5.2.2 Results for HZP and HFP stationary cases

In order to describe the error distribution relative to reference solutions, the two metrics introduced in the final OECD/NEA and U.S. NRC PWR MOX/UO_2 core transient benchmark report (Kozlowski & Downar, 2007), the power-weighted error (PWE) and the error-weighted error (EWE), are also utilized here. Unless stated otherwise, all original benchmark results presented in the following were taken from the final benchmark report (Kozlowski & Downar, 2007).

Eigenvalues and total rod worths for the 2D cases of the benchmark are compared in Table 25. In terms of eigenvalue prediction for the 2D ARI and ARO case, DYNSUB's solutions coincide with the other nodal benchmark results. Analyzing the reported total rod worths, one observes that DYNSUB's diffusion solution like all other nodal benchmark participants overestimates the total rod worth relative to the DeCART reference value. The simplified transport solution, however, slightly underestimates the total rod worth. The overestimation of the total rod worth in diffusion theory is mainly due to its singularity in the vicinity of strongly absorbing materials. Even the used ADF approach in this benchmark's cross section library is not capable of

changing a diffusion solution to a physically correct solution in the vicinity of the inserted control assemblies in the ARI case. The simplified transport solution has no such singularity and, hence, handles strong flux gradients close to the absorbers more realistically.

Table 25: Comparison of eigenvalues and total rod worths for the 2D cases of the OECD/NEA and U.S. NRC PWR MOX/UO_2 core transient benchmark (Kozlowski & Downar, 2007)

Code	ARO k_{eff}	ARI k_{eff}	Total rod worth [dk/k]
DeCART	1.05852	0.98743	6801
CORETRAN 1/FA	1.06387	0.99202	6808
NUREC	1.06378	0.99153	6850
PARCS 2G	1.06379	0.99154	6850
PARCS 8G	1.06354	0.99114	6868
SKETCH-INS	1.06379	0.99153	6850
DYNSUB 8G	1.06365	0.99106	6886
DYNSUB 8G SP3	1.06389	0.99225	6787

DYNSUB's capability to evaluate the assembly power distribution with a nodal simulation is compared with other nodal benchmark solutions (see Table 47 in Appendix G). Even though DYNSUB's eight-group solution should have a lower energy discretization error than the two-group simulations, the error metrics for the assembly power distribution do not reflect it. This is probably due to the fact that eight-group solution also has a larger, competing spatial discretization error because of the more complicated spatial shape of the neutron flux. The resolution of one node per fuel assembly may not be sufficient to capture the group-to-group interactions in the low energy groups correctly. Moreover, the nodal simplified transport does not prove to be more accurate than the diffusion ones for the given radial mesh resolution of one node per assembly despite using assembly discontinuity factors for the zeroth harmonic flux moment and assuming the continuity of the second harmonic moment.

The 3D HFP simulation has been performed with DYNSUB to ensure that thermal-hydraulic feedback for square fuel lattices and the critical boron search model are implemented correctly. A comparison of the critical boron concentration and core averaged thermal-hydraulic properties as predicted with DYNSUB and by the benchmark participants is given in Table 26. The DYNSUB solutions are in line with the results of the original benchmark participants. Moreover, the power field evaluated with DYNSUB diffusion and simplified transport has been compared to the PARCS 2G solution, since PARCS is the qualified reactor simulator of the U.S. NRC. The assembly powers of both DYNSUB simulations are within one percent of the

PARCS reference. Maximal difference in axial power profiles are less than 2 % if one does not count the cells close to top and bottom reflectors. Here, the deviations amount to more than 4 %.

Table 26: Comparison of critical boron concentration and core averaged thermal-hydraulic properties for the 3D HFP case of the OECD/NEA and U.S. NRC PWR MOX/UO_2 core transient benchmark (Kozlowski & Downar, 2007).

Code	CBC [ppm]	Average $T_{Doppler}$ [K]	Average T_{mod} [K]	Average ρ_{mod} [kg/m^3]
CORETRAN 1/FA	1647	908.4	581.0	706.1
NUREC	1683	827.8	581.1	706.1
PARCS 2G	1679	836.0	581.3	706.1
PARCS 8G	1672	836.2	581.3	706.1
SKETCH-INS	1675	836.6	580.9	705.5
DYNSUB 8G	1682	823.9	580.4	705.7
DYNSUB 8G SP3	1688	823.9	580.4	705.7

The 3D hot zero power state is simulated as preparation for the rod ejection scenario. The critical boron concentration, effective delayed neutron fraction and relative assembly power errors as determined by the different reactor simulators have been compiled in Table 27. An effective delayed neutron fraction has not been evaluated for DYNSUB's simplified transport solution as the simplified transport solver lacks support for computing an adjoint-weighted core average value for the delayed neutron fraction.

The axial power profiles of both DYNSUB solutions match within 1 % the DeCART reference solution in the core center and increase to a maximum of 8.5 % near the reflector interfaces.

In order to interpret the results of the HZP REA later on, the 3D rod worth of the control assembly in E5 has been determined. This assembly is the one being ejected in the transient. The DYNSUB nodal diffusion predicts a rod worth of 681 pcm. The simplified transport yields a control assembly at a worth of 670 pcm. Unfortunately, no DeCART reference solution for this rod worth exists. According to the CR worths, of the two DYNSUB simulations the super-prompt critical power peak of the one using simplified transport should appear later in time and lower in magnitude.

Table 27: Comparison of critical boron concentration, effective delayed neutron fraction and relative assembly power errors for the 3D HZP case of the OECD/NEA and U.S. NRC PWR MOX/UO_2 core transient benchmark (Kozlowski & Downar, 2007).

Code	CBC [ppm]	β_{eff} [pcm]	Assembly power PWE	Assembly power EWE
DeCART	1265	--	ref	ref
CORETRAN 1/FA	1351	568	1.26	4.10
NUREC	1343	576	1.05	3.43
PARCS 2G	1341	579	1.05	3.49
PARCS 8G	1334	580	1.20	2.85
SKETCH-INS	1341	579	1.06	3.77
DYNSUB 8G	1336	578	1.23	3.25
DYNSUB 8G SP3	1349	--	1.28	3.91

5.2.3 HZP rod ejection scenario

The evolution of the core power during the 1.0 s transient is shown in Figure 35. DYNSUB's nodal diffusion solution exhibits the earliest (0.307 s) and highest super-prompt critical power peak (196.7 % nominal power). Its simplified transport calculation has a peak timing of 0.33 s which is closer to the majority of the other solutions. So is its peak power of 158 % nominal. Looking at the PARCS 8G results one finds that its peak reactivity of 1.14 $ is lower than that of DYNSUB's diffusion based solution with 1.15 $ (see Figure 77 in Appendix G). Correspondingly, its power peak appears later and is lower but earlier and higher than DYNSUB using simplified transport. The energy released of DYNSUB diffusion is only 1.7 % higher than that of PARCS 8G even though peak powers are 24.7 % apart. Generally, the differences in power peak timing and height can be attributed to the different worth of the ejected rod in each benchmark contribution. Though the worth of the rod was not part of the benchmark itself, the total rod worth was (see Table 25). It can serve as an indicator how the models differ.

As was mentioned earlier, DYNSUB's simplified transport solver cannot yet compute reactivities on-the-fly because of its missing adjoint neutron flux capabilities. Hence, reactivities are only evaluated for the diffusion solution and compared to benchmark results in Figure 77 in Appendix G. All results obtained are in good agreement.

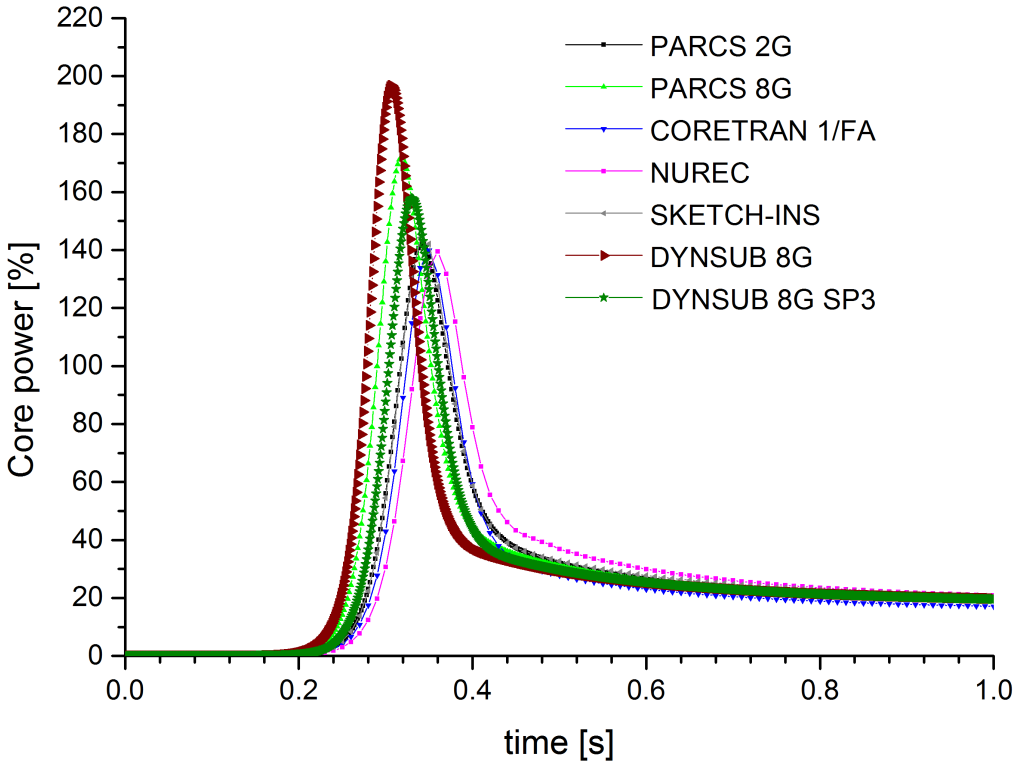

Figure 35: Comparison of transient core power predicted by DYNSUB and benchmark participants for the 3D HZP rod ejection scenario of the OECD/NEA and U.S. NRC PWR MOX/UO_2 core transient benchmark (Kozlowski & Downar, 2007)

To elucidate the consistency of the evolution of the transient power shapes predicted by DYNSUB with those of the benchmark participants, the assembly peaking factor F_{xy} has been determined. The peaking factors for the different transient solutions are compiled in Figure 36. A very good agreement both in temporal behavior and magnitude can be seen. Interestingly, the assembly peaking of DYNSUB's simplified transport solution is slightly higher than that of the diffusion theory based one. An analysis of the assembly power reveals that this higher peaking factor is linked to an increased power peaking in the fresh fuel assemblies in the vicinity of the ejected D-bank control assembly located in E5. In the 2D static calculations, the simplified transport solution is better than the diffusion one in evaluating the total rod worth but not the core power distribution as a whole. Hence, without a transient reference solution it cannot be stated that the simplified transport solution for the shape of the super-prompt critical power peak is more accurate than the benchmark contributions based on diffusion theory.

As a final step in the general consistency assessment of the DYNSUB calculations, the core average Doppler temperature and the moderator density are analyzed and presented in Figure 79 and Figure 78 in Appendix G. Doppler temperature and moderator density are chosen because both serve as the primary and secondary feedback mechanism terminating a super-prompt critical power excursion. Assessing the rise in core averaged Doppler temperatures due to the

power excursion small time delays between the different solutions are observed. These correspond to the different worths of the ejected control rod in the simulations and, consequently, different power peak height and timing (cp. Figure 35). Concerning the core averaged moderator density evolution, a small discrepancy between DYNSUB and the majority of the benchmark participants is noted. This is likely attributed to marginally deviating water properties at given temperatures and pressures used in different TH solvers.

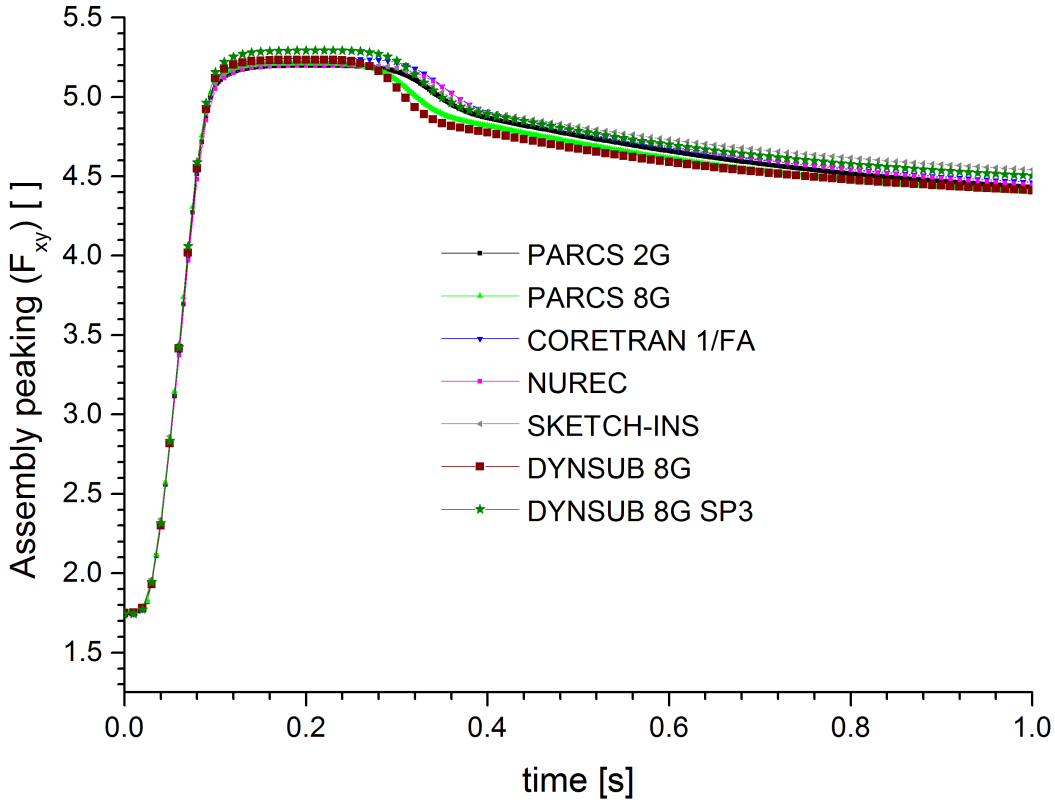

Figure 36: Comparison of assembly peaking evaluated by DYNSUB and benchmark participants for the 3D HZP rod ejection scenario of the OECD/NEA and U.S. NRC PWR MOX/UO_2 core transient benchmark (Kozlowski & Downar, 2007)

5.2.4 Summary of PWR MOX/UO_2 core transient benchmark

The preparatory steady-state multi-group simulations performed by DYNSUB for a Westinghouse PWR using both the diffusion and simplified transport approach are found to match results of other benchmark participants well. This gives confidence in the square fuel lattice coupling routines of DYNSUB. In addition, two of the steady-state cases have been used to verify DYNSUB's critical boron search algorithm.

While the thermal-hydraulically driven transient of the Kalinin-3 evolved slowly, the rod ejection accident studied in this section comprises a fast super-prompt critical power excursion.

DYNSUB is able to predict both timing and height of the observed power peak close to the 8G solution of PARCS, the qualified reactor simulator of the U.S. NRC. Differences between DYNSUB and 2G benchmark contributions are slightly larger, but generally a good agreement is found. Hence, DYNSUB can be considered suitable for modeling such reactivity-initiated accidents.

5.3 NURISP boron dilution benchmark

The NURISP boron dilution benchmark (Kliem, et al., 2011) is a computational benchmark like the OECD/NEA and U.S. NRC PWR MOX/UO_2 core transient benchmark. Here, a boron dilution event occurring during reactor startup is studied. This accident scenario allows for investigating the implementation of the boron transport model in DYNSUB. Additionally, the super-prompt critical power excursions caused by the dilution of the chemical shim are significantly faster and more severe than those of a REA. Hence, they are used to analyze the robustness of DYNSUB's transient algorithm.

5.3.1 Definition of scenarios and models

The first exercise at the level of a full PWR core is a steady-state simulation at HFP conditions to check the correct reading and processing of the 2G diffusion cross section tables provided by the benchmark. The operating conditions are listed in Table 28. The DYNSUB model introduced in subsection 5.2.1 is adapted to match these.

Table 28: Operating conditions at HFP of the NURISP boron dilution benchmark (Kliem, et al., 2011)

Parameter	Value
Core power	3565 MW
Coolant inlet temperature	560 K
Primary system pressure	15.4 MPa
Core mass flow rate	21105 kg/s
Control rod position	ARO
Boron concentration	1423 ppm

For the boron dilution scenarios, it is assumed that a slug of deborated water has accumulated in one of the four loops of the Westinghouse PWR primary system. This slug is not detected and normal start-up procedure is initiated. The main coolant pump in the affected loop is switched

on first. After 14 s, it has reached its maximum throughput transporting the slug of deborated water towards the active reactor core. In the downcomer and the lower plenum, the slug mixes with the water containing 2000 ppm boron. Thereby, a heterogeneous boron concentration distribution at the bottom of the active reactor core is obtained.

The benchmark provides time-dependent boundary conditions for each fuel assembly in three different scenarios. These BC have been evaluated using the CFD code ANSYS CFX. As described above, all of these scenarios depart from HZP start-up conditions. These are tabulated in Table 29. The three scenarios differ in terms of the size of the diluted boron slug. In scenario one, it occupies a volume of 18.0 m^3. The slug of the second scenario is slightly bigger, i.e. 20.0 m^3. Finally, 26.0 m^3 of deborated water enter the active core in the third case. A total of 10 s is to be simulated.

Table 29: Operating conditions at HZP of the NURISP boron dilution benchmark (Kliem, et al., 2011)

Parameter	Value
Core power	1 W
Coolant inlet temperature	473.15 K
Primary system pressure	3.0 MPa
Core mass flow rate	6106.32 kg/s
Control rod position	ARI
Initial boron concentration	2000 ppm

To assess the robustness of the DYNSUB transient algorithm, two simulations with different time step intervals are carried out. One calculation used a fixed time step of 1 ms and the other a time step size dynamically varied between 10 μs and 1 ms. The fixed time step of 1 ms was chosen based on analysis of reactor period of the PWR core. The reactor period is the time the reactor power needs to change by a factor of the Euler constant. For the three scenarios studied the reactor period is estimated based on the inhour equation of point kinetics, the core-wide steady-state effective delayed neutron fraction and decay constant estimated by DYNSUB and the known temporal behavior of the average boron concentration at the core inlet. The latter can be approximately translated into inserted reactivity and reactivity insertion rate using a factor of \$/ppm, which can be obtained from a number steady-state DYNSUB runs with varying concentrations of chemical shim. This analysis found a minimal reactor period of 10 ms for the first slug, 5.3 ms for the second slug and 4.5 ms for the third slug. Thus, a fixed time step of 1 ms is chosen being substantially smaller than the shortest period. This should be sufficient to capture the expected fast power increases during the transients correctly.

5.3.2 Results for HFP stationary case

The hot full power steady-state results are compared with results by COBAYA3/SUBCHANFLOW (Calleja, et al., 2014a) and DYN3D/SCF. DYN3D/SCF is a coupling of the 2G-version of DYN3D and SUBCHANFLOW inside the NURESIM platform (Chauliac, et al., 2011). The HFP steady-state calculation results are summarized in Table 30. All three coupled codes agree well in terms of reactor eigenvalue and power distribution peaking factors. Remaining differences are mostly due to numerical methods used in the nodal neutron diffusion solver, because all models used the same cross section tables and SUBCHANFLOW models. For all parameters the predictions of DYNSUB are in between those of DYN3D/SCF and CBY/SCF.

Table 30: Comparison of the characteristic reactor parameters of the HFP static case of the NURISP boron dilution benchmark evaluated by CBY/SCF, DYN3D/SCF and DYNSUB.

Parameter	CBY/SCF	DYN3D/SCF	DYNSUB
k_{eff} [ ]	1.008201	1.007799	1.007832
F_{xy} [ ]	1.4176	1.4210	1.4208
F_z [ ]	1.4310	1.4403	1.4360
F_q [ ]	2.0147	2.0336	2.0272
Core averaged $T_{Doppler}$ [K]	835.53	835.95	835.85
Core averaged ρ_{mod} [kg/m^3]	702.21	701.58	701.69

5.3.3 Boron dilution scenarios

The main results of the transient simulations of COBAYA3/SUBCHANFLOW, DYN3D/SCF and DYNSUB for scenario one are listed in Table 31. Both CBY/SCF and DYN3D/SCF utilized a 1 ms time step for all the calculations presented below unless stated otherwise. All tools use the same thermal-hydraulics model and produce the same minimal boron concentration. The time this minimum chemical shim concentration occurs differs significantly between CBY/SCF and the other simulations. This is reflected in the deviating peak times for the super-prompt critical power peak (cp. Figure 80 in Appendix H). The spread of maximal powers reached is as large as 1.5 GW even though the average peak height is only 8.07 GW. Comparing both DYNSUB simulations it becomes clear that a 1 ms time step is not sufficiently small to arrive at a space-time converged solution. The predicted peak power

Table 31: Summary of characteristic reactor data for scenario 1 of the NURISP boron dilution benchmark simulated by CBY/SCF, DYN3D/SCF and DYNSUB.

Parameter	CBY/SCF	DYN3D/SCF	DYNSUB	DYNSUB dynamic Δt
Power peak [MW]	8157.7	7235.5	8727.3	8153.4
Peak time [s]	5.593	5.753	5.722	5.720
Max. reactivity [$]	1.4026	1.235	1.237	1.237
Min. boron [ppm]	1314.60	1314.26	1314.95	1314.97
Max. $T_{Doppler}$ [K]	919.04	880.07	899.25	894.55

changes by 574 MW enabling dynamic time stepping. The timing of the power peak, however, does not. The method of exponential transforms employed by DYNSUB assumes that the temporal behavior can be split into the product of exponential amplitude function and a flux form function. As long as the form function does not change significantly during a time step, this numerical scheme is very robust. In this boron dilution transient, however, complicated changing three-dimensional neutron flux shapes occur, which cannot be described by the first few eigenmodes of the system. Hence, time steps have to become small for the assumptions of the DYNSUB time stepper to hold.

The differences in peak height and timing between DYNSUB, CBY/SCF and DYN3D/SCF for the same fixed time step can be attributed fully to differences in the neutronics solutions. Numerically, all DYN3D based tools use an explicit coupling scheme between neutronics and thermal-hydraulics. CBY/SCF, however, employs a staggered time stepping scheme (Jimenez, 2010). It is of order 1.5 and, hence, more robust than a purely explicit scheme. Moreover, all coupled codes utilize a pure exponential time derivative scheme to approximate the change of neutron fluxes with time (Grundmann, et al., 2005; Beckert & Grundmann, 2008; Lozano, et al., 2008).

There are also non-negligible differences, how the coupled codes solve the neutron flux shapes. COBAYA3's solver ANDES utilizes a Analytic Coarse Mesh Finite Difference (ACMFD) method while DYN3D based tools rely on NEM solutions. Effects of the difference methods have been described already in 5.3.2 analyzing the steady-state cases.

Finally, COBAYA3, DYN3D and DYNSUB handle sub-critical systems using diverse methods. The boron dilution transient simulated start from a very sub-critical reactor state illustrated in Figure 81 in Appendix H. All DYN3D based tools calculate the decay of neutron flux and power levels associated with this strong sub-criticality. COBAYA3, on the other hand, employs an artificial external neutron source to maintain both neutron flux and power levels. At the same

time it tracks the sub-criticality of the system. Once the system returns to critical or above, the artificial external source is switched off and a normal transient is computed.

The maximal recorded fuel Doppler temperatures correspond to the computed peak powers for each tool. The evolution of reactivity as computed by each reactor simulator is plotted in Figure 81 in Appendix H. Besides exhibiting the same temporal shift between COBAYA3 and the other DYN3D based tools, the maximal dynamic reactivity of the latter tool group is almost 0.2 $ lower than that of CBY/SCF. The DYN3D based simulations use adjoint neutron fluxes obtained at the end of the HZP steady-state run to evaluate reactivity on-the-fly. CBY/SCF, however, computes its reactivity without the adjoint fluxes at a weighting function. It weights all contributions evenly.

The evolution of the core reactivity after the super-prompt critical power peak is dominated by moderator density effects. The Doppler feedback is only the second most important feedback mechanism. Moreover, after the power peak no re-criticality of the Westinghouse PWR is observed.

The results obtained for the second scenario are summarized in Table 32. While the minimal boron concentration is practically identical for the smallest slug size, in this case, increasing differences between CBY/SCF and the other solutions are observed. Again, the super-prompt critical power peak of CBY/SCF appears first (cp. Figure 82, Appendix H) and corresponds to the highest dynamic reactivity recorded (1.68 $). The deviations in maximal reactivity, however, are significantly smaller than for the previous case. The generic shape of the reactivity over time is depicted in Figure 83 in Appendix H. Once more, the reactor core does not return to criticality after the super-prompt critical power excursion. However, here local boiling occurs and a slug of vapor moves through the core. This enhances the negative feedback from moderator density. For scenario one, differences between DYN3D/SCF and DYNSUB are larger between than DYNSUB and CBY/SCF concerning peak powers and fuel Doppler temperatures. In this scenario, the DYN3D based solutions are closer to each other than they are to COBAYA3.

The effect of allowing DYNSUB to dynamically adjust its own time step is even larger for the second slug of deborated water. The peak power changes by 6.8 GW. With increasing slug size, the severity of the three-dimensional power excursion rises. At the same time, a fixed 1 ms time step for DYNSUB becomes even less appropriate.

Table 32: Summary of characteristic reactor data for scenario 2 of the NURISP boron dilution benchmark simulated by CBY/SCF, DYN3D/SCF and DYNSUB.

Parameter	CBY/SCF	DYN3D/SCF	DYNSUB	DYNSUB dynamic Δt
Power peak [MW]	31786.4	44371.79	43336.8	36548.6
Peak time [s]	5.086	5.170	5.187	5.186
Max. reactivity [$]	1.6774	1.617	1.634	1.631
Min. boron [ppm]	1254.43	1257.05	1257.06	1257.30
Max. $T_{Doppler}$ [K]	1205.28	1226.41	1229.25	1193.08

Finally, the simulation results of the third transient scenario are tabulated in Table 33. Generally, the comparison of the different solutions shows the same trends as for the second slug (Figure 85 and Figure 84 in Appendix H). A 44 % increase in the volume of the deborated water entering the core from the first to the third scenario leads to an approximately 6.3 times higher super-prompt critical power peak.

Table 33: Summary of characteristic reactor data for scenario 3 of the NURISP boron dilution benchmark simulated by CBY/SCF, DYN3D/SCF and DYNSUB.

Parameter	CBY/SCF	DYN3D/SCF	DYNSUB	DYNSUB dynamic Δt
Power peak [MW]	41980.6	57858.6	56375.7	46173.1
Peak time [s]	5.398	5.482	5.499	5.498
Max. reactivity [$]	1.8281	1.709	1.735	1.729
Min. boron [ppm]	1215.14	1217.19	1217.61	1218.47
Max. $T_{Doppler}$ [K]	1232.89	1302.55	1305.12	1249.3

In this scenario, the reactor core becomes critical again and moves on to delayed super-critical for a short period of time after the power peak has passed. As illustrated in Figure 84 (Appendix H), CBY/SCF predicts a second reactivity peak of 0.783 $ at roughly 6.15 s from the start of the transient. This second period of positive reactivity lasts 0.6 s. The DYN3D based solutions predict the re-criticality occurring later. Reactivity reaches a maximum of approximately 0.45 $. Like for the CBY/SCF solution, positive values for reactivity during the second peak are recorded for a duration of about 0.61 s.

For DYNSUB, it has been shown for all three transients that a one millisecond long time step does not lead to a space-time converged solution. Only one CBY/SCF simulation of the third

scenario with a 100 μs time step is done. In that calculation, the super-prompt critical power peak reached 43014.4 MW and happened at 5.388 s after the start of the transient. Unlike for DYNSUB, both height and timing of the power excursion change here. While DYNSUB underestimates TH feedback if discretization in the time domain is too coarse, CBY/SCF overestimates it.

5.3.4 Summary of NURISP boron dilution benchmark

It has been demonstrated that SUBCHANFLOW's boron transport model has been properly integrated into the coupled code. DYNSUB results are close to DYN3D/SCF solutions for all scenarios but especially for the second and third diluted boron slugs if both tools employed a fixed 1 ms time step.

However, it is also observed that DYNSUB requires very small time steps for a time converged solution of these transient cases. The fixed time step size of 1 ms estimated based on the minimal expected point kinetics reactor period fails to lead to a time converged solution due to quickly changing spatial neutron flux shapes. At the moment, no method to determine a sensible time step size for cases limited by fast spatial flux shape changes apriori exists. Thus, a test for time convergence can only be done by means of a sensitivity study. Here, no such proof has been done that the DYNSUB solution using a dynamic time step size is actually time converged, as it would have required runs with even smaller time steps. The same holds for the CBY/SCF and DYN3D/SCF calculations performed.

Finally, a strong influence of the numerics of the neutron transport solver in the different reactor simulators on the results has been reported. A deeper analysis should be conducted in the future.

5.4 OECD/NEA and U.S. NRC Pressurized water reactor main steam line break benchmark

The OECD/NEA and U.S. NRC Pressurized water reactor main steam line break benchmark (Ivanov, et al., 1999) is a computational benchmark that may only be used for DYNSUB solution verification. It evolves around Unit 1 of NPP Three Mile Island. The reactor considered is a two-loop Babcock and Wilcox PWR with a square fuel lattice. An axially strongly non-uniform meshing is employed in the benchmark. This mesh is necessary, because reactor is loaded with high burn-up fuel assemblies. This can be utilized to prove that DYNSUB's coupling routines work properly for arbitrary spaced axial meshes.

The postulated transient in this benchmark is the double-ended break of one of two main steam lines of the reactor. During the transient the reactor is scrammed and the decay heat produced

needs to be taken into account thereafter. Hence, both DYNSUB's internal control logic for tripping the reactor and its simple utility for handling pre-computed decay heat can be analyzed with this code-to-code benchmark.

5.4.1 Definition of scenarios and models

The exercise 2 of this computational benchmark is studied (Ivanov, et al., 1999). It consists of static simulations of the full reactor core at HZP and HFP conditions as well as two main steam line break (MSLB) scenarios with given time-dependent reactor core boundary conditions. All scenarios of exercise 2 take place at the end of cycle (EOC). The point kinetic model benchmarks (exercise 1) and the simulation of the plants primary and secondary systems (exercise 3) are not of interest for the solution verification of DYNSUB. In case of exercise 3, this is mostly because of the missing coupling of DYNSUB to a TH system code to tackle the balance of plant.

The HFP operating conditions of TMI-1 in exercise 2 are listed in Table 34. HZP simulations are carried out using the following fixed thermal-hydraulic conditions: a coolant and fuel temperature of 551 K as well as a coolant density of 766 $\mathrm{kg/m^3}$. The steady-state simulations requested in exercise 2 are summarized in Table 35. The column "scenario" refers to two distinct cross section sets provided for the two MSLB transients. The majority of the cases are HZP calculations. The HFP case is to be done with both homogeneous thermal-hydraulic conditions (case 2A) at the core inlet and heterogeneous ones (case 2). The latter are derived from the time-dependent BC for the MSLB scenarios. For all simulations, reactor eigenvalues as well as radial and axial peaking factors are to be determined.

Table 34: Operating conditions at HFP of the OECD/NEA and U.S. NRC Pressurized water reactor main steam line break benchmark according to (Ivanov, et al., 1999)

Parameter	Value
Core power	2772 MW
Coolant inlet temperature	562.9 K
Primary system pressure	15.72 MPa
Core mass flow rate	16052.4 kg/s
Boron concentration	5.0 ppm

In the DYNSUB model used for all TMI-1 simulations, the reactor core is described by 241 radial nodes corresponding to the number of fuel assemblies (177) and radial reflectors (64).

Axially, 24 non-equidistant mesh layers are utilized. This non-equidistant axial discretization is crucial, since the core is axially highly heterogeneous due to the high burn-up at EOC.

Table 35: Summary of steady-states included in exercise 2 of the OECD/NEA and U.S. NRC Pressurized water reactor main steam line break benchmark (Ivanov, et al., 1999)

Number	TH conditions	CR positions	Scenario
0	HZP	CR #1-7 100 % withdrawn	
1	HZP	CR #1-6 100 % withdrawn CR #7 90 % withdrawn N12 100 % withdrawn	
2	HFP	CR #1-6 100 % withdrawn CR #7 90 % withdrawn N12 100 % withdrawn	
3	HZP	CR #1-7 fully inserted N12 100 % withdrawn	1
4	HZP	CR #1-7 fully inserted N12 100 % withdrawn	2

Radial and axial boundary conditions are zero neutron flux. The 2G diffusion cross section library included in the benchmark specification is used. The thermal-hydraulics model contains one laterally coupled channel per fuel assembly. Each of these channels is divided in 24 axial nodes corresponding one-to-one to the neutronics mesh layers. The top reflector is heated using one of DYNSUB's prebuilt reflector treatment functions in order to exclude it from the thermal-hydraulics model. The fuel rods of each fuel assembly are represented by one average fuel rod. The latter is radially discretized into 12 nodes to solve the heat conduction problem. 10 nodes describe the fuel pellet, one the gas gap and one the clad. The thermo-physical properties for fuel and clad as well as the gap heat transfer coefficient are taken from the benchmark specification (Ivanov, et al., 1999). Moreover, steady-state coupled convergence criteria identical to those of Kalinin-3 and the PWR MOX/UO_2 benchmark are used.

For the transients studied, it is postulated that the main steam line of one loop ruptures upstream of the main steam isolation valve (MSIV). The double-ended rupture leads to a fast depressurization of the affected part of the secondary system. The water inventory flashes and boils off. The heat transfer in the heat exchanger of that loop increases drastically leaving the primary coolant strongly overcooled. Resultantly, roughly half of the reactor core is fed with too cold coolant leading to a positive reactivity insertion. For Babcock and Wilcox two-loop PWRs the worst overcooling happens starting from HFP conditions since the water inventory in the plants once-through steam generators increases with increasing power level. Hence, the postulated transients in this benchmark start from HFP operating conditions.

As a consequence of the overcooling, reactor power starts to rise and a reactor trip is triggered. To be conservative, it is assumed that the control assembly with the highest worth is stuck out (position N12). The evolution of the decay heat is computed based on the ANS-79 standard and provided as part of the benchmark. DYNSUB employs these decay heat tables instead of computing it on-the-fly.

One of the main concerns for MSLB scenarios is that the reactor might return to power and criticality in a latter phase of the accident. Because of this, two scenarios are to be analyzed in this benchmark. One using the conditions described above and one, in which the worth of the control rod banks has been artificially reduced. For both scenarios time-dependent core inlet mass flow rates and coolant temperatures as well as primary system pressures are provided. They have been obtained from a simulation of TMI-1 using the TRAC-PF1/NEM BE coupled code system. For both scenarios, transients lasting 100 s in total are to be computed. DYNSUB used a fixed time step of 5 ms, which has been determined by a sensitivity study on the maximal allowable step size to achieve a converged solution.

5.4.2 Results for HZP and HFP stationary cases

All benchmark results quoted in the following were taken from the final report on exercise 2 (Todorova, et al., 2002). DYNSUB's HZP simulation results are compared to the benchmark mean data in Table 36 as in this benchmark there exists no reference solution. The presented spread of original benchmark contributions corresponds to one standard deviation. A good agreement between DYNSUB and benchmark mean data is observed. As the calculations are done with fixed thermal-hydraulic feedback, they are essentially pure neutronics problems. Given that cross section libraries were provided by the benchmark authors, deviations between benchmark participants and DYNSUB are due to different methods for solving the neutron diffusion problem. From the overall results, it may be concluded that DYNSUB has the same capabilities as other reactor simulators of the benchmark to employ largely different axial mesh sizes in its neutron transport solution.

The HFP simulation results are listed in Table 37. As can be seen the coupled DYNSUB solutions fall within one standard deviation of the benchmark averages, except the axial peaking factor in case 2A. It only matches the benchmark mean data within two standard deviations.

This indicates that SUBCHANFLOW as TH module and the implementation of its coupling to DYN3D inside DYNSUB are capable of treating axially strongly non-uniform meshing.

Table 36: Comparison of the eigenvalue, assembly and axial peaking factors of the HZP static cases of the OECD/NEA and U.S. NRC Pressurized water reactor main steam line break benchmark (Todorova, et al., 2002)

Case	Code	k_{eff} [ ]	F_{xy} [ ]	F_z [ ]
0	Benchmark average	1.0337(0.0072)	1.3609(0.0061)	2.6842(0.019)
	DYNSUB	1.0351	1.3619	2.6740
1	Benchmark average	1.0318(0.0068)	1.4324(0.0136)	2.4522(0.036)
	DYNSUB	1.0329	1.442	2.4201
3	Benchmark average	0.9854(0.0079)	5.4579(0.1735)	2.7538(0.0365)
	DYNSUB	0.9873	5.5064	2.7514
4	Benchmark average	1.0002(0.0078)	3.6304(0.0744)	2.7384(0.0319)
	DYNSUB	1.0021	3.3645	2.7378

Table 37: Comparison of the eigenvalue, assembly and axial peaking factors of the HFP static cases of the OECD/NEA and U.S. NRC Pressurized water reactor main steam line break benchmark (Todorova, et al., 2002)

Case	Code	k_{eff} [ ]	F_{xy} [ ]	F_z [ ]
2	Benchmark average	1.0039(0.0048)	1.3536(0.0555)	1.0858(0.0308)
	DYNSUB	1.0054	1.334	1.1209
2A	Benchmark average	1.0023(0.0064)	1.3320(0.0068)	1.0828(0.0193)
	DYNSUB	1.0052	1.3273	1.1195

5.4.3 Main steam line break transient scenarios

The evolution of reactor power for the first MSLB scenario as predicted by DYNSUB is compared to the benchmark average behavior in Figure 37. The presented results coincide. Two distinct DYNSUB simulations are performed. In one simulation, the control rod banks are free to fall at 6.65 s into the transient as given in benchmark specifications. In the other, DYNSUB's internal control logic is used to initiate the reactor trip and move the CR banks utilizing the information on the I&C system from exercise 3 of the benchmark. In the latter case, the reactor trip signal 'high power level' is reached at 6.35 s. The CR banks begin to fall 0.4 s later.

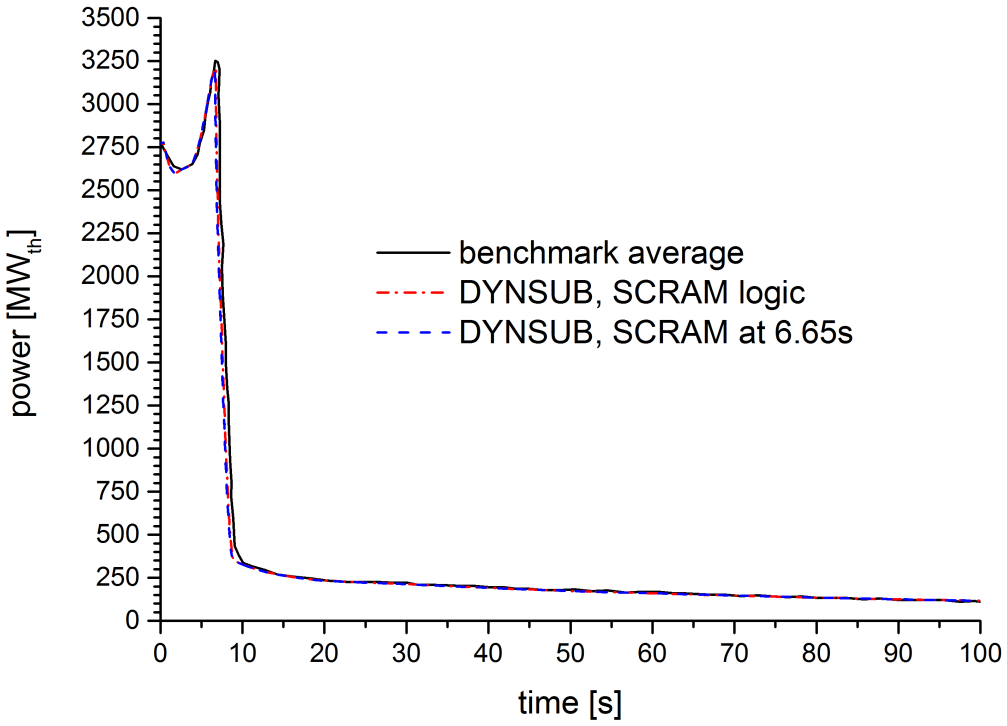

Figure 37: Evolution of power as predicted by DYNSUB and benchmark participants for the first MSLB scenario (Todorova, et al., 2002)

The double-ended break of the main steam line occurs at 0.0 s in this scenario. In the first two and a half seconds, the reactor power decreases. This caused by the overcooling of one of the primary loops leading to a steep decline of the primary system pressure. The density of the moderator in the active core is reduced introducing negative feedback. The overcooled water slug, however, has not reached the active core yet. Once it does, power increases quickly until the reactor is tripped. All CR banks except the control assembly in N12 fall in. The active core inlet coolant density continues to increase until the secondary side of the steam generator is empty after approximately 60 s (see Figure 38). Beyond this point, the primary coolant starts to heat up again due to the deteriorated heat transfer to the secondary system, since one of the steam generators has entirely evaporated its whole inventory.

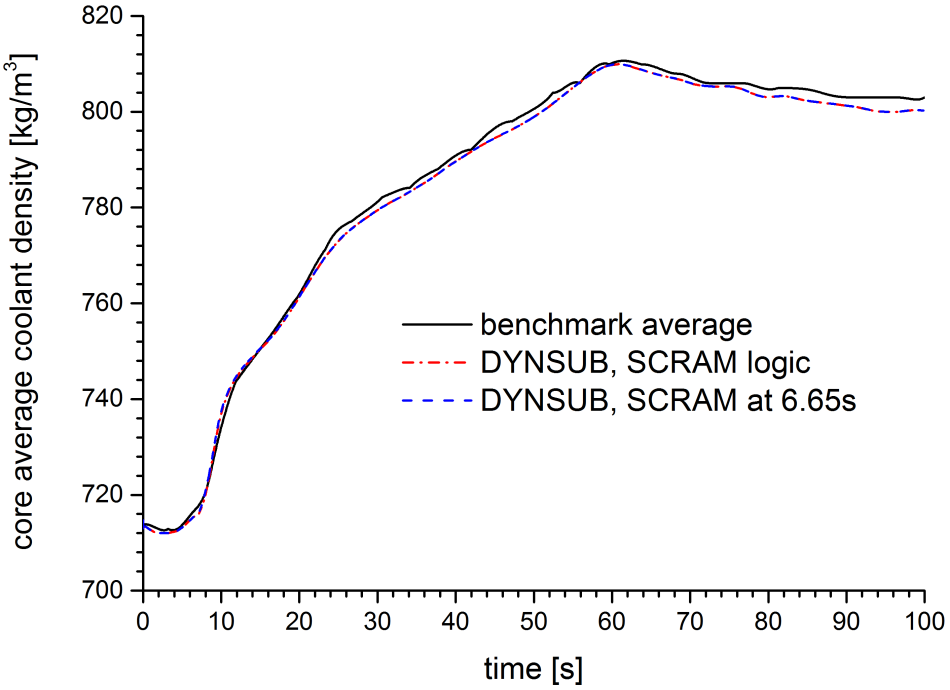

Figure 38: Evolution of core averaged coolant density as predicted by DYNSUB and benchmark participants for the first MSLB scenario (Todorova, et al., 2002)

While results obtained with DYNSUB match the average of benchmark solutions well in terms of reactor power and core averaged moderator density, larger differences in the core averaged Doppler temperature are observed (Figure 86, Appendix I). Deviations are particularly pronounced before the reactor scram. These can be attributed to differences in the thermal-hydraulic models of DYNSUB and the benchmark participants. Some benchmark participants did not use the thermo-physical properties and Doppler temperature correlation given in the benchmark specification (Todorova, et al., 2002). Furthermore, there were not standardized axial and radial nodalization for modeling the fuel rods. Finally, some benchmark contributions used sub-channel TH codes, i.e. COBRA-III and FLICA, considering cross flow between channels. The majority of the contributions, however, relied on TH system codes like RELAP5 and TRAC without taking the lateral coupling of coolant channels into account.

In the second main steam line break transient scenario (return to power), the worth of the control rod banks is artificially reduced. With this less potent shutdown system, reactor power evolves as shown in Figure 39. The most important difference compared to the first MSLB scenario is that the negative tripped rod reactivity is insufficient to counteract positive feedback from coolant density and Doppler temperature (Figure 89, Appendix I). The PWR returns to power before the increasing moderator temperatures eventually shut it down. The shape of the resulting power swing computed with DYNSUB is comparable to the average behavior of core determined in the benchmark. After the SCRAM, the average core behavior exhibits a power

maximum of 870 MW at 60 s after the beginning of the transient. At this point in the transient, the spread of the benchmark contributions used to compute the average is characterized by a standard deviation of 50 MW. DYNSUB predicts this peak to be only 746 MW high, i.e. its solution falls within two standard deviations of the benchmark mean. As the transient continues, the differences between the benchmark contributions increase, the standard deviation of the benchmark mean becomes as large as 120 MW. Thus, the DYNSUB solution now lies within one standard deviation of the benchmark average behavior.

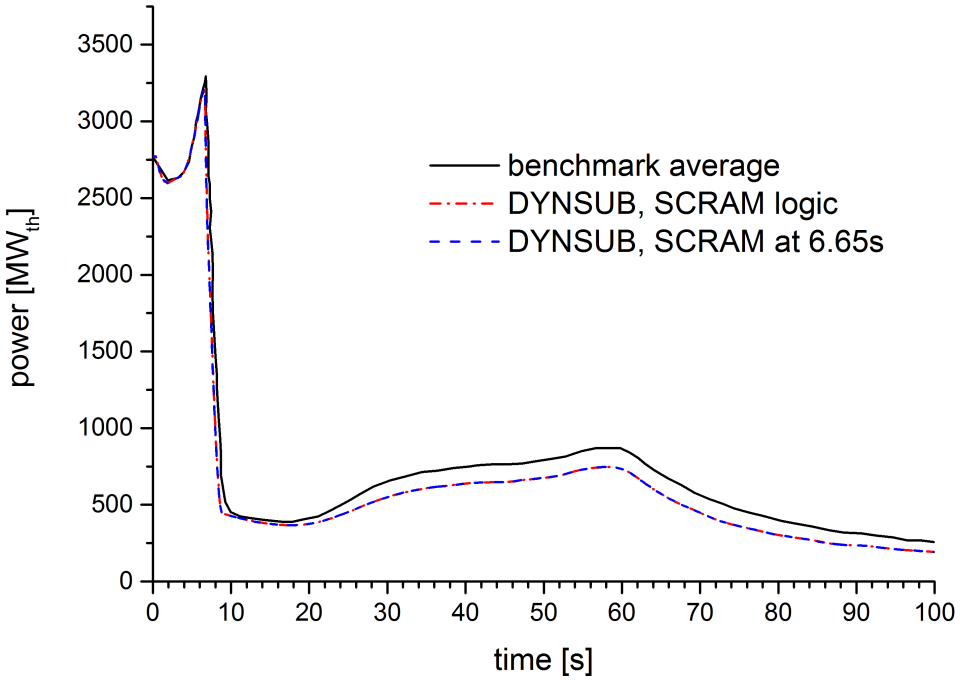

Figure 39: Evolution of power as predicted by DYNSUB and benchmark participants for the second MSLB scenario (Todorova, et al., 2002)

Several effects contribute to the large spread of results and DYNSUB's deviation from the benchmark mean. These are reflected in the different actual inserted reactivity of all benchmark participants and DYNSUB. At the end of the scram, the benchmark average value reactivity of the core is -4.7 $ with values as low as -6.05 $ being in the spectrum. DYNSUB evaluates the core reactivity to be -6.02 $ (cp. Figure 89 in Appendix I). It computes the CR banks to have a higher worth than most of the other solutions do. The 3D dynamic simulation of the scram differs for reactor simulators as evaluating flux re-distribution and changes in local feedback conditions strongly depend on the numerical methods employed in the neutronics problem. Due to the sensitivity study done to determine the optimal time step size, it can be ruled out that the differences observed are due to a non-converged solution.

Discussing reactivities at this point, it has to be pointed out that the PWR core does not become critical again (Figure 89, Appendix I). All benchmark simulations and DYNSUB predict it to stay slightly sub-critical. The maximal reactivity as computed by DYNSUB is -0.135 $ at

approximately 56 s after the beginning of the transient. The increase in power is driven by the high reactivity insertion rate between 10 s and 30 s (approximately 0.2 $/s). The slow power increase up to 60 s afterwards corresponds to a much lower reactivity insertion rate (approximately 0.01 $/s).

The moderator reactivity feedback follows the coolant density. The core averaged moderator density shows a similar temporal evolution as the benchmark averages. But the agreement is not as good as for the first scenario (Figure 87, Appendix I). Here also, core inlet and outlet TH BC were provided. Hence, most of the observed differences can be attributed to different closure correlations and water/steam property tables used by the thermal-hydraulics modules/codes. In addition, whether or not the TH simulation considered cross flows between coolant channels plays a minor role. However, the effect cannot be quantified as the benchmark report does not include the TH fields of any participant over time for either scenario. Due to the generally higher power level of the reactor after the scram in the second scenario as opposed to the first one, the former modeling differences are more important in this case.

The core averaged Doppler temperature for the second MSLB case is depicted in Figure 88 in Appendix I. Before the reactor scram it exhibits the same deviations found in scenario one. Thereafter, it shows the same temporal behavior as the reactor power prediction.

5.4.4 Summary of the TMI-1 MSLB benchmark

DYNSUB has been successfully applied to study the OECD/NEA and U.S. NRC Pressurized water reactor main steam line break benchmark with axially strongly non-uniform meshing. The robustness of the coupled code's coupling scheme concerning arbitrarily spaced axial meshes could be verified. Moreover, it has demonstrated that the simple control logic introduced into DYNSUB is capable of appropriately tripping the PWR in both MSLB scenarios. Last but not least, the MSLB scenarios, especially the first one, proved that DYNSUB's simplistic approach to handle decay heat is sufficient to study transients in PWRs that include reactor scrams.

5.5 Conclusions and next steps

Three solution verification and one validation case consisting of an international benchmark each have been analyzed in this chapter. In all cases, the extended DYNSUB performes well. The broad range of transient cases tested underlines that DYNSUB has become a fully functional reactor simulator for PWRs using assembly-homogenized models.

Both the pin-by-pin and fuel assembly resolution DYNSUB calculations employ identical solvers, transient time steppers, thermal-hydraulic correlations and coupling algorithms. As a

consequence, the conclusion drawn above also holds for DYNSUB as a pin-homogenized reactor simulator.

Since most of the international benchmarks analyzed in this chapter are suitable only for code-to-code solution verification, DYNSUB validation efforts are continued by studying the SPERT III experiments in chapter 6. Because of the necessity to generate multi-dimensional cross section tables to describe the SPERT core, it is at the same time a first step in the validation process of the Serpent 2-DYNSUB code sequence. As presented in section 4.3, Serpent 2 is chosen as lattice code due to the fact that MC based lattice codes are a new and quickly progressing field of research.

6 Validation of the Serpent 2-DYNSUB tool chain using the Special Power Excursion Reactor Test III (SPERT III)

In this chapter, efforts to validate DYNSUB are continued by employing the coupled code to model the SPERT III experiments (Dugone, 1965; McCardell, et al., 1969). As few-group cross section tables need to be created to simulate the SPERT III experiments. This second V&V step concerns the entire Serpent 2-DYNSUB tool chain.

The experiments conducted within the SPERT III program are REAs starting from cold and hot as well as zero, little and full power reactor conditions. Of interest for DYNSUB is the SPERT III E-core experiment series, that was already used to validate the BE tools TRITON/TRACE/PARCS (Wang, et al., 2013), ANCK (Aoki, et al., 2009), GALAXY/COSMO-K (Yamaji, et al., 2014) and CASMO5/Simalute-3K (Grandi, 2014) for PWR applications.

Here, first a Serpent 2 and a SSS2/SCF steady-state reference model for both cold startup, i.e. cold zero power, and operating power, i.e. hot full power, conditions are developed. A hot zero power reactor configuration is not considered, since no new insights on the Serpent 2-DYNSUB code sequence can be gained by studying more than one zero power state.

Results obtained with Monte Carlo tools are then used to foster developing and evaluating a DYNSUB description of the SPERT III E-core. Afterwards, the final DYNSUB model is employed to study selected experimental transients starting from cold startup, hot standby and operating power conditions.

Serpent 2 as a lattice code has been verified and validated for HZP operating conditions and stationary calculations (Leppänen, et al., 2014a; Leppänen, et al., 2014b). Here, for the first time multi-dimensional cross section tables generated with SSS2 are analyzed under non-zero power and transient conditions by modeling SPERT. Only a nodal diffusion DYNSUB SPERT model and SSS2/SCF model using channel level TH are presented in the following. A detailed description of the SPERT III E-core and a discussion of the uncertainties associated with the measurements performed is provided in Appendix K.

6.1 Numerical SPERT III models

6.1.1 Serpent 2 and SSS2/SCF static reference models

The Serpent 2 model for the cold startup state covers all of the active reactor core and its radially and axially supporting structures (see Figure 40). Below the bottom core support grid another 8 cm of the lower water plenum are considered.

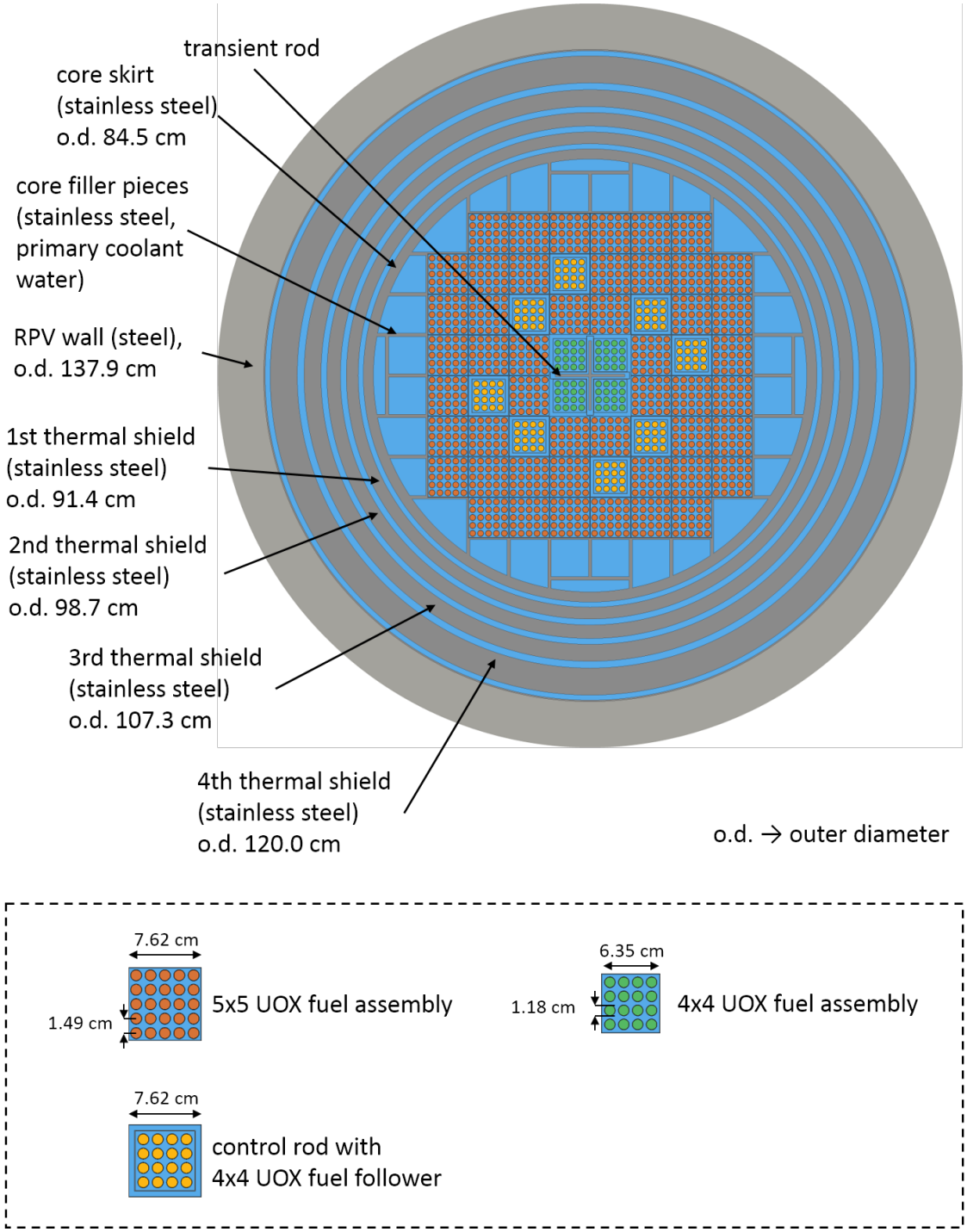

Figure 40: Horizontal cut through SPERT III E-core at mid plane as modeled by Serpent 2

ENDF/B VII.0 nuclear data broadened 294 K is employed by SSS2. The Monte Carlo code simulated $4 \cdot 10^5$ neutrons per cycle. 100 inactive cycles are followed by 2000 active once. Furthermore, the Wielandt shift (cp. section 2.6) as a method to accelerate fission source convergence is utilized.

In order to produce a reference solution at operating power conditions with SSS2/SCF, a thermal-hydraulic model is developed. The SUBCHANFLOW model includes only the active reactor core. The fuel assemblies are represented by single TH channels connecting the lower and upper water plena of the SPERT III RPV. Due to the cans of the assemblies these channels are not coupled laterally. The channels' flow area, wetted and heated perimeters are tabulated in Table 38. Each channel is divided into 20 axial nodes.

Table 38: Flow area, wetted and heated perimeters for both types of TH channels in SPERT III E-core SCF model

TH parameter [unit]	5x5 fuel assembly	4x4 fuel assembly
Flow area [cm^2]	27.5086	20.3871
Wetted perimeter [m]	1.22681	0.84144
Heated perimeter [m]	0.92963	0.59496

One effective fuel rod is used to model all of the fuel pins inside one assembly. For this rod, a radial discretization of 12 nodes to cover fuel (10 nodes), gas gap and clad (2 nodes) is employed. The 4.8 wt% enriched UOX fuel is modeled using SCF's temperature dependent uranium oxide material properties. For the clad, the internal stainless steel property functions are chosen. To approximately model the change of the gas gap heat transfer coefficient with changing reactor and fuel conditions, the Transuranus fuel-clad gap model is enabled in the SCF input. The gamma heating fraction is set to 2.6 % - a typical PWR value.

SSS2/SCF utilized ENDF/B VII.0 nuclear data and a 5 K spaced set of thermal scattering data for its stochastic mixing fallback for TMS. Per coupled iteration 300 inactive and 2000 active cycles of $2 \cdot 10^6$ neutrons each are computed. Instead of employing Wielandt's method, UFS is used for global variance reduction. The coupled convergence targets are 5 pcm for the eigenvalue and 0.05 % for both Doppler temperature and moderator density.

6.1.2 Serpent 2 cross section model description

For simulating the SPERT III E-core experiments series, SSS2 is used as a lattice code to generate homogenized few-group cross section data for DYNSUB. The SSS2 calculations employed ENDF/B VII.0 nuclear data and produced two-group homogenized group constants.

The boundary between the fast and thermal energy group is 0.625 eV. The B1 approximation is enabled in the SSS2 input. With this option, SSS2 uses its tallied homogenized micro-group cross sections to solve the B1 equations. The solution of the latter equations yields the critical spectrum that is then used to re-homogenize the few-group constants for DYNSUB. The micro-group structure used for solving the B1 equations and determining few-group XS is the 44-group structure of one of the SCALE generic XS libraries.

The range and combination of thermal-hydraulic state points included in the XS libraries for DYNSUB for cold startup and operating power conditions are shown in Table 49 and Table 50 in Appendix K. The moderator density branches are determined based on the IAPWS-IF97 water/steam tables. At cold startup and operating power conditions the primary coolant starts to boil at 353 K and 587 K, respectively. For these temperatures, four branches considering 20, 40, 60 and 80 per cent void are included in both libraries to allow for coolant boiling during severe super-prompt critical power excursions. By not including moderator temperature branches in the library for DYNSUB, constant pressure conditions are assumed.

The cold start-up library contains six fuel temperature points, the operating power one five. Sensitivity studies have shown that including more fuel temperature points in either library do not improve the results. Less points, however, lead to a decrease in the DYNSUB solution quality.

The spectral geometries used by Serpent 2 for determining few group constants are depicted in Figure 41. Models shown in subfigure a) through d) utilize reflective boundary conditions. To improve DYNSUB's nodal diffusion solution, the fuel assemblies presented in subfigures a) to c) ADF are evaluated by Serpent 2. Since the absorber section of the SPERT III E-core CR does not contain any fuel, few group cross sections for it can only be computed by means of super cells. The super cell chosen in this work is presented in subfigure d). For the interface of the CR absorber cell with its fuel assembly neighbors, GET IDF are produced according to the method described in section 4.5.4.

The cross section calculations done with the models shown in subfigure a), c) and d) exactly use the branch structure described before. For the central 4x4 fuel assemblies, an additional state variable defining the position of the TR (in or out) has to be added to the cross section library. The small heat up of the primary coolant bypassing the assembly cans and cooling the TR is not considered as it proved to have no effect on the final cross section sets.

In the process of developing the cross section libraries for DYNSUB many different models for both the radial and axial reflectors have been tested. The best-performing, final version of both is shown in subfigures e) and f) of Figure 41.

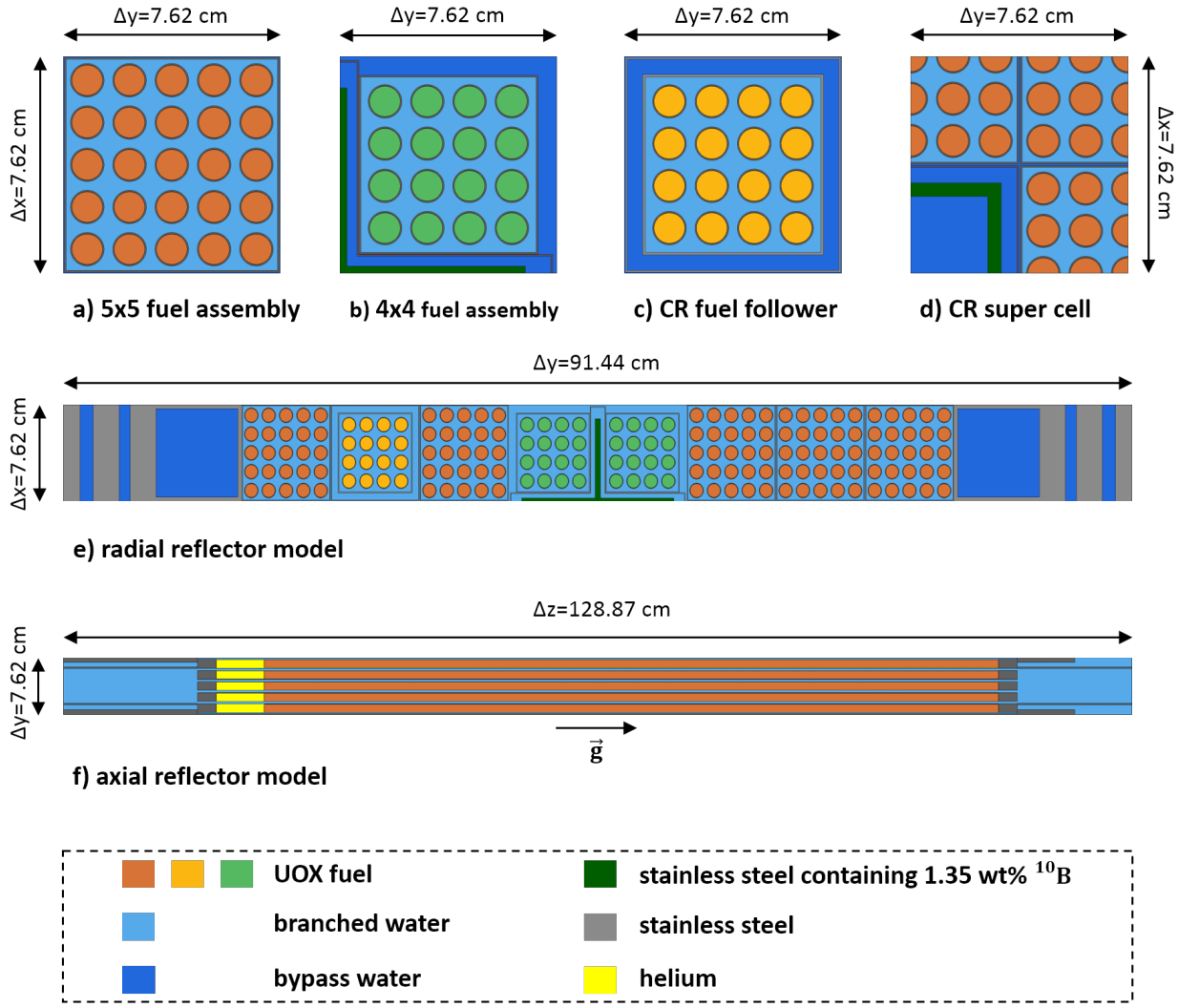

Figure 41: Spectral geometries used to generate few group cross sections for DYNSUB with Serpent 2 for the SPERT III E-core; the term "bypass water" unlike "branched water" refers to all primary coolant for which heating and, hence, XS branching is not considered in the Serpent 2 models

The radial reflector model employs vacuum BC in x- and reflective BC in y-direction. Two cells having the size of a core lattice position describe the active core vicinity in a simplified manner. An analysis of the scalar neutron flux gradients in the SSS2 3D reference model revealed, that one may assume vacuum boundary conditions about two fuel assembly pitches away from the active core. One of the cells represents the filler pieces between active core and core skirt. The other comprises core skirt and part of the numerous thermal shields. For each reflector cell, one few-group cross section set is generated. Discontinuity factors for both radial reflector few group constant data sets are determined.

The axial reflector model depicted in subfigure f) is effectively a vertical cut through a 5x5 fuel assembly. The z-direction BC is vacuum and y-direction one reflection. The bottom axial

reflector cross section set describes the foot of the fuel assembly (in subfigure f) right region not containing orange colored nuclear fuel). The top axial reflector cross section set comprises both the gas plena (yellow) and end plugs of the fuel rods and the fuel assembly head. Since DYNSUB cannot handle discontinuity factors in axial direction, no IDF for the axial reflectors are computed.

Neither the radial nor the axial reflector cross section sets are branched. It has been analyzed whether considering the effect of the core exit temperature coolant following through gaps between thermal shields has a significant effect. This turns out not to be the case. As DYNSUB cannot consider gamma heating, the filler pieces and other structures around the active core are not heated. Thus, there is no need to branch the radial reflector XS. As for the axial reflectors, the bottom reflector is always at inlet conditions. The top reflector mostly sees average reactor coolant heat up corresponding to the SPERT III operating conditions because the majority of RIA transients evolve too quickly to have a significant impact on the coolant properties.

As the few group cross section sets computed for DYNSUB to model SPERT are Monte Carlo neutron transport based estimates, it is important to verify their statistics. In other words: what is the minimum number of neutron histories per transport calculation one needs to simulate with SSS2 such that no inaccuracies caused by undersampling, non-converged fission sources and inter-cycle correlations are propagated into the deterministic reactor simulation by DYNSUB. This question has been addressed in a recent publication studying assembly-homogenized two-group cross sections and ADF for 17x17 Westinghouse PWR fuels (Kaltiaisenaho & Leppänen, 2014). For both fuel assemblies, a total of 50 million neutron histories proved to be sufficient. Thus, to compute the SPERT cross sections for the spectral geometries shown in subfigures a) to d) in Figure 41 SSS2 simulated 25,000 neutrons per cycle in 2000 active cycles for each transport run. 300 cycles are skipped. For the two reflector models, the analysis of Kaltiaisenaho and Leppänen is not applicable. As a result, the number of neutron histories simulated here has been chosen conservatively. SSS2 runs the same number of cycles as for the other models but employed 50,000 neutrons in each cycle. Furthermore, to ensure the reflector regions are well populated the Wielandt shift is enabled.

The lattice calculations for the cold startup cross section library took 47.0 h on a dual socket Intel Xeon E5-2697 v2 with 379 GB of host memory running Mageia release 4 x64. The SSS2 execution used 48 threads. The corresponding simulations for the operating power library consumed 64.5 h on the same machine using an identical number of threads. Based on these numbers it is clear that computational cost of Monte Carlo based homogenization is significantly higher than that of classical deterministic lattice codes. However, it is within the capability to small modern parallel computers to finish SSS2 lattice calculations for cases like the SPERT III experiments in an acceptable amount of time. This finding is in line with the

conclusion on the practical feasibility of Monte Carlo neutron based spatial homogenization drawn by Leppänen and Mattila (Leppänen & Mattila, 2014).

6.1.3 DYNSUB steady-state and transient models

In the DYNSUB model, the SPERT III E-core is represented by 140 radial nodes. 60 of which are fuel assemblies and 80 radial reflectors forming two complete rings around the active core. Axially, 100 equidistant mesh layers describe the axial extend of the fueled region. Another 14 and 19 mesh layers are utilized to simulate the bottom and top axial reflectors. The high axial resolution employed in the DYNSUB model is chosen to capture the fast movement of the TR and the corresponding reactivity insertion as accurately as possible. The axial and radial boundary conditions are set to zero neutron flux.

The two-group diffusion cross section libraries produced with createXSlib (rf. to subsection 4.5.3) based on Serpent 2 calculations presented in the last subsection are utilized. For the SPERT E-core experiments series, a new DYNSUB cross section table type has been developed. Unlike all previously existing XS tables, this one considers the dependence of both the effective delayed neutron fraction and the delayed neutron decay constants for the six delayed neutron precursor families on the thermal-hydraulic state.

The thermal-hydraulics model used by DYNSUB is identical to the one of SSS2/SCF except that it discretizes the axial height of the core with 100 mesh layers (see subsection 6.1.1). The convergence criteria used for the steady-state simulations are $\varepsilon_{\mathrm{keff}} < 10^{-5}$ for the eigenvalue, $\varepsilon_{\mathrm{DT}} < 10^{-4}$ for local Doppler temperature and $\varepsilon_{\mathrm{RM}} < 10^{-4}$ for the local moderator density.

Before turning to modeling the REA experiments, DYNSUB is employed to perform stationary simulations of the SPERT III E-core under cold startup and operating power conditions. DYNSUB results are compared to the Serpent 2 and SSS2/SCF reference solutions in order to evaluate the quality of the developed multi-dimensional cross section tables and the DYNSUB nodalization.

Eight transients starting from cold startup, hot standby and operating power conditions are selected. The hot standby REAs can be modeled using the operating power cross section libraries. For each initial condition the cases to be studied are chosen such that they include at least one delayed super-critical and one super-prompt critical scenario. Whenever possible, a prompt super-critical case is considered. The initial conditions of the selected tests are listed in Table 51 in Appendix K.

Unfortunately, for none of the 58 REAs the initial positions of the TR and eight CRs of the SPERT III E-core are specified in the experimental documentation (McCardell, et al., 1969). Only the system pressure, coolant inlet temperature, coolant flow speed, reactor power and

initial reactivity insertion are known. Therefore, the first step in any DYNSUB transient analysis is to position the TR such that its *static* worth matches the known initial reactivity insertion. The CRs are withdrawn from the core to keep it critical. At the beginning of the transient simulation, the TR is then accelerated towards the bottom of the active core until it is fully withdrawn. For all eight RIA calculations, DYNSUB employs a fixed time step of 0.1 ms as sensivity tests confirmed that this leads to a time-converged solution in all cases. These tests followed a trial and error approach.

6.2 Stationary simulations of the SPERT III E-core

6.2.1 Cold startup

The only quoted measured properties of the E-core under cold startup conditions mentioned in the report (McCardell, et al., 1969) are compared with simulation results obtained with Serpent 2 and DYNSUB in Table 39. The Monte Carlo code captures the experimentally determined control rod position quite well. The reactor eigenvalue predicted by SSS2 for the measured critical CR position is 0.99702(0.00004). The critical CR position computed by DYNSUB is significantly further off but shows the same the behavior like other deterministic assembly-homogenized models such as the CASMO5/SIMULATE-3K qualification model (Grandi & Moberg, 2012). The latter evaluated the SPERT III E-core to be critical with the CR tips positioned at 30.1 cm.

Table 39: Comparison of simulated integral quantities of SSS2 and DYNSUB with corresponding cold startup measurements (McCardell, et al., 1969)

Quantity	Measured	SSS2	DYNSUB
Critical CR position	37.084 cm	37.719 cm	30.1498 cm
Excess reactivity	14 $	14.21 $	13.7 $
TR worth	4.8 $	4.54 $	4.67 $
Reduced generation time	2.15 ms	2.15 ms	--

The experimental report mentions that the excess reactivity of the E-core is 14 $. Both SSS2 and DYNSUB reproduce the experimental data within one standard deviation (0.56 $). For the worth of the TR, the Serpent 2 result only falls within two standard deviations of the measurement. DYNSUB's prediction, however, differs by less than a standard deviation due to advantageous error cancellation in the low order neutronics model.

Unlike SSS2, DYNSUB cannot compute the reduced generation time. The value obtained with the Monte Carlo code matches the experiment perfectly. In the SPERT report, no information on the uncertainty of the reduced generation time evaluation could be found.

In order to verify the cold startup cross section library and the DYNSUB model further, a more detailed comparison between the SSS2 reference results and the DYNSUB nodal diffusion predictions are carried out. With the eight control rods and the transient rod withdrawn from the core, the effective multiplication factor determined by Serpent 2 becomes 1.11454(0.00004). DYNSUB evaluates the same factor to be 1.11106, which is 438.4 pcm less. When comparing low order deterministic transport to high order reference solution differences of this magnitude are expected. For example, in the OECD/NEA and U.S. NRC PWR MOX/UO_2 core transient benchmark the differences in eigenvalue between the 47G MOC DeCART reference and nodal solutions are of the same order of magnitude (see subsection 5.2.2).

In a next step, the relative differences in assembly power evaluated with Serpent 2 and DYNSUB have been determined. They are visualized in Figure 42. The maximal difference in assembly power is below 3.4 % everywhere. Serpent 2 predicts fuel assembly power to be higher than that of DYNSUB in most of the fuel assemblies near the core periphery and in the four 4x4 fuel assemblies surrounding the TR. As can be seen in Figure 43, the production of power in the DYNSUB model is slightly more shifted to the lower half of the core than in the SSS2 calculation. This is consistent with the reported difference in critical control rod position between the both reactor simulators.

	A	B	C	D	E	F	G	H
1		-0.69	2.88	2.67	2.94	3.39	-0.54	
2	-0.54	1.50	-0.35	-0.79	0.29	-0.12	1.50	-0.69
3	3.39	-0.13	-1.32	-2.87	-2.65	-1.32	-0.34	2.88
4	2.94	0.29	-2.65	2.11	2.12	-2.87	-0.79	2.69
5	2.69	-0.78	-2.87	2.11	2.11	-2.64	0.29	2.94
6	2.89	-0.35	-1.32	-2.64	-2.87	-1.32	-0.12	3.39
7	-0.69	1.50	-0.12	0.30	-0.79	-0.35	1.50	-0.54
8		-0.54	3.39	2.95	2.69	2.89	-0.69	

Figure 42: Relative spatial differences in SPERT III assembly powers in percent between SSS2 and DYNSUB at cold startup conditions.

Due to the significantly higher axial resolution of the DYNSUB results, the effects of the large axial reflectors are noticeable. Especially at the bottom of the active core but also at its top a slight increase of the neutron flux towards the boundaries of the core can be observed (see Figure 43). This increase corresponds to the built-up of thermal neutron flux in the axial reflectors, which contain large quantities of water. Generally, an acceptable agreement in terms of axial power profiles between SSS2 and DYNSUB is observed.

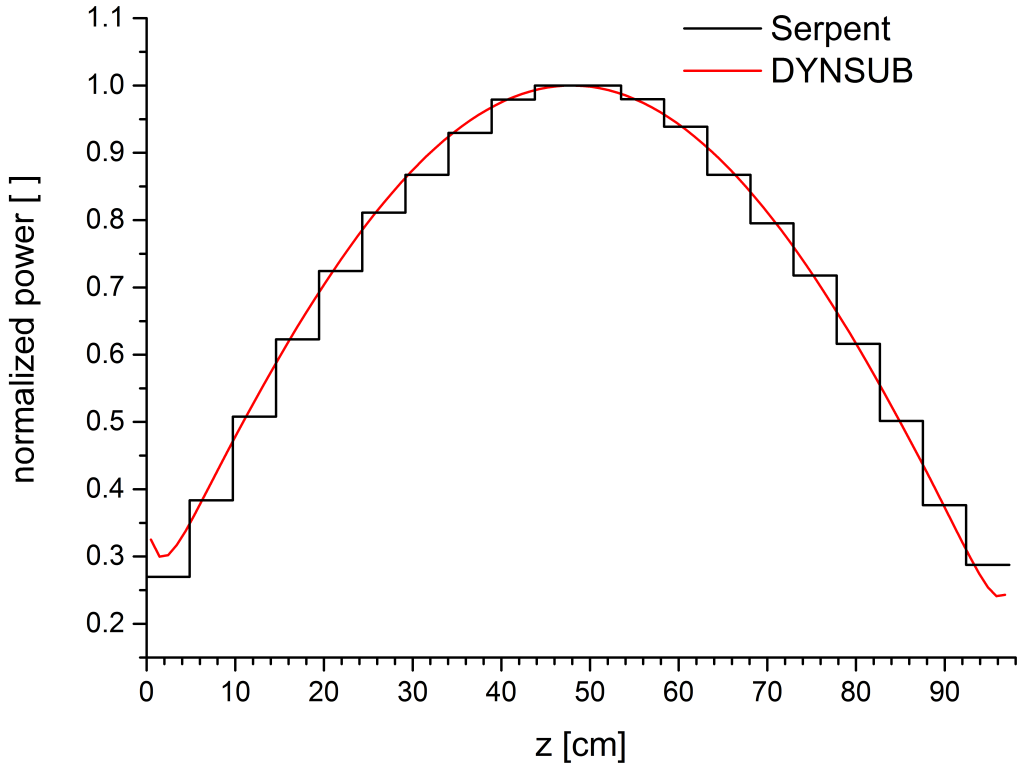

Figure 43: Comparison of SPERT III cold startup normalized axial power profiles as computed by SSS2 and DYNSUB as a function of axial height z

6.2.2 Operating power

While the cold startup steady-state is essentially a neutronics problem, the assessment of the Serpent 2-DYNSUB code sequence is continued by including thermal hydraulic feedback, i.e. analyzing a steady-state at operating power.

SSS2/SCF reference solution of the all rods out state converged after five coupled iterations. The eigenvalue determined with the Monte Carlo neutron transport based tool is 1.04041(0.00001). DYNSUB's value of 1.041319 closely matches the high order prediction by only overestimating core multiplication by 90.9 pcm.

	A	B	C	D	E	F	G	H
1		-5.91	0.23	0.45	0.68	0.56	-5.85	
2	-5.79	1.60	0.81	0.50	2.25	0.54	1.59	-5.95
3	0.63	0.64	0.70	-1.50	-1.46	0.69	0.76	0.25
4	0.67	2.28	-1.46	3.48	3.47	-1.52	0.46	0.39
5	0.42	0.43	-1.47	3.49	3.51	-1.49	2.31	0.73
6	0.25	0.76	0.72	-1.42	-1.49	0.69	0.65	0.58
7	-5.93	1.58	0.67	2.28	0.47	0.79	1.60	-5.82
8		-5.85	0.66	0.74	0.42	0.24	-5.95	

Figure 44: Relative spatial differences in SPERT III assembly powers in percent between SSS2 and DYNSUB under operating power conditions

Because of enabling thermal-hydraulic feedback the differences in eigenvalue decrease. But the maximal difference in fuel assembly power is increased to almost 6 % in the corner assemblies at the core periphery, as shown in Figure 44. The assembly powers computed with SSS2/SCF are higher than DYNSUB results in almost all fuel assemblies except for the corner fuel assemblies at the core periphery and eight fuel assemblies surrounding the central 4x4 fuel. In the corner fuel assemblies DYNSUB strongly misjudges the neutron leakage from the system. It becomes apparent comparing neutron currents over fuel reflector interface predicted by both tools. A special set of corner fuel assembly and corner reflector cross section sets can in theory solve the observed issue. However, none of the spectral geometries tested to produce such cross section sets led to an improved DYNSUB solution in practice.

Like for the cold startup, the axial power profile evaluated using DYNSUB is slightly more bottom peaked than the one determined with SSS2/SCF as Figure 45 depicts. Again, the effects of the axial reflectors are clearly visible in the DYNSUB profile, especially at the bottom of the active core. The axial dependence of the radially averaged fuel Doppler temperatures computed with both reactor simulators generally follows the same gross trends as the axial power profiles except that DYNSUB's predictions are slightly higher than SSS2/SCF's (cp. Figure 90 in Appendix K). Even though DYNSUB underestimates the power produced in most of the other colder fuel assemblies, the lower Doppler temperature predictions in these cannot counteract the large contribution from the eight fuel assemblies near the core center to the radial Doppler temperature average.

The radially averaged heat up of the primary coolant as evaluated by SSS2/SCF and DYNSUB was found to be in very good agreement within in convergence limits of the Monte Carlo thermal-hydraulics reference (see Figure 91 in Appendix K).

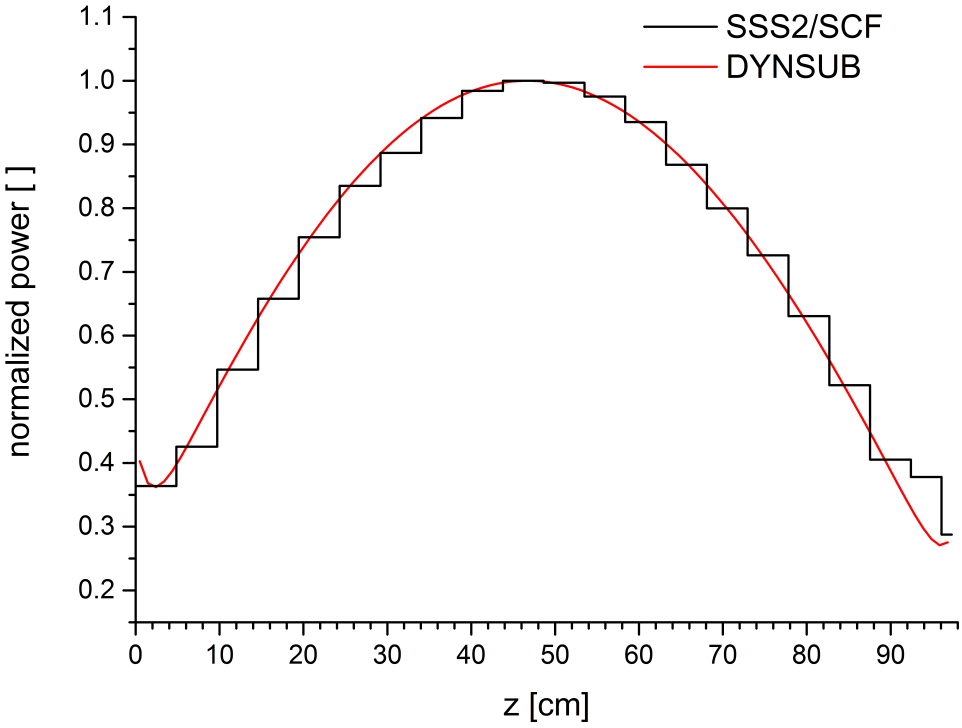

Figure 45: Comparison of SPERT III operating power normalized axial power profiles as computed by SSS2/SCF and DYNSUB as a function of axial height z

6.2.3 Summary of stationary SPERT III E-core calculations

Considering that DYNSUB's solutions are obtained with a 2G nodal diffusion neutronics model, the observed agreement with the Monte Carlo neutron transport based reference computations for cold startup and operating power conditions is satisfactory indicating that the Serpent 2-DYNSUB code sequence has been set up correctly for stationary problems. More importantly the comparison for the latter conditions proves that Serpent 2 newly introduced automatic branching capability for calculating multi-dimensional few-group cross section tables functions properly. The operating power steady-state simulation can be viewed as the first successfully completed solution verification case for the cross section generation methodology of Serpent 2 as a whole at hot full power conditions.

6.3 Simulation of selected SPERT III E-core reactivity-initiated accident tests

The transients studied in the SPERT III E-core experimental series belong to the class of reactivity-initiated accidents (RIAs). They were realized as rod ejection events. In order to be able to insert a defined positive reactivity into the core, all control rods are withdrawn to a position corresponding to the desired reactivity insertion. For achieving a steady reactor state, this excess reactivity is compensated by inserting the poison section of the TR into the lower part of the active core. In the experiments, the transient is initiated by accelerating the TR from its initial position out of the core, thus, releasing the predefined positive reactivity and leaving the reactor in a super-critical state. This reactivity insertion leads to a self-limiting power excursion, whose shape depends mainly on the amount of inserted reactivity and the steady-state operating conditions of the E-core before the transient.

The amount of inserted reactivity is measured in the unit of dollars ($). One dollar corresponds to the effective delayed neutron fraction of the nuclear reactor studied. Delayed neutrons as opposed to prompt neutrons are not released immediately by the fission event itself but by the decay of exited fission products and their daughter nuclides called precursors. For example, the halflife of precursors produced in the fission of U-235 can be as high as 56 s. Current reactors are designed such that the delayed neutrons are required to achieve a critical state. Thus, the speed with which a small perturbation in the self-sustaining chain reaction is propagated is limited by the time it takes for the delayed neutrons of a generation to appear in the system. Without delayed neutrons it would be technologically impossible to control a fission chain reaction in a manner necessary to safely operate a nuclear reactor.

If the reactivity is inserted in the experiment is below 1 $, like in steady-state reactor, the time it takes to emit delayed neutrons dominates the time constant of observed power excursion. The reactor period, i.e. the time the reactor power needs to increase by a factor of the Euler constant, is in the order of several hundred milliseconds for an LWR as thermal system. The reactor is said to be delayed super-critical. If the inserted reactivity amounts to exactly 1 $, the reactor is in prompt super-critical state. Influence of the delayed neutrons on the reactor period has diminished as they are no longer needed to sustain a chain reaction. Now, the time neutrons require to thermalize is more important and the period in a LWR is in the order of 10s of milliseconds. For any higher positive reactivity insertion, the reactor becomes super-prompt critical. The reactor period declines even further. In a LWR, it is typically 10 ms or less.

The initial power rise in a super-critical LWR reactor core is quickly counteracted by rising fuel and coolant temperatures introducing negative reactivity. Due to the Doppler effect, the neutron absorption in the fuel greatly increases non-linearly with temperature. The higher coolant

temperatures correspond to lower densities, which in turn mean worse neutron moderation. Of both effects, the Doppler feedback is the primary mechanism to stop the power excursion, as it is higher in magnitude and appears earlier – the moderator feedback can only occur once a significant amount of heat has been conducted to the fuel rod surfaces and from there transferred to the primary coolant. Hence, if the reactor has been in a zero-power state before the transient, it takes significantly longer for the system to heat up and negative feedback to kick in than for transients starting from a hot (full) power state. This is reflected in the ratio of the maximal power during the excursion and the initial one. It is higher the colder the core initially and the higher the reactivity insertion was. In terms of the timing of the power peak, it can be said that it is reached earlier the hotter the core initially and the higher inserted reactivity was. Moreover, for one given set of reactor steady-state operating conditions before the transient, the width of the power peak decreases with increasing inserted reactivity since the latter corresponds to a faster, fiercer excursion, which springs a strong negative feedback into action. The evolution of reactor power in time with strong Doppler and moderator feedback approximately takes the shape of a bell curve – an initial exponential power rise followed by an exponential decline.

A summary of the DYNSUB transient results for experiments done with cold startup initial conditions compared to documented measured data is presented in Table 40. Values obtained with DYNSUB written in italic are not within one standard deviation of the experimentally determined ones. All other computed data is.

Table 40: Comparison of simulated and experimental data for the selected cold startup RIA tests (McCardell, et al., 1969), DYNSUB results written in italic are not within on standard deviation of experimental data

Test No.		Initial Reactivity [$]	Max. power [MW]	Peak time [s]	Energy release [MJ]	Reactivity compen-sation [$]	Reactor period [ms]
18	Exp.	0.90(0.04)	4.3(0.6)	5.3(0.1)	6.7(1.1)	0.23(0.03)	351(7)
	DYNSUB	0.879	***5.08***	5.36	7.8	0.226	***360.2***
49	Exp.	1.00(0.04)	11.0(2.0)	0.97(0.04)	2.1(0.4)	0.08(0.01)	68.4(1.4)
	DYNSUB	1.02	***13.09***	1.003	***2.56***	0.0835	***74.6***
43	Exp.	1.21(0.05)	280(42)	0.230(0.006)	6.0(1.0)	0.22(0.02)	10.0(0.2)
	DYNSUB	1.20	284.48	0.231	6.65	0.228	***11.4***

For all RIAs starting from cold startup conditions the reactor periods computed based on DYNSUB simulations are larger than the experimentally obtained ones but they are in the same

order of magnitude. Also cold startup reactor periods determined with CASMO5/SIMULATE-3K did not agree with the measured data within one standard deviation for many RIA tests (Grandi & Moberg, 2012). Furthermore, if one considers that for cold startup RIA tests with the same initial reactivity insertion, i.e. test 19 and 20, the measured reactor period deviated by 9 ms even though the quoted uncertainty of the measurement is less than 1 ms in both cases (McCardell, et al., 1969), DYNSUB's performance is considered to be acceptable.

The evolution of SPERT III reactor power and reactivity for the delayed super-critical test 18 are depicted in Figure 46. DYNSUB's reactivity prediction follows the experimentally determined curve closely. After an initial very good agreement between the simulated reactor core power and the measured one (up to 3.5 s into the transient), the computed values start to deviate once thermal-hydraulic feedback starts to play a significant role. While the overall shape of the delayed super-critical power peak is similar to the experiment the maximal power computed with DYNSUB is 5.08 MW instead of 4.3(0.6) MW measured. While the original experiments were carried without any primary coolant flow (see Table 51 in Appendix K), DYNSUB cannot simulate such an experimental condition due to a limitation originating from SUBCHANFLOW. The coolant flow has been set to a small value, i.e. 1 kg/s.

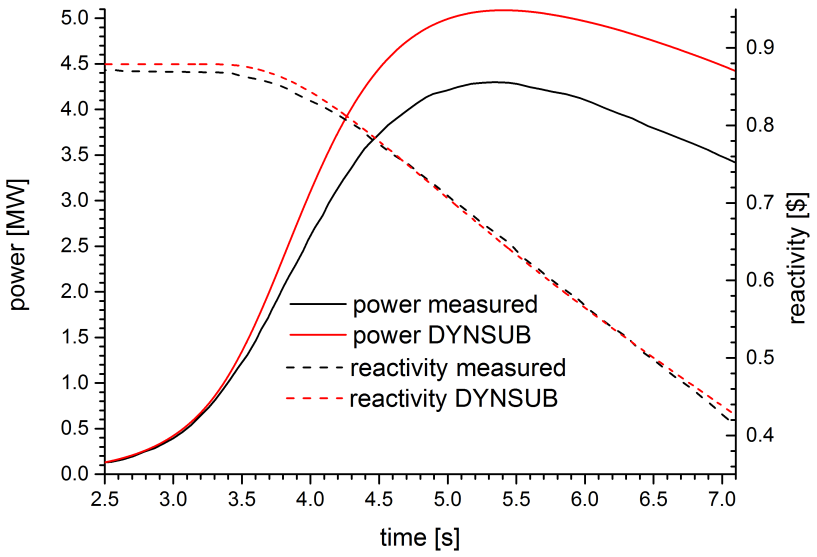

Figure 46: DYNSUB core power and reactivity evolution for cold startup test 18 compared with experimental data (McCardell, et al., 1969)

The addition of some forced convection improves the cooling of the SPERT III E-core in the DYNSUB model reflected in the overestimation of peak power. Due to the design of the SPERT RPV (see Appendix K) natural circulation cannot establish itself and plays no role in the cold startup experiments.

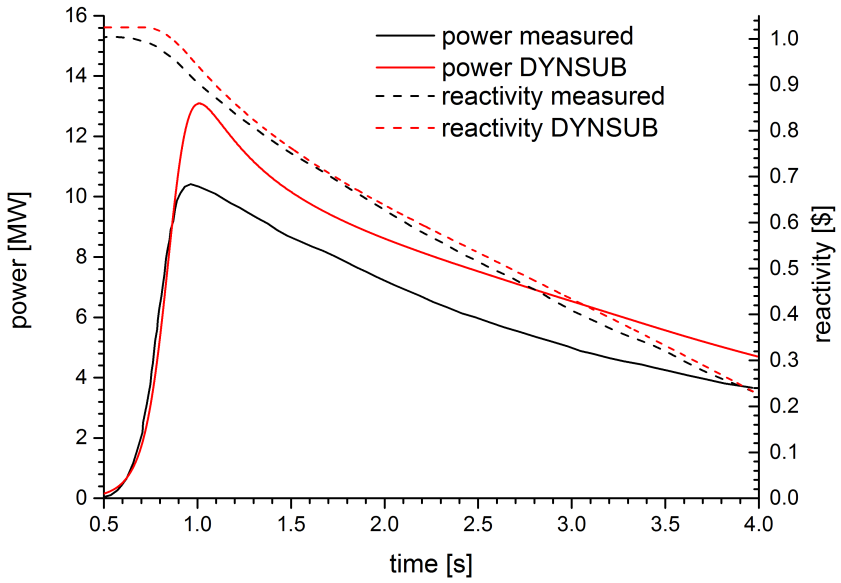

Figure 47: DYNSUB core power and reactivity evolution for cold startup test 49 compared with experimental data (McCardell, et al., 1969)

Figure 47 shows the temporal DYNSUB core power and reactivity evolution for the prompt super-critical cold startup test 49. As expected, the power excursion happens significantly faster and a peak is reached after 1.0 s. As for test 18, the measured and computed core reactivity match well. DYNSUB once more overestimates the height of the power peak. Like for the delayed super-critical case, this is partially due to the small coolant flow modeled in DYNSUB.

The last cold startup REA experiment studied with DYNSUB is a super-prompt critical power excursion characterized by a reactor period as low as 10.0 ms in its initial phase. The core power and reactivity evaluated using DYNSUB are also compared with measurements in Figure 48. The DYNSUB model captures the power peak well both in terms of shape and height. Differences between calculated and measured reactivities in the later phase of the transient are mostly due to the fact that DYNSUB computed dynamic reactivities employing adjoint fluxes, while the experimental values were inferred from reactor power and period measurements using point kinetics.

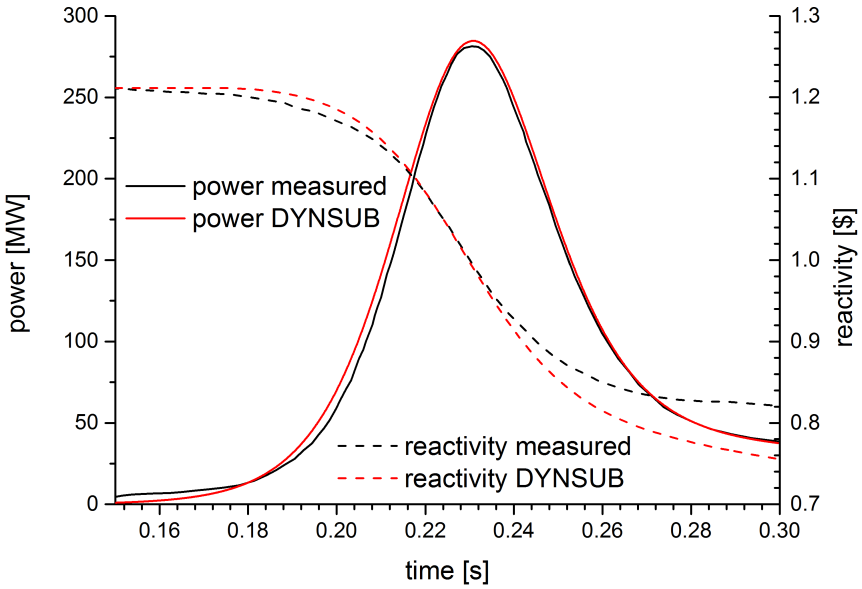

Figure 48: DYNSUB core power and reactivity results for cold startup case 43 compared with experimental data (McCardell, et al., 1969)

At hot standby conditions, all DYNSUB simulations predict the measured data within one standard deviation as listed in Table 41. As seen in Figure 92 through Figure 94 in Appendix K, the DYNSUB transient computations are generally in good agreement with the measured evolution of reactor power and reactivity in time. For two super-prompt critical RIAs, test 81 and 82, the power level after the peak determined with DYNSUB is higher than measurements. Sensitivity studies performed identified the fuel-clad gap model to have the largest impact on the simulation results in this phase of the transients. Of the models available in SUBCHANFLOW the Transuranus one did best. However, there is room for further improvement.

Table 41: Comparison of simulated and experimental data for the selected hot standby RIA tests (McCardell, et al., 1969)

Test No.		Initial Reactivity [$]	Max. power [MW]	Peak time [s]	Energy release [MJ]	Reactivity compensation [$]
79	Exp.	0.86(0.03)	13.0(1.0)	0.68(0.08)	6.7(0.9)	0.09
	DYNSUB	0.856	13.34	0.751	7.34	0.092
81	Exp.	1.17(0.04)	330(30)	0.135(0.003)	7.8(1.0)	0.180
	DYNSUB	1.16	324.90	0.138	8.20	0.181
82	Exp.	1.29(0.04)	880(90)	0.118(0.002)	15.0(2.0)	0.30
	DYNSUB	1.293	871.50	0.120	13.70	0.306

For test 81 and 82, the reactivity insertion modeled with DYNSUB in the early phase of the transient differs from the measured behavior. However, it has to be kept in mind that the experimental reactivities were computed from reactor power measurements using point kinetics. Due to the fact that reactivity compensation already occurs early during the on-going reactivity insertion for these RIAs no point kinetics reactor period could be obtained experimentally. Hence, the point kinetic based reactivity evaluation had to use *computed* concentrations of the delayed neutron precursors as initial conditions.

For both RIAs starting from operating power conditions analyzed with DYNSUB, the reactor simulator only failed to determine the energy released within one standard deviation in test 85 (see Table 42). For completeness, the change of SPERT III E-core power and reactivity as predicted by DYNSUB is compared to measured curves in Figure 95 and Figure 96 in Appendix K.

Table 42: Comparison of simulated and experimental data for the selected operating power RIA tests (McCardell, et al., 1969)

Test No.		Initial Reactivity [$]	Max. power [MW]	Peak time [s]	Energy release [MJ]	Reactivity compensation [$]
85	Exp.	0.87(0.04)	130(10)	0.155(0.005)	8.7(1.1)	0.04
	DYNSUB	0.868	121.5	0.153	***7.5***	0.039
86	Exp.	1.17(0.05)	610(60)	0.110(0.005)	17.0(2.2)	0.22
	DYNSUB	1.17	607.2	0.107	16.17	0.22

6.4 Conclusion and next steps

The objective has been to validate the Serpent 2-DYNSUB code utilizing the SPERT III E-core experiment series. The Serpent 2 and SSS2/SCF numerical reference models as well as the coupled DYNSUB and Serpent 2 cross section generation models have been developed using data from the original SPERT experimental reports (Dugone, 1965; McCardell, et al., 1969). The DYNSUB stationary simulations reproduce the Monte Carlo neutron transport reference solutions obtained with Serpent 2 (cold startup conditions) and SSS2/SCF (operating power conditions) with acceptable accuracy. With the latter MC/TH reference, the cross section calculation methodology of Serpent 2 has been verified for the first time for operating conditions other than HZP.

The nodal diffusion DYNSUB simulations of eight selected experiments are generally in good agreement with measurements. As the selected experiments cover much of the possible transient (delayed super-critical, prompt super-critical and super-prompt critical excursion) and initial conditions (cold and hot as well as zero, little and full power reactor states) one expects in commercial PWRs, the obtained results give confidence that DYNSUB employing nodal diffusion is suitable to model REAs and other RIAs in PWRs. Furthermore, the successful application of the Serpent 2-DYNSUB code sequence to model the SPERT III E-core RIA tests underlines that the Serpent 2 methodology to determine homogenized few-group constants not only works fine under hot full power conditions but also for RIA transients starting from various initial conditions. The study also is a validation of Serpent 2's methods to evaluate neutron kinetic parameters for reactor simulators like DYNSUB.

In the future, the remainder of the 58 SPERT III E-core RIA tests is to be analyzed with DYNSUB to complete the Serpent 2-DYNSUB validation base. Afterwards, validation efforts are to be repeated for assembly-homogenized DYNSUB calculations using the simplified transport solver and pin-homogenized DYNSUB simulations employing both the diffusion and simplified transport approximations. For the validation of pin-homogenized solution, a SSS2/SCF reference model with a sub-channel TH model has to be developed. Since DYNSUB offers multi-group solutions for any of its neutronics solvers, work on optimizing the few group energy structure of the cross sections for the SPERT III E-core should be carried out. In the framework of completing the full sets of REA simulations, efforts to obtain more detailed information on the properties of the materials in the SPERT III E-core should be undertaken since an additional potential to further improve DYNSUB simulations exists. Finally, to complete the VVUQ process (see section 1.4) of the Serpent 2-DYNSUB code sequence for REAs a formal sensitivity and uncertainty analysis of the DYNSUB results is to be done. This should be based on the uncertainty quantification methods established in the framework of the OECD UAM benchmark (Ivanov, et al., 2007b).

While the SPERT III E-core experiments series are ideal to validate the Serpent 2-DYNSUB tool chain for REAs / RIAs, the validation base of the code sequence has to be extended to cover all major design basis accident scenarios and in-core fuel management in the near term.

7 Demonstration of pin-by-pin simulations for industry-like problems using DYNSUB and Serpent 2/SUBCHANFLOW

The ultimate goal of this work is to show that both the pin-homogenized reactor simulator DYNSUB and the pin-resolved reactor simulator SSS2/SCF may be employed to study realistic, engineering-sized and industry-like cases. To this end, both tools are utilized to model the OECD/NEA and U.S. NRC PWR MOX/UO_2 core transient benchmark (Kozlowski & Downar, 2003). This benchmark was selected as it includes nuclide compositions of all fuel types loaded in the reactor allowing for producing pin-by-pin cross section tables for DYNSUB and performing Monte Carlo neutron transport calculations. DYNSUB and SSS2/SCF are used to simulate the HFP steady-state of the full PWR core first introduced in subsection 5.2.1. The pin-homogenized reactor simulator DYNSUB is afterwards also employed to model the rod ejection accident from HZP conditions, which is also described in the subsection referenced beforehand.

The review of the state-of-the-art pin-homogenized reactor simulators in section 4.1 revealed that the other pin-homogenized coupled codes SCOPE2 and COBAYA3/COBRA-TF had both been used to describe full PWR core steady-states with fuel pin/sub-channel resolution. However, for neither tool coupled full core evaluations of operational occurrences or design basis accident scenarios are reported in literature. Thus, the DYNSUB simulation of the HZP REA is the first safety relevant transient scenario for a full PWR core being calculated using pin-by-pin neutron transport coupled to a sub-channel TH model.

Concerning Monte Carlo neutron transport based pin-resolved reactor simulators, the only simulation of a quarter PWR core has been recently published by Ivanov (Ivanov, et al., 2014; Ivanov, et al., 2015). Ivanov's coupled MC/TH tool utilizes the pseudo material mixing approach to treat the temperature dependence of nuclear data. The SSS2/SCF calculation presented hereafter is a proof of principle for on-the-fly cross section treatment schemes such as TMS. No tool using such a method has been employed to study a full reactor core under hot full power conditions with a pin-by-pin/sub-channel resolution (see section 2.1).

7.1 OECD/NEA and U.S. NRC PWR MOX/UO_2 core transient benchmark

In subsection 5.2.1, the HFP steady-state and HZP REA scenarios of the OECD/NEA and U.S. NRC PWR MOX/UO_2 core transient benchmark are described in detail. In the following, both the SSS2/SCF and the DYNSUB models are introduced. Thereafter, in subsection 7.1.2 the steady-state simulations are compared to each other and benchmark solutions. DYNSUB's

capability to simulate the ejection of a control assembly is then assessed in the following subsection. Before finally evaluating the pin-homogenized and pin-resolved reactor simulator, the numerical performance of both coupled codes is analyzed based on the HFP static scenario of the OECD/NEA and U.S. NRC PWR MOX/UO_2 core transient benchmark.

7.1.1 Description of SSS2/SCF and DYNSUB models

To be able to perform the critical boron search that is part of the HFP steady-state case, SSS2/SCF was extended. The critical boron search is realized as a loop over coupled Monte Carlo neutron transport and thermal-hydraulics simulations. The relation to estimate the new soluble poison concentration $c_{b,i}$ in iteration i is given in equation (25). Serpent 2 adjusts the boron concentration in materials flagged as coolant in the internal coupling to SUBCHANFLOW. Thereafter, it re-computes all macroscopic and majorant cross sections required by the transport simulation including the thermal-hydraulic feedback. For the first iteration, a guess of the slope dc_b/dk_{eff} is required. It has to be given as an input by the user. In later iterations, the slope is evaluated based on previous simulation results.

$$c_{b,i} = c_{b,i-1} - (k_{\text{eff}} - 1)\frac{dc_b}{dk_{\text{eff}}}. \tag{25}$$

The stopping criterion for the critical boron search is provided by equation (26). This criterion considers that the SSS2/SCF solution is subject to statistical uncertainties, which depend on the total number of neutron histories simulated as $\sigma_{k_{\text{eff}}}$ is the standard deviation of the tallied eigenvalue.

$$|k_{\text{eff}} - 1| < \sigma_{k_{\text{eff}}}. \tag{26}$$

Serpent 2/SUBCHANFLOW is employed to model the active core of the PWR considered with two different spatial resolutions in the thermal-hydraulics model. One SSS2/SCF model uses channel level (CH), the other sub-channel level (SBCH) thermal-hydraulics. The purpose of having two Serpent 2/SUBCHANFLOW models with different resolution in the thermal-hydraulics domain is to evaluate the influence of the spatial resolution in that domain on steady-state simulation results.

The channel thermal-hydraulics model includes one channel per fuel assembly, i.e. 193 parallel laterally coupled channels in total. In axial direction, each channel is subdivided in 20 nodes. The fuel rods of each fuel assembly are represented by an average rod. For solving the heat

conduction problem, this rod is radially discretized using 12 nodes. 10 of these nodes describe the fuel pellet and 2 nodes are left for gap and cladding. The thermo-physical properties of fuel and cladding material as well as the gap heat transfer coefficient are taken from the benchmark specifications (Kozlowski & Downar, 2003).

The sub-channel thermal-hydraulics model consists of 62,532 sub-channels divided into 35 axial mesh layers. All 55,777 fuel rods and guide tubes of the PWR core are modeled explicitly. Radially, the discretization of each fuel rod is identical to the one of the average rod in the channel resolution model. The resulting sub-channel thermal-hydraulic model consists of 2.2 million cells in the fluid domain and 23.4 million in the solid domain.

ENDF/B VII.0 evaluated nuclear data is utilized. For Serpent 2's stochastic mixing fall back, a 5 K spacing of thermal scattering data sets was chosen. The Wielandt shift is used to compute a well-converged fission source the SSS2/SCF simulations can start from. Moreover, a power distribution produced by DYNSUB is used as initial power shape in SUBCHANFLOW. The local Doppler temperature and moderator density convergence targets are set to 0.5 %. The convergence criterion for the effective multiplication factor is 5 pcm.

Per coupled iteration step, Serpent 2 modeled $4 \cdot 10^6$ neutrons per cycle. 650 inactive cycles are employed followed by 2500 active ones. The number of inactive cycles is chosen conservatively to ensure a converged fission source, assessed using the Shannon entropy evaluated on a 5x5 mesh, and sufficient statistics for the UFS method. Furthermore, possible changes in the convergence behavior of the Monte Carlo simulation between different coupled iterations are also taken into account.

Moreover, the author wishes to assess the quality of the coupled SSS2/SCF solutions obtained by analyzing the propagated statistical uncertainties of the coupled data fields, i.e. powers, fuel and moderator temperatures as well as coolant densities. 10 replica runs of both the CH and SBCH models are performed. A replica run refers to rerunning the same simulation with a different seed for random number generator. In this way, the influence of the pseudo-random distribution of the numbers generated by it on the results can be assessed. After the runs have finished, the spread of the results is analyzed using statistical methods to estimate the propagated uncertainties.

The pin-by-pin DYNSUB model utilizes the same SUBCHANFLOW input as the SSS2/SCF SBCH simulation. The PWR core is modeled using 257 radial nodes (193 fuel assemblies and 64 reflectors) each of which is subdivided into 289 neutronics mesh cells corresponding to the pin cells of the 17x17-25 fuel lattice. The active core is described using 70 equidistant axial mesh layers plus an extra four at the top and the bottom of the core to take care of axial reflectors. This is the minimum number of axial mesh layers required for a mesh independent

neutronics solution with the radial resolution at pin cell level. The resulting neutronics mesh contains a total of 5.8 million cells.

For the pin-by-pin DYNSUB model, the radial and axial boundary conditions are set to zero flux. Furthermore, these steady-state coupled convergence criteria are used: $\varepsilon_{\mathrm{keff}} < 10^{-5}$ for the eigenvalue, $\varepsilon_{\mathrm{DT}} < 10^{-4}$ for local Doppler temperature and $\varepsilon_{\mathrm{RM}} < 10^{-4}$ for the local moderator density.

Since the pin-by-pin diffusion benchmark cross section library does not contain any homogenization corrections and DYNSUB's pin-by-pin diffusion solutions have been found to perform poorly without homogenization corrections (see section 4.5), an eight-group library for a simplified transport simulation containing SPH factors is prepared using the lattice code HELIOS. HELIOS is chosen because it was the lattice code to generate the benchmark XS tables and its problem-dependent, self-shielded 47G cross section library was used by the code DeCART to produce the HZP reference solutions of this benchmark. The HELIOS calculations were carried out by the Helmholtz-Zentrum Dresden Rossendorf (HZDR). Their preliminary cross section library was processed into one containing thermal-hydraulic state dependent SPH factors using DYNSUB (refer to subsection 4.5.4 for more details on the method).

For the HZP REA, benchmark participants are asked to study the evolution of the state of the reactor for 1.0 s in total. To do so, DYNSUB employed a fixed time step of 4 ms.

7.1.2 Stationary simulation

A comparison of the critical boron concentration and the core average thermal-hydraulic properties of the HFP state simulated is given in Table 43. The statistical uncertainties quoted on the SSS2/SCF results in this table are based on the 10 replica runs. Since neither the benchmark nor any participant provided a pin-by-pin/sub-channel reference transport solution, the table below only contains SSS2/SCF and DYNSUB results.

Both the low order deterministic DYNSUB as well as Serpent 2/SUBCHANFLOW produce a significantly lower critical boron concentration than the nodal benchmark solutions (see Table 26 in subsection 5.2.2). The corresponding lower core multiplication of the pin-by-pin solutions is in line with the observations made for the 2D HZP case, which was studied to test the Wielandt shift implementation (refer to Table 44). The eigenvalue predicted by Serpent 2 matches that of the reference DeCART solution of the original benchmark very well, however, the differences in assembly powers are larger than between DeCART and MCNP. The DeCART solution used the method of characteristics employing a 47G cross section library produced with HELIOS.

Table 43: Comparison of critical boron concentration and core average thermal-hydraulic properties for the 3D HFP case of the OECD/NEA and U.S. NRC PWR MOX/UO_2 core transient benchmark simulated with pin-by-pin resolution

Code	CBC [ppm]	Average $T_{Doppler}$ [K]	Average T_{mod} [K]	Average ρ_{mod} [kg/m^3]
SSS2/SCF CH	1599(0.23)	824.6(0.006)	582.5(0.005)	702.8(0.010)
SSS2/SCF SBCH	1598(0.21)	824.4(0.005)	582.05(0.005)	703.6(0.011)
DYNSUB 8G SP3	1600	824.3	580.6	705.1

DeCART like Serpent 2 modeled the heterogeneity of each fuel pin cell. The differences can be attributed to energy as well as spatial discretization and cross section evaluation. Deviations between MCNP and Serpent 2 for this benchmark exercise are due to differences in cross sections. MCNP used ENDF/B VI. Employing ENDF/B VI.8 nuclear data Serpent estimates the eigenvalue to be 1.05705(0.00001) and assembly power errors are very close to the values for MCNP.

The core average thermal-hydraulic properties match benchmark contributions well (cp. Table 43 and Table 26 in subsection 5.2.2). Only the core average Doppler is found to be slightly lower than all other benchmark values. The benchmark definition specifies a correlation to compute effective Doppler temperature, heat capacity and thermal conductivity for both fuel and cladding as well as the heat transfer coefficient for the gas gap. As a consequence, differences in calculated Doppler temperatures can be partially attributed to code specific correlations to compute the heat transfer from cladding to coolant. Moreover, the numerical method and radial discretization for solving the heat conduction problem in the fuel rods play a role.

The agreement between the 8G pin-homogenized simplified transport solution of DYNSUB and SSS2/SCF's continuous energy Monte Carlo neutron transport in terms of critical boron concentration is to a degree surprising indicating that low order deterministic methods are capable of accurately describing this PWR core. Furthermore, no significant differences between the Serpent 2/SUBCHANFLOW solutions employing a channel and a subchannel resolution thermal-hydraulics model are noticed.

Table 44: Comparison of eigenvalues and assembly power errors for one 2D case of the OECD/NEA and U.S. NRC PWR MOX/UO_2 core transient benchmark simulated with pin-by-pin resolution, PWE refers to power-weighted error and EWE to error-weighted error (Kozlowski & Downar, 2007)

Code	Eigenvalue	Assembly power PWE	Assembly power EWE
DeCART	1.05852	ref	ref
MCNP	1.05699	0.67	1.26
SSS2	1.05862(0.00001)	1.22	1.68
DYNSUB 8G SP3	1.05888	0.70	1.09

In Figure 49, the axial power profiles produced by Serpent 2/SUBCHANFLOW with both thermal-hydraulics models are compared with the PARCS 2G solution as a typical assembly-homogenized benchmark solution. Moreover, the MCNP5/ATHLET simulation done (Bernnat, et al., 2012) and pin-by-pin DYNSUB one are included. The statistical uncertainty of the SSS2/SCF results is not shown in the plots as it was too small (well below 0.05 % everywhere). It can be observed that the power profiles determined by coupled Monte Carlo thermal-hydraulics tools agree perfectly. The PARCS profile is slightly shifted to the upper part of the core. DYNSUB produces a profile very close to those of the Monte Carlo neutron transport based tools.

The corresponding radially averaged effective Doppler temperature profiles are shown in Figure 50. They exhibit no such perfect match. All solutions agree reasonably well, but the following general observations can be made: Firstly, the MCNP5/ATHLET effective Doppler does not follow the shape of its axial power profile. The reason for this behavior could not be identified. Secondly, the temperature profiles computed by PARCS and SSS2/SCF are very similar in shape but the maximal effective Doppler temperature seen by Serpent 2 is 944.2 K for the subchannel and 941.0 K for channel TH model as opposed to 954.9 K for PARCS. This is a significant difference as SSS2/SCF Doppler temperatures exhibit a maximum statistical uncertainty of 0.1 K.

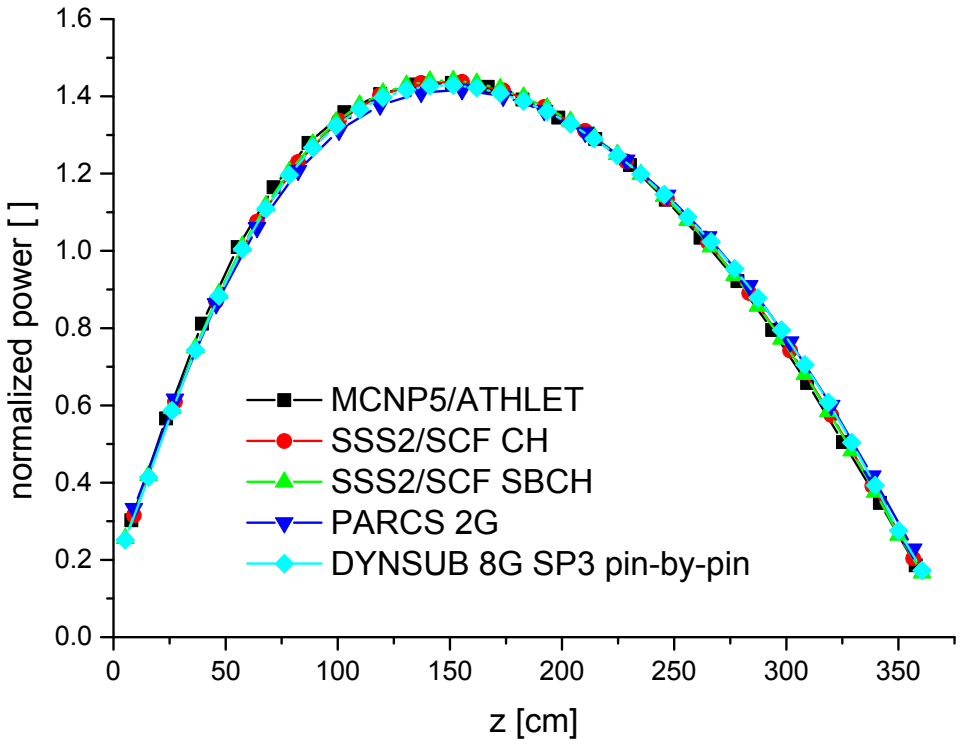

Figure 49: Comparison of normalized axial power profiles as computed with DYNSUB and SSS2/SCF at pin level resolution as well as selected other benchmark solutions for the 3D HFP case of the OECD/NEA and U.S. NRC PWR MOX/UO_2 core transient benchmark (Kozlowski & Downar, 2007; Bernnat, et al., 2012)

On top of the modeling differences pointed out during the discussion of differences in core average Doppler temperatures, PARCS employed the thermal conductivity of uranium oxide also for mixed uranium plutonium oxides. Its thermal-hydraulics model unlike SUBCHANFLOW considered no cross flows between fuel assemblies. The DYNSUB pin-by-pin solution follows the SSS2/SCF ones closely. The core wide averages of the effective Doppler temperature listed in Table 43 and Table 26 in subsection 5.2.2 show the same trend.

Here, DYNSUB is also used with a nodal/channel thermal-hydraulic resolution to study the second exercise of the OECD/NEA and U.S. NRC PWR MOX/UO_2 core transient benchmark (see section 5.2). The core average Doppler temperatures and axial Doppler temperature profiles are found to be slightly lower than other benchmark solutions, but comparable to the values and behavior presented here for SSS2/SCF and DYNSUB pin-by-pin/subchannel.

It may be concluded that the observed differences are mostly due to the different thermal-hydraulic codes used, since all simulations using SUBCHANFLOW agree very well regardless of spatial resolution and transport approximation in their neutronics models.

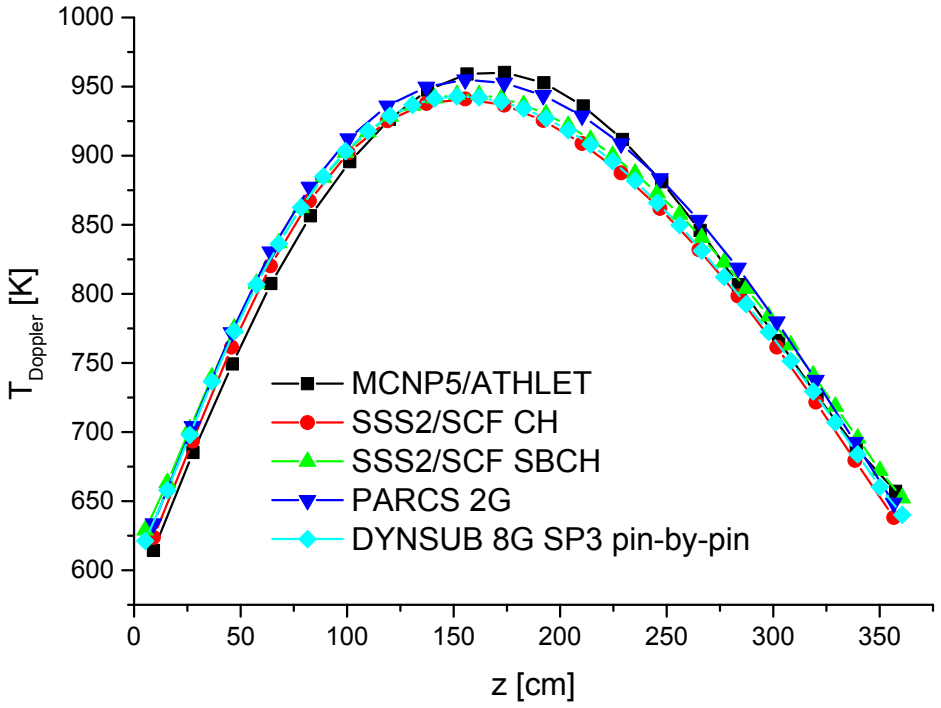

Figure 50: Comparison of core averaged axial Doppler temperatures as computed with DYNSUB and SSS2/SCF at pin level resolution as well as selected other benchmark solutions for the 3D HFP case of the OECD/NEA and U.S. NRC PWR MOX/UO_2 core transient benchmark (Kozlowski & Downar, 2007; Bernnat, et al., 2012)

As a final step in this analysis of the second exercise, the pin-by-pin/subchannel solutions fields determined with Serpent 2/SUBCHANFLOW and DYNSUB 8G SP3 are to be benchmarked. The pin power distribution obtained with the SSS2/SCF SBCH is depicted in Figure 51. The maximal local pin power difference between DYNSUB and Monte Carlo neutron transport based solution is 14.94 % at the core periphery in assembly G2 at 162 cm above the bottom of the active core. For this particular low power pin segment, the estimated statistical uncertainty is 3.9 %. At the core mid plane, the maximal local deviation in pin power is 7.57 %. Here, the statistical uncertainty is 2.18 % only.

The overall distribution of local pin power differences at the core mid plane is shown in Figure 52. For most of the axial layer the pin powers predicted by DYNSUB 8G SP3 fall within 2.5 % of the Serpent 2/SUBCHANFLOW solution. DYNSUB computes pin powers to be higher in the second and third batch assemblies in the central region of the core. SSS2/SCF sees higher pin powers in the ring of first batch UOX fuel assemblies near the outer boundary of the core.

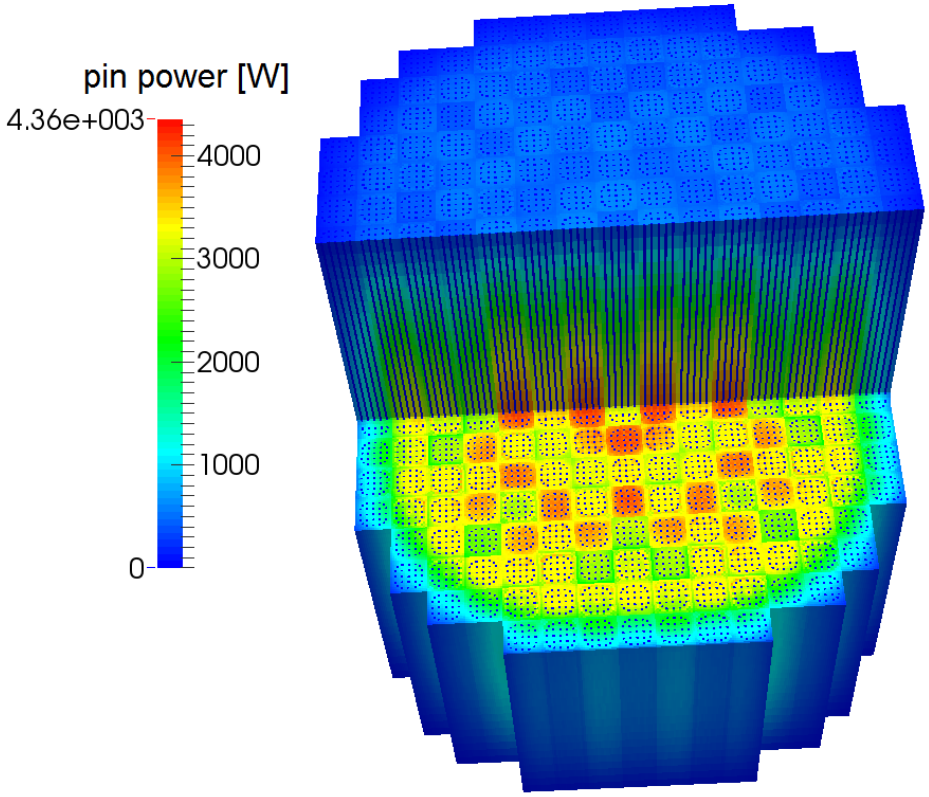

Figure 51: Pin power distribution in Watts as predicted by SSS2/SCF SBCH for the 3D HFP case of the OECD/NEA and U.S. NRC PWR MOX/UO_2 core transient benchmark

Taking a closer look at the 2D projection in Figure 52 reveals the tilt of the Monte Carlo power tally, which is of the order of 3.0 % between fuel pins in symmetry positions. This is larger than the estimated statistical uncertainty between 0.73 and 1.52 per cent in the affected regions.

After the pin powers also the thermal-hydraulic fields are compared. The maximal local pin power difference translates into a maximal change in local effective Doppler temperature by 3.97 %. In the core mid plane, this maximal differences is slightly lower, i.e. 3.25 %. It is observed that the local moderator temperature is quite insensitive to local power and Doppler temperature deviations. The maximal relative difference between DYNSUB and SSS2/SCF is as low as 0.503 %. In the core mid plane it drops to 0.29 %.

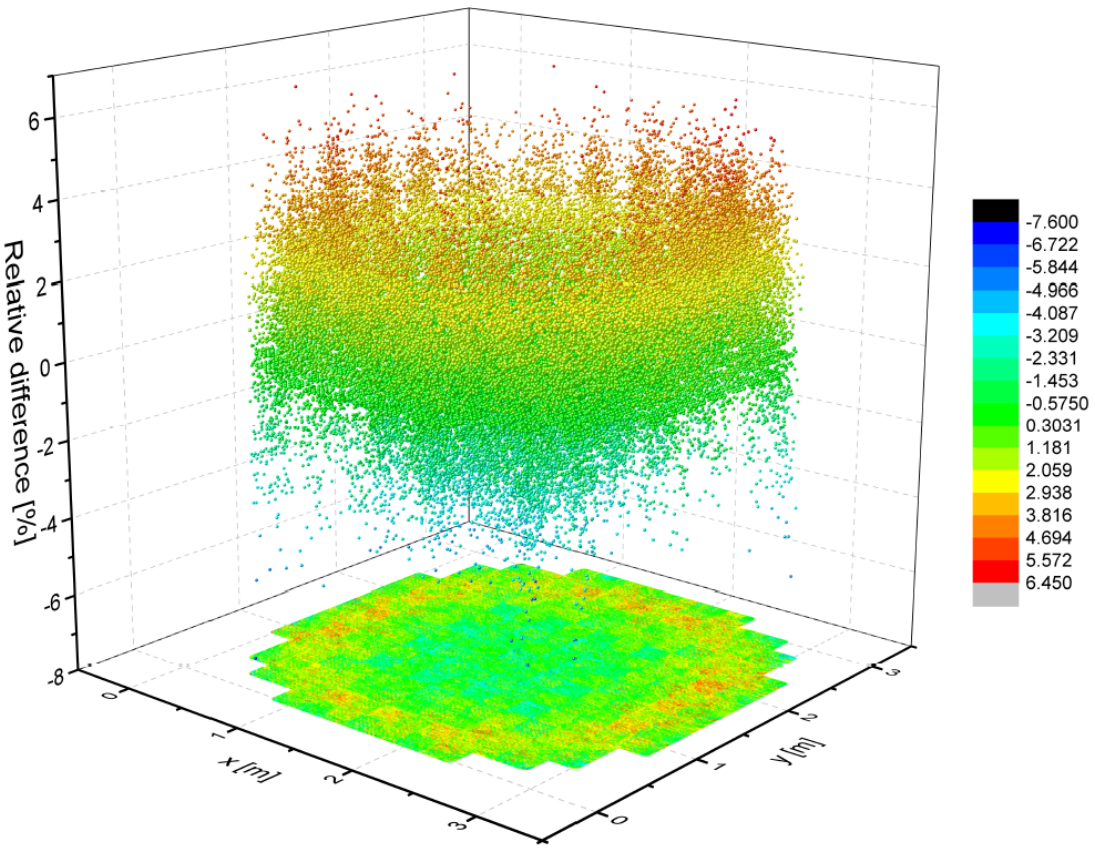

Figure 52: Relative differences in pin powers in percent between SSS2/SCF SBCH and DYNSUB at the core mid plane for the 3D HFP case of the OECD/NEA and U.S. NRC PWR MOX/UO_2 core transient benchmark simulated

7.1.3 HZP REA transient simulation

Before presenting the DYNSUB pin-by-pin simulation results for the HZP REA scenario in detail, the coupled codes performance is compared to the DeCART reference solution for the stationary 3D hot zero power case as the latter is the starting point of the transient to be studied. The critical boron concentration and assembly power errors are listed in Table 45.

Table 45: Comparison of critical boron concentration and assembly power errors for the 3D HZP case of the OECD/NEA and U.S. NRC PWR MOX/UO_2 core transient benchmark simulated with DYNSUB using pin-by-pin resolution (Kozlowski & Downar, 2007)

Code	CBC [ppm]	Assembly power PWE	Assembly power EWE
DeCART	1265	ref	ref
DYNSUB 8G SP3	1274	1.31	1.96

The critical boron concentration determined with a pin-by-pin DYNSUB model is very close to the DeCART reference solution. This fact gives confidence in the simplified transport cross section library developed for DYNSUB and, hence, in the hot full power steady-state simulation presented in the previous subsection.

The assembly power PWE for both codes is similar to that of the nodal solutions. DYNSUB's error-weighted error, however, is significantly lower indicating smaller maximal errors or a smaller error spread. DYNSUB's pin-by-pin simulation does significantly better than the nodal, assembly-homogenized DYNSUB solutions (see subsection 5.2.2) in capturing the DeCART axial power distribution within 0.3 % away from the bottom and top reflector. Also the maximal error to the axial reflectors is limited to 3.5%.

Like for the assembly-homogenized simulations in subsection 5.2.2, the 3D rod worth of the D-bank control assembly to be ejected is determined for DYNSUB pin-by-pin. DYNSUB computes a rod worth of only 640 pcm which is significantly less than the 681 pcm for nodal diffusion and 670 pcm for nodal simplified transport calculations presented in subsection 5.2.2. Unfortunately, no DeCART reference solution for this rod worth exists to help evaluating this result. The author suspects DYNSUB's pin-by-pin solution to underestimate the rod worth. An indicator is that the nodal diffusion solution has a relative power error for the assembly with the control rod to be ejected of -0.2 % compared to the DeCART reference. The pin-by-pin simulation, however, overestimates the power produced in the rodded assembly by 0.63 %. As a result of the above evaluation, the super-prompt critical power peak for the pin-by-pin calculation should appear later and be lower than the peaks predicted by the nodal simulations.

The power evolution of the Westinghouse PWR computed with DYNSUB pin-by-pin and by selected benchmark participants is shown in Figure 53. Due to the 6 % lower rod worth predicted by DYNSUB pin-by-pin as opposed to the nodal diffusion solution, the peak power is observed as late as 0.48 s and as low as 71.8 % nominal power. The integral of this peak over the entire simulation time is only 638 MJ as opposed to 1.059 GJ of nodal diffusion and 973 MJ of nodal simplified transport DYNSUB. The shape of the axially cumulated power density distribution at the time of the power peak is depicted in Figure 54. The lower power assembly in the center of the power peak is the one from which the D-bank control assembly is ejected. Due to its relatively high burn-up of 37.5 GWd/tU the local power peak is shifted to the four adjacent fresh UOX fuel assemblies, which have only been burned up to 0.15 GWd/tU. As the shutdown banks are withdrawn from the core, the power peak spreads along the corridors of higher reactivity they left. This leads to the mirrored L-shape of the peak.

One way of quantifying the severity of the local power peaking in the DYNSUB pin-by-pin simulation is to compute the point-pin peaking F_q at certain times during the rod ejection scenario. The results of this evaluation are compared with pin power reconstruction peaking

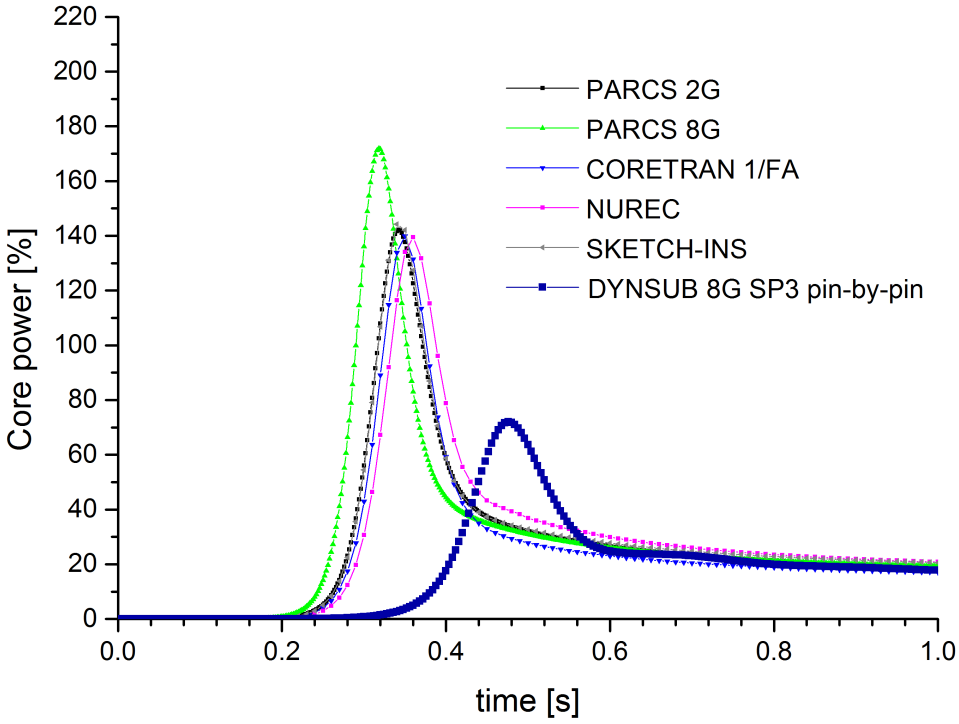

Figure 53: Comparison of the transient core power predicted by DYNSUB pin-by-pin and benchmark participants for the 3D HZP rod ejection scenario of the OECD/NEA and U.S. NRC PWR MOX/UO_2 core transient benchmark (Kozlowski & Downar, 2007)

factors from the original benchmark participants in Figure 55. The observed differences between the nodal solutions are found to be due to differences in their pin power reconstruction methods (Kozlowski & Downar, 2007). It is interesting to note that DYNSUB pin-by-pin predicts a roughly 25 % higher point-pin peaking at 0.0 s. This is presumably related to both the higher axial resolution of the DYNSUB pin-by-pin model and its more accurate prediction of the reference DeCART axial power profile.

Because of the largely different peak powers and timings between the nodal solutions employing pin power reconstruction methods and DYNSUB pin-by-pin, no detailed quantitative comparison of the transient point-pin peaking factors is viable. However, it is observed that they are generally of the similar magnitude and exhibit comparable temporal behavior.

For completeness, the transient core averaged Doppler temperatures and moderator densities predicted by DYNSUB are compared to results from benchmark participants in Figure 97 and Figure 98 in Appendix L. The observed differences between DYNSUB's pin-by-pin transient simulation and all other nodal solutions are mostly due to discrepancy in the rod worth for the D-bank control assembly being ejected and the resultant later and lower super-prompt critical power peak. Against the background of the significantly lower rod worth, all results of the transient pin-by-pin simulation are internally consistent.

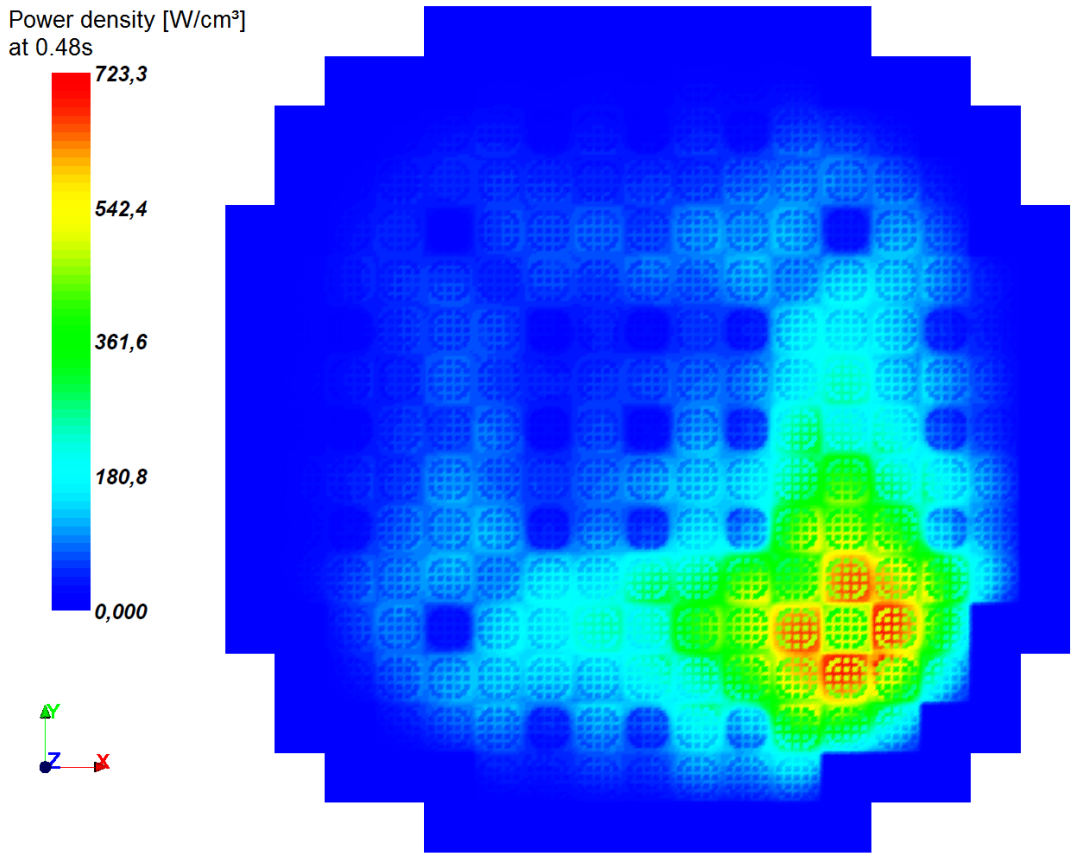

Figure 54: Spatial distribution of axially cumulated power density distribution in Watts per cubic centimeter as computed by DYNSUB pin-by-pin at 0.48 s into the 3D HZP rod ejection scenario of the OECD/NEA and U.S. NRC PWR MOX/UO_2 core transient

Last but not least, it is worthwhile to take a look at the computational resources consumed by DYNSUB pin-by-pin and the assembly-homogenized simulations presented in chapter 5. The transient nodal diffusion run finished in 148 min on a single Intel Xeon E5620 core. The simplified transport calculation took roughly 4 h to simulate 1.0 s on the same core.

The pin-by-pin DYNSUB model, however, ran on 12 cores of a dual socket Intel Xeon E5-2697 v2 machine for 12 days and 15 h. This demonstrates that even though DYNSUB's numerical performance has been improved, its execution times for pin-by-pin models are still too high for a routine application of the code. Especially when compared with the runtime of the nodal simulations.

The static 3D HZP simulation that is executed by DYNSUB pin-by-pin before performing the transient calculation takes 9 h to compute. SUBCHANFLOW consumes less than 50 % of the overall run time. During the calculation of the rod ejection transient, SUBCHANFLOW is then only responsible for an average 10 % of the overall run time. Early in the transient, the thermal-

hydraulic fraction of the solution time is as low as 1.5 % After the occurrence of the super-prompt critical power peak it rises with a maximal value of 25 %.

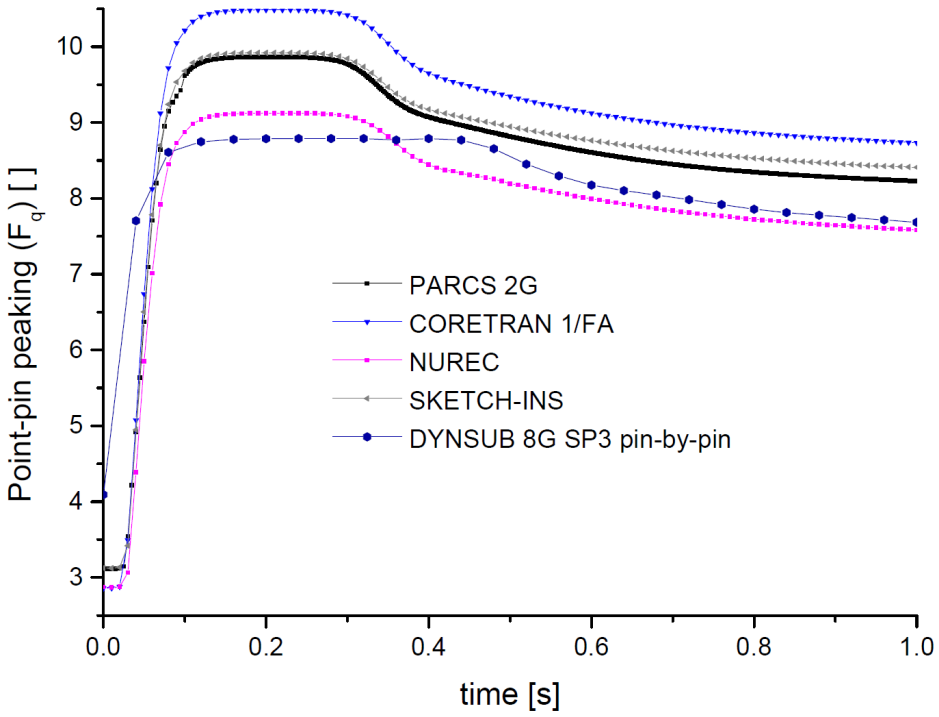

Figure 55: Comparison of point-pin peaking predicted by DYNSUB and benchmark participants for the 3D HZP rod ejection scenario of the OECD/NEA and U.S. NRC PWR MOX/UO_2 core transient benchmark (Kozlowski & Downar, 2007)

7.2 Numerical performance of Serpent 2/SUBCHANFLOW

Serpent 2/SUBCHANFLOW has been successfully used to study the second exercise of the OECD/NEA and U.S. NRC PWR MOX/UO_2 core transient benchmark. For a routine application of the coupled code, however, its numerical performance is of utmost importance. The full PWR core critical boron concentration search simulation consumed 3.7 CPU-years for the channel and 5.8 CPU-years for the sub-channel thermal-hydraulics resolution. Both calculations are run on KIT SCC's IC2 cluster, which consists of Intel Xeon E5-2670 nodes interconnected with InfiniBand.

The author took the channel and sub-channel thermal-hydraulics models for the 3D hot full power exercise of the OECD/NEA and U.S. NRC PWR MOX/UO_2 core transient benchmark and looked at speed up S (ref. equation (27)) as well as parallel efficiency E (ref. equation (28)) achieved on the IC2 cluster. Both quantities were measured relative to the execution on one compute node, i.e. 16 physical cores.

$$S(N) = \frac{T_{\text{elapsed, parallel}}}{T_{\text{elapsed, serial}}} . \quad (27)$$

with N being the number of used compute nodes.

$$E(N) = \frac{S(N)}{N} . \quad (28)$$

The results of the speed up measurements are displayed in Figure 56. SSS2/SCF behaves well for the channel thermal-hydraulics model. If there were no communication overhead and no remaining serial or non-scaling fraction of the code, the theoretical maximum speed up at 2048 cores or 128 nodes would be 128 relative to the execution one node. A speed-up of 96.4 has been determined experimentally for the latter case.

The sub-channel thermal-hydraulics Serpent 2/SUBCHANFLOW model of the full PWR core does considerably worse. As the sub-channel thermal-hydraulics is far more expensive to solve than the channel level one (32 CPUh vs 8 CPUmin), the parallel speed up levels off much earlier. This is reflected by the parallel efficiency shown in Figure 57. While SSS2/SCF CH model still achieves a parallel efficiency of 78 % when running on 128 compute nodes, the efficiency of the SBCH model has plunged to a mere 29 %.

As a tool to provide high-fidelity pin-resolved reference solution Serpent 2/SUBCHANFLOW should be employed with sub-channel thermal-hydraulics models. The fact that SUBCHANFLOW does not scale with the hybrid-parallel Serpent 2 Monte Carlo code, prohibits a routine application. As a consequence, a domain decomposition methodology has to be introduced into SUBCHANFLOW in the near future. The successful implementation of a domain decomposition in sub-channel thermal-hydraulics code COBRA-TF within the framework of the CASL project (Salko, et al., 2014) will serve as a reference for the future efforts.

Once this has been accomplished, extending the coupling of Serpent 2 and SUBCHANFLOW to the burn-up mode of Monte Carlo tool can be considered. This is a prerequisite to finish the validation of SSS2/SCF using the BEAVRS benchmark (Horelik, et al., 2016) which was started in section 3.3. To handle the terabyte tallies associated with full core pin-by-pin burn-up (Smith & Forget, 2013), also a form of domain decomposition will have to be implemented in Serpent 2 to enable core follow calculations on clusters like IC2. On IC2, each compute node with 16 cores has only 64 GB main memory.

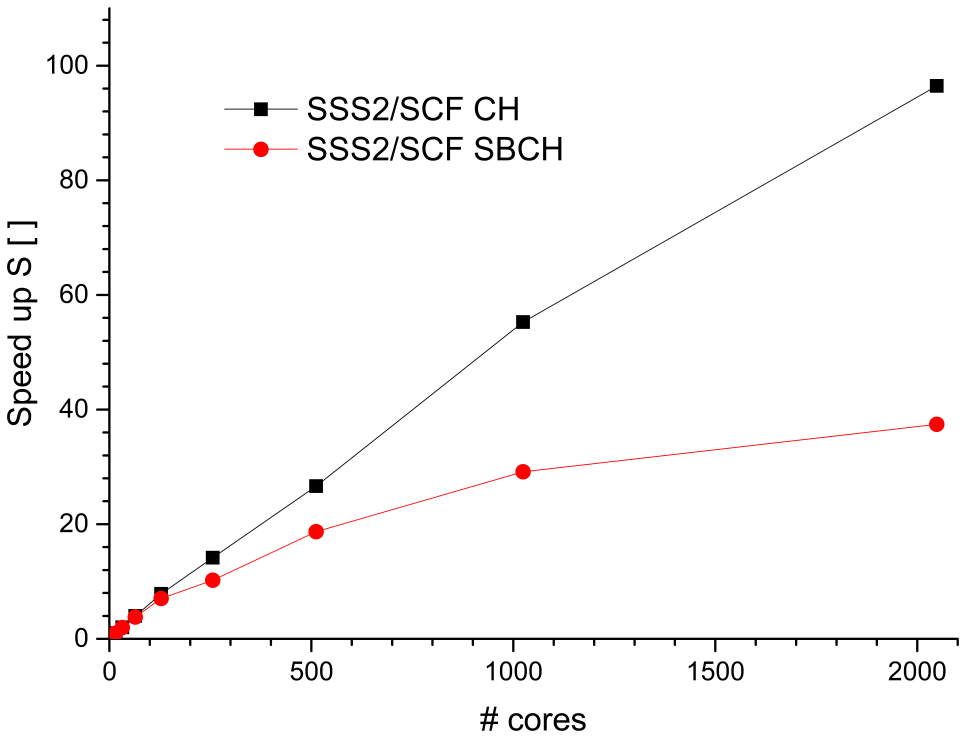

Figure 56: Speedup of SSS2/SCF measured relative to execution on one node of IC2, i.e. 16 cores

Similar conclusions have been drawn by Horelik and Mervin who work on domain decompositions methodologies in the Monte Carlo neutron transport code OpenMC and Shift respectively (Mervin, et al., 2012; Horelik, et al., 2014). With domain decomposition the issue of load balancing becomes more pressing. Even the SSS2/SCF simulations discussed beforehand have not been perfectly load balanced, since the length of a neutron history is a distributed quantity. In a domain decomposed situation, different sub-domains may have very different physical properties leading to a significant imbalance of computational load. With the decomposition, methodologies to balance the load for Serpent 2/SUBCHANFLOW have to be developed additionally.

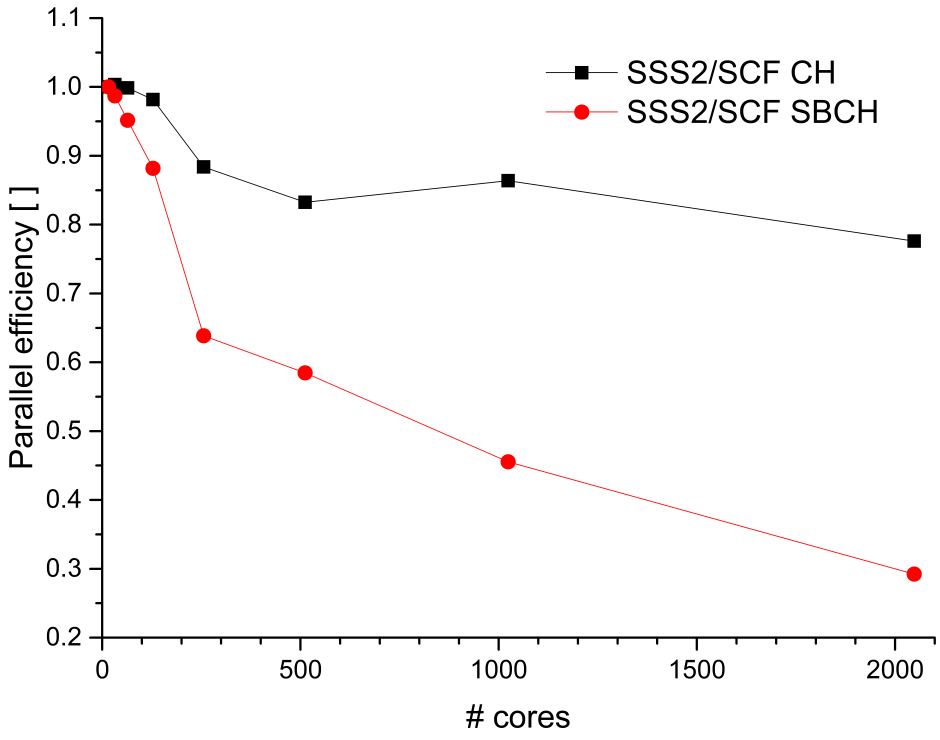

Figure 57: Parallel efficiency of SSS2/SCF measured relative to the execution on one node of IC2, i.e. 16 cores

7.3 Numerical performance of DYNSUB

Besides measuring speed up of the new version of DYNSUB compared to the former one (cp. Appendix E), the achievable parallel speed up and efficiency dependent on the number of cores utilized are of interest to assess the quality of the symmetric multi-processing parallelism in DYNSUB (OpenMP API). As this chapter focuses on DYNSUB's application to study full PWR cores at pin level resolution, the measurements of parallel speed up and efficiency presented here are done for a model of the full PWR core of the OECD/NEA and U.S. NRC PWR MOX/UO_2 core transient benchmark under HFP.

The measurements are performed on a dual socket Intel Xeon E5-2697 v2 with 379 GB of host memory running Mageia release 4 x64. DYNSUB was compiled using the Intel Fortran Compiler version 14.0.1. The LIKWID tool suite is employed to ensure proper page placement and thread hardware affinity. The results of the measurements are visualized in Figure 58.

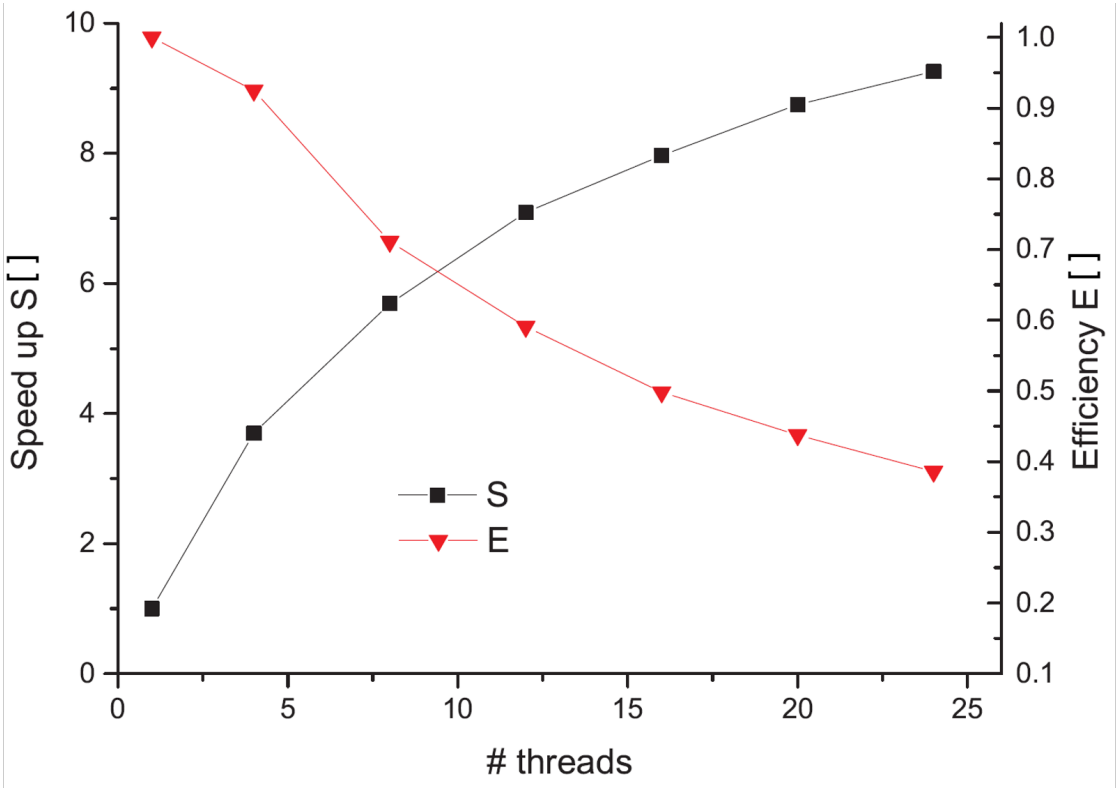

Figure 58: Speed up and parallel efficiency of DYNSUB measured on a dual socket Intel Xeon E5-2697 v2

Using 24 threads a maximum parallel speed up of 9.26 may be achieved. In this case, the coupled steady-state calculation finishes in just under 18 h. Due to the remaining serial fraction of DYNSUB in the order of a few percent and memory bandwidth limitations, the achievable speed up already starts to level off at a low number of involved cores. Correspondingly, the parallel efficiency sharply decreases from 93 % for four cores to 39 % for 24.

For this full PWR core under HFP conditions, 71 % of the 18 h of solution time using 24 threads are spent in the sub-channel thermal-hydraulics module. Only 29 % can be attributed to the pin-by-pin neutron transport problem.

To conclude, even though the introduced level of parallelism in DYNSUB enables the application of the code to full core steady-state and transient scenarios discussed previously, it is only weakly parallel. Further work on improving the coupled code's performance, i.e. reducing the serial code fraction and optimizing the memory usage, should be done in future.

7.4 Conclusions and next steps

In this chapter, it has been demonstrated that both DYNSUB and SSS2/SCF may be used to analyze realistic, industry-like cases with a pin-by-pin/sub-channel resolution by successfully completing exercise 2, i.e. the hot full power static simulation, of the OECD/NEA and U.S.

NRC PWR MOX/UO_2 core transient benchmark. For SSS2/SCF, a channel and a sub-channel resolution thermal-hydraulics model are considered. No significant differences in the obtained integral reactor properties utilizing either model have been observed. Moreover, an overall good agreement between the 8G pin-by-pin simplified transport based solution of DYNSUB and SSS2/SCF using the sub-channel TH model has been noted. On the one hand, this gives confidence in the quality of the pin-by-pin cross section library with SPH factors especially generated for this DYNSUB calculation. On the other hand, it is to a degree surprising indicating the low order pin-homogenized deterministic neutron transport methods might be sufficient to accurately describe the PWR core in question.

A detailed analysis of the obtained SSS2/SCF SBCH results, however, revealed that further work on improving the symmetry of the Monte Carlo tallies on an underlying symmetric geometry and fission source convergence needs to be done.

Moreover, thinking of a routine code application Serpent 2/SUBCHANFLOW's numerical performance is found to be satisfactory for channel thermal-hydraulics models but not for sub-channel ones. This is mostly linked to the fact that SUBCHANFLOW lacks the capability to decompose its solution domain for execution on distributed memory architectures.

Like SSS2/SCF for sub-channel TH, DYNSUB's numerical performance is assessed using the hot full power steady-state simulation. Here, the coupled code is only weakly parallel for full core pin-by-pin/sub-channel simulations. To enable a routine application of the tool, more work on improving the code's numerical performance should be done.

Finally, DYNSUB has been used to study the OECD/NEA and U.S. NRC PWR MOX/UO_2 core transient benchmark HZP REA with pin level model resolution. This is the first time that a safety relevant transient scenario for a full PWR core has been simulated using pin-by-pin simplified transport coupled to a sub-channel thermal-hydraulics model. However, the reported transient DYNSUB execution time of more almost 13 days on 12 cores is too high for any production calculation.

During this analysis, DYNSUB's pin-by-pin simulation predicts a significantly lower worth of the ejected rod than the nodal simulations. Due to the lack of a reference solution, this effect could not be finally evaluated. Hence, DYNSUB's capability to correctly predict rod worths employing pin-by-pin resolution is to be assessed in detail in the near future. This assessment has to be based on high order reference solutions as well as measured rod worths available for example in the MIT BEAVRS benchmark (Horelik, et al., 2016; Becker, et al., 2009).

8 Conclusions and future work

Worldwide efforts are ongoing to develop the next generation of reactor simulators. These belong either to the class of pin-homogenized or pin-resolved reactor simulators as opposed to the assembly-homogenized or nodal state-of-the-art reactor simulators. Both simulator types aim at reducing the physics modeling errors caused by the coarse spatial and energy discretization and low-order deterministic transport methods in the state-of-the-art codes. It is the purpose of this work to develop one tool of each class, assess it and demonstrate its capability to treat engineering-sized, industry-like PWR problems.

To obtain a pin-resolved reactor simulator, an internal coupling between the continuous energy Monte Carlo code Serpent 2 and the sub-channel code SUBCHANFLOW has been developed. Employing a MC tool like Serpent 2 to compute neutron transport has the advantage of not using any spatial or energy discretization, thus, being completely free of spatial discretization and group collapsing effects that limit the accuracy of any simulator based on deterministic neutron transport. The accuracy of the MC neutron transport is determined by the quality of the implementation of the physical laws in the code and the underlying nuclear data libraries. Since SSS2's on-the-fly temperature treatment method TMS in its current form can treat neither thermal bound-atom scattering nor unresolved resonances, a fall back to stochastic mixing has been implemented in Serpent 2 to enable the simulation of thermal reactors operating at hot (full) power. Moreover, the Wielandt shift as method to speed up fission source convergence and reduce unphysical asymmetries in the neutron flux distribution has been implemented. The verification and validation work for SSS2/SCF followed the multilevel validation methodology. As a first step, Serpent 2 has been successfully used to model VENUS-1 and VENUS-2 critical experiments, which represent modern PWRs in terms of fuel. Thereafter, the coupled code SSS2/SCF is verified by a code-to-code comparison with TRIPOLI4/SUBCHANFLOW as well as MCNP5/SUBCHANFLOW. In both cases, a good agreement between the solutions has been found. Moreover, SSS2/SCF simulations captured the HZP physics measurements included in the BEAVRS benchmark well.

As a pin-homogenized reactor simulator, DYNSUB is chosen here. This pin-homogenized tool allows for a refined spatial and energy resolution compared to state-of-the-art simulators which reduces physics modeling errors introduced by spatial discretization and group collapsing. The development of DYNSUB started in a previous doctoral research study and the efforts concentrated on extending the first version of the tool into a fully functional pin-homogenized reactor simulator. Moreover, its numerical performance has been improved in order to enable full PWR core pin-by-pin/subchannel simulations. Since DYNSUB unlike SSS2/SCF requires

pre-computed tables containing effective macroscopic cross sections, a calculation route to determine such multi-dimensional cross section tables for DYNSUB with or without homogenization corrections derived from 2D spectral geometries has been developed. Moreover, different homogenization methodologies for evaluating fuel pin level cross section sets for homogeneous pin-by-pin neutron transport calculations using the reactor simulator DYNSUB have been assessed.

Thereafter, DYNSUB is utilized to study a main coolant pump trip, a rod ejection accident, boron dilution and main steam line break design basis accident scenarios from international benchmarks. In all cases, the newly extended DYNSUB performed well. The broad range of benchmark transient cases tested underlines that DYNSUB has become a fully functional reactor simulator for PWRs using assembly-homogenized models.

DYNSUB validation efforts then continued by studying the SPERT III REA experiments. Due to the need to generate multi-dimensional cross section tables to describe the SPERT III core it has been an additional validation case for the cross section calculation route. The DYNSUB simulations of eight selected experiments are generally in good agreement with the measurements. As the selected experiments cover much of the possible transient and initial conditions one expects in commercial PWRs, the obtained results give confidence that DYNSUB is suitable to model REAs and other RIAs in PWRs.

In addition, SPERT III simulations have shown for the first time that the Serpent 2 methodology to determine homogenized few-group constants performs well for hot full power conditions and reactivity insertion accidents. Previous V&V work for cross section tables generated with Serpent 2 was limited to hot zero power steady-states.

Last but not least, it is demonstrated that both DYNSUB and SSS2/SCF may be used to analyze realistic, industry-like cases with a pin-by-pin/sub-channel resolution by successfully completing exercise 2, i.e. a full PWR core under hot full power conditions, of the OECD/NEA and U.S. NRC PWR MOX/UO_2 core transient benchmark. For the hot zero and hot full power simulations, an overall good agreement between the 8G pin-by-pin simplified transport based solution of DYNSUB and SSS2/SCF using the sub-channel TH model as well as the DeCART deterministic transport reference solution has been achieved. For these cases, DYNSUB also clearly outperformed the state-of-the-art benchmark contributions giving further confidence in the quality of its neutron transport modeling.

Moreover, DYNSUB has been used to study the hot zero power rod ejection scenario of the same benchmark on a pin level resolution. This is the first time that a safety relevant transient scenario for a full PWR core is simulated using pin-by-pin simplified transport coupled to a sub-channel thermal-hydraulics model. However, an analysis of the numerical performance of both tools revealed that neither runs efficiently enough for a routine application.

In order to be able to use the improved physics modeling of both DYNSUB and SSS2/SCF routinely in future, the following areas of work concerning numerical aspects of both tools have been identified in this work:

- introduce domain decomposition into SUBCHANFLOW such that the tool scales with SSS2 in SSS2/SCF in order to enable routine application
- introduce domain decomposition in SSS2 to be able to handle terabyte tallies associated with pin-by-pin burn-up problems
- for the domain decomposed SSS2 develop a methodology to balance the computational load of the processes of the hybrid parallel Monte Carlo code
- once the three previous bullets have been achieved, extend SSS2/SCF to include pin-resolved burn-up with thermal-hydraulic feedback
- keep on developing global variance reduction schemes for SSS2 in order to continue to improve both the symmetry of the tallies and the convergence of the fission source
- for DYNSUB, re-factor the code to be able to utilize modern hybrid-parallel pre-conditioned Krylov subspace solvers from third party libraries
- adapt DYNSUB coupling routines to benefit from the domain decomposition available in the updated SUBCHANFLOW.

Compared to state-of-the-art assembly-homogenized reactor simulators, both DYNSUB and especially SSS2/SCF have a largely improved description of neutron transport physics. However, to further improve the description of physics in the coupled codes, the topics listed below can be considered:

- further develop methodologies to determine pin-level homogenized few-group constants based on two-dimensional super cell spectral geometries for DYNSUB
- derive a tool chain to approximately evaluate SPH factors and IDF for pin-by-pin simplified transport simulations
- consider deriving cross section calculation routes for DYNSUB based on three-dimensional spectral geometries as their homogenization corrections can also treat axial leakage effects in the low order solution
- assess and, once more, improve DYNSUB's control rod models with a focus on pin-by-pin simulations
- replace the stochastic mixing fall back for thermal bound-atom scattering in SSS2 with with an on-the-fly sampling of thermal scattering data. Consider a method being developed at Rennselaer Polytechnic Institute (Pavlou & Ji, 2014)
- in SSS2 make the sampling of unresolved resonance probability tables compatible with the TMS method

- Once SSS2's coupled neutron-gamma transport mode is fully functional, expand the coupling of SSS2/SCF to directly heat coolant and structures.

Even though a large fraction of this thesis has been devoted to verify and validate SSS2/SCF and DYNSUB, the V&V process for either tool is still incomplete. The validation base of DYNSUB has to be extended to cover all major design basis accident scenarios and in-core fuel management in the near term. To continue validating SSS2/SCF, core follow calculations for the two operational cycles included in the BEAVRS benchmark should be performed after finishing the necessary numerical code updates listed above. Furthermore, additional V&V cases for the Monte Carlo thermal-hydraulics code should be identified.

Finally, to complete the VVUQ software development process, the V&V work for both tools should be complemented with a formal sensitivity and uncertainty study. It should be based on the uncertainty quantification methods established in the framework of the OECD UAM benchmark (Ivanov, et al., 2007b).

List of figures

List of tables

Appendix A Stochastic mixing fall back for TMS

Table 46: Geometry and material details of stochastic mixing fall back verification model

Quantity	Value / Unit
Pellet radius	0.3951 cm
Inner clad radius	0.4010 cm
Outer clad radius	0.4583 cm
Fuel material	UOX 4.2 wt%
Gap material	oxygen
Clad material	zircalloy 4
Coolant material	water
UOX density	10.242 g/cm^3
Gas density	10^{-3} g/cm^3
Clad density	6.5047 g/cm^3
Coolant density	0.75311 g/cm^3

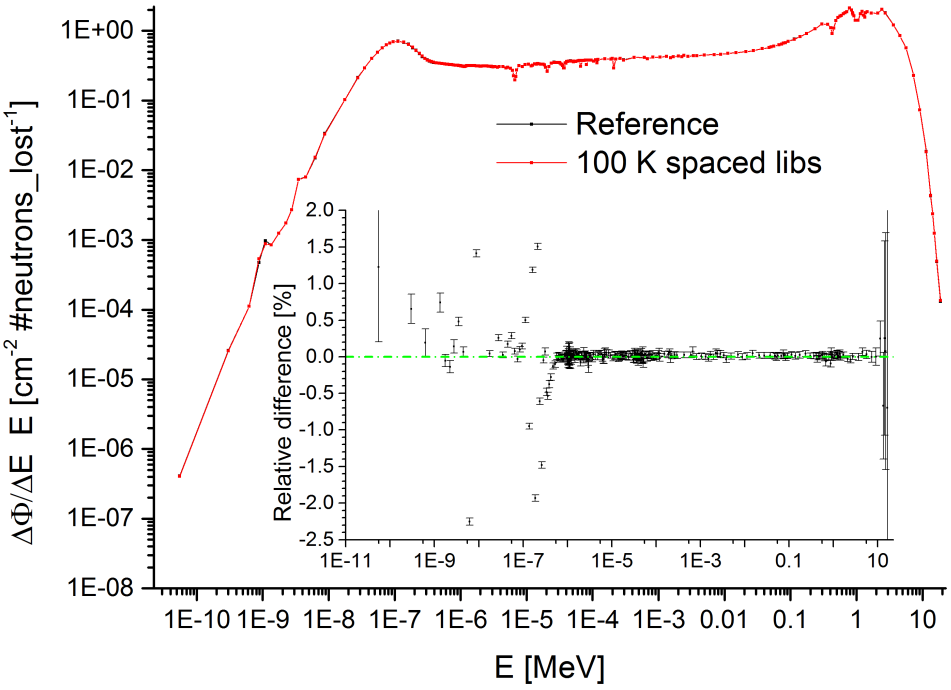

Figure 59: Comparison of neutron spectra normalized to unit neutron loss rate in first water zone of the fall back verification model predicted with and without stochastic mixing fall back using 100 K spaced libraries

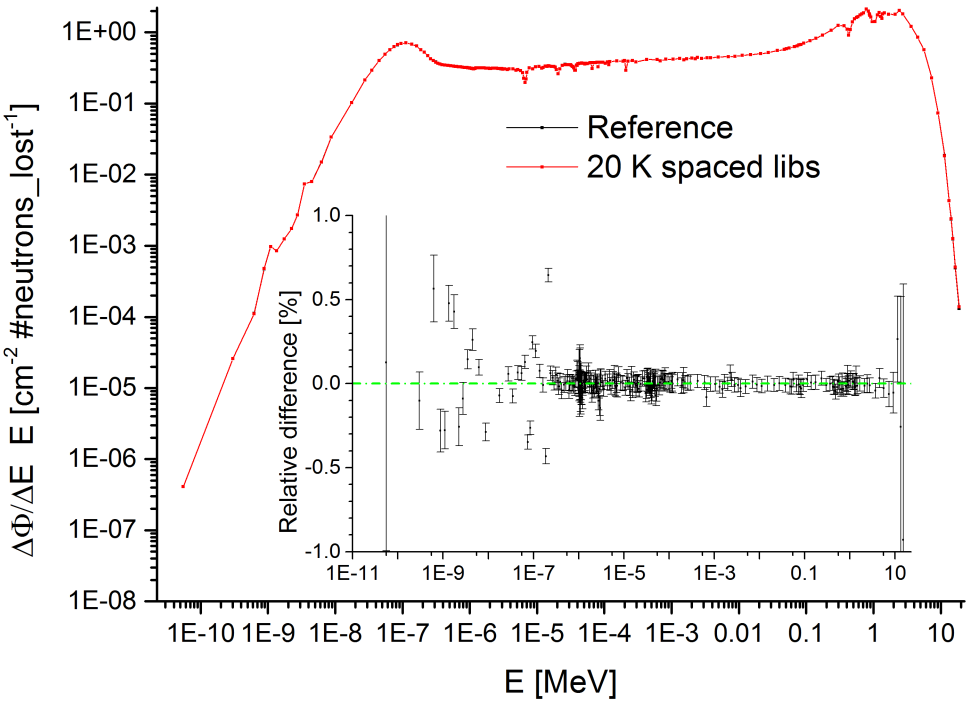

Figure 60: Comparison of neutron spectra normalized to unit neutron loss rate in first water zone of the fall back verification model predicted with and without stochastic mixing fall back using 20 K spaced libraries

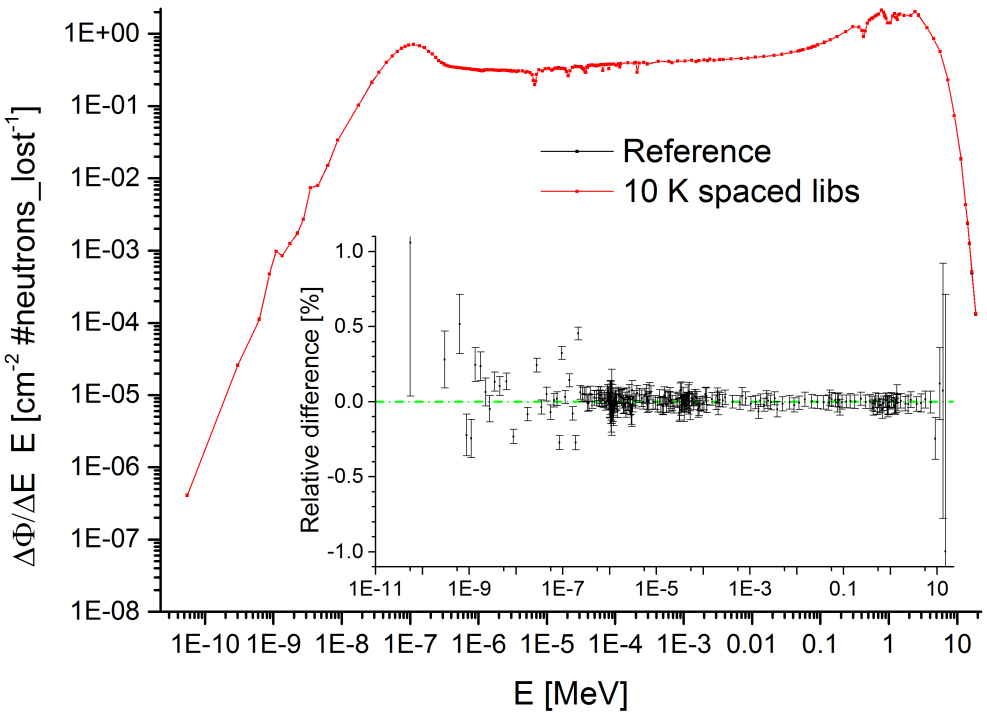

Figure 61: Comparison of neutron spectra normalized to unit neutron loss rate in first water zone of the fall back verification model predicted with and without stochastic mixing fall back using 10 K spaced libraries

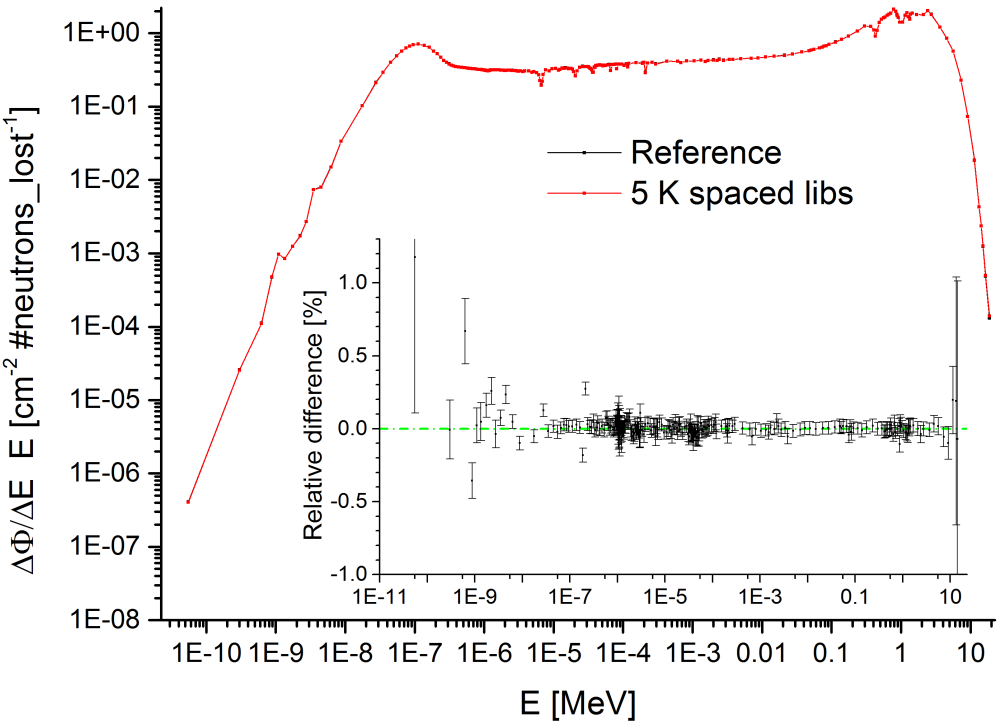

Figure 62: Comparison of neutron spectra normalized to unit neutron loss rate in first water zone of the fall back verification model predicted with and without stochastic mixing fall back using 5 K spaced libraries

Appendix B VENUS critical experiments

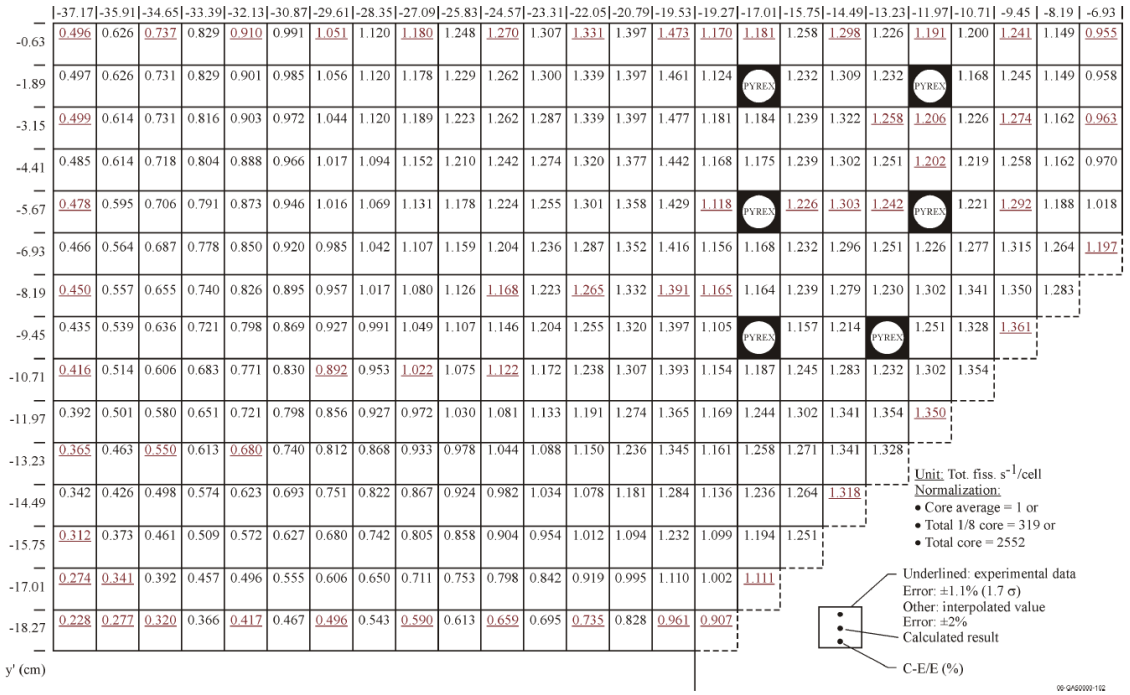

Figure 63: VENUS-1 normalized radial power distribution measurements, taken from (Moon, et al., 2006)

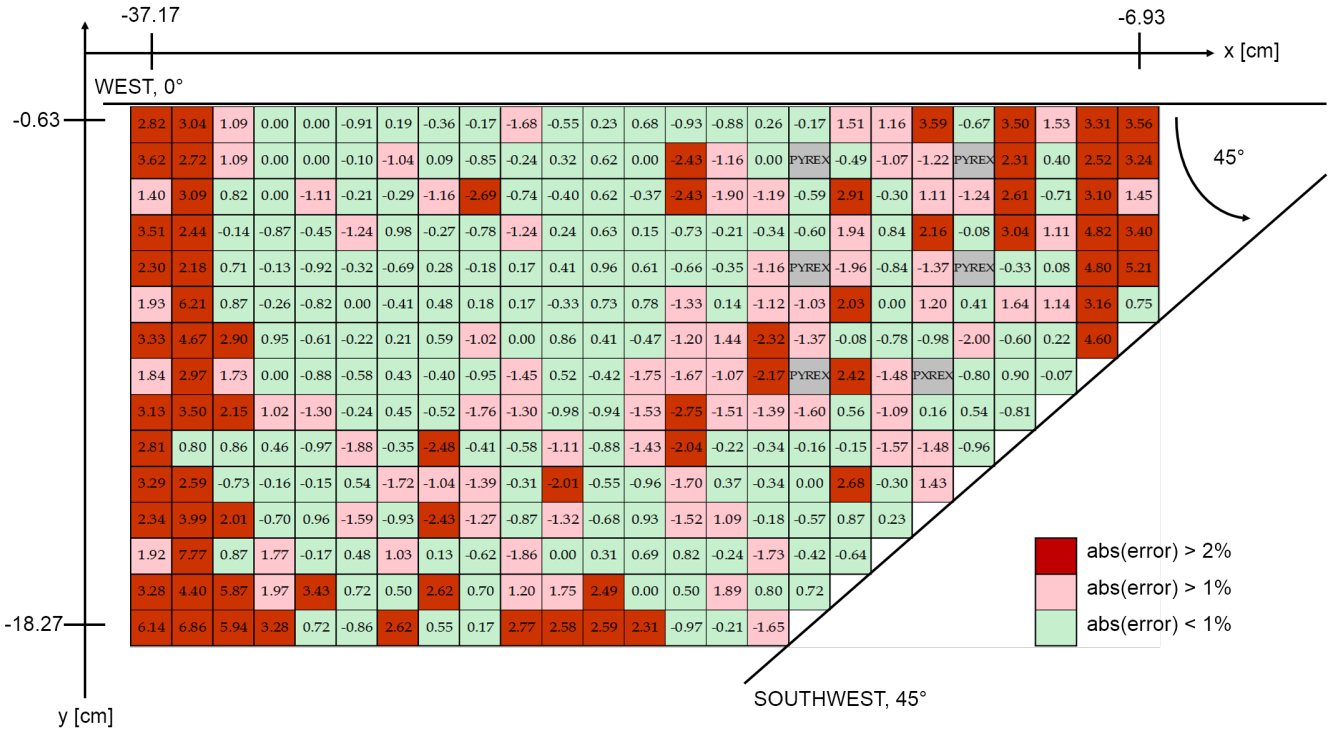

Figure 64: Relative deviation (C/E-1) in percent for VENUS-1 pin power distribution as predicted by MCNP, origin of the x-y-coordinate system is the center of the central water hole, adapted from (Moon, et al., 2006).

X→ Y↓	-37.17	-35.91	-34.65	-33.39	-32.13	-30.87	-29.61	-28.35	-27.09	-25.83	-24.57	-23.31	-22.05	-20.79	-19.53	-18.27	-17.01	-15.75	-14.49	-13.23	-11.97	-10.71	-9.45	-8.19	-6.93
0.63	0.433	0.517	*0.577*	0.641	*0.713*	0.804	*0.902*	1.059	1.035	1.177	1.279	*1.34*	1.393	*1.469*	1.561	1.236	1.223	1.349	1.397	1.397	1.293	1.334	*1.329*	1.248	1.08
1.89	*0.438*	*0.514*	*0.577*	*0.643*	*0.717*	*0.797*	*0.907*	*1.065*	*1.033*	*1.17*	*1.27*	*1.336*	*1.391*	*1.464*	*1.556*	1.183	Pyrex	*1.283*	*1.399*	1.321	Pyrex	*1.283*	*1.345*	*1.25*	*1.053*
3.15	0.442	0.506	*0.571*	0.643	*0.717*	0.797	*0.909*	1.061	1.027	*1.16*	1.262	*1.323*	1.38	*1.454*	1.557	1.246	*1.233*	1.358	*1.395*	1.388	*1.324*	1.364	1.329	1.26	1.026
4.41	*0.428*	*0.5*	*0.563*	*0.631*	*0.705*	*0.79*	*0.895*	*1.049*	*1.022*	*1.141*	*1.25*	*1.312*	*1.374*	*1.452*	*1.544*	*1.25*	*1.237*	*1.366*	*1.387*	*1.374*	*1.308*	*1.382*	*1.387*	*1.27*	*1.076*
5.67	0.422	0.497	*0.547*	0.614	*0.692*	0.781	*0.882*	1.031	1.016	*1.126*	1.241	*1.304*	1.36	*1.446*	1.536	1.187	Pyrex	1.313	*1.362*	1.331	Pyrex	1.336	*1.374*	1.298	1.131
6.93	*0.41*	*0.477*	*0.531*	*0.599*	*0.673*	*0.756*	*0.859*	*1.013*	*1.001*	*1.05*	*1.213*	*1.282*	*1.357*	*1.437*	*1.536*	*1.237*	*1.26*	*1.345*	*1.378*	*1.399*	*1.374*	*1.449*	*1.428*	*1.378*	1.303
8.19	0.39	0.451	*0.513*	0.579	*0.65*	0.736	*0.842*	0.978	0.971	*1.081*	1.174	*1.264*	1.348	*1.425*	1.526	1.265	*1.279*	1.286	*1.399*	1.454	*1.488*	1.507	*1.482*	1.46	
9.45	*0.382*	*0.447*	*0.494*	*0.559*	*0.628*	*0.715*	*0.811*	*0.952*	*0.943*	*1.056*	*1.146*	*1.236*	*1.323*	*1.418*	*1.518*	*1.275*	1.271	Pyrex	*1.382*	*1.477*	*1.515*	*1.515*	*1.509*		
10.71	0.366	0.422	*0.474*	0.535	*0.602*	0.689	*0.79*	0.927	0.91	*1.024*	1.114	*1.2*	1.287	*1.387*	1.506	1.278	*1.304*	1.339	*1.436*	1.492	*1.519*	1.522			
11.97	*0.343*	*0.402*	*0.449*	*0.506*	*0.578*	*0.655*	*0.742*	*0.884*	*0.87*	*0.992*	*1.075*	*1.166*	*1.256*	*1.362*	*1.479*	*1.267*	*1.329*	*1.39*	*1.465*	*1.506*	*1.523*				
13.23	0.317	0.375	*0.429*	*0.477*	*0.539*	0.62	0.689	0.826	0.823	0.953	1.032	*1.12*	1.219	*1.327*	1.446	1.244	*1.362*	1.411	*1.461*	1.501					
14.49	*0.3*	*0.354*	*0.394*	*0.447*	*0.508*	*0.582*	*0.65*	*0.774*	*0.776*	*0.883*	*0.975*	*1.069*	*1.164*	*1.27*	*1.398*	*1.209*	*1.349*	*1.387*	*1.449*						
15.75	0.278	0.331	*0.366*	0.414	*0.473*	0.541	*0.607*	0.721	0.716	*0.808*	0.907	*0.988*	1.08	*1.198*	1.327	1.149	*1.262*	1.353							
17.01	0.251	0.296	*0.337*	0.38	*0.427*	*0.482*	*0.54*	*0.643*	*0.64*	*0.719*	*0.81*	*0.882*	*0.95*	*1.06*	*1.209*	*1.068*	*1.24*								
18.27	0.224	0.267	*0.302*	0.338	*0.376*	0.423	0.465	0.561	0.536	0.608	0.673	*0.727*	0.787	*0.88*	1.019	0.926									

Measured values: in bold
Interpolated values: in italics

Figure 65: VENUS-2 radial power distribution measurement, taken from (Na, et al., 2000)

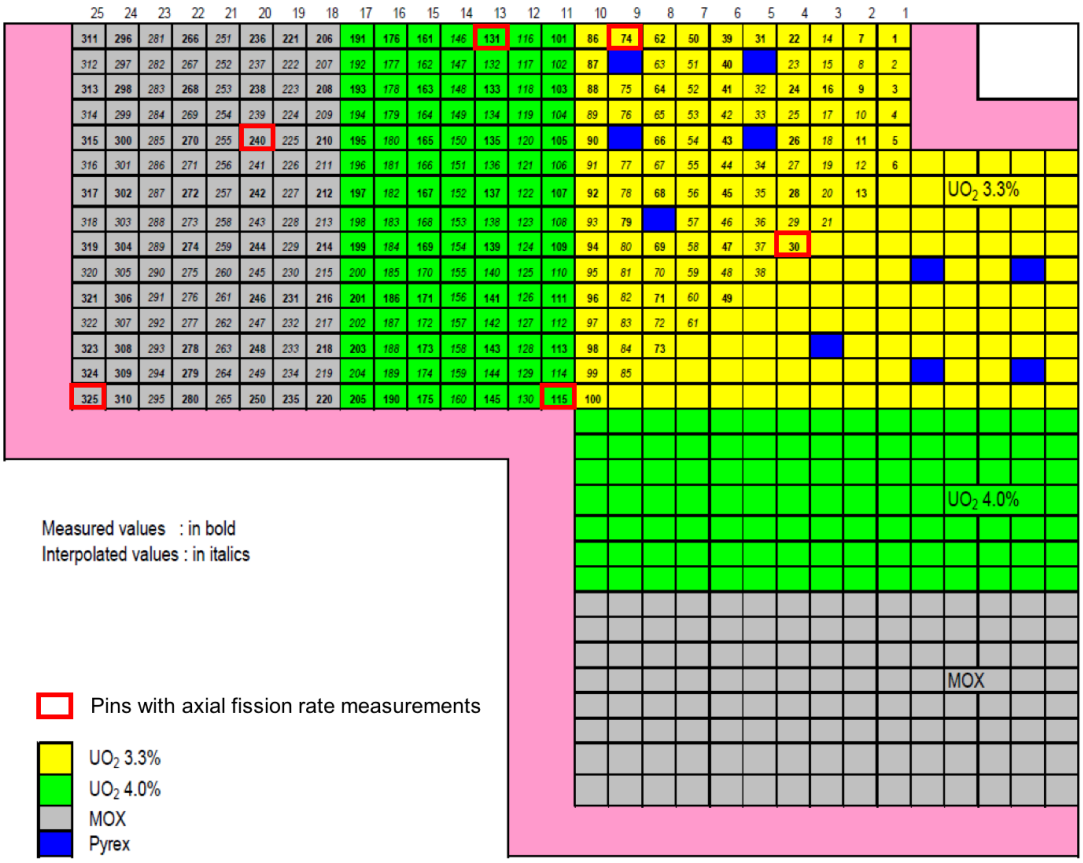

Figure 66: Numbering of fuel pins for measurements in VENUS-2, adapted from (Na, et al., 2000)

Pin type	MOX		4/0 UO_2		3/0 UO_2	
Pin position	(-27,-12)	(-22,-2)	(-15,+2)	(-13,-12)	(-11,+2)	(-6,-6)
Pin number	325	240	131	115	74	30
Axial position (cm)	Measured fission rates (normalised to 1)					
110	0.0333	0.0322	0.0321	0.0323	0.0322	0.0324
112	0.0356	0.0366	0.0363	0.0358	0.0366	0.0364
114	0.0399	0.0395*	0.0404	0.0402	0.0399	0.0405
116	0.0438	0.0424	0.0441	0.0444	0.0441	0.0440
118	0.0466	0.0478	0.0477	0.0472	0.0481	0.0477
120	0.0500	0.0507	0.0504	0.0503	0.0500	0.0505
122	0.0527	0.0516	0.0531	0.0527	0.0528	0.0524
124	0.0548	0.0545	0.0542	0.0544	0.0550	0.0546
126	0.0558	0.0559	0.0564	0.0557	0.0563	0.0554
128	0.0557	0.0558	0.0572	0.0564	0.0563	0.0567
130	0.0574	0.0567	0.0568	0.0564	0.0571	0.0562
132	0.0567*	0.0578	0.0565	0.0572	0.0565	0.0569
134	0.0559	0.0564	0.0562	0.0561	0.0560	0.0559
136	0.0548	0.0560	0.0548	0.0555	0.0546	0.0545
138	0.0529	0.0533	0.0530	0.0524	0.0526	0.0524
140	0.0506	0.0508	0.0504	0.0506	0.0503	0.0504
142	0.0481	0.0477	0.0477	0.0476	0.0476	0.0474
144	0.0438	0.0445	0.0439	0.0446	0.0442	0.0446
146	0.0411	0.0412	0.0403	0.0413	0.0409	0.0407
148	0.0375	0.0366*	0.0365	0.0366	0.0366	0.0369
150	0.0331	0.0320	0.0321	0.0321	0.0325	0.0337

* Interpolated values.

Figure 67: VENUS-2 axial pin power measurements, taken from (Messaoudi, et al., 2004)

Appendix C Benchmark with MCNP5/SCF

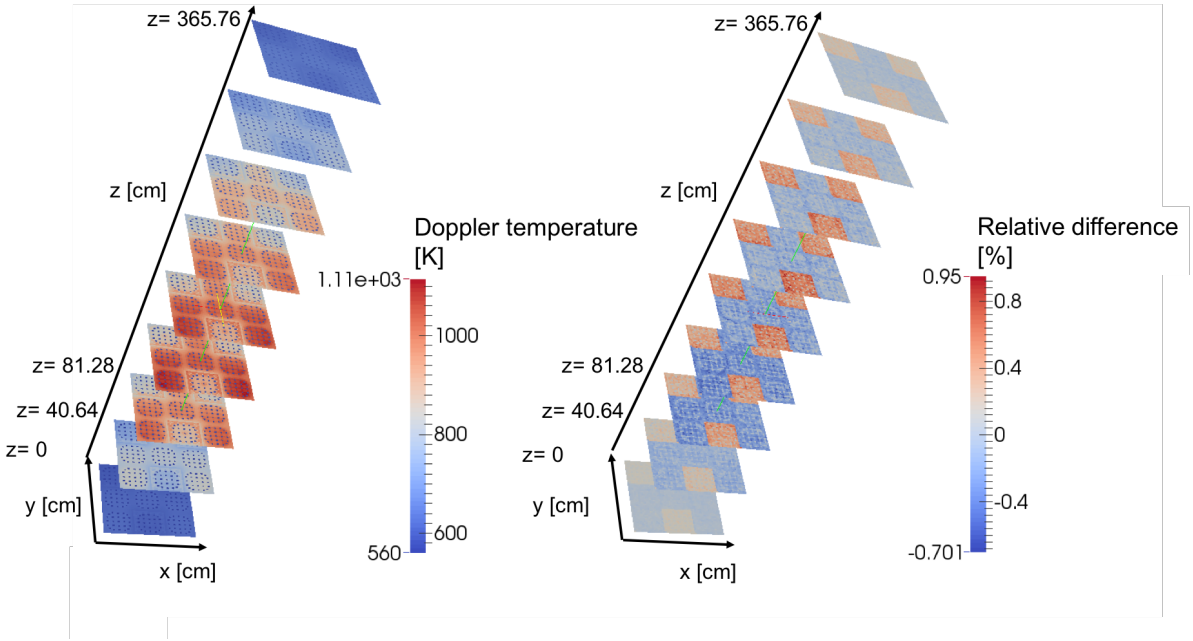

Figure 68: Axial Doppler temperature distribution in Kelvin as predicted by SSS2/SCF [left], relative differences between MCNP5/SCF and SSS2/SCF Doppler temperature fields in percent [right] at nine equidistantly spaced horizontal cuts

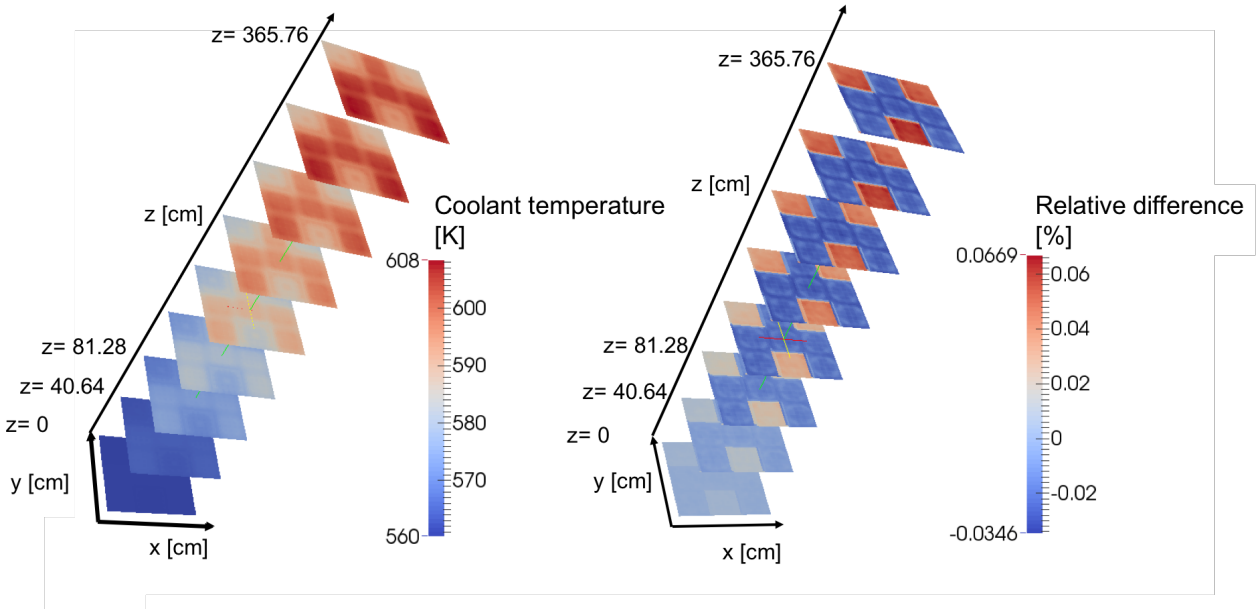

Figure 69: Axial coolant temperature distribution in Kelvin as predicted by SSS2/SCF [left], relative differences between MCNP5/SCF and SSS2/SCF coolant temperature fields in percent [right] at nine equidistantly spaced horizontal cuts

Appendix D BEAVRS benchmark

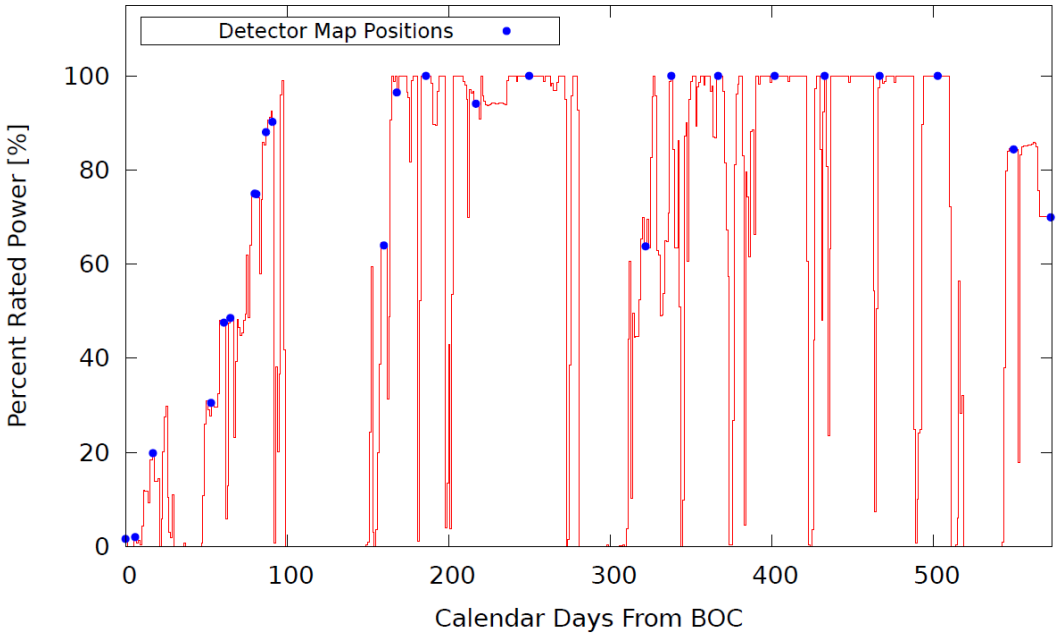

Figure 70: Power history of cycle 1 of the BEAVRS benchmark (Horelik, et al., 2016)

Appendix E Improvement of DYNSUB numerical performance

When analyzing the version of DYNSUB discussed in Gomez et al. (Gomez-Torres, et al., 2012a; Gomez-Torres, et al., 2012b), several redundancies and inefficiencies in DYNSUB's coupling scheme have been detected. These have been removed leading to a measurable reduction in execution time and memory requirements.

As a second step, a profiler has been employed to monitor DYNSUB runs in order to identify computational bottlenecks to be parallelized using the OpenMP API. DYNSUB employs explicit iterative solvers to treat the neutron diffusion or simplified transport problem. While these solvers are very fast for small models, they were found to scale unsatisfactorily with increasing numerical problem size. It was considered to replace the explicit iterative solvers with modern parallel pre-conditioned Krylov subspace solvers readily available from third-party libraries such as PETSc. However, an analysis of the source code revealed an incompatibility of the used data structures with such libraries. The use of such libraries requires a major re-factoring of the neutronics code. While the re-factoring is planned for the near term, parallelizing the explicit iterative neutronic solvers using OpenMP has been chosen as short term intermediate solution.

For the subroutines identified by profiling DYNSUB, the dependencies of all instructions have been analyzed and the possible level of parallelization has been introduced.

In order to determine the overall speed up relative to the original DYNSUB version applied in Gomez et al. (Gomez-Torres, et al., 2012a; Gomez-Torres, et al., 2012b), a PWR core having one-eighth symmetry is modeled. The configuration is based on the OECD/NEA and U.S. NRC PWR MOX/UO_2 core transient benchmark (Kozlowski & Downar, 2003). Details on the core layout, hot zero power operating conditions are given by Gomez (Gomez-Torres, et al., 2012a). The steady-state convergence criteria used are $\varepsilon_{\mathrm{keff}} < 10^{-5}$ for the eigenvalue, $\varepsilon_{\mathrm{DT}} < 10^{-4}$ for local Doppler temperature and $\varepsilon_{\mathrm{RM}} < 10^{-4}$ for the local moderator density. A meshing study was performed to determine the necessary number of axial mesh cells to ensure a mesh independent solution with radial mesh resolution at pin level. At least 68 equidistant axial cells are required for this specific case. In total, the resulting problem has 609k nodes in the neutronic mesh, 683k nodes in fluid and 7.31M nodes in the solid domain. The case to be studied is a steady-state eigenvalue problem.

Measurements of elapsed wall clock time were performed for both the original and improvement DYNSUB version on a dual socket Intel Xeon E5620 platform with 48 GB of host memory running Mandriva Linux 2010.2 x64. Both code versions were compiled with the Intel

Fortran compiler version 12.1.3. The hardware affinity of the threads and the proper page placement has been assured using the LIKWID tool suite (Treibig, et al., 2010).

Simulating the PWR core with one-eighth symmetry using simplified transport took 85 min on the above machine running on 8 cores. This is 10.5 times less elapsed time than measured for the previous serial DYNSUB version. Comparing the serial execution of the revised DYNSUB and its predecessor, one finds that the new version runs 3.64 times faster for the given test problem.

Appendix F Kalinin-3 benchmark

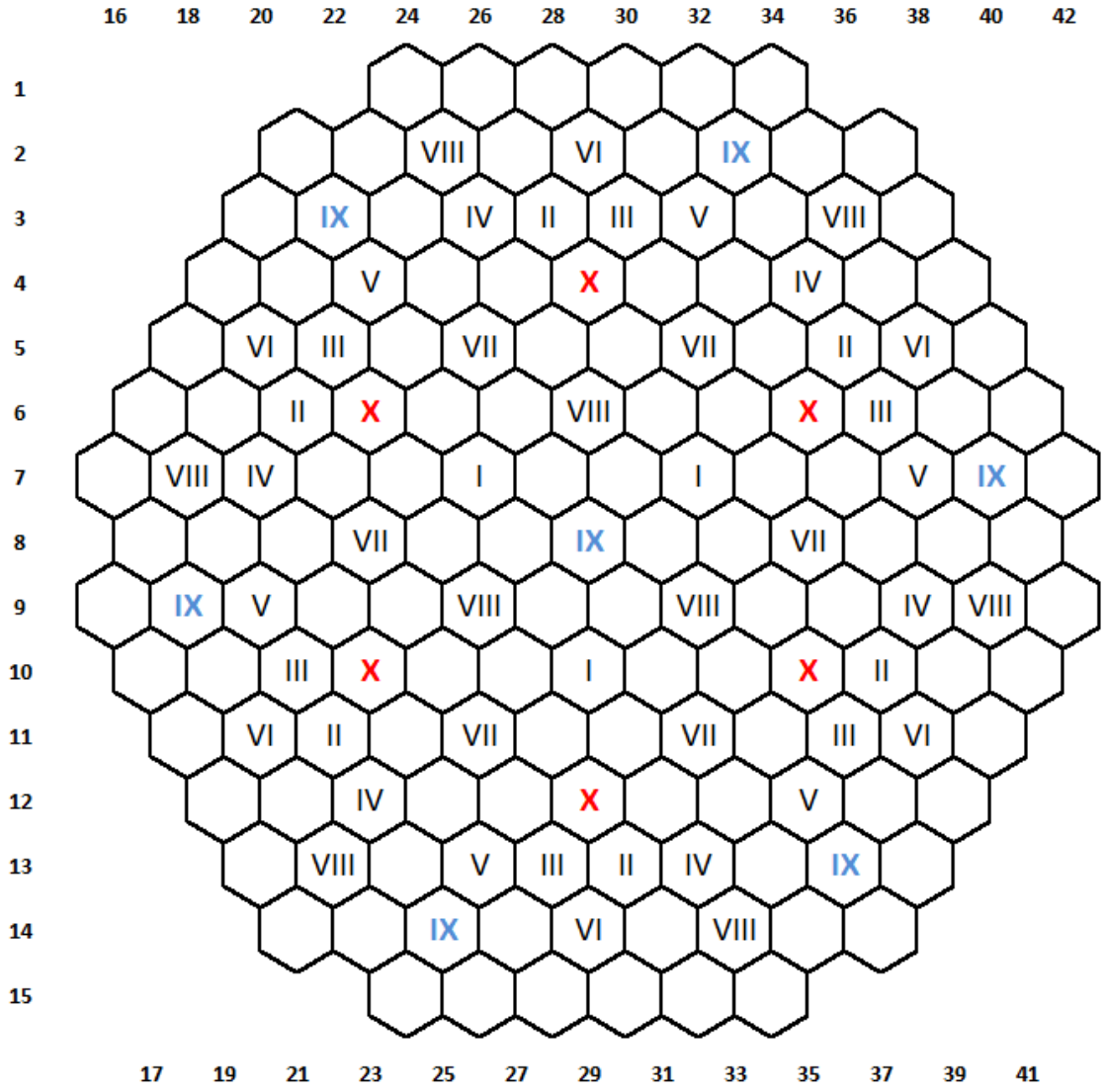

Figure 71: Arrangement of the CR banks #1 - #10 in the Kalinin-3 NPP, banks #9 and #10 move during the coolant transient and have been highlighted, based on (Tereshonok, et al., 2008)

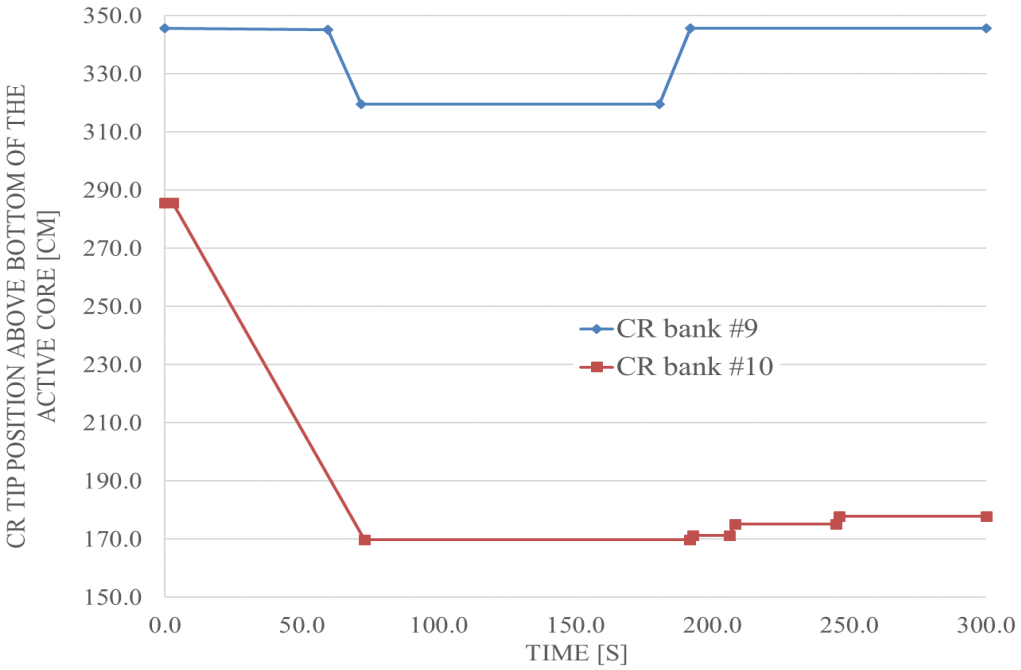

Figure 72: Position of the tip of CR banks #9 and #10 of Kalinin-3 NPP during the coolant transient experiment, based on (Tereshonok, et al., 2008)

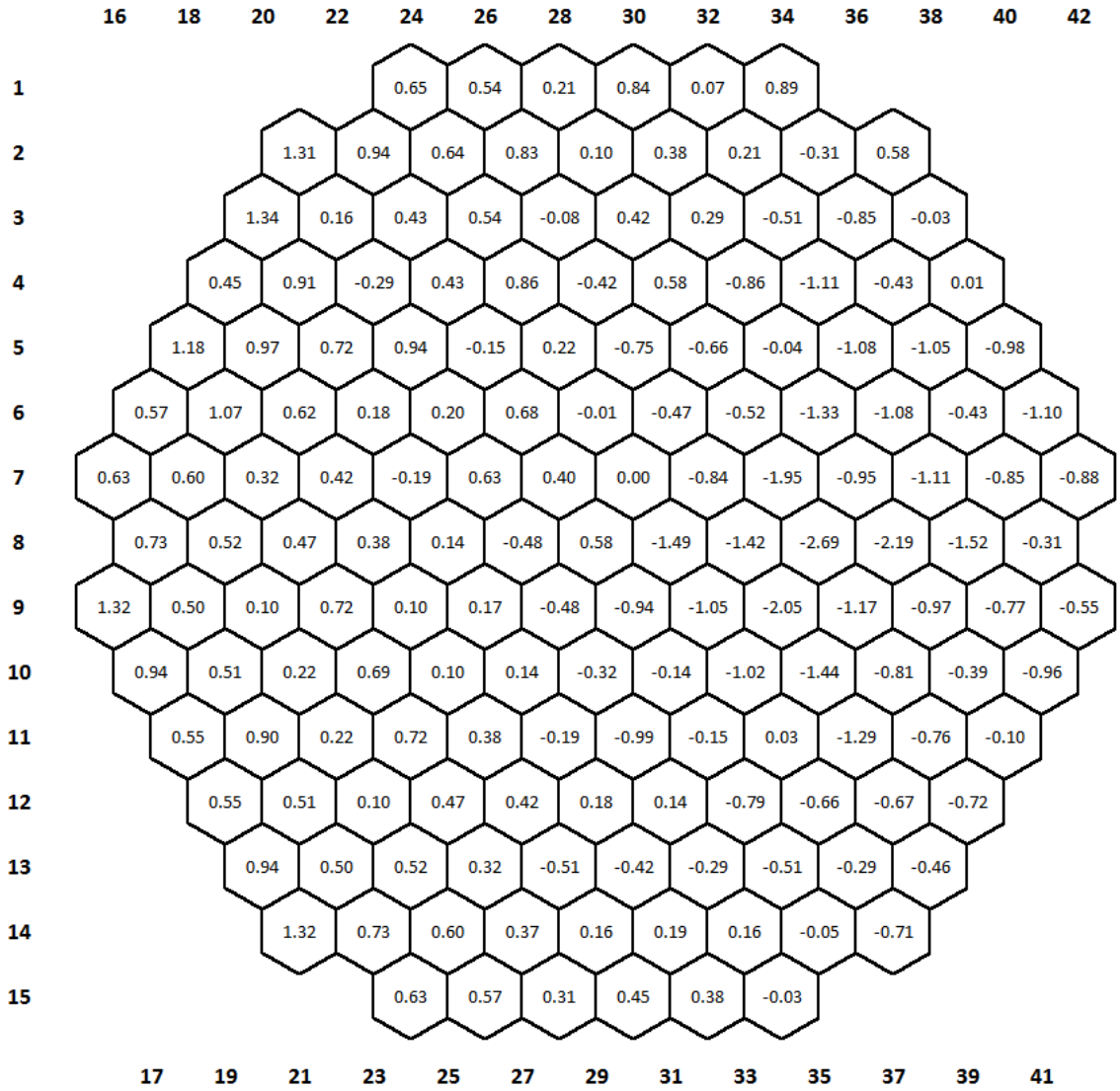

Figure 73: Relative difference in percent in assembly powers between CBY/SCF and DYNSUB for the Kalinin-3 NPP at HZP

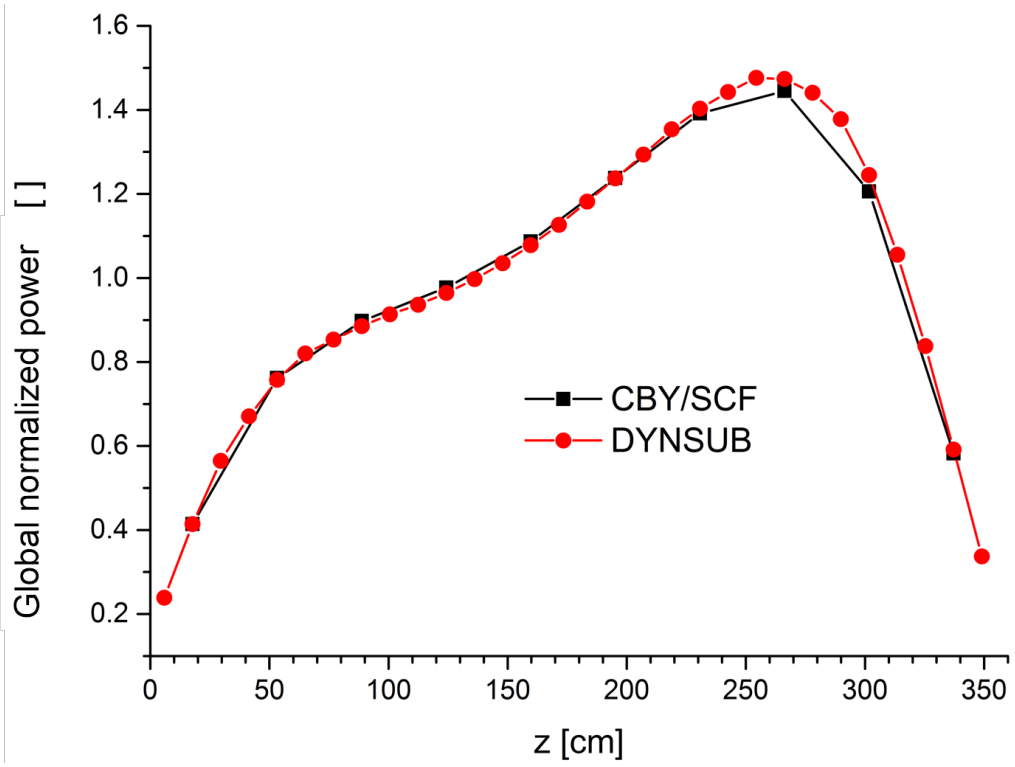

Figure 74: Global normalized axial power profiles for Kalinin-3 NPP at HZP as computed by CBY/SCF and DYNSUB

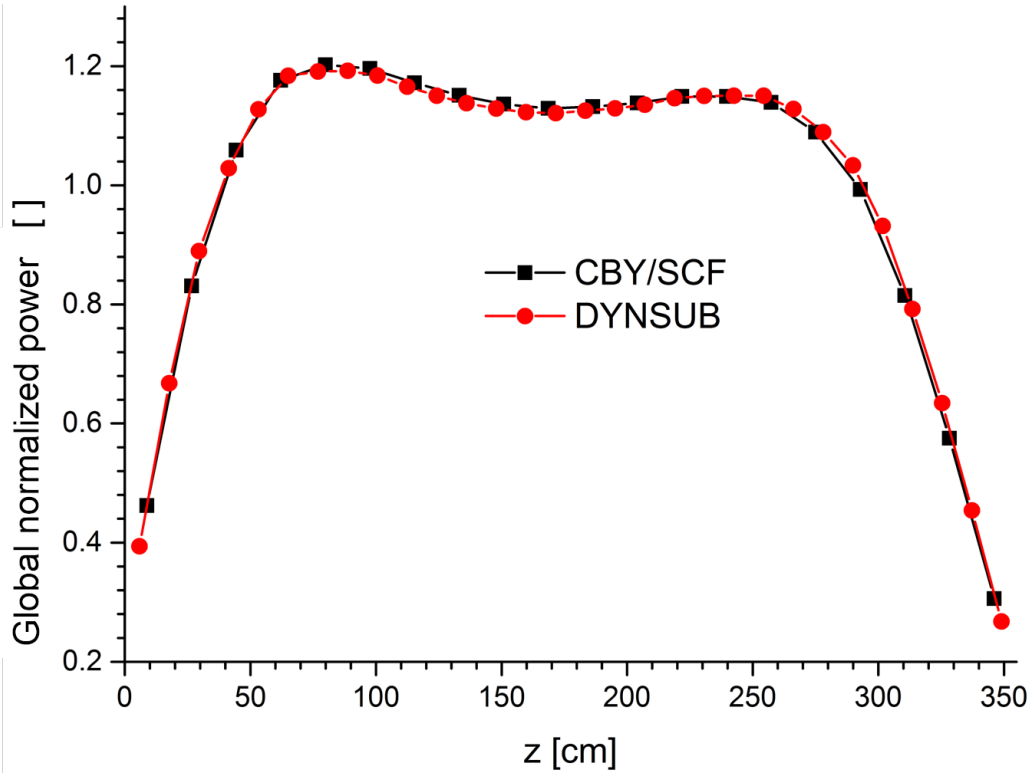

Figure 75: Global normalized axial power profiles for Kalinin-3 NPP at HFP as computed by CBY/SCF and DYNSUB

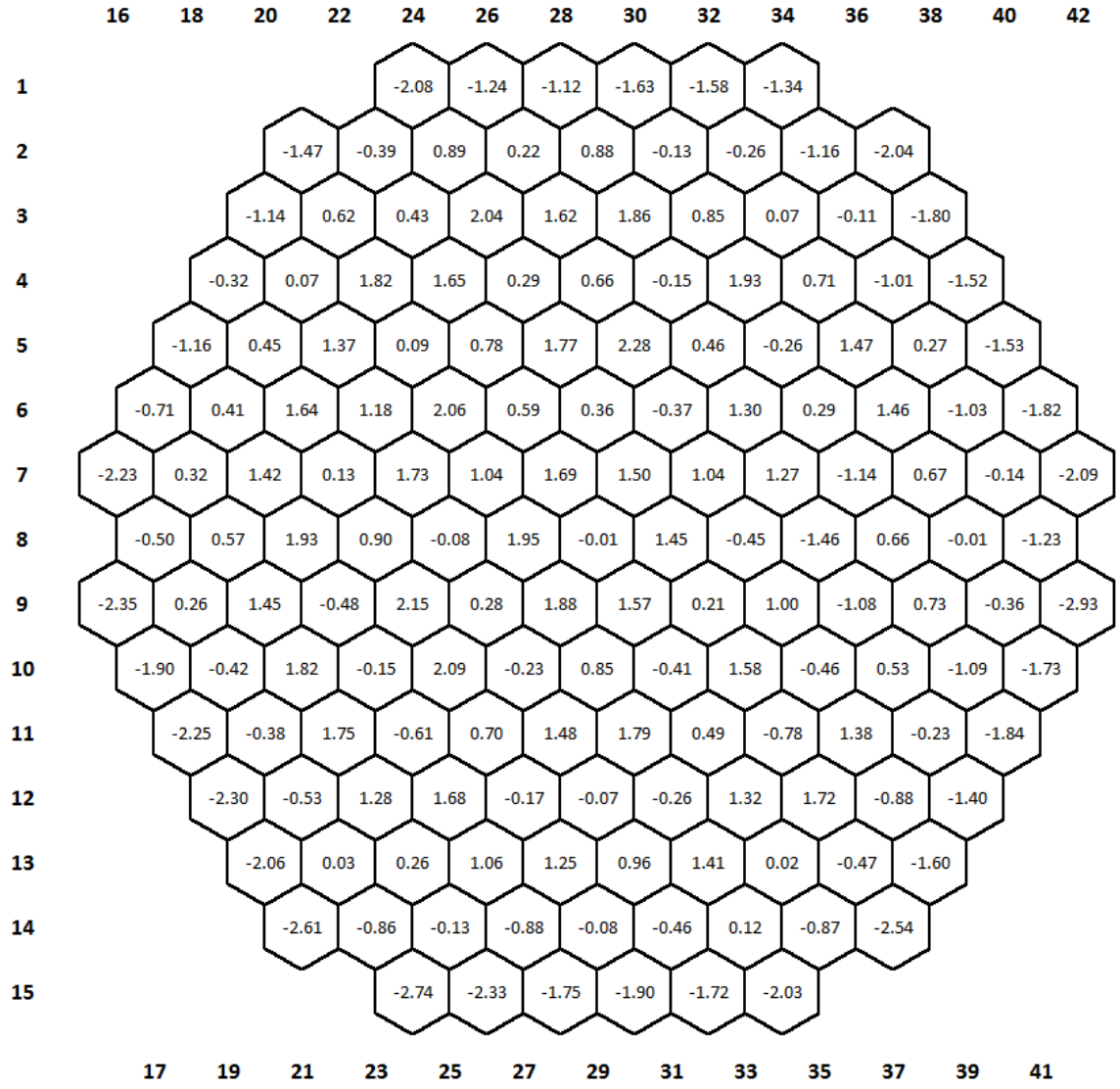

Figure 76: Relative difference in percent in assembly powers between CBY/SCF and DYNSUB for the Kalinin-3 NPP at HFP

Appendix G PWR MOX/UO_2 core transient benchmark

Table 47: Comparison of the PWE and EWE relative assembly power errors in percent for the 2D cases of the OECD/NEA and U.S. NRC PWR MOX/UO_2 core transient benchmark (Kozlowski & Downar, 2007).

Code	ARO PWE	ARO EWE	ARI PWE	ARI EWE
DeCART	ref	ref	ref	ref
CORETRAN 1/FA	1.06	1.69	2.01	2.52
NUREC	0.96	1.63	1.64	2.16
PARCS 2G	0.96	1.63	1.67	2.18
PARCS 8G	0.86	1.25	1.65	2.49
SKETCH-INS	0.97	1.67	1.67	2.16
DYNSUB 8G	0.98	1.48	1.92	2.76
DYNSUB 8G SP3	1.28	1.84	1.99	2.28

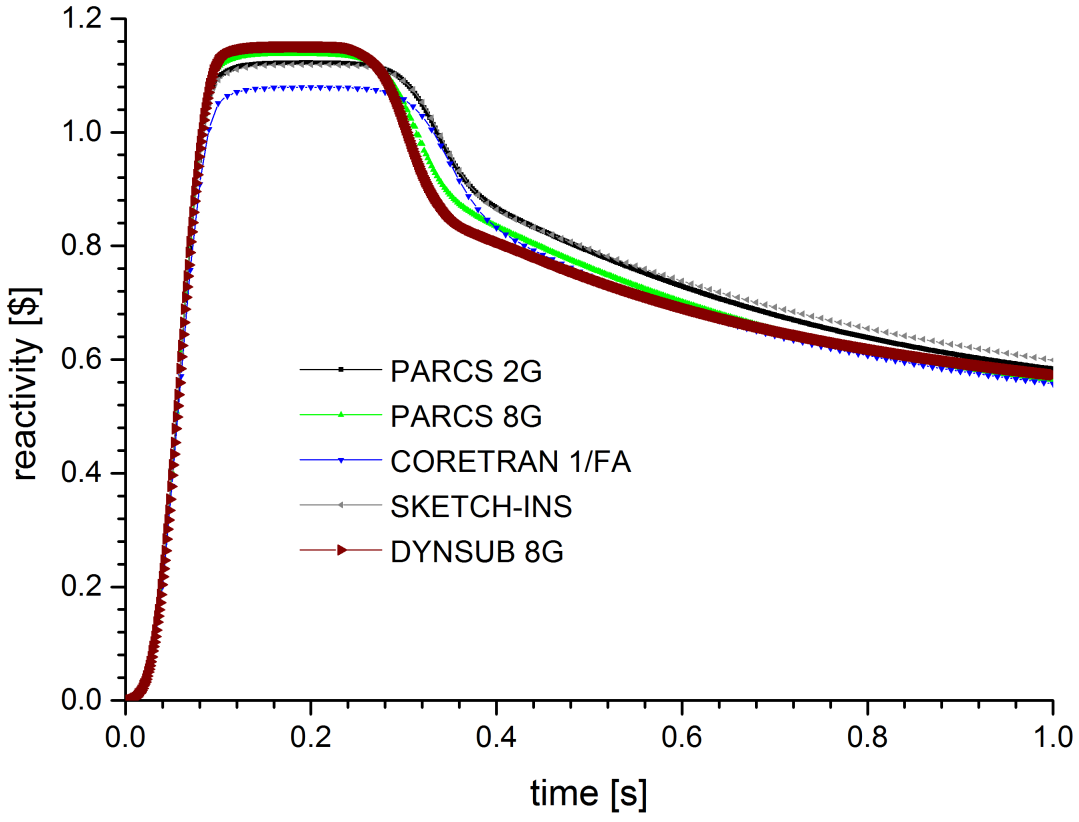

Figure 77: Comparison of transient core reactivity [$] as predicted by DYNSUB and benchmark participants for the 3D HZP rod ejection scenario of the OECD/NEA and U.S. NRC PWR MOX/UO_2 core transient benchmark (Kozlowski & Downar, 2007).

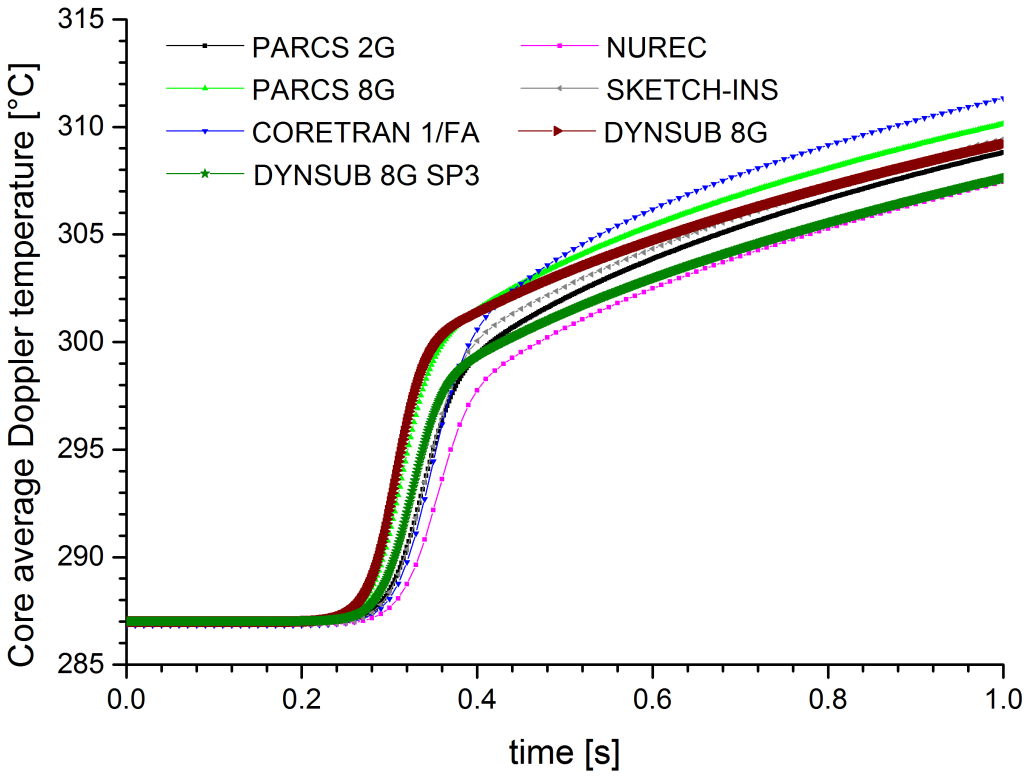

Figure 79: Comparison of transient core averaged Doppler temperature evaluated by DYNSUB and benchmark participants for the 3D HZP rod ejection scenario of the OECD/NEA and U.S. NRC PWR MOX/UO_2 core transient benchmark (Kozlowski & Downar, 2007).

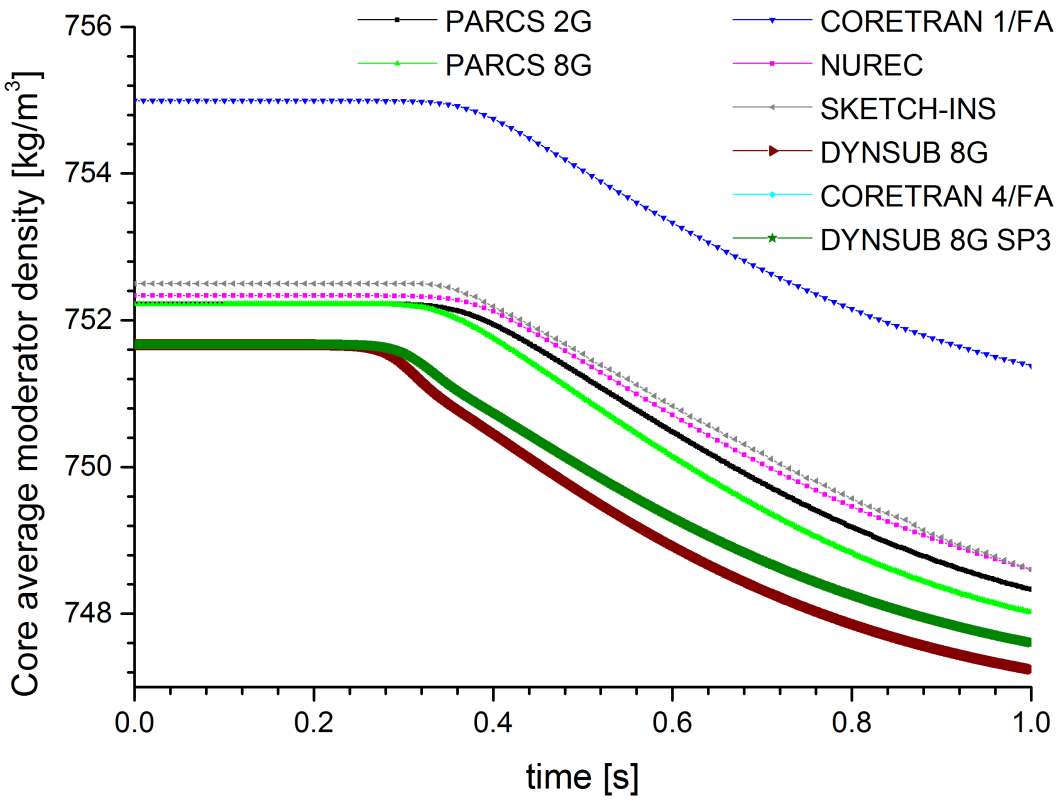

Figure 78: Comparison of transient core average moderator density computed by DYNSUB and benchmark participants for the 3D HZP rod ejection scenario of the OECD/NEA and U.S. NRC PWR MOX/UO_2 core transient benchmark (Kozlowski & Downar, 2007).

Appendix H NURISP boron dilution benchmark

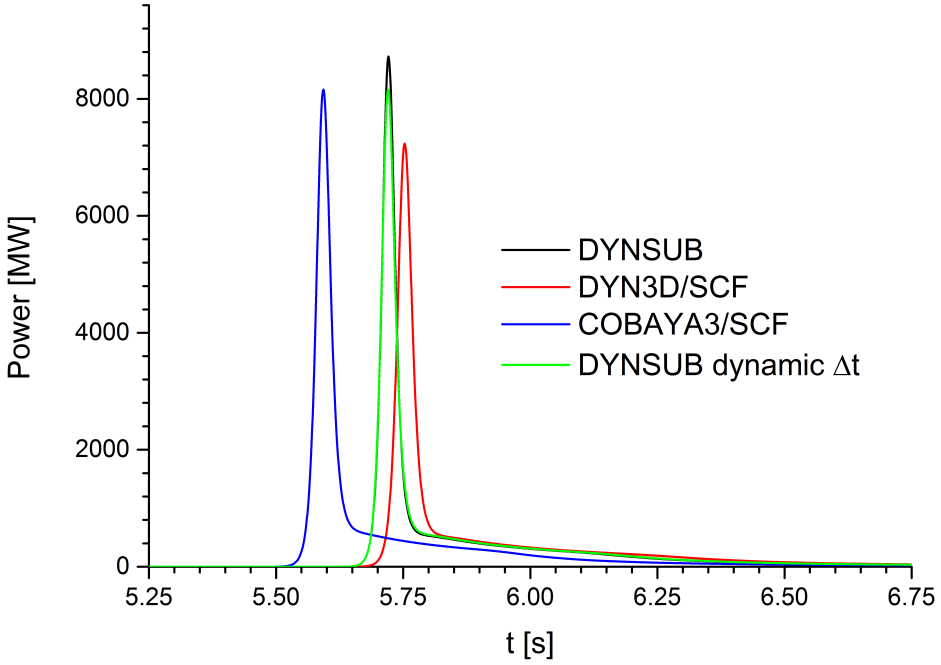

Figure 80: Temporal evolution of the thermal reactor power determined by DYNSUB, DYN3D/SCF and CBY/SCF for scenario 1 of the NURISP boron dilution benchmark

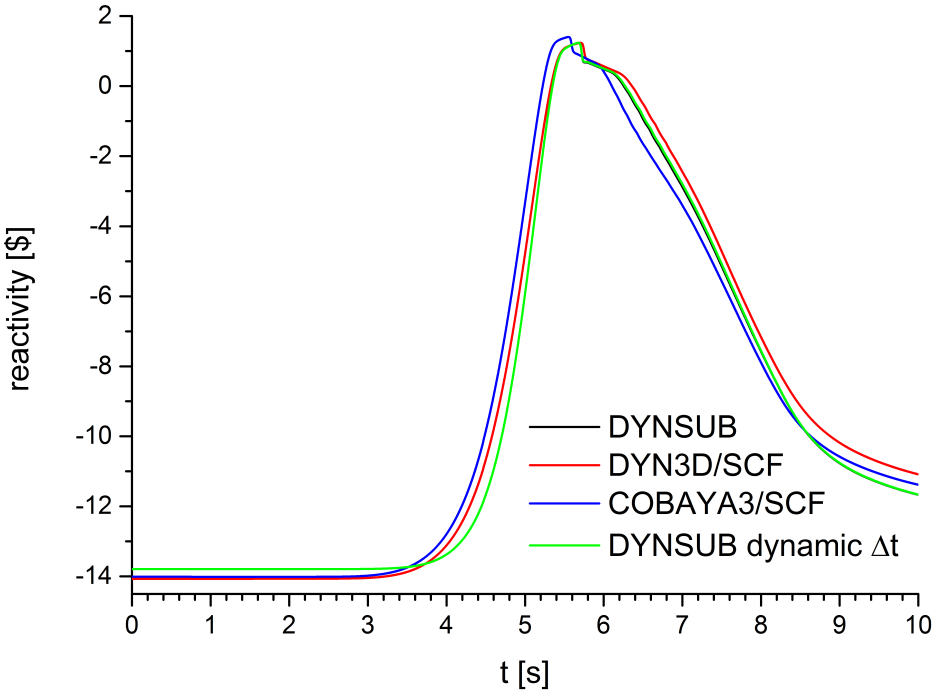

Figure 81: Temporal evolution of the reactivity determined by DYNSUB, DYN3D/SCF and CBY/SCF for scenario 1 of the NURISP boron dilution benchmark

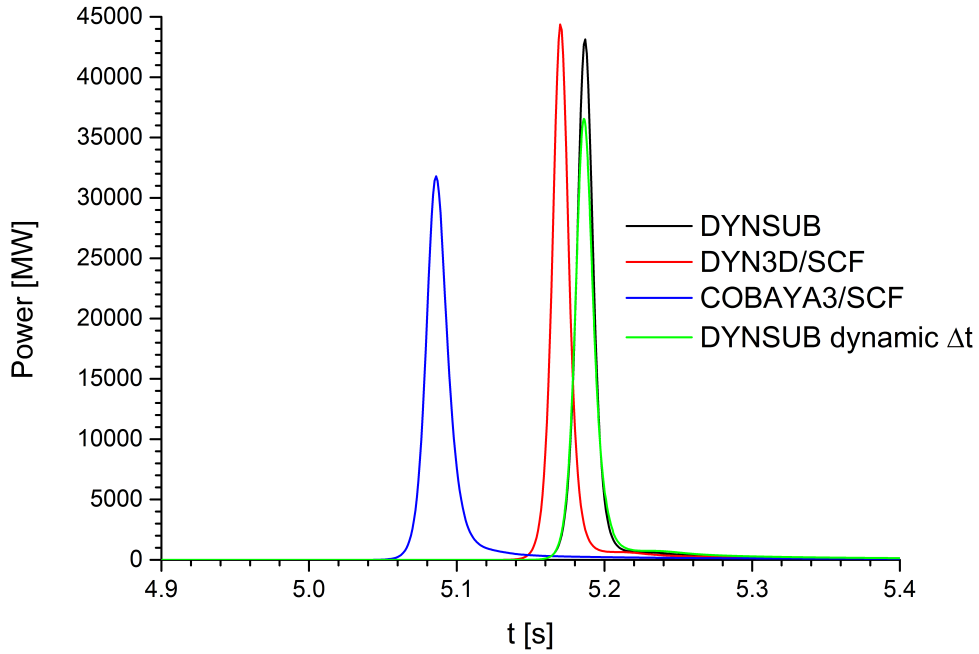

Figure 82: Temporal evolution of the thermal reactor power determined by DYNSUB, DYN3D/SCF and CBY/SCF for scenario 2 of the NURISP boron dilution benchmark

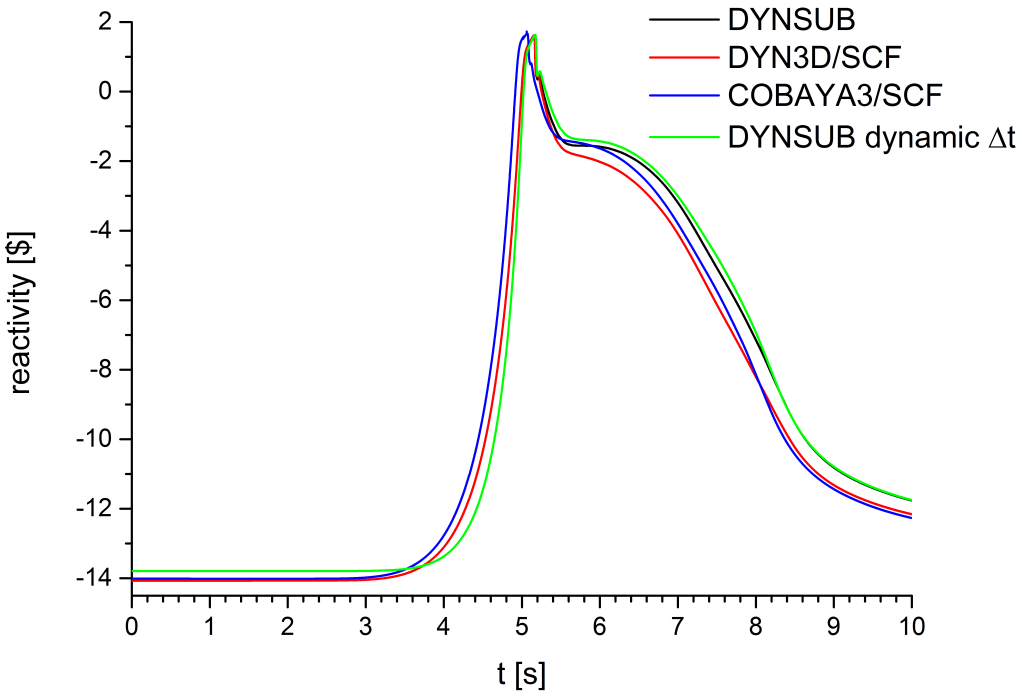

Figure 83: Temporal evolution of the reactivity determined by DYNSUB, DYN3D/SCF and CBY/SCF for scenario 2 of the NURISP boron dilution benchmark

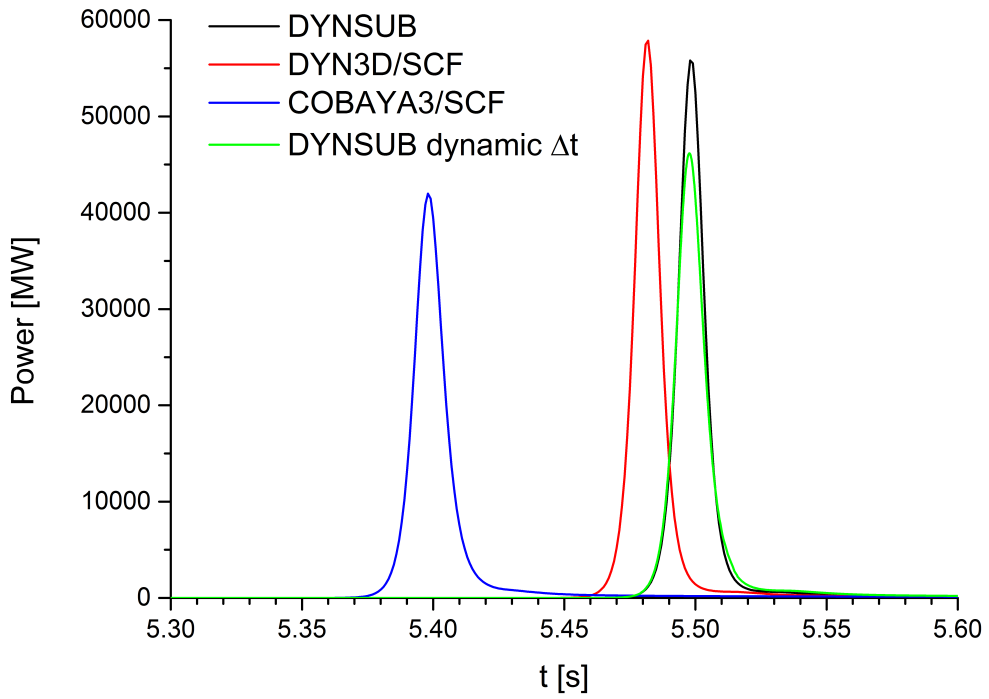

Figure 85: Temporal evolution of the thermal reactor power determined by DYNSUB, DYN3D/SCF and CBY/SCF for scenario 3 of the NURISP boron dilution benchmark

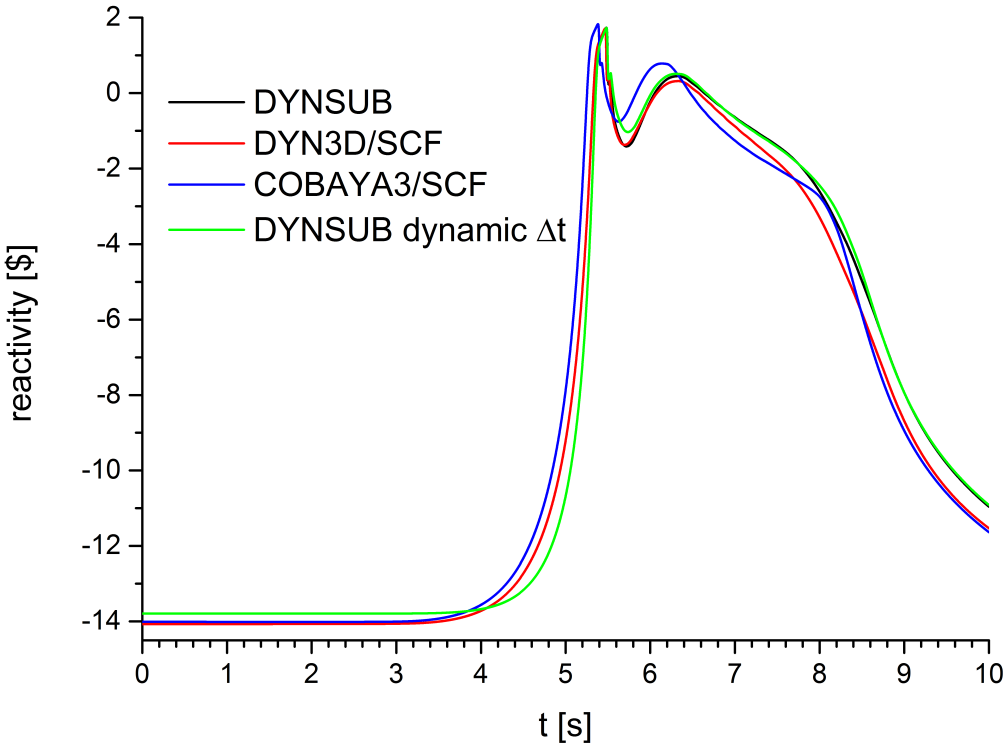

Figure 84: Temporal evolution of the reactivity determined by DYNSUB, DYN3D/SCF and CBY/SCF for scenario 3 of the NURISP boron dilution benchmark

Appendix I PWR Main Steam Line Break benchmark

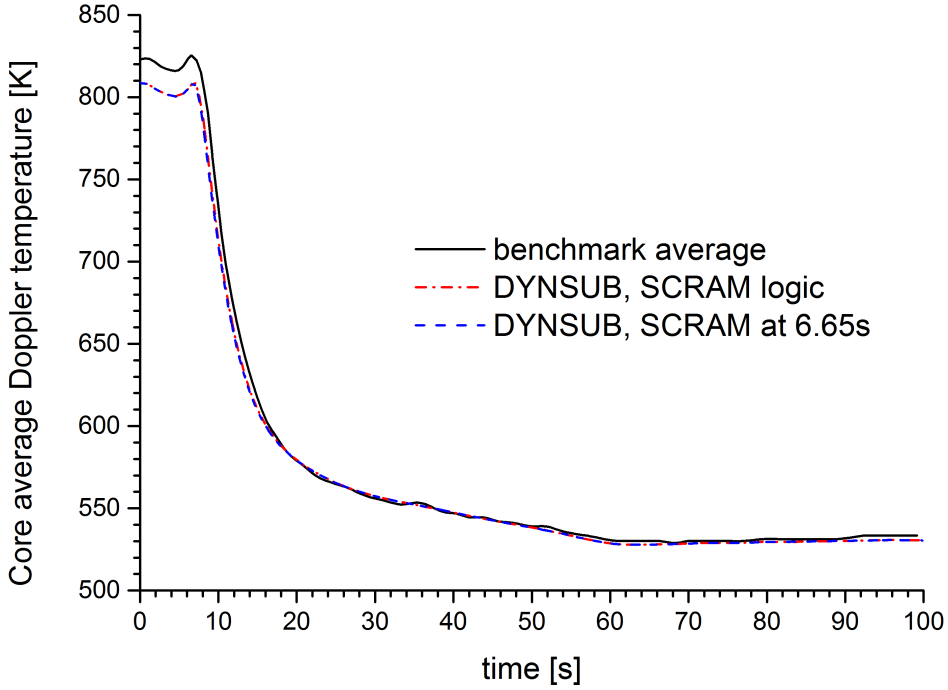

Figure 86: Temporal evolution of core averaged Doppler temperature as predicted by DYNSUB and benchmark participants for the first MSLB scenario (Todorova, et al., 2002)

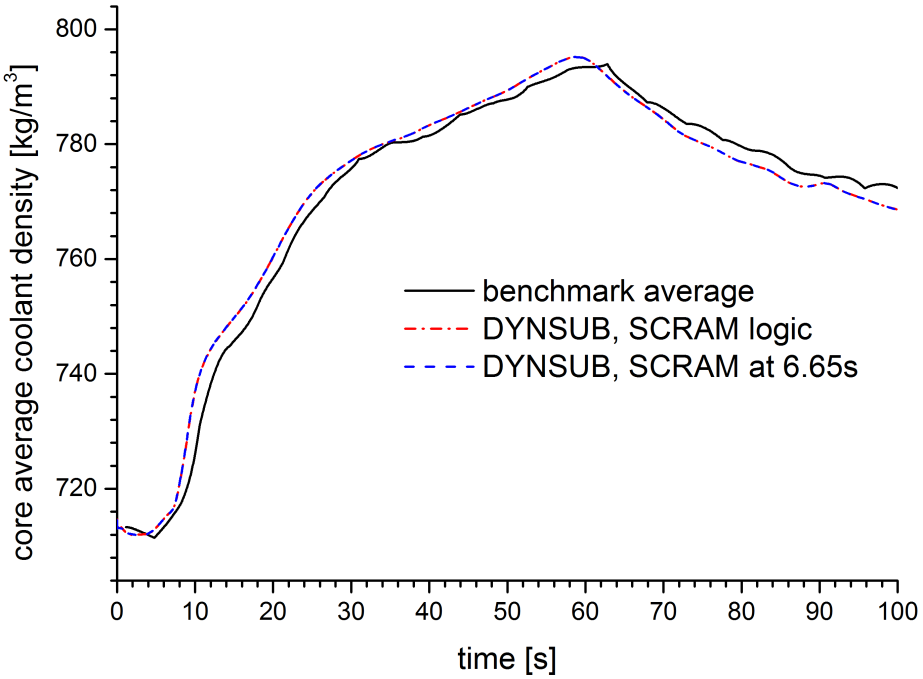

Figure 87: Temporal evolution of core averaged coolant density as predicted by DYNSUB and benchmark participants for the second MSLB scenario (Todorova, et al., 2002)

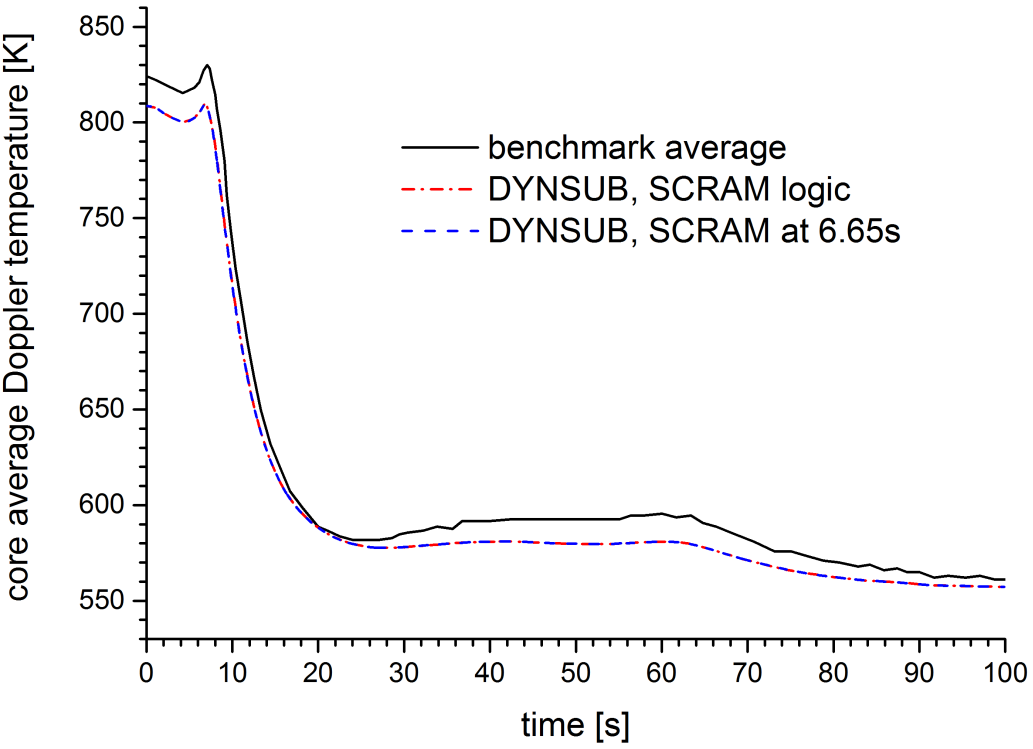

Figure 88: Temporal evolution of core averaged Doppler temperature as predicted by DYNSUB and benchmark participants for the second MSLB scenario (Todorova, et al., 2002)

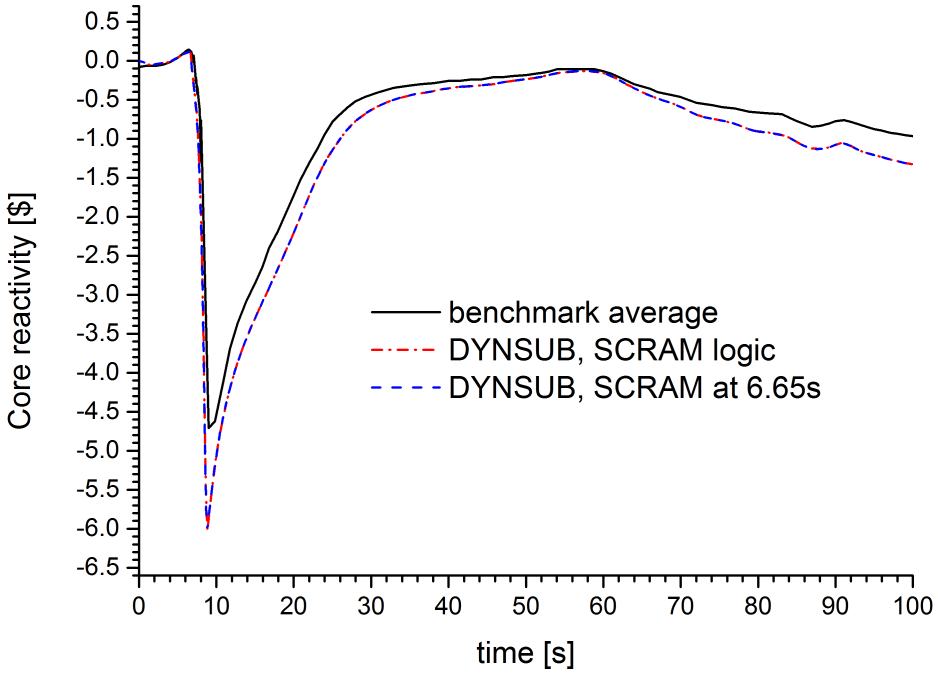

Figure 89: Temporal evolution of core reactivity as evaluated by DYNSUB and benchmark participants for the second MSLB scenario (Todorova, et al., 2002)

Appendix K SPERT III E-core

The SPERT III facility is a small thermal research reactor constructed to analyze its dynamic behavior. The E-core was designed to represent a typical commercial PWR (Dugone, 1965). It resembles the latter reactor type in terms of fuel, moderator, coolant flow rate and system pressure but not its size. Unlike the commercial PWRs, the primary coolant of SPERT III E-core, however, does not contain any soluble boron. Moreover, the core also had a minimal fission product inventory allowing for modeling it with SSS2, SSS2/SCF and DYNSUB without considering fuel depletion.

The radial layout of the SPERT III E-core at the mid plane as modeled with Serpent 2 based on (Dugone, 1965) is shown in Figure 40 in section 6.1.1. The core contains a total of 60 fuel assemblies and has an active height of only 97.282 cm. In the core center, one finds the cross shaped transient rod (TR) surrounded by four fuel assemblies that contain 16 rods in a 4x4 square array. The blades of the TR are 13.0175 cm wide and 0.476 cm thick. As a whole the TR is 2.3876 m long consisting of two sections. The lower absorber section of the transient rod is made from 1.35 wt% ^{10}B in stainless steel and extends over 96.52 cm. Its upper section is pure stainless steel and is usually in the active core.

The 4x4 fuel assemblies are 6.35 x 6.35 cm square. Their 4.8 % enriched UOX fuel rods are placed inside with 1.486 cm pitch. Furthermore, they have an overall length of 1.03632 m and a diameter of 1.184 cm. Both the fuel rod cladding with a thickness of 0.051 cm and the assembly cans are made from stainless steel. The gas gap and plenum in the pins is filled with helium. The UOX fuel pellets have a density of 10.5 g/cm^3 and a diameter of 1.067 cm.

The majority of the SPERT III E-core fuel assemblies unlike the ones surrounding the TR contain 25 fuel rods in a canned 5x5 array. These assemblies have the same pin pitch and are made from the same type of fuel rods as their 16-rod counterparts. They are 7.62 x 7.62 cm square.

As seen in Figure 40, on top of the 4x4 fuel assemblies surrounding the TR eight more are located throughout the reactor core. They are the fuel followers of the eight control rods of the E-core. The poison section of these control rods is square box constructed from a 0.472 cm thick stainless steel plate containing 1.35 wt% ^{10}B. The poison section has a length of 1.168 m and its follower occupies 1.15927 m in axial direction.

Several filler pieces consisting of stainless steel and filled with water hold the 60 fuel assemblies in place inside the reactor core skirt. Between core skirt and the reactor pressure vessel (RPV) wall, there are four thermal shields with water separating them.

The active reactor core rests between a bottom and a top support grid both of which are described in detail in (Olson, 2012). In the RPV, there are water plena below and above the core support structures (Dugone, 1965).

SPERT III's primary system consists of two loops. The primary system and the RPV have been designed for an operating pressure and temperature of 17.33 MPa and 616 K. Each of the loops contains two canned-rotor pumps operating in parallel and a single heat exchanger. The heat removal capacity of the primary system is 60 MW. The E-core, however, has been designed to produce 20 MW under nominal conditions.

The primary coolant enters the RPV at the bottom at passes upward through the active core. In the upper part of the vessel, it reverses direction and flows downwards in the gaps between the thermal shields. The primary coolant exists the RPV near the bottom.

For the RIA experiments conducted with the SPERT III E-core (McCardell, et al., 1969), all control rods were withdrawn to a position corresponding to the desired reactivity insertion. The reactor is then maintained critical by inserting the poison section of the TR into the lower part of the core. Afterwards, the transient is initiated by accelerating the TR from its initial position out of the core. Its acceleration was measured to be 50.8 $\mathrm{m/s^2}$.

The initial operating conditions of the REA tests can be classified into four groups listed in Table 48 (McCardell, et al., 1969). For each groups many different reactivity insertions were studied. These range from delayed super-critical over prompt super-critical into super-prompt critical. A total of 58 accident scenarios were tested.

The experimental data available for all transients of the SPERT III E-core studied are the maximal reactor power, the timing of the power peak, the energy release up to peak power and the reactivity compensation at peak power. For the startup experiments, also the reactor period was determined. Besides these single values, the evolution of core power, reactivity and integral energy release with time has been recorded. The latter data is included in the report (McCardell, et al., 1969) as plots whose time scales have been optimized to clearly visualize the shape of the power bursts. As a consequence, this data is only available a time interval depending on the test case and not over the length of the entire experiment.

The dynamic reactor response was obtained by analyzing reactor power measurements. For these measurements five ex-core uncompensated ^{10}B lined ion chambers were used. The chambers were positioned at different distances from the core. Their current output as a function of reactor power was calibrated using a series of static reactor operation experiments. Cobalt wire activation measurements were carried out for 294 K, 394 K and 478 K. Results had a standard deviation of 15 % for reactor power measurements and 17 % for energy released.

Table 48: Accident conditions of the SPERT III E-core RIA tests (McCardell, et al., 1969)

Initial condition	Coolant inlet T [K]	System pressure [MPa]	Average coolant flow rate [m/s]	Initial reactor power [MW]
Cold startup	294	0.1013	0	0.00005
Hot startup	400 / 533	10.43	≤ 7.3152	0.00005
Hot standby	533	10.43	4.2672	1.0
Operating power	533	10.43	4.2672	20.0

Furthermore, a number of low- and high-power primary system heat balance experiments were performed with a coolant inlet temperature of 533 K. The one standard deviation spread in the experimental data was 10 % for reactor power and 13 % for energy released.

For the startup experiments, the reactor period was calculated from the power measurements assuming an initial exponential power rise. To enable a reliable measurement, experiments were designed such that two decades of pure exponential power rise could be observed before the evolution of power being affected by feedback effects. The standard deviation of reactor periods was estimated to be 2 %.

For the low initial power RIAs, the inserted reactivity was computed based on the inhour equation of the point kinetic model. To do so, one needs the reactor period, the reduced prompt neutron generation time and delayed neutron parameters. Combining the measurements uncertainties of the contributing quantities one standard deviation for the inserted reactivity is evaluated to be 4 %.

For high power tests, it is not possible to measure an undisturbed reactor period. Consequently, the inhour equation was not utilized to determine inserted reactivity. Instead a control rod worth curve had to be established. The variance of the control worth data about a least-squares fit was used as uncertainty estimate. Thus, one standard deviation becomes 4 %.

The reactivity compensation at peak power was computed employing the point kinetics model. The input quantities are the evolution of reactor power, reduced prompt neutron generation time, reactor period and delayed neutron parameters. Combining the uncertainties of the inputs, one standard deviation for the reactivity compensation is about 11 %. Since no reactor period measurements can be performed for high power tests, the reactivity compensations quoted for these cases have been approximated based on the reactivity over time evolution curves obtained from point kinetics by specifying the steady-state conditions at the beginning of the transient. For these, no estimate of the measurement uncertainty can be made.

Table 49: Branch structure of cold startup DYNSUB SPERT III E-core cross section library

Moderator density [kg/m^3]	Fuel Doppler temperature [K]
998.027	300
992.281	490
983.288	720
971.896	900
958.462	1200
766.882	1500
575.303	
383.723	
192.143	

Table 50: Branch structure of hot standby and operating power DYNSUB SPERT III E-core cross section library

Moderator density [kg/m^3]	Fuel Doppler temperature [K]
790.058	533
762.456	720
731.661	900
681.971	1200
545.771	1500
409.183	
272.789	
136.394	

Table 51: Overview of initial conditions of the eight selected SPERT III E-core RIA tests (McCardell, et al., 1969)

Test No.	Reactivity insertion [$]	Inlet coolant T [K]	Average coolant flow speed [m/s]	Reactor power [MW]	System pressure [MPa]
18	0.90(0.04)	294.3(2.2)	0.0	0.00005	0.1013
49	1.00(0.04)	297.6(2.2)	0.0	0.00005	0.1013
43	1.21(0.05)	298.7(2.2)	0.0	0.00005	0.1013
79	0.86(0.03)	540.4(2.2)	4.2672	1.1(0.1)	10.43
81	1.17(0.04)	535.4(2.2)	4.2672	0.9(0.1)	10.43
82	1.29(0.04)	535.9(2.2)	4.2672	1.2(0.1)	10.43
85	0.87(0.04)	534.8(2.2)	4.2672	19.0(1.0)	10.43
86	1.17(0.05)	534.3(2.2)	4.2672	19.0(1.0)	10.43

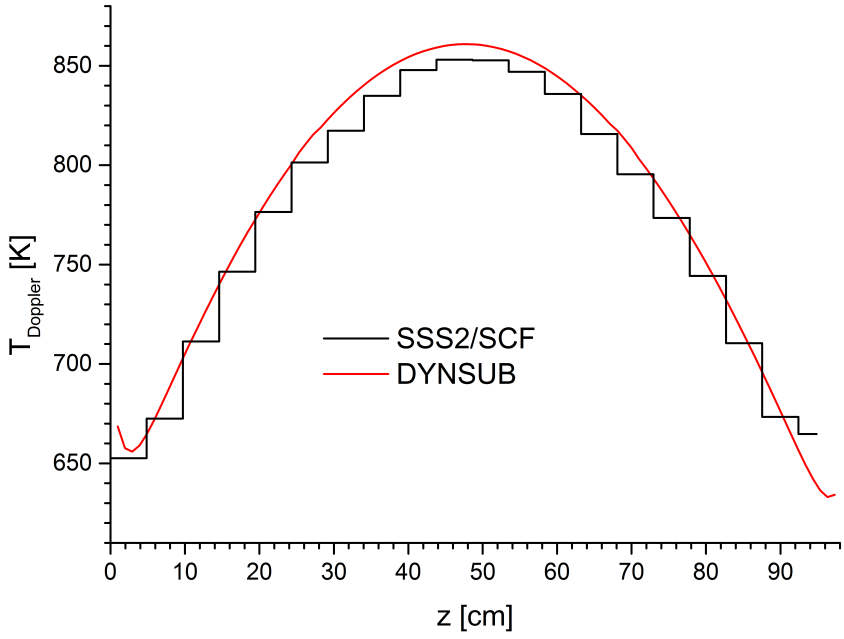

Figure 90: Comparison of SPERT III operating power radially averaged Doppler temperature profiles as computed by SSS2/SCF and DYNSUB

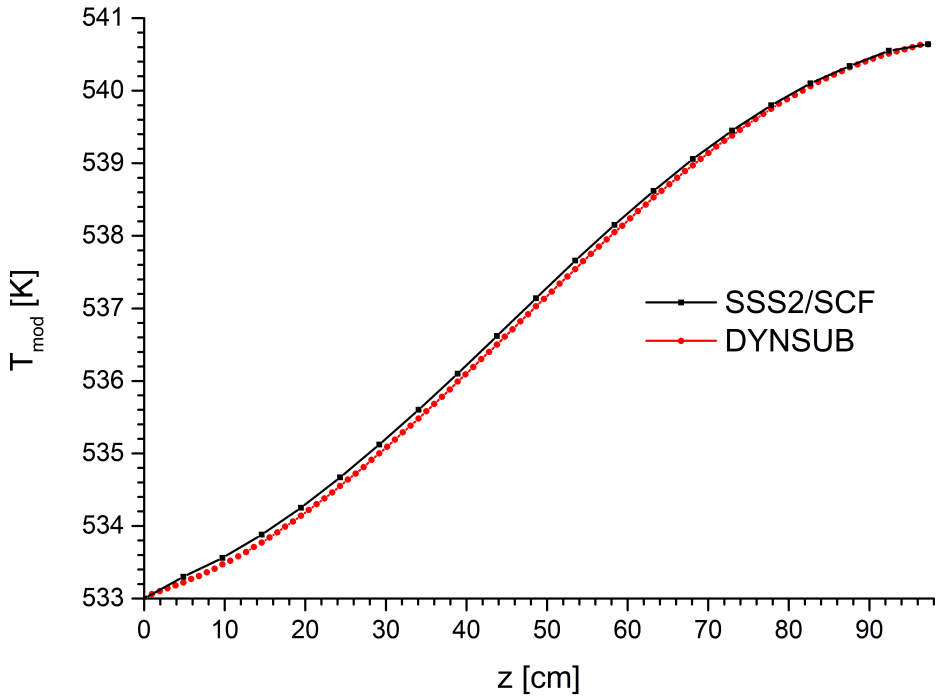

Figure 91: Comparison of SPERT III operating power radially averaged moderator temperature profiles as predicted by SSS2/SCF and DYNSUB

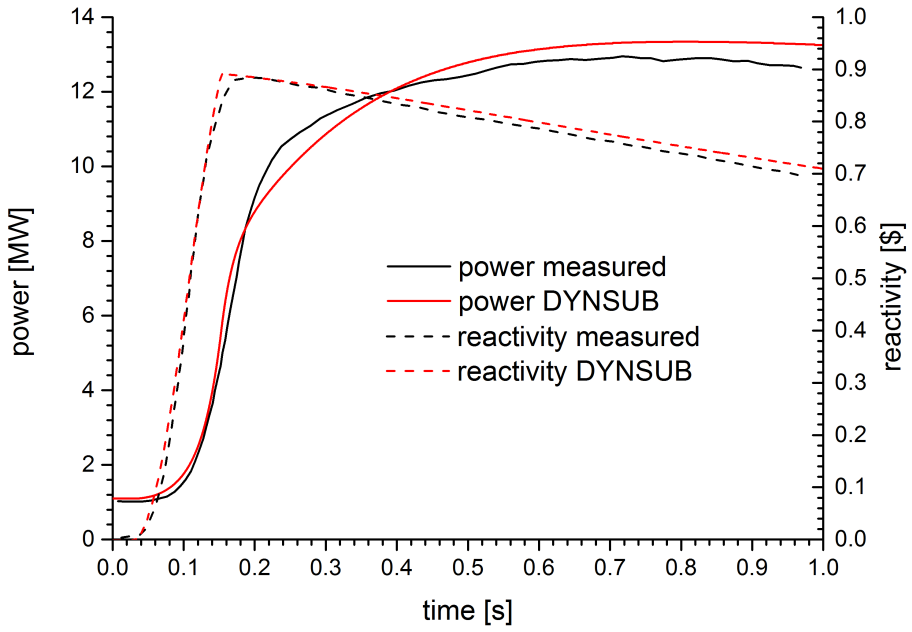

Figure 92: DYNSUB core power and reactivity results for hot standby test 79 compared with experimental data (McCardell, et al., 1969)

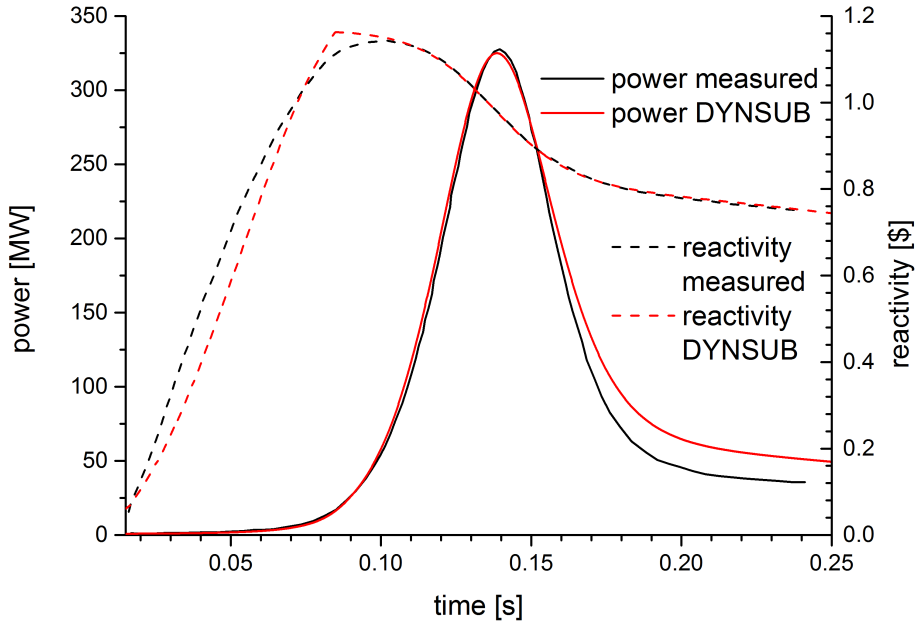

Figure 93: DYNSUB core power and reactivity results for hot standby test 81 compared with experimental data (McCardell, et al., 1969)

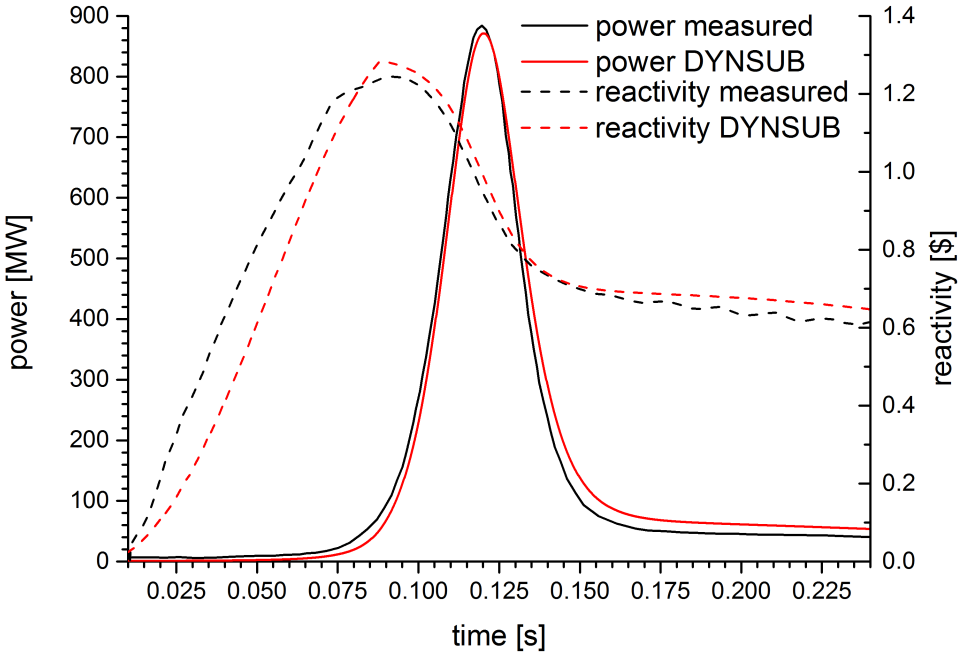

Figure 94: DYNSUB core power and reactivity results for hot standby test 82 compared with experimental data (McCardell, et al., 1969)

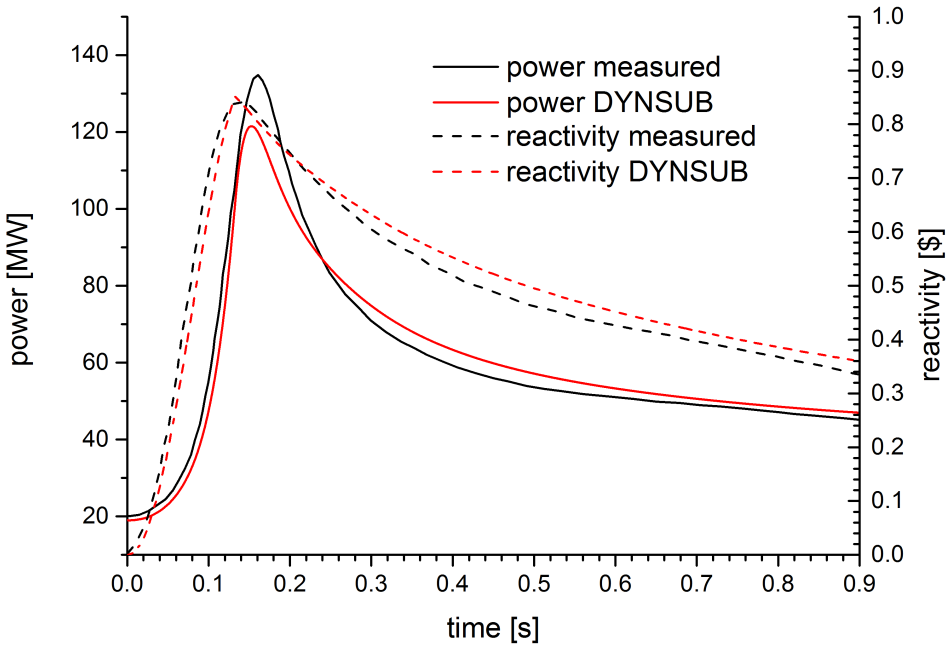

Figure 95: DYNSUB core power and reactivity results for operating power test 85 compared with experimental data (McCardell, et al., 1969)

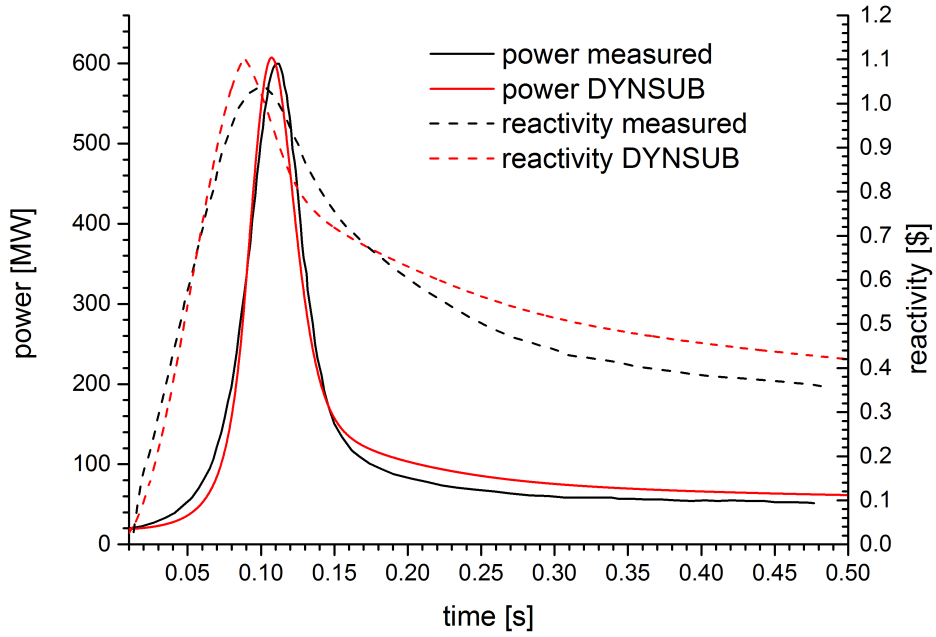

Figure 96: DYNSUB core power and reactivity results for operating power test 86 compared with experimental data (McCardell, et al., 1969)

Appendix L PWR MOX/UO_2 benchmark pin-by-pin

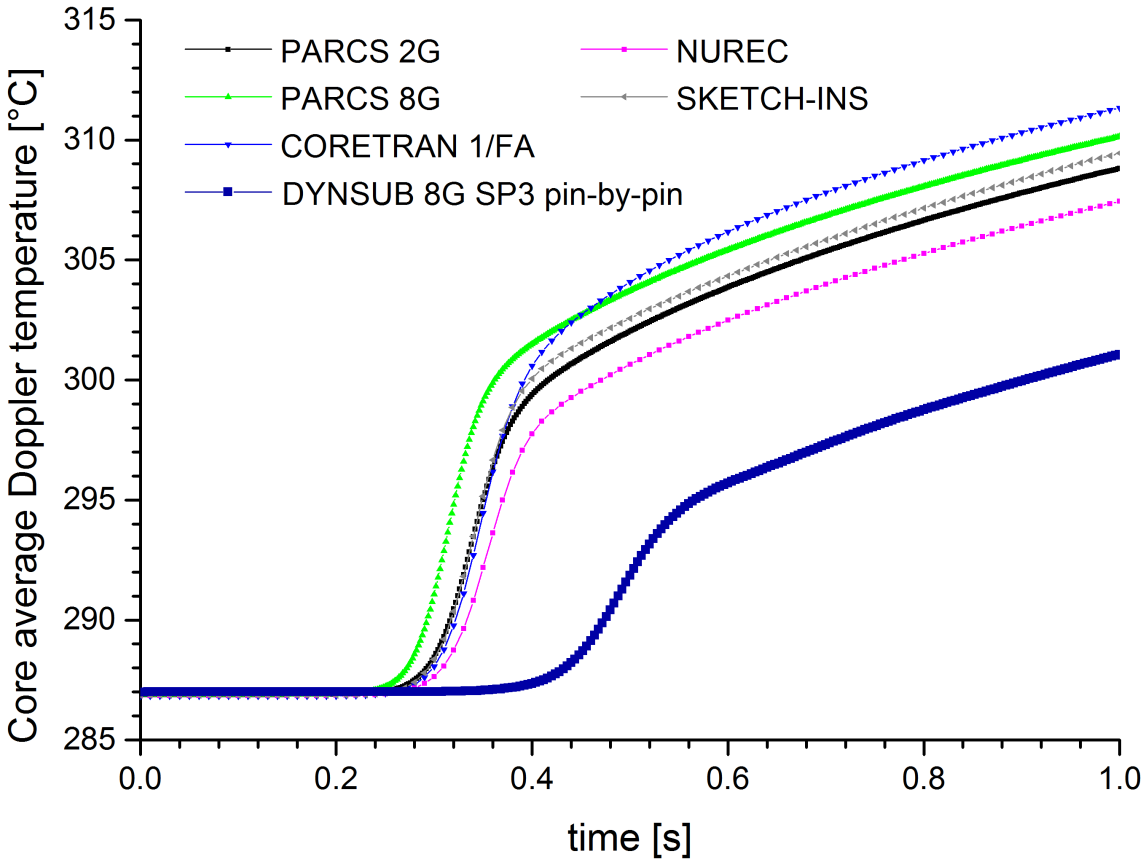

Figure 97: Comparison of transient core averaged Doppler temperature as predicted by DYNSUB pin-by-pin and benchmark participants for the 3D HZP rod ejection scenario of the OECD/NEA and U.S. NRC PWR MOX/UO_2 core transient benchmark (Kozlowski & Downar, 2007)

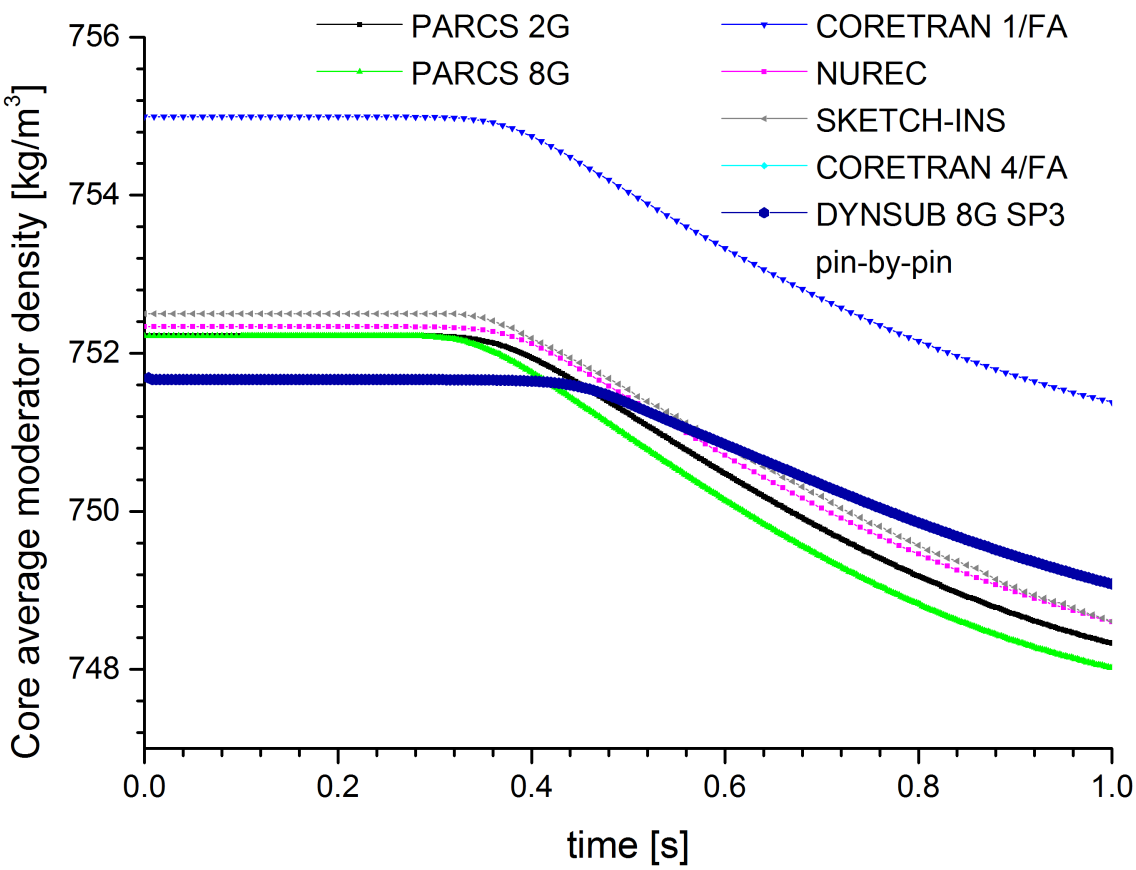

Figure 98: Comparison of transient core averaged moderator density evaluated by DYNSUB pin-by-pin and benchmark participants for the 3D HZP rod ejection scenario of the OECD/NEA and U.S. NRC PWR MOX/UO_2 core transient benchmark (Kozlowski & Downar, 2007)

References

Anchel, F. et al., 2012. Uncertainty and sensitivity analysis in the neutronic parameters generation for BWR and PWR coupled thermal-hydraulic-neutronic simulations. *Nuclear Engineering and Design 246*, pp. 98-106.

Anon., 2013. [Online]
Available at: http://www.nucleartourist.com/images/fuel.gif
[Accessed 06 03 2015].

Aoki, S., Suemura, T., Ogawa, J. & Takeda, T., 2009. Analysis of the SPERT III E-core Using ANCK Code with Chord Weighting Method. *Nuclear Science and Technology 46*, pp. 239-251.

Avramova, M. & Ivanov, K., 2010. Verification, validation and uncertainty quantification in multi-physics modeling for nuclear reactor design and safety analysis. *Progress in Nuclear Energy 52*, pp. 601-614.

Becker, B., Dagan, R. & Lohnert, G., 2009. Proof and implementation of the stochastic formula for the ideal gas, energy dependent scattering kernel. *Annals of Nuclear Energy 36*, pp. 470-474.

Beckert, C. & Grundmann, U., 2008. *Entwicklung einer Transportnäherung für das reaktordynamische Rechenprogramm DYN3D,* s.l.: s.n.

Bernnat, W. et al., 2012. *Coupled Monte Carlo Neutronics and Thermal Hydraulics for Power Reactors.* Knoxville, Tennessee, USA, s.n.

Borkowsky, J., 1997. *SIMULATE-3K: The Transient Analysis Module for the Studsvik CMS.* s.l., s.n.

Bousbia-Salah, A. & D'Auria, F., 2007. Use of coupled code technique for Best Estimate safety analysis of nuclear power plants. *Progress in Nuclear Energy 49*, pp. 1-13.

Bowman, S. & Gill, D., 2006. *Validation of Standardized Computer Analyses for Licensing Evaluation/TRITON Two-Dimensional and Three-Dimensional Models for Light Water Reactor Fuel.* Vancouver, Canada, s.n.

Brantley, P. & Larsen, E., 2000. The Simplified P3 Approximation. *Nuclear Science and Engineering 134*, pp. 1-12.

Brown, F., 2006. *On the Use of Shannon Entropy of the Fission Distribution for Assessing Convergence of Monte Carlo Criticality Calculations.* Vancouver, Canada, s.n.

Brown, F., 2007. *Wielandt acceleration for MCNP5 Monte Carlo eigenvalue calculations.* s.l., s.n.

Calleja, M. et al., 2014a. Investigations of boron transport in a PWR core with COBAYA3/SUBCHANFLOW inside the NURESIM platform. *Annals of Nuclear Energy 66*, pp. 74-84.

Calleja, M. et al., 2014b. Coupling of COBAYA3/SUBCHANFLOW inside the NURESIM platform and validation using selected benchmarks. *Annals of Nuclear Energy 71*, pp. 145-158.

Chao, Y. A. & Yamamoto, A., 2012. *The Explicit Representation for the Angular Flux Solution in the Simplified PN (SPN) Theory*. Knoxville, Tennessee, s.n.

Chauliac, C. et al., 2011. NURESIM - A European simulation platform for nuclear reactor safety: Multi-scale and multi-physics calculations, sensitivity and uncertainty analysis. *Nuclear Engineering and Design 241*, pp. 3416-3426.

Collins, B., Seker, V., Downar, T. & Xu, Y., 2012. *Post-refinement Multiscale Method for Pin Power Reconstruction.* Knoxville, Tennessee, s.n.

Colson, L., n.d. [Online]
Available at: http://www.eia.doe.gov/cneaf/nuclear/page/nuc_reactors/pwr.html
[Accessed 06 03 2015].

Cooper, J. & Dooley, R., 2007. *Revised Release in the IAPWS Industrial Formulation 1997 for the Thermodynamic Properties of Water and Steam,* s.l.: s.n.

Dürigen, S., 2013. *Neutron Transport in Hexagonal Reactor Cores Modeled by Trigonal-Geometry Diffusion and Simplified P3 Nodal Methods,* s.l.: s.n.

Dall'Osso, A., 2002. *Reducing Rod Cusping Effect in Nodal Expansion Method Calculations.* Seoul, Korea, s.n.

DeHart, M. & Bowman, S., 2011. Reactor Physics Methods and Analysis Capabilities in SCALE. *Nuclear Technology 174*, pp. 196-213.

Downar, T., Lee, C. & Jiang, G., 2000. *An Assessment of Advanced Nodal Methods for MOX Fuel Analysis in Light Water Reactors.* Pittsburg, Pennsylvania, s.n.

Dufek, J. & Hoogenboom, J., 2014. Description of a stable scheme for steady-state coupled Monte Carlo-thermal-hydraulic calculations. *Annals of Nuclear Energy 68*, pp. 1-3.

Dugone, J., 1965. *SPERT III Reactor Facility: E-core Revision,* s.l.: U.S. Atomic Energy Commission.

Dumonteil, E. et al., 2014. Particle clustering in Monte Carlo criticality calculations. *Annals of Nuclear Energy 63*, pp. 612-618.

Ellis, M., Watson, J. & Ivanov, K., 2013. Progress in the development of an implicit steady state solution in the coupled code TRACE/PARCS. *Progress in Nuclear Energy 66*, pp. 1-12.

Endo, T. & Tatsumi, M., 2008. *Study on kinetic transport solvers for pin-by-pin core calculation.* Interlaken, Switzerland, s.n.

Espel, F., Avramova, M., Ivanov, K. & Misu, S., 2013. New developments of the MCNP/CTF/NEM/NJOY code system - Monte Carlo based coupled code for high accuracy modeling. *Annals of Nuclear Energy 51*, pp. 18-26.

Forget, B., Xu, S. & Smith, K., 2014. Direct Doppler broadening in Monte Carlo simulations using the multipole representation. *Annals of Nuclear Energy 64*, p. 78–85.

Fridman, E. & Leppänen, J., 2011. On the use of the Serpent Monte Carlo code for few-group cross section generation. *Annals of Nuclear Energy 38*, pp. 1399-1405.

Gaston, D. et al., 2012. Parallel multiphysics algorithms and software for computational nuclear engineering. *Journal of Physics: Conference Series, Vol. 180*.

Gaston, D., Newman, C., Hansen, G. & Lebrun-Grandie, D., 2009. MOOSE: A parallel computational framework for coupled code systems of non-linear equations. *Nuclear Engineering and Design 239*, pp. 1768-1778.

Gill, D., Aumiller, D. & Griesheimer, D., 2014. *Monte Carlo and thermal-hydraulic coupling via PVMEXEC.* Kyoto, Japan, s.n.

Glaeser, H., 2008. GRS method for uncertainty and sensitivity evaluation of code results and applications. *Science and Technology of Nuclear Installations*.

Gleicher, F. et al., 2014. *The coupling of the Neutron Transport Application RattleSnake to the Nuclear Fuels Performance Application Bison under the MOOSE Framework.* Kyoto, Japan, s.n.

Gomez-Torres, A., Sanchez-Espinoza, V., Ivanov, K. & Macian-Juan, R., 2012a. DYNSUB: A high fidelity coupled code system for the evaluation of local safety parameters - Part I: Development, implementation and verification. *Annals of Nuclear Energy 48*, pp. 108-122.

Gomez-Torres, A., Sanchez-Espinoza, V., Ivanov, K. & Macian-Juan, R., 2012b. DYNSUB: A high fidelity coupled code system for the evaluation of local safety parameters - Part II: Comparison of different temporal schemes. *Annals of Nuclear Energy 48*, pp. 123-129.

Grandi, G., 2014. *Validation of CASMO5/SIMULATE-3K using the Special Power Excursion Reactor Test Reactor III E-core: Cold start-up, hot start-up, hot standby and full power conditions.* Kyoto, Japan, s.n.

Grandi, G. & Moberg, L., 2012. *Qualification of the CASMO5/SIMULATE-3K Against the SPERT III E-core cold startup experiments.* Knoxville, Tennessee, s.n.

Grimm, P., Aboudy, M., Galperin, A. & Segev, M., 1996. A Test of Main Stream Pin Power Reconstruction Methods. *Nuclear Science and Engineering*, Volume 122, pp. 395-406.

Grundmann, U. & Mittag, S., 2011. Super-homogenization factors in pinwise calculations by the reactor dynamics code DYN3D. *Annals of Nuclear Energy 38*, pp. 2111-2119.

Grundmann, U. & Mittag, S., 2011. Super-homogenization factors in pinwise calculations by the reactor dynamics code DYN3D. *Annals of Nuclear Energy,* Volume 38, pp. 2111-2119.

Grundmann, U., Rohde, U., Mittag, S. & Kliem, S., 2005. *DYN3D Version 3.2 - Code for Calculation of Transients in Light Water Reactors (LWR) with Hexagonal and Quadratic Fuel Elements,* s.l.: s.n.

Hadek, J. & Mittag, S., 2009. *Validation of DYN3D pin-power calculation against experimental VVER-full-core benchmark.* Saratoga Springs, New York, s.n.

Hébert, A., 1993a. A Consistent Technique for the Pin-by-Pin Homogenization of a Pressurized Water Reactor Assembly. *Nuclear Science and Engineering,* Volume 115, pp. 227-238.

Hebért, A. & Mathonniere, G., 1993b. Development of a Third-Generation Superhomogenization Method for the Homogenization of a Pressurized Water Reactor Assembly. *Nuclear Science and Engineering 115*, pp. 129-141.

Hermann, O., 2000. *Benchmark of SCALE (SAS2H) Isotopic Predictions of Depletion Analyses for San Onofre PWR MOX Fuel,* s.l.: s.n.

Hermann, O., Bowman, S., Brady, M. & Parks, C., 1995. *Validation of the SCALE System for PWR Spent Fuel Isotopic Composition Analyses,* s.l.: s.n.

Herrero, J., Garcia-Herranz, N., Cuervo, D. & Ahnert, C., 2012. Neighborhood-corrected inetrface discontinuity factors for multi-group pin-by-pin diffusion calculations for LWR. *Annals of Nuclear Energy 46*, pp. 106-115.

Herrero, J., Jimenez, J., Aragones, J. & Ahnert, C., 2009. *Performance of whole core pin-by-pin calculations by domain decomposition through alternate dissections in steady-state and transient calculations.* Saratoga Springs, New York, USA, s.n.

Horelik, N., Forget, B., Smith, K. & Siegel, A., 2014. *Domain decomposition and terabyte tallies with the OpenMC Monte Carlo neutron transport code.* Kyoto, Japan, s.n.

Horelik, N., Herman, B., Forget, B. & Smith, K., 2016. *Benchmark for Evaluation and Validation of Reactor Simulations (BEAVRS), rev 2.0.* Sun Valley, Idaho, USA, s.n.

Illas, G., Gauld, I. & Radulescu, G., 2012. Validation of new depletion capabilities and ENDF/B-VII data libraries in SCALE. *Annals of Nuclear Energy 46*, pp. 43-55.

Imke, U. & Sanchez, V., 2012. Validation of the Subchannel Code SUBCHANFLOW Using NUPEC PWR Tests (PSBT). *Science and Technology of Nuclear Installations*, pp. 1-12.

Ivanov, A., Sanchez, V., Stieglitz, R. & Ivanov, K., 2013. High fidelity simulation of conventional and innovative LWR with the coupled Monte-Carlo thermal-hydraulic system MCNP-SUBCHANFLOW. *Nuclear Engineering and Design 262*, pp. 264-275.

Ivanov, A., Sanchez, V., Stieglitz, R. & Ivanov, K., 2014. *Large-Scale Monte Carlo calculations with thermal-hydraulic feedback.* Kyoto, Japan, s.n.

Ivanov, A., Sanchez, V., Stieglitz, R. & Ivanov, K., 2015. Large-scale Monte Carlo neutron transport calculations with thermal-hydraulic feedback. *Annals of Nuclear Energy*, Volume In press.

Ivanov, B. et al., 2002. *VVER-1000 Coolant Transient Benchmark - Phase 1 (V1000CT-1),* s.l.: OECD Nuclear Energy Agency/Nuclear Science Committee.

Ivanov, K. & Avramova, M., 2007. Challenges in coupled thermal-hydraulics and neutronic simulations for LWR safety analysis. *Annals of Nuclear Energy 34*, pp. 501-513.

Ivanov, K., Avramova, M., Kodeli, I. & Sartori, E., 2007b. *Benchmark for Uncertainty Analysis in Modeling (UAM) for Design, Operation and Safety Analysis of LWRs,* s.l.: OECD Nuclear Energy Agency/Nuclear Science Committee.

Ivanov, K. et al., 1999. *Pressurized Water Reactor Main Steam Line Break (MSLB) Benchmark - Volume I: Final Specification,* s.l.: OECD Nuclear Energy Agency/Nuclear Science Committee.

Ivanov, K. et al., 2007a. Validation of coupled thermal-hydraulics and neutronics codes for safety analysis by international cooperation. *Nuclear Teachnology 157*, pp. 177-195.

Jaeger, W. et al., 2013. Comparison of Two-Phase Flow Modeling Capabilities of CFD, Sub Channel and System Codes by means of Post-Test Calculations of BFBT Transients. *Nuclear Engineering and Design 263*, October, pp. 313-326.

Jarrell, J., Godfrey, A., Evans, T. & Davidson, G., 2012. *Full Core Reactor Analysis: Running Denovo on Jaguar.* Knoxville, Tennessee, s.n.

Jimenez, J., 2010. *Desarrollo e implementacion de la decomposition en subdominios del acolplamiento neutronico-termohidraulico mediante disecciones alternadas con un sistema de calculo multiscala,* s.l.: s.n.

Jimenez, J., Herrero, J., Cuervo, D. & Aragones, J., 2010. *Whole Core Pin-by-Pin Coupled Neutronic-Thermal-hydraulic Steady-State and Transient Calculations using COBAYA3 code.* s.l., s.n.

Jung, Y., Joo, H. & Yoon, J., 2013. *Core Follow Calculation with the nTRACER Numerical Reactor and Verification using Power Reactor Measurement Data.* Sun Valley, Idaho, USA, s.n.

Kaltiaisenaho, T. & Leppänen, J., 2014. *Analysing the Statistics of Group Constant Generated by the Serpent 2 Monte Carlo Code.* Kyoto, Japan, s.n.

Kaushik, D. et al., 2009. *Enabling High-Fidelity Neutron Transport Simulations on Petascale Architectures.* Portland, Oregon, s.n.

Kelly, D., Aviles, B. & Herman, B., 2013. *MC21 analysis of the MIT PWR benchmark: hot zero power results.* Sun Valley, Idaho, USA, s.n.

Kelly, D. et al., 2014. *Analysis of Select BEAVRS PWR Benchmark Cycle 1 Results Using MC21 and OpenMC.* Kyoto, Japan, s.n.

Kelly, D., Sutton, T. & Wilson, S., 2012. *MC21 analysis of the Nuclear Energy Agency Monte Carlo performance benchmark problem.* Knoxville, Tennessee, USA, s.n.

Kliem, S., Mittag, S., Gommlich, A. & Apanadevich, P., 2011. *D3.1.2.2: Definition of a PWR boron dilution benchmark,* s.l.: Nuclear Reactor Integrated Simulation Project.

Kochunas, B., Downar, T. & Liu, Z., 2013. *Parallel 3-D Method of Characteristics in MPACT.* Sun Valley, Idaho, s.n.

Kochunas, B. et al., 2012. *Coupled Full Core Neutron Transport/CFD Simulations of Pressurized Water Reactors.* Knoxville, Tennessee, USA, s.n.

Kotlyar, D., Shaposhnik, Y., Fridman, E. & Shwageraus, E., 2011. Coupled neutronic thermo-hydraulic analysis of full PWR core with Monte-Carlo based BGCore system. *Nuclear Engineering and Design 241*, p. 3777 – 3786.

Kozlowski, T., 2005. *Spatial homogenization methods for pin-by-pin neutron transport calculation,* s.l.: s.n.

Kozlowski, T., 2011. Cell homogenization method for pin-by-pin neutron transport calculations. *Nuclear Science and Engineering,* Volume 169, pp. 1-18.

Kozlowski, T. & Downar, T., 2003. *OECD/NEA AND U.S. NRC PWR MOX/UO2 CORE TRANSIENT BENCHMARK - Final Specification,* s.l.: OECD Nuclear Energy Agency/Nuclear Science Committee.

Kozlowski, T. & Downar, T., 2007. *OECD/NEA and U.S. NRC PWR MOX/UO2 core transient benchmark - Final report,* s.l.: OECD Nuclear Energy Agency/Nuclear Science Committee.

Leppänen, J., 2009. Two practical methods for unionized energy grid construction in continuous-energy Monte Carlo neutron transport calculation. *Annals of Nuclear Energy 36*, p. 878–885.

Leppänen, J., 2010. Performance of Woodcock delta-tracking in lattice physics applications using the Serpent Monte Carlo reactor physics burnup calculation code. *Annals of Nuclear Energy 37*, p. 715–722.

Leppänen, J., 2012. Modeling of Nonuniform Density Distributions in the Serpent 2 Monte Carlo Code. *Nuclear Science and Engineering 174*, p. 318–325.

Leppänen, J., 2013. *Serpent a Continuous-energy Monte Carlo Reactor Physics Burnup Calculation Code,* s.l.: VTT Technical Research Centre of Finland.

Leppänen, J., 2014. *Methodology for spatial homogenization in Serpent 2,* s.l.: s.n.

Leppänen, J. et al., 2014c. Calculation of effective point kinetics parameters in the Serpent 2 Monte Carlo code. *Annals of Nuclear Energy 65*, pp. 272-279.

Leppänen, J. & Mattila, R., 2014. *On the Practical Feasibility of Continuous-Energy Monte Carlo in Spatial Homogenization.* Kyoto, Japan, s.n.

Leppänen, J., Mattila, R. & Pusa, M., 2014b. Validation of the Serpent-ARES code sequence using the MIT BEAVRS benchmark - Initial core at HZP conditions. *Annals of Nuclear Energy*, Volume 69, pp. 212-225.

Leppänen, J. et al., 2014a. The Serpent Monte Carlo code: Status, development and applications in 2013. *Annals of Nuclear Energy*, p. in press.

Leppänen, J., Valtavirta, V. & Aufiero, M., 2014d. *Unstructured Mesh Based Multi-physics Interface for CFD Code Coupling in the Serpent 2 Monte Carlo Code.* Kyoto, Japan, s.n.

Li, L. & Wang, K., 2012. *The First-Principle Coupled Calculations Using TMCC and CFX for the Pinwise Simulation of LWR.* Knoxville, Tennessee, USA, s.n.

Lozano, J., Aragones, J. & Garcia-Herranz, N., 2008. *Transient analysis in the 3D nodal kinetics and thermal-hydraulics ANDES/COBRA coupled code system.* Interlaken, Switzerland, s.n.

Lozano, J., Jimenez, J., Garcia-Herranz, N. & Aragones, J., 2010. Extension of the analytic nodal diffusion solver ANDES to triangular-z geometry and coupling with COBRA-IIIc for hexagonal core analysis. *Annals of Nuclear Energy 37*, pp. 380-388.

Magedanz, J. et al., 2012. *High-fidelity multiphysics simulation of BWR fuel assembly with coupled TORT-TD/CTF.* Knoxville, Tennessee, s.n.

Marck, S. C. v. d., 2006. Benchmarking ENDF/B-VII.0. *Nuclear Data Sheets,* Issue 107, p. 3061–3118.

Marck, S. C. v. d., 2012. Benchmarking ENDF/B-VII.1, JENDL-4.0 and JEFF-3.1.1 with MCNP6. *Nuclear Data Sheets,* Issue 113, p. 2935–3005.

Martin, W., Brown, F., Wilderman, S. & Yesilyurt, G., 2013. *On-The-Fly Neutron Doppler Broadening in MCNP.* Paris, France, s.n.

Mattes, M. & Keinert, J., 2005. *Thermal Neutron Scattering Data for Moderator Materials H20, D20 and ZrHx in the ENDF-6 Format and as ACE Library for the MCNP(X) Codes,* s.l.: s.n.

McCardell, R., Herborn, D. & Houghtaling, J., 1969. *Reactivity Accident Test Results and Analysis for the SPERT III E-core - A Small Oxide-fueled, pressurized-water reactor,* s.l.: U.S. Atomic Energy Commission.

Mervin, B. et al., 2012. *Variance estimation on domain decomposed Monte Carlo eigenvalue calculations.* Knoxville, Tennessee, s.n.

Messaoudi, N. et al., 2004. *Benchmark on the Three-dimensional VENUS-2 MOX Core Measurements - Final Report,* s.l.: s.n.

Misu, S., Spierling, H., Hoju, M. & Anja, K., 2000. *Pin-by-pin gamma scan measurement on MOX and UO2 fuel assemblies and evaluation.* Pittsburg, PA, USA, Proceedings of PHYSOR 2000 conference.

Mittag, S. et al., 2005. Neutron-kinetic code validation against measurements in the Moscow V-1000 zero power facility. *Nuclear Engineering and Design 235*, pp. 485-506.

Moon, B., Kim, Y., Ahn, J. & Rozhikhin, Y., 2006. *VENUS-1 PWR UO2 CORE 2-DIMENSIONAL BENCHMARK EXPERIMENT,* s.l.: s.n.

Na, B. et al., 2000. *Benchmark on the VENUS-2 MOX Core Measurements,* s.l.: s.n.

Olson, A., 2012. *Innovative Methods for Research Reactors, SPERT III E-core Reactor Specification,* s.l.: IAEA CRP.

Palmtag, S. et al., 2014. *Coupled Neutronics and Thermal-hydraulic Solution of a Full-Core PWR Using VERA-CS.* Kyoto, Japan, s.n.

Pavlou, A. & Ji, W., 2014. On-the-fly sampling of temperature-dependent thermal neutron scattering data for Monte Carlo simulations. *Annals of Nuclear Energy 71*, p. 411–426.

Porsch, D. et al., 2012. *Status of Verification & Validation of AREVA's ARCADIA Code System for PWR Applications.* Knoxville, Tennessee, s.n.

Ragusa, J. & Mahadevan, V., 2008. *High-oder spatio-temporal schemes for coupled, multi-physics reactor simulations,* s.l.: s.n.

Ragusa, J. & Mahadevan, V., 2009. Consistent and accurate schemes for coupled neutronics thermal-hydraulics reactor analysis. *Nuclear Engineering and Design 239*, pp. 566-579.

Rempe, K., Smith, K. & Henry, A., 1989. SIMULATE-3 Pin Power Reconstruction: Methodology and Benchmarking. *Nuclear Science and Engineering*, Volume 103, pp. 334-342.

Rohde, U. et al., 2009. *Application of a step-wise verification and validation procedure to the 3D neutron kinetics code DYN3D within the European NURESIM project.* Brussels, Belgium, s.n.

Romano, P. & Forget, B., 2013. The OpenMC Monte Carlo particle transport code. *Annals of Nuclear Energy 51*, pp. 274-281.

Ryu, M., Jung, Y., Cho, H. & Joo, H., 2014. *Solution of the BEAVRS benchmark using the nTRACER direct whole core transport code.* Kyoto, Japan, s.n.

Salko, R., Schmidt, R. & Avramova, M., 2014. Optimization and Parallelization of the Thermal-hydraulic Subchannel Code CTF for High-Fidelity Multi-physics Applications. *Annals of Nuclear Energy*, Volume in press.

Sanchez, R., 2009. Assembly homogenization techniques for core calculations. *Progress in Nuclear Energy,* Volume 51, pp. 14-31.

Sanchez, V., Imke, U., Ivanov, A. & Gomez, R., 2010. *SUBCHANFLOW: A Thermal-Hydraulic Sub-Channel Program to Analyse Fuel Rod Bundles and Reactor Cores.* Cancun, Mexiko, s.n.

Sanders, C. & Gauld, I., 2003. *Isotopic Analysis of High-Burnup PWR Spent Fuel Samples From the Takahama-3 Reactor,* s.l.: s.n.

Shemon, E., Lee, C., Smith, M. & Marin-Lafleche, A., 2014. *NEAMS neutronics: Development and Validation Status.* Charlotte, North Carolina, s.n.

Sjenitzer, B., Hoogenboom, J., Jiménez Escalante, J. & Sanchez Espinoza, V., 2015. Coupling of dynamic Monte Carlo with thermal-hydraulic feedback. *Annals of Nuclear Energy 76*, pp. 27-39.

Smith, K., 1986. Assembly Homogenization Techniques for Light Water Reactor Analysis. *Progress in Nuclear Energy,* 17(3), pp. 303-335.

Smith, K. & Forget, B., 2013. *Challenges in the Development of High-Fidelity LWR Core Neutronics Tools.* Sun Valley, Idaho, USA, s.n.

Sutton, T., Trumbull, T. & Lubitz, C., 2009. *Comparison of Some Monte Carlo Models for Bound Hydrogen Scattering.* LaGrange Park, IL, s.n.

Takeda, T. et al., 2008. *Leakage Dependent SPH Factor for PWR Whole Core Transport Calculation.* Interlaken, Switzerland, s.n.

Tatsumi, M., Hyoudou, H. & Sugiura, K., 2005. *Development and Verification of SCOPE2: Advanced Core Calculation for PWRs.* Avignon, France, s.n.

Tatsumi, M. & Yamamoto, A., 2003. Advanced PWR core calculation based on multi-group nodal transport method in three-dimensional pin-by-pin geometry. *Nuclear Science and Technology 40*, pp. 376-387.

Tereshonok, V. et al., 2008. *Description of a transient casued by the switching-off of one of the four operating MCP at nominal reactor power at NPP Kalinin Unit 3,* s.l.: OECD Nuclear Energy Agency/Nuclear Science Committee.

Todorova, N., Taylor, B. & Ivanov, K., 2002. *Pressurized Water Reactor Main Steam Line Break (MSLB) benchmark - Volume III: Results of Phase 2 on 3-D Core Boundary Conditions Model,* s.l.: OECD Nuclear Energy Agency/Nuclear Science Committee.

Treibig, J., Hager, G. & Wellein, G., 2010. *LIKWID: A Lighweight Performance-Orientated Tool Suites for x86 Multicore Environments.* s.l., s.n., pp. 207-216.

Trumbull, T., 2006. Treatment of nuclear data for transport problems containing detailed temperature distributions. *Nuclear Technology 156*, p. 75–86.

Unal, C. et al., 2011. Improved best estimate plus uncertainty methodology, including advanced validation concepts, to license evolving nuclear reactors. *Nuclear Engineering and Design 241*, pp. 1813-1833.

United States Nuclear Regulatory Commission, 1975. *Reactor Safety Study: An Assessment of Accident Risks in U.S. Commercial Nuclear Power Plants,* s.l.: s.n.

van der Marck, S., Meulekamp, R. & Hogenbirk, A., 2005. *New temperature interpolation in MCNP.* Avignon, France, s.n.

Vazquez, M., Tsige-Tamirat, H., Ammirabile, L. & Martin-Fuertes, F., 2012. Coupled neutronics thermal-hydraulics analysis using Monte Carlo and sub-channel codes. *Nuclear Engineering and Design 250*, pp. 403-411.

Viitanen, T., 2009. *Implementing a Doppler-preprocessor of cross section libraries in reactor physics code Serpent,* s.l.: Master's thesis. Helsinki University.

Viitanen, T. & Leppänen, J., 2012a. *Explicit Temperature Treatment in the Monte Carlo Neutron Tracking Routines - First Results.* Knoxville, Tennessee, s.n.

Viitanen, T. & Leppänen, J., 2012b. Explicit Treatment of Thermal Motion in Continuous-Energy Monte Carlo Tracking Routines. *Nuclear Science and Engineering 171*, p. 165–173.

Viitanen, T. & Leppänen, J., 2013. *Optimizing the Implementation of the Target Motion Sampling Temperature Treatment Technique - How Fast Can It Get?.* Sun Valley, Idaho, USA, s.n.

Wang, R., Xu, Y., Hudson, N. & Downar, T., 2013. Validation of the U.S. NRC Coupled Code System TRITON/TRACE/PARCS using the Special Power Excursion Reactor Test III. *Nuclear Technology 183*, pp. 504-514.

Weber, D. et al., 2007. High-Fidelity Light Water Reactor Analysis with the Numerical Nuclear Reactor. *Nuclear Science and Engineering 155*, pp. 395-408.

Williams, M. & Rearden, B., 2008. SCALE-6 Sensitivity/Uncertainty Methods and Covariance Data. *Nuclear Data Sheets 109*, pp. 2796-2800.

Williamson, R. et al., 2012. Multidimensional multiphysics simulation of nuclear fuel behavior. *Journal of Nuclear Materials 423*, pp. 149-163.

Xu, Y., 2006. *Multi-physics coupled code reactor analysis with U.S. NRC code system TRACE/PARCS.* Vancouver, Canada, s.n.

Yamaji, K. et al., 2014. *Validation of the Nodal Kinetics Code System GALAXY/COSMO-K Using the SPERT-III E-core Experiments.* Kyoto, Japan, s.n.

Yamamoto, A. et al., 2010. AEGIS: an advanced lattice physics code for light water reactor analysis. *Nuclear Engineering and Technology 42*, pp. 500-519.

Yamamoto, A. & Ikeno, T., 2005. Impact of pin-by-pin thermal-hydraulic feedback modelling on steady-state core characteristics. *Nuclear Technology 149*, pp. 175-188.

Yamamoto, A., Kitamura, Y. & Yamane, Y., 2004a. Cell homogenization methods for pin-by-pin calculations tested in slab geometry. *Annals of Nuclear Energy 31*, pp. 825-847.

Yamamoto, A., Tatsumi, M., Kitamura, M. & Yamane, Y., 2004b. Improvement of the SPH method for pin-by-pin core calculations. *Nuclear Science and Technology 41*, pp. 1155-1165.